AFRL-AFOSR-UK-TR-2022-0033

Theoretical and experimental investigation of second-order atmospheric effects impairing W-band SatCom systems

Luini, Lorenzo
POLITECNICO DI MILANO
PIAZZA LEONARDO DA VINCI 32
MILANO, MILANO, 20133
ITA

03/18/2022
Final Technical Report

DISTRIBUTION A: Distribution approved for public release.

Air Force Research Laboratory
Air Force Office of Scientific Research
European Office of Aerospace Research and Development
Unit 4515 Box 14, APO AE 09421

REPORT DOCUMENTATION PAGE

PLEASE DO NOT RETURN YOUR FORM TO THE ABOVE ORGANIZATION.

1. REPORT DATE	2. REPORT TYPE	3. DATES COVERED	
20220318	Final	START DATE 20170930	END DATE 20200529

4. TITLE AND SUBTITLE
Theoretical and experimental investigation of second-order atmospheric effects impairing W-band SatCom systems

5a. CONTRACT NUMBER	5b. GRANT NUMBER	5c. PROGRAM ELEMENT NUMBER
	FA9550-17-1-0335	61102F

5d. PROJECT NUMBER	5e. TASK NUMBER	5f. WORK UNIT NUMBER

6. AUTHOR(S)
Lorenzo Luini

7. PERFORMING ORGANIZATION NAME(S) AND ADDRESS(ES)
POLITECNICO DI MILANO
PIAZZA LEONARDO DA VINCI 32
MILANO, MILANO 20133
ITA

8. PERFORMING ORGANIZATION REPORT NUMBER

9. SPONSORING/MONITORING AGENCY NAME(S) AND ADDRESS(ES)	10. SPONSOR/MONITOR'S ACRONYM(S)	11. SPONSOR/MONITOR'S REPORT NUMBER(S)
EOARD UNIT 4515 APO AE 09421-4515	AFRL/AFOSR IOE	AFRL-AFOSR-UK-TR-2022-0033

12. DISTRIBUTION/AVAILABILITY STATEMENT
A Distribution Unlimited: PB Public Release

13. SUPPLEMENTARY NOTES

14. ABSTRACT
The main goal of this work was to develop physically-based models, which can be used
to predict the propagation conditions for Earth-space communication systems operating at W band, for which no experimental data are currently available. To this aim, the first part of this work was devoted to a brief overview on the main impairments induced by tropospheric constituents on EM waves in the 10-100 GHz range, among which the signal attenuation is the prevalent one. The second part of the work on the experimental activities was devoted to evaluating the
effectiveness of two Fade Mitigation Techniques.

15. SUBJECT TERMS

16. SECURITY CLASSIFICATION OF:			17. LIMITATION OF ABSTRACT	18. NUMBER OF PAGES
a. REPORT	b. ABSTRACT	c. THIS PAGE		
U	U	U	SAR	182

19a. NAME OF RESPONSIBLE PERSON	19b. PHONE NUMBER *(Include area code)*
ATTILA SZEP	314 235 6044

Dipartimento di Elettronica, Informazione e Biongegneria

Politecnico di Milano

20133 Milano (Italy)
Piazza Leonardo Da Vinci 32
Tel. (+39) 02-23993400
Telefax (+39) 02-23993587

Reference: Final Report of EOARD Award FA9550-17-1-0335

THEORETICAL AND EXPERIMENTAL INVESTIGATION OF SECOND-ORDER ATMOSPHERIC EFFECTS IMPAIRING W-BAND SATCOM SYSTEMS

Title:	Final report
Contract:	EOARD Award FA9550-17-1-0335
Period of Performance:	30th September 2017 – 29th May 2020
Emitting Entity:	Politecnico di Milano
Principal Investigator:	Dr. Lorenzo Luini
Authors:	Dr. Lorenzo Luini, Prof. Carlo Riva

DISTRIBUTION A: Distribution approved for public release. Distribution unlimited

DISTRIBUTION A: Distribution approved for public release. Distribution unlimited

EOARD AWARD FA9550-17-1-0335

EOARD Program Manager: Dr. Barrett Flake

THEORETICAL AND EXPERIMENTAL INVESTIGATION OF SECOND-ORDER ATMOSPHERIC EFFECTS IMPAIRING W-BAND SATCOM SYSTEMS

Final report (30th September 2017 – 29th May 2020)

DISTRIBUTION A: Distribution approved for public release. Distribution unlimited

DISTRIBUTION A: Distribution approved for public release. Distribution unlimited

Table of contents

LIST OF FIGURES **VII**

LIST OF TABLES **XVI**

1. INTRODUCTION **1-1**

2. MAIN EFFECTS OF THE TROPOSPHERE ON ELECTROMAGNETIC WAVES **2-1**
2.1. Tropospheric attenuation 2-1
2.1.1. Gaseous attenuation 2-1
2.1.2. Clouds and fog attenuation 2-6
2.1.3. Rain attenuation 2-11
2.1.4. Melting layer effects 2-17

3. THE ALPHASAT ALDO PARABONI PROPAGATION EXPERIMENT **3-1**
3.1. Introduction and scientific motivation 3-1
3.2. The Alphasat Aldo Paraboni experiment 3-2
3.2.1. System architecture 3-2
3.2.2. The Communication Experiment 3-9
3.2.3. The Propagation Experiment 3-12
3.3. The NASA/EOARD propagation experiment station 3-13
3.3.1. System architecture 3-13
3.3.2. Measurements 3-16
3.3.3. Beacon data calibration 3-24
3.3.4. Statistical analysis 3-36
3.3.5. Site diversity 3-45
3.3.6. Time diversity 3-49
3.3.7. Fade duration 3-53
3.3.8. Fade slope 3-58

4. SPACE-TIME MULTIEXCELL **4-1**
4.1. Introduction 4-1
4.2. Rain attenuation modeling 4-1
4.3. Single rain cell temporal evolution 4-2

DISTRIBUTION A: Distribution approved for public release. Distribution unlimited

4.4. Rain field temporal evolution: single event 4-3
4.5. Combination of rain events: ST MultiEXCELL 4-7
4.6. Preliminary validation of ST MultiEXCELL 4-11
4.7. Reference application scenario: Rome, NY (USA) and V/W band SatCom system 4-16

5. RAIN ATTENUATION FREQUENCY SCALING: DATA AND MODELS 5-1
5.1. Introduction 5-1
5.2. Experimental setup and data processing 5-2
5.2.1. Processing of disdrometer data 5-2
5.2.2. Vertical atmospheric profiles 5-2
5.2.2. Processing of beacon data to extract rain attenuation 5-2
5.3. The Enhanced Synthetic Storm Technique (E-SST) 5-6
5.4. Results and discussion 5-8
5.4.1. Rain attenuation prediction: direct application of the E-SST 5-8
5.4.2. Rain attenuation prediction: direct application of the E-SST 5-11

6. TOTAL ATTENUATION FREQUENCY SCALING: FROM KA BAND TO W BAND 6-1
6.1. Introduction 6-1
6.2. Frequency scaling of total tropospheric attenuation: model development 6-1
6.2.1. Water vapour attenuation 6-2
6.2.2. Cloud attenuation 6-3
6.2.3. Rain attenuation 6-4
6.2.4. Total attenuation 6-4
6.3. Frequency scaling of tropospheric attenuation: the simplified model 6-8
6.3.1. Separation of tropospheric attenuation components: the simplified approach 6-8
6.3.2. Frequency scaling using the simplified approach 6-11
6.4. Results and discussion 6-16
6.5. Prediction of total attenuation at W band 6-17
6.5.1. Time diversity 6-19
6.5.2. Fade duration 6-22
6.5.3. Fade slope 6-24

7. CONCLUSIONS 7-1

REFERENCES R-1

LIST OF SYMBOLS, ABBREVIATIONS, AND ACRONYMS S-1

DISTRIBUTION A: Distribution approved for public release. Distribution unlimited

List of Figures

Fig. 2-1. Frequency spectrum of the specific attenuation due to gases, calculated using the Liebe MPM93 model [Liebe et al., 1993]. 2-6

Fig. 2-2. Real and imaginary part of the refractive index of water for T = 0 °C and 5 °C. 2-9

Fig. 2-3. Specific attenuation due to fog (T = 0 °C) as a function of frequency and for different liquid water content values [ITU-R P.840-8]. 2-10

Fig. 2-4. Typical shape of falling rain drops, for different sizes; the black line represents the most probable shape derived from several drops within the same size class (figure extracted from [Thurai et al., 2014]). 2-12

Fig. 2-5. Trend of the specific attenuation due to rain with frequency, for different rain rates, calculated according to recommendation ITU-R P.838-3 [ITU-R P.838-3]. 2-15

Fig. 2-6. Specific attenuation at 12.5 GHz: comparison among 6 analytical DSDs. 2-16

Fig. 2-7. Specific attenuation at 27.5 GHz: comparison among 6 analytical DSDs. 2-16

Fig. 2-8. Specific attenuation at 49.5 GHz: comparison among 6 analytical DSDs. 2-17

Fig. 2-9. Schematic view of the vertical profile for stratiform rain with the melting layer in evidence 2-18

Fig. 2-10. Typical average vertical profile of specific attenuation, estimated using the physically-based simulator of the effects of the melting layer on electromagnetic waves (ESA/POLIMI model, [D'Amico et al., 1998]). 2-18

Fig. 3-1. Q-band horn antenna of the propagation payload onboard the Alphasat satellite (curtesy of Space Engineering). 3-3

Fig. 3-2. TDP#5 Aldo Paraboni propagation experiment: calculated and measured coverage (gain) of the Ka band (left) and Q band (right) beacons. 3-4

Fig. 3-3. Overview of the Spino d'Adda experimental station hosting the Alphasat terminal.....3-5

Fig. 3-4. Alphasat terminal installed at Tito Scalo. 3-5

Fig. 3-5. Architecture of the Alphasat grounds station installed at Spino d'Adda and Tito Scalo. 3-7

Fig. 3-6. System architecture of the Alphasat Aldo Paraboni experiment. Green and black arrows refer to the channels for the propagation and communication experiments, respectively. 3-8

Fig. 3-7. Location of the current receiving stations for the Alphasat propagation experiment (May 2020)…… 3-8

Fig. 3-8. Sites in Milan and Spino d'Adda where the NASA and ASI experimental equipment is installed, respectively. 3-13

DISTRIBUTION A: Distribution approved for public release. Distribution unlimited

Fig. 3-9. NASA equipment on the rooftop of the Dipartimento di Elettronica, Informazione e Bioingegneria (DEIB), Politecnico di Milano. 3-14

Fig. 3-10. Complete system architecture of the NASA station. 3-16

Fig. 3-11. Sample screenshot (July 1st, 2014) of the NASA DRX data acquisition software: real-time FFT spectra of the Ka-band and Q-band signals (top side) and recent time series of P_{lev} and f_{peak} for both channels (bottom side)....3-17

Fig. 3-12. Example of the power levels received on the 29th of June, 2014. 3-18

Fig. 3-13. Temporal trend of f_{peak} associated to signal reported in Fig. 3-12. 3-18

Fig. 3-14. Sample screenshot of the Young Weather Station data acquisition software (14th July, 2014). 3-19

Fig. 3-15. Time series of the meteorological quantities collected by the weather station (29th June, 2014)....3-21

Fig. 3-16. Sample screenshot of the disdrometer data acquisition software (2nd July, 2014). 3-22

Fig. 3-17. Time series of the some of the data collected by the disdrometer (29th June, 2014)....3-23

Fig. 3-18. Sample time series of the brightness temperature collected by the radiometer (19th December, 2016) along the path to Alphasat (35.42° elevation). 3-24

Fig. 3-19. Procedure for the calculation of propagation parameters. T is the temperature; p is the pressure; RH is the relative humidity; A_L, A_V and A_{ox} are the path attenuations due to clouds, water vapor and oxygen, respectively; V and L are the integrated water vapor and integrated liquid water, respectively; T_B is the brightness temperature and T_{mr} is the mean radiating temperature. 3-28

Fig. 3-20. Time series of the brightness temperature collected by the radiometer (19th December, 2016). 3-30

Fig. 3-21. Time series of the integrated water vapor content V estimated from the radiometric measurements (19th December, 2016). 3-31

Fig. 3-22. Time series of the integrated liquid water content L estimated from the radiometric measurements (19th December, 2016). 3-31

Fig. 3-23. Time series of the total tropospheric attenuation estimated from the radiometric measurements (19th December, 2016). 3-32

Fig. 3-24. Time series of the brightness temperature at 31.4 GHz, with preliminary identification of rainy periods (1st May, 2016). 3-33

Fig. 3-25. Time series of the rain rate derived from the disdrometer (1st May, 2016). 3-33

Fig. 3-26. Power levels derived from the beacon receivers (1st May, 2016). 3-34

Fig. 3-27. Time series of A_B, A_{MWR} and A_{diff}' (1st May, 2016). 3-35

DISTRIBUTION A: Distribution approved for public release. Distribution unlimited

Fig. 3-28. Time series of the calibrated total attenuation derived from the beacon power levels and estimated by the radiometer (1st May, 2016). 3-35

Fig. 3-29. Yearly CCDFs of total attenuation (separate years, Ka band) 3-36

Fig. 3-30. Yearly CCDFs of total attenuation (separate years, Q band).....3-37

Fig. 3-31. Yearly CCDFs of total attenuation (full 5-year period, Ka band and Q band)......3-37

Fig. 3-32. Monthly CCDFs of total attenuation (Ka band). 3-38

Fig. 3-33. Monthly CCDFs of total attenuation (Q band).....3-38

Fig. 3-34. CCDF of the rain rate derived from the disdrometer (full 5-year period).....3-41

Fig. 3-35. Monthly CCDF of the rain rate derived from the disdrometer (full 5-year period).....3-41

Fig. 3-36. Scatterplot between T_{mr} and the ground temperature T_G, along with fitting linear expression (f = 72.5 GHz)......3-42

Fig. 3-37. Scatterplot between T_{mr} and the ground relative humidity RH_G, along with fitting linear expression (f = 72.5 GHz)......3-42

Fig. 3-38. Scatterplot between T_{mr} and the ground pressure P_G, along with fitting linear expression (f = 72.5 GHz). 3-43

Fig. 3-39. Comparison between T_{mr} as calculated from RAOBS data plus the Liebe MPM93 model and as estimated from the ground temperature through (3-16) (f = 72.5 GHz). 3-44

Fig. 3-40. CCDFs of the attenuation derived from the radiometer: comparison between the data filtered using the SSI and the full dataset. 3-45

Fig. 3-41. CCDFs of the brightness temperature: comparison between the data filtered using the SSI and the full dataset......3-45

Fig. 3-42. Example of total attenuation data (5th of November, 2014) for Spino d'Adda (top) and for Milan (bottom) 3-46

Fig. 3-43. Sample signals collected at the two sites during a rainy day (Ka band on the top, Q band on the bottom); red and green lines are associated to Spino d'Adda and Milan receivers, respectively, while the black line represents the site diversity attenuation level. 3-47

Fig. 3-44. Rain rate time series as measured by the 1-minute integration time raingauge installed at Spino d'Adda and by the 1-minute integration time disdrometer installed in Milan (same day as in Fig. 3-45).....3-47

Fig. 3-45. CCDFs of total total attenuation at 19.7 GHz for the two receivers installed in Spino d'Adda and in Milan. Also the two-station site diversity CCDF is reported in the figure, as well as the curve that would be obtained by a two-site diversity scheme with statistical independent stations...3-48

Fig. 3-46. CCDFs of total tropospheric attenuation at 39.4 GHz for the two receivers installed in Spino d'Adda and in Milan. Also the two-station site diversity CCDF is reported in the figure, as well as the curve that would be obtained by a two-site diversity scheme with statistical independent stations 3-48

DISTRIBUTION A: Distribution approved for public release. Distribution unlimited

Fig. 3-47. Procedure to estimate the time diversity gain from attenuation time series: selection of the minimum attenuation value between A(t) and A(t+Δt) for each instant t.....3-49

Fig. 3-48. Calculation of time diversity gain from the reference and the time diversity CCDFs. 3-50

Fig. 3-49. CCDFs of attenuation (f = 19.7 GHz), obtained from the original beacon measurements (i.e. no FMT, sampling frequency equal to 8 Hz), as well as the attenuation statistics achieved by implementing time diversity, for different retransmission delays. Full 2014-2019 period.....3-51

Fig. 3-50. Time diversity gain G as a function of the retransmission delay and of the exceedance probability P (f = 19.7 GHz). Full 2014-2019 period. 3-52

Fig. 3-51. CCDFs of attenuation (f = 39.4 GHz), obtained from the original beacon measurements (i.e. no FMT, sampling frequency equal to 8 Hz), as well as the attenuation statistics achieved by implementing time diversity, for different retransmission delays. Full 2014-2019 period.....3-52

Fig. 3-52. Time diversity gain G as a function of the retransmission delay and of the exceedance probability P (f = 39.4 GHz). Full 2014-2019 period. 3-53

Fig. 3-53. Definition of fade duration, i.e. the duration for which a certain attenuation threshold is exceeded. 3-54

Fig. 3-54. CCDFs of the fade duration (f = 19.7 GHz), obtained from the beacon measurements collected in Milan (full 5-year period). 3-55

Fig. 3-55. CCDFs of the fade duration (f = 39.4 GHz), obtained from the beacon measurements collected in Milan (full 5-year period). 3-55

Fig. 3-56. CCDFs of the number of fades (f = 19.7 GHz), obtained from the beacon measurements collected in Milan (full 5-year period). 3-56

Fig. 3-57. CCDFs of the number of fades (f = 39.4 GHz), obtained from the beacon measurements collected in Milan (full 5-year period). 3-56

Fig. 3-58. Definition of fade slope, i.e. the rate of attenuation change in time (dB/s). 3-57

Fig. 3-59. CCDFs of the fade slope (f = 19.7 GHz), obtained from the beacon measurements collected in Milan (full 5-year period).....3-58

Fig. 3-60. CCDFs of the fade slope (f = 39.4 GHz), obtained from the beacon measurements collected in Milan (full 5-year period).....3-58

Fig. 3-61. Probability density function of the fade slope (f = 19.7 GHz), obtained from the beacon measurements collected in Milan (full 5-year period). 3-59

Fig. 3-62. Probability density function of the fade slope (f = 39.4 GHz), obtained from the beacon measurements collected in Milan (full 5-year period). 3-59

Fig. 4-1. Example of temporal evolution for a rain cell (i.e. $R_M(t)$ and $\rho_0(t)$) with R_P = 50 mm/h and k = 30. 4-3

DISTRIBUTION A: Distribution approved for public release. Distribution unlimited

Fig. 4-2. Top graph: temporal evolution of the rainy area, normalized to the maximum value reached during a rain event η_P (calculated over 81 rain events). Results expressed in terms of mean and median values, and percentiles (0.2 and 0.8). Bottom graph: percentage of the events used to produce the statistics in the top graph. 4-3

Fig. 4-3. Sample radar-derived rain map showing different rain cells forming larger clusters. 4-4

Fig. 4-4. PDF of the intercellular distance NNICD and of the interaggregate distance NNIAD used to produce realistic rain fields with MultiEXCELL [Luini and Capsoni, 2011]. 4-4

Fig. 4-5. Sample temporal trend of the normalized rainy area η_P. 4-6

Fig. 4-6. Example of map evolution with v = 18 m/s (westward horizontal wind). 4-6

Fig. 4-7. PDF of the target fractional rainy area η_P for Spino d'Adda, Italy. 4-8

Fig. 4-8. Fractional rainy area rate of change s_η as a function of the maximum fractional rainy area within the event, $\eta_P^{\max}$ 4-9

Fig. 4-9. Progressive generation of the rain events and associated P(R).....4-10

Fig. 4-10. Trend of the rain amount accumulated in 6 hours for a sample year in Spino d'Adda: ERA40 database and ST MultiEXCELL. 4-11

Fig. 4-11. P(R) calculated from the rain events generated by ST MultiEXCELL and from rain gauge data (Spino d'Adda, Italy). 4-12

Fig. 4-12. Reference and model-derived PDF of the fractional rainy area η_P (Spino d'Adda, Italy).4-12

Fig. 4-13. Sample time series of the rain rate for three different positions of the "virtual rain gauge" on the map (Spino d'Adda, Italy).....4-13

Fig. 4-14. Sample ST MultiEXCELL rain map and positions of the virtual rain gauge.....4-14

Fig. 4-15. Trend of the temporal correlation coefficient ρ_T as a function of the time lag Δt, derived from the rain events generated by ST MultiEXCELL and from rain gauge data (Spino d'Adda, Italy)……..4-14

Fig. 4-16. Trend of the spatial correlation coefficient ρ_S as a function of the distance d, derived from the ST MultiEXCELL rain events and from MultiEXCELL rain maps (Spino d'Adda, Italy). 4-15

Fig. 4-17. Rain attenuation statistics at 50 GHz for Rome, NY, obtained from the ST MultiEXCELL synthetic maps: single site (blue line) and two-site (several baseline values) system. 4-17

Fig. 4-18. Rain attenuation statistics at 70 GHz for Rome, NY, obtained from the ST MultiEXCELL synthetic maps: single site (blue line) and two-site (several baseline values) system. 4-18

Fig. 4-19. Rain attenuation statistics at 80 GHz for Rome, NY, obtained from the ST MultiEXCELL synthetic maps: single site (blue line) and two-site (several baseline values) system. 4-18

Fig. 4-20. Rain attenuation statistics at 90 GHz for Rome, NY, obtained from the ST MultiEXCELL synthetic maps: single site (blue line) and two-site (several baseline values) system. 4-19

DISTRIBUTION A: Distribution approved for public release. Distribution unlimited

Fig. 4-21. Site diversity gain at 50 GHz for Rome, NY, obtained from the ST MultiEXCELL rain maps: two-site diversity scheme. *4-20*

Fig. 4-22. Site diversity gain at 70 GHz for Rome, NY, obtained from the ST MultiEXCELL rain maps: two-site diversity scheme. *4-20*

Fig. 4-23. Site diversity gain at 80 GHz for Rome, NY, obtained from the ST MultiEXCELL rain maps: two-site diversity scheme. *4-21*

Fig. 4-24. Site diversity gain at 90 GHz for Rome, NY, obtained from the ST MultiEXCELL rain maps: two-site diversity scheme. *4-21*

Fig. 4-25. Rain attenuation statistics at 50 GHz for Rome, NY, obtained from ST MultiEXCELL maps: single site (blue line) and two-site system (several values of A_{th} for fixed baseline of 20 km). *4-23*

Fig. 4-26. Number of switches in a year between the stations as a function of the threshold A_{th} (50 GHz, 20 km baseline in Rome, NY). *4-23*

Fig. 4-27. Rain attenuation statistics at 50 GHz for Rome, NY, obtained from ST MultiEXCELL maps: single site (blue line) and two-site system (several values of A_{th} for fixed baseline of 50 km). *4-24*

Fig. 4-28. Number of switches in a year between the stations as a function of the threshold A_{th} (50 GHz, 50 km baseline in Rome, NY). *4-24*

Fig. 4-29. Rain attenuation statistics at 70 GHz for Rome, NY, obtained from ST MultiEXCELL maps: single site (blue line) and two-site system (several values of A_{th} for fixed baseline of 20 km). *4-25*

Fig. 4-30. Number of switches in a year between the stations as a function of the threshold A_{th} (70 GHz, 20 km baseline in Rome, NY). *4-25*

Fig. 4-31. Rain attenuation statistics at 70 GHz for Rome, NY, obtained from ST MultiEXCELL maps: single site (blue line) and two-site system (several values of A_{th} for fixed baseline of 50 km). *4-26*

Fig. 4-32. Number of switches in a year between the stations as a function of the threshold A_{th} (70 GHz, 50 km baseline in Rome, NY). *4-26*

Fig. 4-33. Rain attenuation statistics at 80 GHz for Rome, NY, obtained from ST MultiEXCELL maps: single site (blue line) and two-site system (several values of A_{th} for fixed baseline of 20 km). *4-27*

Fig. 4-34. Number of switches in a year between the stations as a function of the threshold A_{th} (80 GHz, 20 km baseline in Rome, NY). *4-27*

Fig. 4-35. Rain attenuation statistics at 80 GHz for Rome, NY, obtained from ST MultiEXCELL maps: single site (blue line) and two-site system (several values of A_{th} for fixed baseline of 50 km). *4-28*

Fig. 4-36. Number of switches in a year between the stations as a function of the threshold A_{th} (80 GHz, 50 km baseline in Rome, NY). *4-28*

Fig. 4-37. Rain attenuation statistics at 90 GHz for Rome, NY, obtained from ST MultiEXCELL maps: single site (blue line) and two-site system (several values of A_{th} for fixed baseline of 20 km). *4-29*

Fig. 4-38. Number of switches in a year between the stations as a function of the threshold A_{th} (90 GHz, 20 km baseline in Rome, NY). *4-29*

DISTRIBUTION A: Distribution approved for public release. Distribution unlimited

Fig. 4-39. Rain attenuation statistics at 90 GHz for Rome, NY, obtained from ST MultiEXCELL maps: single site (blue line) and two-site system (several values of A_{th} for fixed baseline of 50 km). 4-30

Fig. 4-40. Number of switches in a year between the stations as a function of the threshold A_{th} (90 GHz, 50 km baseline in Rome, NY). 4-30

Fig. 5-1. Trend of R_{RC} as a function of A_{rc} for both frequencies. 5-4

Fig. 5-2. CCDFs of the cloud attenuation obtained from RAOBS data (10 full years) and from the beacon data (one full year) by using equation (5-5) at Q band. 5-5

Fig. 5-3. Separation of the attenuation contributions due to gases, clouds and rain for a sample day (4th of February 2017) at Q band. 5-6

Fig. 5-4. Reference outline for the application of the SST: geometry of the link and of the vertical structure of precipitation (top side) and identification of the rain rate values for the calculation of A_{rain} (bottom side). 5-7

Fig. 5-5. Direct application of the SST and the E-SST to a stratiform rain event on the 3rd of February 2017 (peak rain rate R < 10 mm/h), at Q band. 5-9

Fig. 5-6. Direct application of the SST and the E-SST: convective rain event on the 5th of May 2017 (peak rain rate R > 10 mm/h), Ka band data. 5-10

Fig. 5-7. Direct application of the SST and the E-SST at Ka band, whole year statistics. 5-11

Fig. 5-8. Direct application of the SST and the E-SST at Q band, whole year statistics. 5-11

Fig. 5-9. Frequency scaling ratio R_{FS} for the same stratiform event in Fig. 5-5 as calculated using the E-SST model and DSD data, as well as derived from the model included in Recommendation ITU-R P.618-13. 5-13

Fig. 5-10. Frequency scaling ratio R_{FS} for the same convective event in Fig. 5-6 as calculated using the E-SST model and DSD data, as well as derived from the model included in Recommendation ITU-R P.618-13. 5-13

Fig. 5-11. Scaling of the attenuation measured at 19.7 GHz to 39.4 GHz for the stratiform rain event on the 3rd of February 2017 (peak rain rate R < 10 mm/h) in Fig. 5-5. 5-14

Fig. 5-12. Scaling of the attenuation measured at 19.7 GHz to 39.4 GHz for the convective rain event on the 5th of May 2017 (peak rain rate R > 10 mm/h) in Fig. 5-6. 5-14

Fig. 6-1. Workflow of the the Total Attenuation Frequency Scaling (TAFS) model. 6-2

Fig. 6-2. Procedure to calculate a_V from RAOBS data. 6-3

Fig. 6-3. Procedure to calculate a_L from RAOBS data. 6-3

Fig. 6-4. Separation of the attenuation contributions due to gases, clouds and rain for the stratiform rain event collected on the 4th of February 2017 at Ka band. 6-5

DISTRIBUTION A: Distribution approved for public release. Distribution unlimited

Fig. 6-5. Scaling of the water vapour attenuation for the stratiform rain event collected on the 4th of February 2017 from Ka to Q band. 6-5

Fig. 6-6. Scaling of the oxygen attenuation for the stratiform rain event collected on the 4th of February 2017 from Ka to Q band. 6-6

Fig. 6-7. Scaling of the cloud attenuation for the stratiform rain event collected on the 4th of February 2017 from Ka to Q band. 6-6

Fig. 6-8. Scaling of the rain attenuation for the stratiform rain event collected on the 4th of February 2017 from Ka to Q band. 6-7

Fig. 6-9. Application of TAFS to the stratiform rain event collected on the 4th of February 2017; attenuation data scaled from 19.7 GHz to 39.4 GHz. 6-7

Fig. 6-10. The meteorological parameters and the gaseous attenuation prediction on the 4th of February 2017 at Q band (39.4 GHz). 6-9

Fig. 6-11. Procedure to separate between cloud attenuation and rain attenuation. 6-9

Fig. 6-12. Workflow to identify the threshold value of A_f, the key parameter to carry out the separation between cloud attenuation and rain attenuation. 6-10

Fig. 6-13. Separation of the attenuation contributions due to gases, clouds and rain for a sample day (4th of February 2017) at Ka band, adopting S-TAFS. 6-11

Fig. 6-14. Workflow for the Simplified Total Attenuation Frequency Scaling model. 6-12

Fig. 6-15. Scaling of the water vapour attenuation for the stratiform rain event collected on the 4th of February 2017 from Ka to Q band. 6-13

Fig. 6-16. Scaling of the oxygen attenuation for the stratiform rain event collected on the 4th of February 2017 from Ka to Q band. 6-14

Fig. 6-17. Scaling of the cloud attenuation for the stratiform rain event collected on the 4th of February 2017 from Ka to Q band. 6-14

Fig. 6-18. Scaling of the rain attenuation for the stratiform rain event collected on the 4th of February 2017 from Ka to Q band. 6-15

Fig. 6-19. Application of S-TAFS (Drufuca power law for rain attenuation) to the stratiform rain event collected on the 4th of February 2017, at Q band. 6-15

Fig. 6-20. Application of TAFS and S-TAFS for the prediction of the CCDF of total attenuation at 39.4 GHz band; whole year statistics. 6-16

Fig. 6-21. Time series of total attenuation (4th of February 2017) at 39.4 GHz as measured by the experimental equipment and as estimated using TAFS and S-TAFS. 6-17

Fig. 6-22. Application of TAFS at 80 and 90 GHz, whole year statistics. 6-18

Fig. 6-23. Total attenuation scaled from 19.7 GHz to 80 and 90 GHz using TAFS, for the stratiform rain event on the 4th of February 2017. 6-19

DISTRIBUTION A: Distribution approved for public release. Distribution unlimited

Fig. 6-24. Application of TAFS at 80 GHz, whole year statistics. Results without time diversity and implementing time diversity, for different retransmission delays. 6-20

Fig. 6-25. Application of TAFS at 90 GHz, whole year statistics. Results without time diversity and implementing time diversity, for different retransmission delays. 6-20

Fig. 6-26. Time diversity gain G as a function of the retransmission delay and of the outage probability P (f = 80 GHz, year 2017). 6-21

Fig. 6-27. Time diversity gain G as a function of the retransmission delay and of the outage probability P (f = 90 GHz, year 2017). 6-21

Fig. 6-28. CCDFs of the fade duration (f = 80 GHz), obtained from the TAFS predictions, considering different attenuation thresholds.....6-22

Fig. 6-29. CCDFs of the fade duration (f = 90 GHz), obtained from the TAFS predictions, considering different attenuation thresholds.....6-23

Fig. 6-30. CCDFs of the number of fades (f = 80 GHz), obtained from the TAFS predictions, considering different attenuation thresholds. 6-23

Fig. 6-31. CCDFs of the number of fades (f = 90 GHz), obtained from the TAFS predictions, considering different attenuation thresholds. 6-24

Fig. 6-32. CCDFs of the absolute fade slope (f = 80 GHz), obtained from TAFS predictions, considering different attenuation thresholds.. 6-25

Fig. 6-33. CCDFs of the absolute fade slope (f = 90 GHz), obtained from TAFS predictions, considering different attenuation thresholds.. 6-25

Fig. 6-34. Fade slope distribution (f = 80 GHz), obtained from TAFS predictions, considering different attenuation thresholds.....6-26

Fig. 6-35. Fade slope distribution (f = 90 GHz), obtained from TAFS predictions, considering different attenuation thresholds.....6-26

DISTRIBUTION A: Distribution approved for public release. Distribution unlimited

List of Tables

Table 2-1. Spectroscopic data for oxygen attenuation.....2-2

Table 2-2. Spectroscopic data for water-vapour attenuation. 2-3

Table 3-1. Main characteristics of propagation experiment beacons.....3-3

Table 3-2. Main technical characteristics of the Spino d'Adda and Tito Scalo ground stations. 3-6

Table 3-3. List of receiving stations for the Alphasat propagation experiment (May 2020).....3-9

Table 3-4. Details on the NASA station site and geometrical features of the link.....3-15

Table 3-5. Detailed list of the quantities recorded by NASA beacon receivers.....3-16

Table 3-6. Detailed list of the quantities recorded by NASA Young Weather Station.....3-19

Table 3-7. Detailed list of the quantities recorded by NASA disdrometer. 3-21

Table 3-8. Detailed list of the quantities recorded by the radiometer. 3-23

Table 3-9. Frequency channels of the MWR (GHz).....3-26

Table 3-10. RAOBS data used to derive radiometric coefficients.....3-27

Table 3-11. Yearly average and standard deviation (σ) values of T_{mr} (K) as a function of frequency (GHz). 3-28

Table 3-12. Monthly average values of T_{mr} (K) as a function of frequency (GHz).....3-28

Table 3-13. Monthly standard deviation (σ) values of T_{mr} (K) as a function of frequency (GHz).....3-29

Table 3-14. Coefficients for the estimation of the atmospheric attenuation at operational frequencies of the Alphasat propagation experiment (GHz).....3-29

Table 3-15. Yearly average values of A_{ox} (dB) as a function of frequency (GHz).....3-29

Table 3-16. Yearly average mass absorption coefficients a_V and a_W (dB/mm) as a function of frequency (GHz).....3-29

Table 3-17. Beacon data availability: all months.....3-39

Table 3-18. Average monthly beacon data availability. 3-40

Table 3-19. Yearly beacon data availability.....3-40

Table 3-20. Coefficients in (3-16).....3-43

DISTRIBUTION A: Distribution approved for public release. Distribution unlimited

Table 4-1. Main geometrical and electrical characteristics of the Earth-space link in Rome, NY (USA). 4-16

Table 4-2. Values of the k and α coefficients extracted from recommendation ITU-R P.838-3 for the prediction of rain attenuation statistics. 4-16

Table 5-1. Coefficients in (5-7) and values in (5-5). 5-4

Table 5-2. Overall prediction accuracy of the SST and the E-SST (direct application): rain attenuation CCDFs (2017), both bands. 5-11

Table 5-3. Overall prediction accuracy using the frequency scaling approach: rain attenuation CCDFs (2017), Q Band. 5-15

Table 5-4. Overall prediction accuracy of the E-SST (both direct application and frequency scaling approach) on rain attenuation time series (2017), Q band. Included is also the performance of reference frequency scaling using DSD data 5-15

Table 6-1. Water vapor mass absorption coefficient values at different frequencies. 6-3

Table 6-2. Liquid water mass absorption coefficient values at different frequencies. 6-4

Table 6-3. Overall prediction accuracy of TAFS and S-TAFS: total attenuation CCDFs (full 2017), Q band (CCDF). 6-16

Table 6-4. Overall prediction accuracy of TAFS and S-TAFS: total attenuation CCDFs (full 2017), Q band (time series). 6-17

DISTRIBUTION A: Distribution approved for public release. Distribution unlimited

1. INTRODUCTION

The operational frequency of modern satellite communication (SatCom) systems is gradually shifting to the spectrum portion above the traditional Ku band, on the one side to take advantage of the larger bandwidths available, on the other side to avoid channel congestion and interference issues. This is the case of satellites already operating in the Ka band (e.g. Ka-SAT in Europe [KASAT] and DirectTV-12 in the USA [DTV], as for geostationary satellites, and the O3b fleet, as for Medium Earth Orbit – MEO – satellites [O3b]) and of Smart Gateways, which are foreseen to upload contents with carriers in the Q/V band [Jeannin et al., 2014]. Recently, interest has also arisen in SatCom systems planned to operate even at higher frequencies, namely in the W band [EOARD, 2013], [DoD], [Riva et al., 2014], [EOARD 2017]. The same increase in the operational frequency is also occurring in Earth Observation (EO) systems (shift from the X band to the Ka band) because of the need of larger bandwidths required to download at high symbol rates the always increasing amounts of data from EO satellites to ground stations [Arapoglou and Panagopoulos, 2011], [ESA 21083].

As is well known, the main drawback to the use of higher frequencies comes from atmospheric constituents, namely gases, clouds and hydrometeors, which cause extinction (absorption and scattering) of the radiated electromagnetic power [Allnutt, 2010]. Detrimental effects increase significantly with frequency and, accordingly, the availability and Quality of Service (QoS) of SatCom systems become progressively more critical [Riva et al., 2014]. As a result, significant research activities have been promoted so far for the in-depth investigation of such impairments to radio waves propagating in the atmosphere. This also includes propagation experiments such as those involving the ATS, COMSTAR and ACTS satellites in the USA, and the SIRIO, OLYMPUS, ITALSAT and Alphasat satellites in Europe. The latter was selected by the European Space Agency (ESA) for a new experimental activity, conceived (and also supported) by the Italian Space Agency (ASI): the geosynchronous satellite (successfully launched in July of 2013) embarks, among others, a telecommunication payload implementing ACM (Adaptive Coding and Modulation), as well as a propagation payload hosting two continuous-wave transmitters in the Ka (19.7 GHz, vertical polarization) and in the Q (39.4 GHz, 45° tilted linear polarization) bands designed to cover all Europe, where several receiving stations were deployed [Rossi et al., 2016]. The experiment aims not only at increasing the knowledge of the atmospheric impairments at high frequency, but also at verifying the effectiveness of a class of advanced techniques devised to mitigate the detrimental effects of the atmosphere, generally known as Fade Mitigation Techniques (FMTs): ACM [Luini et al., 2011a] and site diversity [Luini et al., 2011b] are typical examples of this kind of solutions.

Besides experiments, also theoretical research activities have been promoted in the past (e.g. [EOARD 2013], [EOARD 2017], [ESA 17760], [ESA 20887]), mainly with the goal of developing models for the prediction of propagation impairments, as well as for the simulation and performance evaluation of systems implementing FMTs. These investigations assume even higher significance when very high frequencies are addressed, such as the V and W bands: as no or scarce experimental data are available, in this case, only models can be used for system design [Riva et al., 2014]. As a result, with the increase in frequency, prediction models are requested to be not only more and more accurate and reliable, but also

DISTRIBUTION A: Distribution approved for public release. Distribution unlimited

flexible enough to be adapted to different scenarios involving the implementation of complex FMTs (e.g. site diversity schemes with more than two stations with different separation distances). For this reason, the recent tendency in theoretical research activities on electromagnetic wave propagation is to move from empirical models, typically developed on the basis of experimental data and valid only in specific climatic regions and/or frequency ranges, to physically-based methodologies which inherently aim at being globally applicable as well as reliable also outside the range of frequencies in which they have been tested. This is the case, for instance, of MultiEXCELL (Multi EXponential CELL) [Luini and Capsoni, 2011], SMOC (Stochastic MOdel of Clouds) [Luini and Capsoni, 2014] and SMOV (Stochastic MOdel of water Vapor) [Luini, 2016], comprehensive methodologies aimed at synthesizing realistic three-dimensional fields of rain, clouds and water vapor, reflecting first-order (Complementary Cumulative Distribution Function – CCDF) and second-order (e.g. spatial correlation) statistics of the above mentioned atmospheric constituents. Supported by EOARD [EOARD 2017], these models have been recently merged into ATM PROP (ATMospheric simulator for PROPagation applications), a methodology to combine rain, cloud and water vapor fields so as to maintain their mutual correlation [Luini, 2017]. As a result, ATM PROP enables to accurately predict the atmospheric effects on EHF (Extremely High Frequency) communication systems of different complexity and in several scenarios such as LEO (Low Earth Orbit), MEO (Medium Earth Orbit), GEO (Geostationary Orbit) satellites, deep-space probes, terrestrial links, etc [Luini and Capsoni, 2015]. On the other side, ATM PROP can generate only "static snapshots" of the meteorological environment, i.e. atmospheric fields that are not correlated in time.

With the aim of improving physically-based models to be applied to scenarios involving complex EHF telecommunications systems, this research activity focuses on extending the capabilities of ATM PROP by studying and modeling the temporal evolution of the atmospheric constituents affecting EM waves in the EHF range. Specifically, a key goal of the effort was to enhance MultiEXCELL by enabling the synthesis of rain fields correlated both in space and time. This activity, initiated in [Capsoni and Luini, 2009], relies on the large set of rain fields observed by the weather radar installed at the experimental station of Spino d'Adda: such data, consisting of rain fields collected every 77 seconds, offer the unique chance to investigate and model the temporal evolution of single rain cells (structural modification), as well as of full rain fields (including combination of rain cells and their translation due to wind). Besides maintaining the local rainfall statistics (only input required to the model) and correctly reproducing the space-time correlation of precipitation, Space-Time (ST) MultiEXCELL generates rain events reflecting both stratiform and convective precipitation types. The main benefit originating from enhancing MultiEXCELL is the chance to predict the time evolution of the interaction between EM waves with the surrounding precipitation environment. In turn, this allows investigating more in detail also aspects of high-frequency SatCom systems typically regarded as secondary effects, which, however, gain more and more significance as the frequency increases (i.e. the performance of the system becomes more and more critical) such as the number and frequency of station switching in diversity schemes.

The second part of the research effort was focused on exploiting the experimental equipment that NASA installed at Politecnico di Milano (Dipartimento di Elettronica, Informazione e Bioingegneria – DEIB) to join the Alphasat propagation experiment [EOARD

DISTRIBUTION A: Distribution approved for public release. Distribution unlimited

2017]. The experimental equipment consists of instruments, which have been continuously collecting propagation data since April 2014: besides the two beacon receivers (Ka band, 19.7 GHz and Q band, 39.6 GHz), the equipment also includes a weather station (monitoring pressure, temperature and relative humidity) and a laser-based disdrometer. The latter instrument (Thies Clima Disdrometer) derives distributions of particle diameters (commonly referred to as Drop Size Distribution – DSD) and velocities based on the magnitude and duration of the recorder fades. In addition, in the frame of the EM wave propagation research activities supported by EOARD [EOARD 2017], a microwave radiometer (4 channels in the Ka, V and W bands) was installed in November 2016. This unique experimental setup has allowed studying the statistics and the temporal dynamics of tropospheric attenuation at W band (of specific interest to EOARD), hence investigating also fade slope and fade duration. This goal was achieved by exploiting a complex and accurate frequency scaling approach, which relies on the combination of several instruments, namely, the radiometer, the beacon receivers and the disdrometer. Specifically, this methodology, developed in this work, allows scaling the beacon-derived attenuation at 19.7 GHz by first separating the total attenuation into its contributions associated to gases, clouds and rain, which are afterwards scaled separately to a higher frequency (including those in the W band) using physically-based approaches: for example, rain attenuation is scaled taking into account the variability of the DSD on a 1-minute basis.

As is clear from the activities listed above, the collection of high-quality experimental data is of key importance: this research activity also included maintaining the NASA receiving equipment, as well as elaborating the collected data until May 2019.

More in detail, Chapter 2 of this report briefly recalls the main effects induced by the troposphere on the propagation of electromagnetic waves. Chapter 3 is fully devoted to the experimental activities: the Alphasat Aldo Paraboni experiment is described, along with the NASA experimental equipment installed at Politecnico di Milano; the chapter also deals with how the data are processed to derive the long-term (5 years) statistics of the total attenuation at 19.7 and 39.4 GHz − both first-order (CCDFs) and second-order (fade slope and fade duration) ones, as well as results on the advantage of implementing time diversity and site diversity, the latter obtained using the concurrent data collected in Spino d'Adda (25 km from Politecnico di Milano). Chapter 4 focuses on the development of ST MultiEXCELL for the generation of rain fields correlated in space and time; the model is afterwards used to simulate a realistic site diversity system deployed in Rome, NY, and more specifically to investigate the impact on the system performance of a hysteresis threshold, introduced to limit the number of station switching. Chapter 5 describes the development of the physically-based methodology aimed at up-scaling in frequency the total attenuation collected at 19.7 GHz. Such frequency scaling method is applied in Chapter 6 to obtain time series of the total attenuation at W band, from which first-order (CCDF) and second-order (fade slope and fade duration) statistics are calculated and investigated.

DISTRIBUTION A: Distribution approved for public release. Distribution unlimited

2. MAIN EFFECTS OF THE TROPOSPHERE ON ELECTROMAGNETIC WAVES

This Chapter offers an overview on the key physical concepts at the basis of the effects induced by tropospheric constituents on electromagnetic waves.

2.1. Tropospheric attenuation

The atmosphere is a thermodynamic system containing water in vapour, liquid and solid state, gases and aerosol, surrounding the Earth up to 400 km. The atmosphere is commonly characterized through temperature, pressure, relative humidity and density of its main components (gases and water).

2.1.1. Gaseous attenuation

Oxygen and water vapour are the gaseous components of the atmosphere influencing the electromagnetic wave propagation in the frequency range from 10 GHz up to 350 GHz. Other gases need to be taken into account only at higher frequencies (e.g. CO_2 for optical wavelengths).

The *oxygen* absorption is mainly due to the resonance of oxygen molecules, which occurs in specific bands: for example, oxygen attenuation is basically negligible up to 40 GHz, but it becomes important around 50 GHz and is dominant around 60 GHz.

The oxygen concentration depends on the air pressure and temperature. The former is characterized by a decreasing exponential profile with the height, while the latter is highly influenced by daily, seasonal and geographical variations. Oxygen absorption increases with the decrease in temperature.

The *water vapour* absorption, due to the molecular interaction with electromagnetic waves, can be calculated as the sum of two terms, which are linear and quadratic functions of the water vapour density, respectively. Water vapour absorption is linked to meteorological parameters like pressure, temperature and water vapour density.

In principle, the procedure to calculate the gaseous attenuation along Earth-space paths consists in two steps:

1) calculation of the specific attenuation due to gases γ_G (dB/km) at any point along the propagation path;
2) calculation of the total path attenuation due to gases A_G by integration of all the contributions.

In practice, this approach is complex because it requires the knowledge at any time of the complete spatial distribution along the path of meteorological parameters like air pressure, temperature and gases concentration. Indeed, this information can be retrieved from radiosonde observations (RAOBS), typically collected between two to four times per day at airports. As an aternative, semi-empirical expressions exist to define an effective height for oxygen and water vapor, h_G, such that the path attenuation A_G is simply given by [ITU-R P.676-11]:

$$A_G = \gamma_G \, h_G \quad \text{(dB)} \tag{2-1}$$

DISTRIBUTION A: Distribution approved for public release. Distribution unlimited

In (2-1), γ_G is the gaseous specific attenuation at ground level. Different simplified expressions have been proposed for h_G, which depends on the pressure, temperature and relative humidy at ground level [Luini and Riva, 2016], [Luini and Riva, 2017], [ITU-R P.676-12].

The most acknowledged methodology for the prediction of γ_G is named MPM93 and was proposed by Liebe *et al.* in [Liebe et al., 1993]. The model, which is currently adopted in Annex 1 of recommendation ITU-R P.676-12 [ITU-R P.676-12], defines the intensity and the width of oxygen and water vapor spectral absorption lines in the 1-1000 GHz frequency range. The contribution of each line, which depends on pressure *P*, relative humidity *RH* and temperature *T*, is summed up to yield the overall specific attenuation due to gases.

The specific gaseous attenuation γ_G is given by:

$$\gamma_G = \gamma_{OX} + \gamma_{WV} = 0.182\, f \left[N''_{OX}(f) + N''_{WV}(f) \right] \quad \text{(dB/km)} \tag{2-2}$$

where γ_{OX} and γ_{WV} are the specific attenuations due to oxygen and water vapour, respectively, f is the frequency (in GHz), while $N''_{OX}(f)$ and $N''_{WV}(f)$ are the imaginary parts of the frequency-dependent complex refractivities:

$$N''_{OX}(f) = \sum_{i(OX)} S_i F_i + N''_D(f) \tag{2-3}$$

$$N''_{WV}(f) = \sum_{i(WV)} S_i F_i \tag{2-4}$$

In (2-3) and (2-4), S_i is the intensity of the *i*-th oxygen or water vapour line, F_i is the oxygen or water vapour line shape factor, and the summations extend over all the lines listed in Table 2-1 and Table 2-2.

Table 2-1. Spectroscopic data for oxygen attenuation.

f_0	a_1	a_2	a_3	a_4	a_5	a_6
50.474214	0.975	9.651	6.690	0.0	2.566	6.850
50.987745	2.529	8.653	7.170	0.0	2.246	6.800
51.503360	6.193	7.709	7.640	0.0	1.947	6.729
52.021429	14.320	6.819	8.110	0.0	1.667	6.640
52.542418	31.240	5.983	8.580	0.0	1.388	6.526
53.066934	64.290	5.201	9.060	0.0	1.349	6.206
53.595775	124.600	4.474	9.550	0.0	2.227	5.085
54.130025	227.300	3.800	9.960	0.0	3.170	3.750
54.671180	389.700	3.182	10.370	0.0	3.558	2.654
55.221384	627.100	2.618	10.890	0.0	2.560	2.952
55.783815	945.300	2.109	11.340	0.0	–1.172	6.135
56.264774	543.400	0.014	17.030	0.0	3.525	–0.978
56.363399	1331.800	1.654	11.890	0.0	–2.378	6.547

DISTRIBUTION A: Distribution approved for public release. Distribution unlimited

56.968211	1746.600	1.255	12.230	0.0	–3.545	6.451
57.612486	2120.100	0.910	12.620	0.0	–5.416	6.056
58.323877	2363.700	0.621	12.950	0.0	–1.932	0.436
58.446588	1442.100	0.083	14.910	0.0	6.768	–1.273
59.164204	2379.900	0.387	13.530	0.0	–6.561	2.309
59.590983	2090.700	0.207	14.080	0.0	6.957	–0.776
60.306056	2103.400	0.207	14.150	0.0	–6.395	0.699
60.434778	2438.000	0.386	13.390	0.0	6.342	–2.825
61.150562	2479.500	0.621	12.920	0.0	1.014	–0.584
61.800158	2275.900	0.910	12.630	0.0	5.014	–6.619
62.411220	1915.400	1.255	12.170	0.0	3.029	–6.759
62.486253	1503.000	0.083	15.130	0.0	–4.499	0.844
62.997984	1490.200	1.654	11.740	0.0	1.856	–6.675
63.568526	1078.000	2.108	11.340	0.0	0.658	–6.139
64.127775	728.700	2.617	10.880	0.0	–3.036	–2.895
64.678910	461.300	3.181	10.380	0.0	–3.968	–2.590
65.224078	274.000	3.800	9.960	0.0	–3.528	–3.680
65.764779	153.000	4.473	9.550	0.0	–2.548	–5.002
66.302096	80.400	5.200	9.060	0.0	–1.660	–6.091
66.836834	39.800	5.982	8.580	0.0	–1.680	–6.393
67.369601	18.560	6.818	8.110	0.0	–1.956	–6.475
67.900868	8.172	7.708	7.640	0.0	–2.216	–6.545
68.431006	3.397	8.652	7.170	0.0	–2.492	–6.600
68.960312	1.334	9.650	6.690	0.0	–2.773	–6.650
118.750334	940.300	0.010	16.640	0.0	–0.439	0.079
368.498246	67.400	0.048	16.400	0.0	0.000	0.000
424.763020	637.700	0.044	16.400	0.0	0.000	0.000
487.249273	237.400	0.049	16.000	0.0	0.000	0.000
715.392902	98.100	0.145	16.000	0.0	0.000	0.000
773.839490	572.300	0.141	16.200	0.0	0.000	0.000
834.145546	183.100	0.145	14.700	0.0	0.000	0.000

Table 2-2. Spectroscopic data for water-vapour attenuation.

f_0	b_1	b_2	b_3	b_4	b_5	b_6
22.235080	.1079	2.144	26.38	.76	5.087	1.00
67.803960	.0011	8.732	28.58	.69	4.930	.82
119.995940	.0007	8.353	29.48	.70	4.780	.79
183.310087	2.273	.668	29.06	.77	5.022	.85
321.225630	.0470	6.179	24.04	.67	4.398	.54
325.152888	1.514	1.541	28.23	.64	4.893	.74

DISTRIBUTION A: Distribution approved for public release. Distribution unlimited

f_0	b_1	b_2	b_3	b_4	b_5	b_6
336.227764	.0010	9.825	26.93	.69	4.740	.61
380.197353	11.67	1.048	28.11	.54	5.063	.89
390.134508	.0045	7.347	21.52	.63	4.810	.55
437.346667	.0632	5.048	18.45	.60	4.230	.48
439.150807	.9098	3.595	20.07	.63	4.483	.52
443.018343	.1920	5.048	15.55	.60	5.083	.50
448.001085	10.41	1.405	25.64	.66	5.028	.67
470.888999	.3254	3.597	21.34	.66	4.506	.65
474.689092	1.260	2.379	23.20	.65	4.804	.64
488.490108	.2529	2.852	25.86	.69	5.201	.72
503.568532	.0372	6.731	16.12	.61	3.980	.43
504.482692	.0124	6.731	16.12	.61	4.010	.45
547.676440	.9785	.158	26.00	.70	4.500	1.00
552.020960	.1840	.158	26.00	.70	4.500	1.00
556.935985	497.0	.159	30.86	.69	4.552	1.00
620.700807	5.015	2.391	24.38	.71	4.856	.68
645.766085	.0067	8.633	18.00	.60	4.000	.50
658.005280	.2732	7.816	32.10	.69	4.140	1.00
752.033113	243.4	.396	30.86	.68	4.352	.84
841.051732	.0134	8.177	15.90	.33	5.760	.45
859.965698	.1325	8.055	30.60	.68	4.090	.84
899.303175	.0547	7.914	29.85	.68	4.530	.90
902.611085	.0386	8.429	28.65	.70	5.100	.95
906.205957	.1836	5.110	24.08	.70	4.700	.53
916.171582	8.400	1.441	26.73	.70	5.150	.78
923.112692	.0079	10.293	29.00	.70	5.000	.80
970.315022	9.009	1.919	25.50	.64	4.940	.67
987.926764	134.6	.257	29.85	.68	4.550	.90

$N_D^{"}(f)$ is the dry continuum due to pressure-induced nitrogen absorption and the Debye spectrum as given by equation (2-11) below.

The line intensity S_i is given by:

$$S_i = \begin{cases} a_1 \cdot 10^{-7} P_{dry} \theta^3 e^{a_2(1-\theta)} & \text{for oxygen} \\ b_1 \cdot 10^{-1} e \theta^{3.5} e^{b_2(1-\theta)} & \text{for water vapor} \end{cases} \quad (2\text{-}5)$$

where:

P_{dry} = dry air pressure (mbar)

e = water vapour partial pressure (mbar) (total barometric pressure $P = P_{dry} + e$)

T = temperature (K)

$\theta = 300/T$.

DISTRIBUTION A: Distribution approved for public release. Distribution unlimited

The water-vapour partial pressure, *e*, can be obtained from the water vapour content, ρ_V (g/m^3) and the temperature, *T* (K), using the expression:

$$e = \frac{\rho_V T}{216.7} \tag{2-6}$$

Spectroscopic data for oxygen are given in Table 2-1, and spectroscopic data for water vapour are given in Table 2-2.

The line-shape factor F_i is calculated as:

$$F_i = \frac{f}{f_i}\left[\frac{\Delta f - \delta(f_i - f)}{(f_i - f)^2 + \Delta f^2} + \frac{\Delta f - \delta(f_i + f)}{(f_i + f)^2 + \Delta f^2}\right] \tag{2-7}$$

where f_i is the oxygen or water vapour line frequency and Δf is the width of the line, given by:

$$\Delta f = \begin{cases} a_3 \cdot 10^{-4}\left(P_{dry}\,\theta^{(0.8-a_4)} 1.1 e\theta\right) & \text{for oxygen} \\ b_3 \cdot 10^{-4}\left(P_{dry}\,\theta^{b_4} + b_5 e\theta^{b_6}\right) & \text{for water vapor} \end{cases} \tag{2-8}$$

The line width Δf is modified to account for Zeeman splitting of oxygen lines and Doppler broadening of water vapour lines:

$$\Delta f = \begin{cases} \sqrt{\Delta f^2 + 2.25 \cdot 10^{-6}} & \text{for oxygen} \\ 0.535\Delta f + \sqrt{0.217\Delta f^2 + \dfrac{2.1316 \cdot 10^{-12} f_i^2}{\theta}} & \text{for water vapor} \end{cases} \tag{2-9}$$

δ in (2-7) is a correction factor that arises due to interference effects in oxygen lines:

$$\delta = \begin{cases} \left(a_5 + a_6\theta\right) \cdot 10^{-4}\left(P_{dry} + e\right)\theta^{0.8} & \text{for oxygen} \\ 0 & \text{for water vapor} \end{cases} \tag{2-10}$$

The dry air continuum arises from the non-resonant Debye spectrum of oxygen below 10 GHz and a pressure-induced nitrogen attenuation above 100 GHz.

$$N_D''(f) = f\,P_{dry}\,\theta^2 \left\{ \frac{6.14 \cdot 10^{-5}}{d\left[1 + \left(\dfrac{f}{d}\right)^2\right]} + \frac{1.4 \cdot 10^{-12} P_{dry}\theta^{1.5}}{1 + 1.19 \cdot 10^{-5} f^{1.5}} \right\} \tag{2-11}$$

where *d* is the width parameter for the Debye spectrum:

$$d = 5.6 \cdot 10^{-4}\left(P_{dry} + e\right)\theta^{0.8} \tag{2-12}$$

Fig. 2-1 shows the specific attenuation due to gases, calculated using the Liebe MPM93 model reported above, for the following standard reference meteorological parameters [STD ATM]: *T* = 15 °C, *P* = 1013.25 mbar and water vapor content (which is tighly linked to *RH*) ρ_V = 7.5 g/m^3. As is clear from the figure, the contribution coming from oxygen is mainly limited to the frequency bands around 60 GHz and 120 GHz, where the specific attenuation can reach values as high as 15 dB/km. On the other hand, the impact of water vapor is associated to three main absorption peaks (centered approximately around 22, 183 and 325

DISTRIBUTION A: Distribution approved for public release. Distribution unlimited

GHz), but it is also given by a linear term providing, in general, more attenuation than the one induced by oxygen (see especially the 210-310 frequency range).

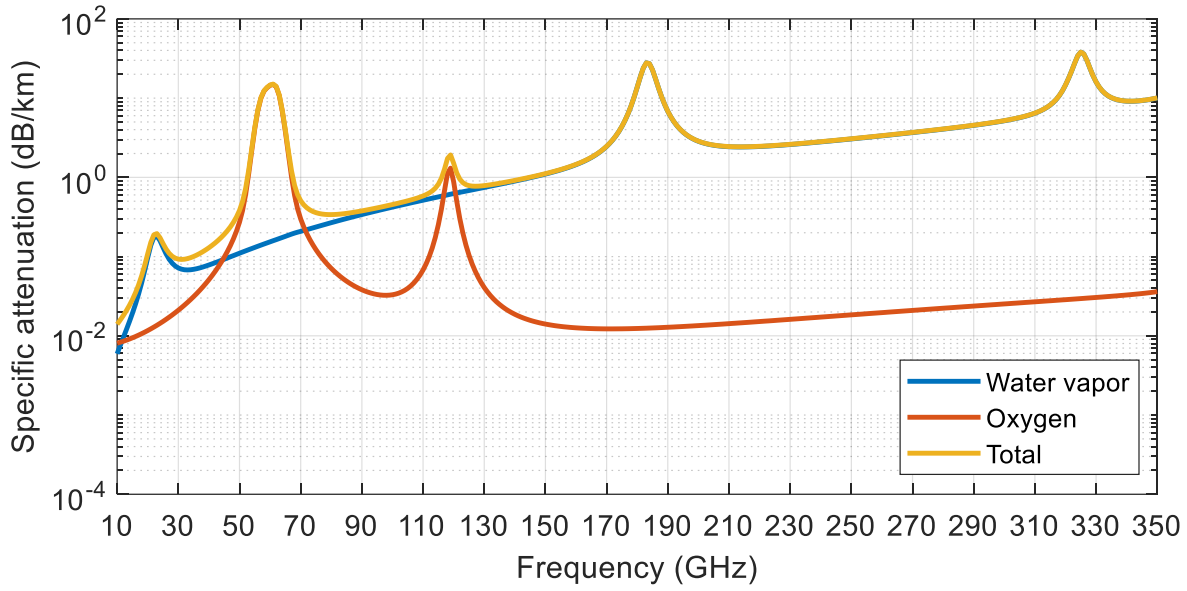

Fig. 2-1. Frequency spectrum of the specific attenuation due to gases, calculated using the Liebe MPM93 model [Liebe et al., 1993].

2.1.2. Cloud and fog attenuation

Clouds and fog consist in the suspension of microscopic water droplets (in the order of microns) formed by condensation of the atmospheric water vapor on the surface of suspended hygroscopic particles, named condensation nuclei.

In meteorology, the term fog is used when the visibility is less than 1 km, whereas mist is an intermediate state where the relative humidity is above 60% and the visibility exceeds 1 km. Finally, haze is any suspension of dry solid particles (smoke, dust, sand, salt, etc.) of microscopic size. Fog, produced by cooling of the air, can be classified into [Ahrens, 1994]:

- *Radiation fog*: generated by radiational cooling of the Earth surface that lowers the air temperature enough to reach saturation. It is usually observed at night during the cold season and in calm wind conditions and it is typical of continental areas.
- *Advection fog*: due to a wet and warm air mass moving over a cool surface. It is more frequent during spring and requires moderate or fresh breeze blowing. It is further divided into marine fog (produced by advection of marine air from warm to cold oceanic areas) and coastal or maritime fog (originated by warm air masses migrating inland from the sea).
- *Upslope or hill fog*: due to adiabatic cooling of air masses moved up by wind along hill or mountain flanks.
- *Steam fog or sea smoke*: when a cold air mass moves over a warm water surface, the humid air rising over the surface can be cooled enough to form liquid droplets.

DISTRIBUTION A: Distribution approved for public release. Distribution unlimited

- *Frontal fog*: caused by evaporation of the hydrometeors of a warm front when falling into underlying cold air layers. A rapid supersaturation may occur leading to the formation of fog.

As for clouds, they are typically classified into four major classes based on the cloud base height [Ahrens, 1994]:

- *High-level clouds*: cold bodies consisting of ice crystals whose height is typically between 5 and 13 km (in temperate regions). According to their appearance, they are further divided into Cirrus (Ci), Cirrocumulus (Cc) and Cirrostratus (Cs).
- *Mid-level clouds*: primarily made of water droplets with ice-crystals sometimes present (height 2-7 km). They are divided into Altostratus (As) and Altocumulus (Ac).
- *Low-level clouds*: composed of water droplets and, if the air temperature is cold enough, of ice and snow (height < 2 km). They are divided into Stratus (St), Stratocumulus (Sc) and Nimbostratus (Ns), the latter being associated with light-to-moderate precipitation.
- *Vertically developed clouds*: turbulent structures generated through either thermal convection or frontal lifting. The fluffy Cumulus (Cu) associated with fair weather and the Cumulonimbus (Cb), a thunderstorm cloud, belong to this class.

2.1.2.1. Liquid water droplets

The effects of suspended liquid water droplets on EM waves is markedly different from the one induced by gases. Every droplet has a twofold impact on the incoming EM wave: part of the electromagnetic energy is scattered in several directions around the particle, while part of it is absorbed by the particle itself, which causes an increase in its temperature. Accordingly, it is possible to define two effective parameters associated to each particle. Specifically, let us define an area σ_{sc} such that the total energy flux P_{sc} scattered around the droplet equals the power density S (W/m^2) of the incoming wave multiplied by σ_{sc}, i.e [Van de Hulst, 1957], [Deirmendjian, 1969]:

$$P_{sc} = \sigma_{sc} S \tag{2-13}$$

In a similar way, if part of the incoming wave is absorbed by the particle, we define an area σ_{abs} such that

$$P_{abs} = \sigma_{abs} S \tag{2-14}$$

Finally, if P_{ext} is the amount of energy flux subtracted to the incoming wave, then:

$$P_{ext} = \sigma_{ext} S \tag{2-15}$$

Energy conservation requires that

$$\sigma_{ext} = \sigma_{sc} + \sigma_{abs} \tag{2-16}$$

σ_{sc}, σ_{abs}, and σ_{ext} are referred to as scattering cross section, absorption cross section and extinction cross section, respectively. In general, σ_{ext} depends on the wavelength and on the polarization of the incident wave, on particle shape, size and temperature, and on its orientation with respect to the direction of the incident wave.

DISTRIBUTION A: Distribution approved for public release. Distribution unlimited

As anticipated above, the dimension of the water droplets forming clouds and fog is very small: they are in the order of microns. When considering EM waves in the 10-300 GHz, the shortest wavelength is λ = 1 mm (for f = 300 GHz), which is three order of magnitude larger than the size of such droplets. In this case, i.e. when the ratio between the particle size and the wavelength is much smaller than one, the Rayleigh approximation applies. If this is the case, σ_{ext} takes the following expression derived from the Rayleigh theory [McCartney, 1976]:

$$\sigma_{ext} = \sigma_{abs} + \sigma_{sca} = \frac{8\pi^2 r^3}{\lambda} \mathrm{Im}\left(\frac{n^2-1}{n^2+2}\right) + \frac{128}{3}\frac{\pi^5 r^6}{\lambda^4}\left|\frac{n^2-1}{n^2+2}\right|^2 \tag{2-17}$$

where r is the radius of the particle and n is the complex refractive index of water.

Moreover, if absorption prevails over scattering, as it is the case for suspended liquid water in the microwave region, we obtain

$$\sigma_{ext} \approx \sigma_{abs} = \frac{8\pi^2 r^3}{\lambda} \mathrm{Im}\left(\frac{n^2-1}{n^2+2}\right) \tag{2-18}$$

According to (2-18), σ_{ext} is proportional to the particle volume.

The refractive index n quantifies the effect of the chemical composition, thermodynamic phase and temperature of the drops on EM waves. The double-Debye model [Manabe et al., 1987] provides an analytical expression for the real and imaginary parts of the permittivity of water, ε' and ε'', respectively, for frequencies up to 300 GHz, and over a temperature range from -40 °C to 30 °C:

$$\varepsilon'(f) = \varepsilon_2 + \frac{(\varepsilon_0 - \varepsilon_1)}{1+(f/f_D)^2} + \frac{(\varepsilon_1 - \varepsilon_2)}{1+(f/f_S)^2} \tag{2-19}$$

$$\varepsilon''(f) = \frac{f(\varepsilon_0 - \varepsilon_1)}{f_D\left[1+(f/f_D)^2\right]} + \frac{f(\varepsilon_1 - \varepsilon_2)}{f_S\left[1+(f/f_S)^2\right]} \tag{2-20}$$

where:

$\varepsilon = \varepsilon' + j\varepsilon'' = n^2$

$\varepsilon_0 = 77.67 + 103.3(\theta - 1)$, $\varepsilon_1 = 5.48$ and $\varepsilon_2 = 3.51$

$f_D = 20.09 - 142.4(\theta - 1) + 294(\theta - 1)^2$ and $f_s = 590 - 1500(\theta - 1)$ (GHz)

Fig. 2-2 depicts the real and imaginary parts of the refractive index of liquid water in the microwave band (10-300 GHz) according to the double-Debye model. n is plotted for T = 0 °C and T = 5 °C.

DISTRIBUTION A: Distribution approved for public release. Distribution unlimited

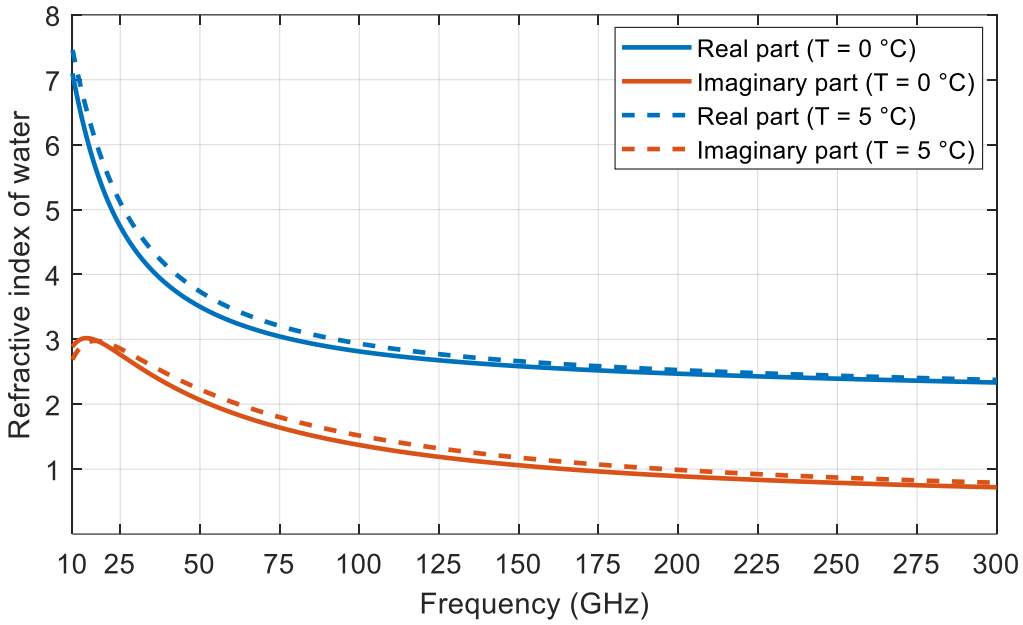

Fig. 2-2. Real and imaginary part of the refractive index of water for T = 0 °C and 5 °C.

Besides simplifying the calculation of the extinction cross section, the Rayleigh approximation also allows expressing the specific attenuation due clouds and fog (cumulative effects of several droplets) as follows:

$$\gamma_{CF} = \frac{0.819\, f}{\varepsilon''(1+\eta^2)}\, w \quad \text{(dB/km)} \tag{2-21}$$

where f is expressed in GHz, and w is the liquid water content in g/m^3, $\eta = (2+\varepsilon')/\varepsilon''$, while ε' and ε'' are calculated as in (2-19) and (2-20).

Fig. 2-3 depicts the trend of γ_{CF} as a function of frequency, for different liquid water contents (T is fixed to 0 °C) [ITU-R P.840-8]. The impact of clouds and fog increases continuously with frequency, reaching up to 7 dB/km at 300 GHz with w = 3 g/m^3, which is a limit value associated to cumulonimbus [Thompson, 2007].

DISTRIBUTION A: Distribution approved for public release. Distribution unlimited

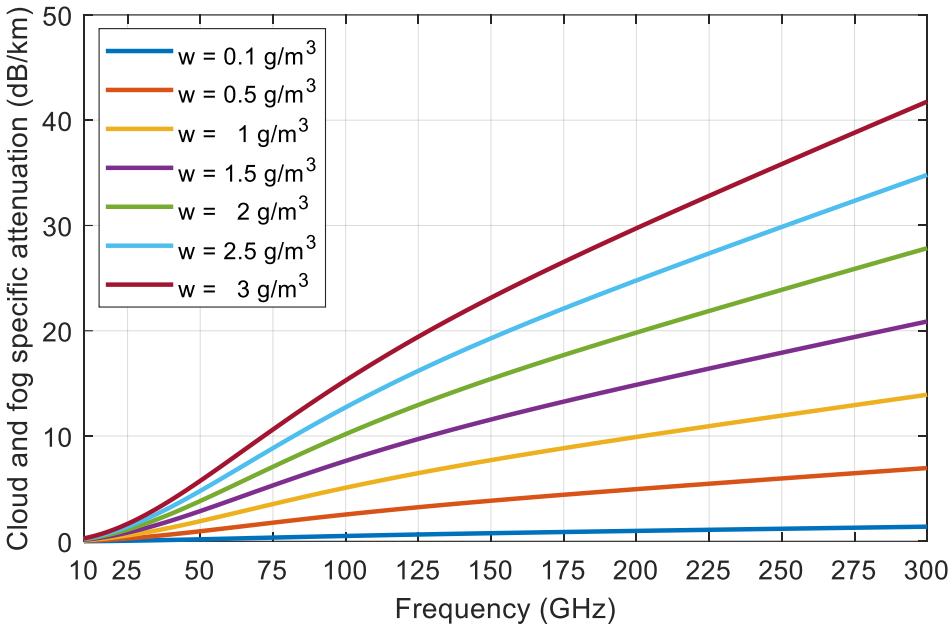

Fig. 2-3. Specific attenuation due to cloud and fog (T = 0 °C) as a function of frequency and for different liquid water content values [ITU-R P.840-8].

2.1.2.2. Ice particles

Ice clouds lie at high altitude. Suspended ice crystals are present for temperatures in the range 0º C < *T* < -70º and the most frequent habits are plates and needles. At temperatures below -25 °C ice crystals are mainly needles, at temperatures from -25 °C to -9 °C they are mainly plates with a hexagonal basis.

The size varies from 20 μm to 4 mm. Characteristic relationships exist between the thickness *h* of plates and their diameter *D*. Similar relationships exist between the diameter *d* and the length *l* of needles [Pruppacher and Klett, 2010].

Common geometrical models used to describe these habits are oblate or prolate spheroids as they are much simpler to manage by electromagnetic solvers. In particular:

- ice needles are modeled as long and narrow prolate spheroids;
- ice plates are modeled as flat oblate spheroids.

The PSD (Particle Size Distribution) is modelled with parameters related to the air temperature *T* and the total ice content.

As in the case of water droplets, aerodynamic effects tend to align the major axes of ice crystals with the horizontal plane. However, differently from what happens with the water droplets, electromagnetic fields of high intensity and rapid variation, as the ones generated during thunderstorms, can orient ice crystals in a preferred direction. This is one of the reasons for sudden changes that occur in depolarization measurements, while the attenuation due to ice, up to 100 GHz, is very limited and is often neglected.

DISTRIBUTION A: Distribution approved for public release. Distribution unlimited

2.1.3. Rain attenuation

Rain is the prevailing phenomenon related to precipitating particles in the atmosphere and, depending on the site, it occurs for a period of time approximately comprised between 1% and 10% in a year (the year is considered as the basic repetition period for weather phenomena). Values as large as 3%-7% are quite common in temperate climates [Luini and Capsoni, 2013]. Rain affects the lower part of the atmosphere; specifically, making reference to temperate climates, rain develops up to a few kilometers during winter because of the low heights of the 0 °C isotherm layer (usually assumed as the vertical limit for the presence of water particles during stratiform events) and up to 10-15 km during thunderstorms (typical of summer periods) because of the strong updrafts/downdrafts which carry water/ice particles even to the highest layers of the atmosphere. Rain consists of drops of spheroidal shape with equivolumetric diameters varying between few tenths of millimeters to a maximum of 6 millimeters (larger drops are not common because the cohesive force is not as strong as the aerodynamical force). In fact, the hydrometeor shape is far from being spherical if its dimension is large, because of the balance between the internal and external forces acting on the lower surface of the drop in its falling path. Measurements have shown that drops larger than about 1 mm in radius are of oblate spheroidal shape with flattened base [Oguchi, 1983]. As an example, Fig. 2-4 depicts the typical shape of a falling rain drop, for different sizes. The black line represents the most probable shape derived from several drops within the same size class (figure extracted from [Thurai et al., 2014]), which points out that the oblatness increases with the drop dimension.

DISTRIBUTION A: Distribution approved for public release. Distribution unlimited

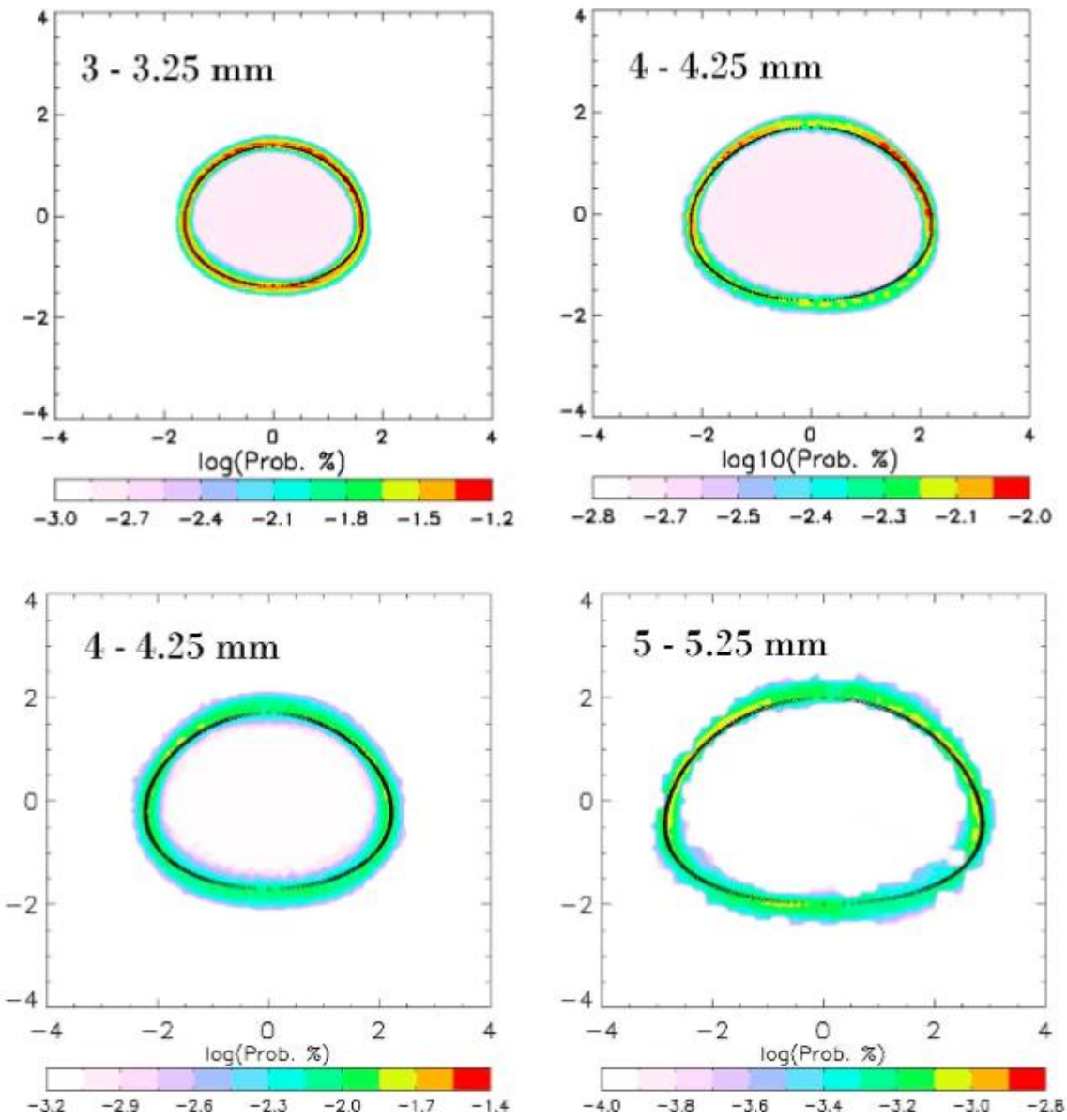

Fig. 2-4. Typical shape of falling rain drops, for different sizes; the black line represents the most probable shape derived from several drops within the same size class (figure extracted from [Thurai et al., 2014]).

For what concerns the impact of hydrometeors on electromagnetic waves, rain represents the main drawback to their propagation at frequencies above 10 GHz because the hydrometeor size is comparable with the wavelength of the incident wave. Other types of precipitation such as hail and snow are not considered in this study because their effects on the propagation of the electromagnetic waves are marginal and their occurrence most likely well below the one of rain.

As already discuseed in Section 2.1.2, each rain drop causes scattering and absorption (i.e. attenuation, overall) on EM waves, and both effects can be expressed in terms of $\sigma_{ext} = \sigma_{sc} + \sigma_{abs}$. However, differently from the water droplets forming fog, the size of rain drops is of the same order of the wavelength considered in the 10-350 GHz range (millimeters

for both). This has a twofold effect: on the one side, abosorption and scattering are comparable (while for clouds and fog, $\sigma_{ext} \approx \sigma_{abs}$ as indicated in (2-18)), and, on the other side, the specific attenuation due to rain, γ_R, has a more complex expression compared to (2-21). Indeed, γ_R depends on the size of each drop as follows:

$$\gamma_R = 4.343 \cdot 10^3 \int_D \sigma_{ext}(D, f)\, N(D)\, dD \quad \text{(dB/km)} \tag{2-22}$$

Equation (2-22) points out that the specific attenuation due to rain is obtained by weighting the fade induced by a rain drop with given diameter D (σ_{ext}) with the number of rain drops with that size. This latter information is provided by $N(D)$ (typically referred to as Drop Size Distribution − DSD), which indicates the number of rain drops with given diameter D contained in 1 m^3. The DSD, whose units are mm^{-1} m^{-3}, is typically measured by specific instruments, named disdrometers, which count and classify drops according to their size; the DSD can be derived from the output of a disdrometer as follows [Lam et al., 2012]:

$$N(D_i) = \frac{10^6 n_i}{S\, v(D_i)\, T\, \Delta D_i} \quad (\text{mm}^{-1}\ \text{m}^{-3}) \tag{2-23}$$

In (2-23), n_i is the number of raindrops whose diameter falls in the i-th class (with mean diameter D_i), ΔD_i (mm) represents the width of each drop-size class, S (mm^2) is the disdrometer sampling area, T (seconds) is the instrument integration time, $v(D_i)$ (m/s) is the terminal velocity of rain drops, which, for example, can be extracted from the work of Gunn and Kinzer [Gunn and Kinzer, 1949] or derived directly from the disdrometer measurements. From the DSD, the rain rate R (mm/h) can be calculated as [Lam et al., 2012]:

$$R = 600 \cdot 10^{-6} \pi \int_D N(D) D^3 v(D) dD \quad \text{(mm/h)} \tag{2-24}$$

Besides measured from a disdrometer, the DSD can also be modeled using analytical functions that have been proposed in the past by several authors (see e.g. [Shettle, 1989] and [Ulbrich, 1983]). The most acknowledged ones are:

- Marshall and Palmer (1948)
- Joss et al.- drizzle (1968)
- Joss et al.- widespread (1968)
- Joss et al.- thunderstorm (1968)
- Moupfouma and Tiffon (1982)
- Ulbrich (Gamma distribution) (1983)
- Ulbrich (Laws & Parson) (1983)
- Ajayi and Olsen (1985)
- Brussard and Watson (1995)

The Gamma function proposed by Ulbricht in [Ulbrich, 1983] is one of the most used models for the DSD of rain:

$$N(D) = N_0 D^{\mu} e^{-\Lambda D} \tag{2-25}$$

DISTRIBUTION A: Distribution approved for public release. Distribution unlimited

where N_0 is the intercept parameter, measured in $mm^{-1-\mu}\ m^{-3}$, Λ is the slope parameter measured in mm^{-1}, and μ is the shape parameter. Measurements show that μ typically ranges between –3 and 8 [Ulbrich, 1983]. Moreover, according to [Atlas et al., 1973], it is possible to relate both N_0 and Λ to μ, such that the latter turns out to be the only parameter driving the shape of (2-25):

$$N_0 = 6 \cdot 10^3 e^{(3.2-\ln 5)\mu - \ln 5} \tag{2-26}$$

$$\Lambda = 0.2\left[\frac{R}{33.31 N_0 5^{1+\mu}\Gamma(4.67+\mu)}\right]^{\frac{1}{4.67+\mu}} \tag{2-27}$$

where Γ the Gamma function and R is the rain rate in mm/h.

According to the ratio of the size of the drop to the wavelength inside the particle and to the shape of the drop, different electromagnetic techniques can be used to compute the extinction cross section σ_{ext}. In fact, as already mentioned, if drops are small with respect to the wavelength, the Rayleigh scattering approach can be used; if they are large, but spherical, the exact Mie solution can be applied; in the most general case, including oblate spheroids, approximate numerical methods have to be used. The most popular computational methods are:

- Rayleigh (1871)
- Mie (1908)
- Point Matching (1960)
- Extended Boundary Condition Method (EBCM) or T- matrix (1975) [Mishchenko et al., 2002]
- Fredholm-Integral-Method (FIM) (1978)
- Unimoment method (1978)
- Spheroidal expansion (1980)
- Boundary element method (1993)

In order to calculate σ_{ext} of a drop with equivolumetric diameter D at a given frequency f, with specified wave polarization, it is necessary to choose the shape of the drop, usually expressed in terms of aspect ratio, i.e. the ratio of the minor to the major axis of the drop b/a. The most popular models in the propagation community are:

- Pruppacher and Beard (1970)
- Pruppacher and Pitter (1971)
- Oghuci (1973)
- Beard and Chuang (1987) [Beard and Chuang, 1987]
- Chuang and Beard (1990)
- RAL/Beard-Chuang (1995)

DISTRIBUTION A: Distribution approved for public release. Distribution unlimited

From f and T, the complex refractive index of water is deduced; from f and λ the so called size parameter of the drop, i.e. its electrical dimension, is derived; from the assumed drop shape and the equivolumetric diameter D, the aspect ratio is found. These parameters are the input data of any electromagnetic technique for the calculation of σ_{ext} and, hence, of γ_R, using (2-22).

As extensively shown in the literature [ITU-R P.838-3], [Lam et al., 2012], the results from (2-22), obtained for different rain intensity values, can be fitted with high accuracy using the following power law equation:

$$\gamma_R = kR^{\alpha} \quad \text{(dB/km)} \tag{2-28}$$

Fig. 2-5 reports the trend of γ_R with frequency, for different rain rates, calculated according to recommendation ITU-R P.838-3 [ITU-R P.838-3]: while specific attenuation increases monotonically with R, reaching even values as high 50 dB/km for 200 mm/h ($f \approx 115$ GHz), γ_R with frequency increases up tp 100 GHz, after which, depending on R, a stable or slightly decreasing trend emerges.

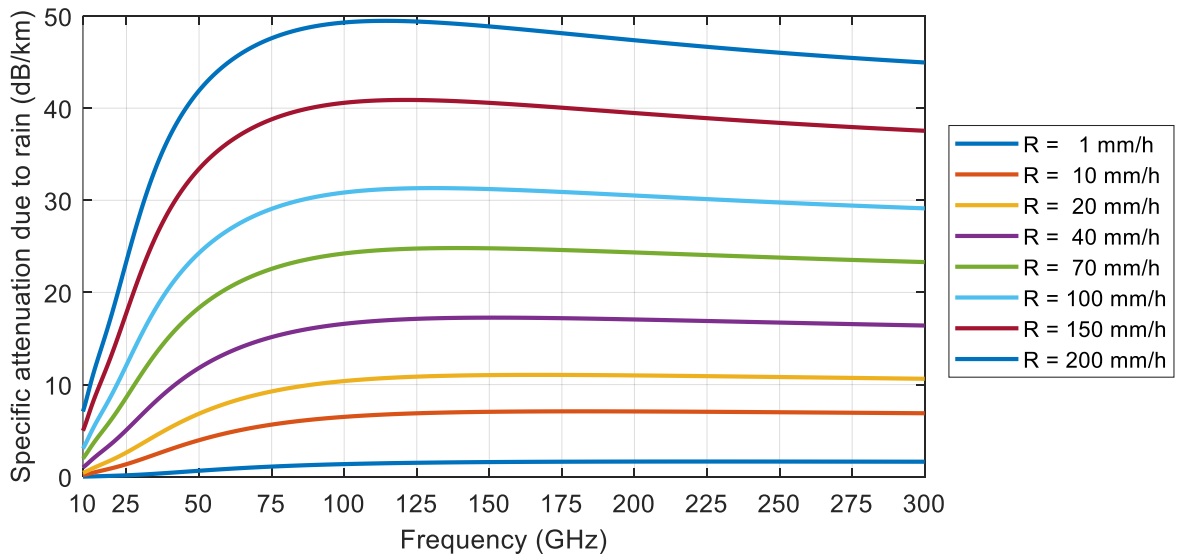

Fig. 2-5. Trend of the specific attenuation due to rain with frequency, for different rain rates, calculated according to recommendation ITU-R P.838-3 [ITU-R P.838-3].

The specific attenuation values depicted in Fig. 2-5 are actually just a reference to give a hint about how intense the fades caused by rain can be. Indeed, out of all the parameters on which γ_R depends on, the DSD has the stronger impact. This is shown in Fig. 2-6, Fig. 2-7 and Fig. 2-8, which depict γ_R calculated according to (2-22) at 12.5, 27.5 and 49.5 GHz, respectively, using different analytical DSDs (wave polarization: horizontal; link elevation: 0°; extinction cross section calculation: FIM method; water temperature: T = 10 ºC; drop shape: Pruppacher and Beard). Indeed, the discrepancy among the curves is quite marked and frequency dependent, being the difference in specific attenuation for a given value of the rain rate at 12.5 and 49.5 GHz as large as a factor of 1.5 when moving between the two extreme DSDs, but almost negligible at 27.5 GHz. Overall, these sample results point out the

DISTRIBUTION A: Distribution approved for public release. Distribution unlimited

importance of using local disdromteric data for a proper prediction of the specific attenuation due to rain.

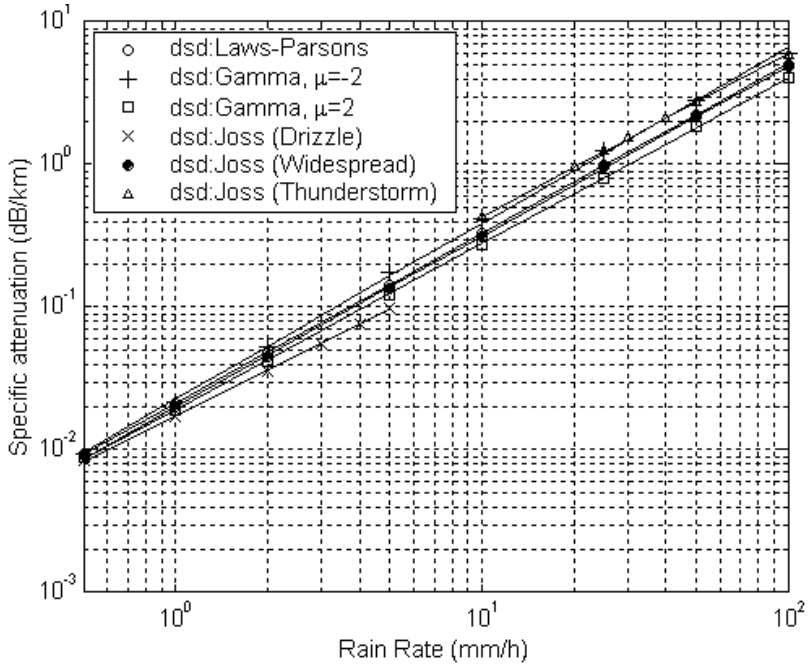

Fig. 2-6. Specific attenuation at 12.5 GHz: comparison among 6 analytical DSDs.

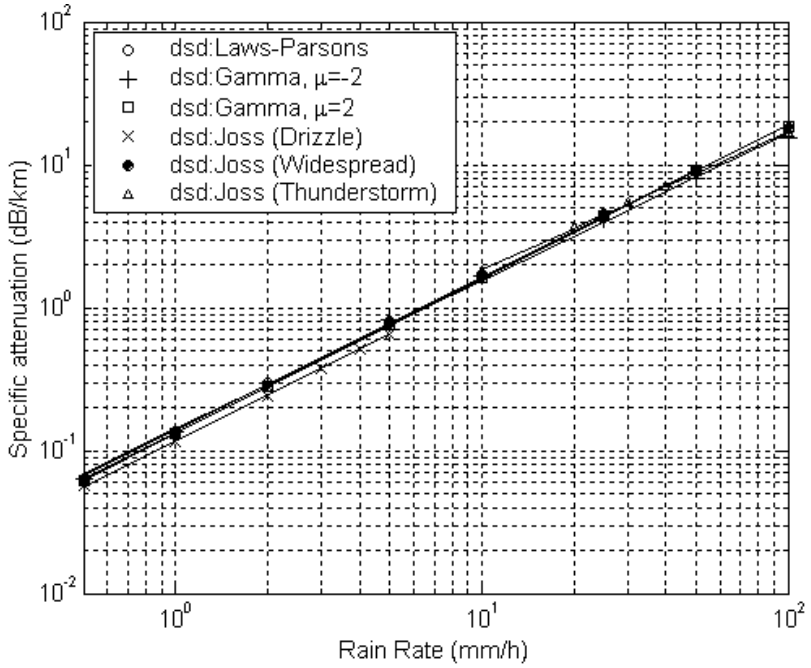

Fig. 2-7. Specific attenuation at 27.5 GHz: comparison among 6 analytical DSDs.

DISTRIBUTION A: Distribution approved for public release. Distribution unlimited

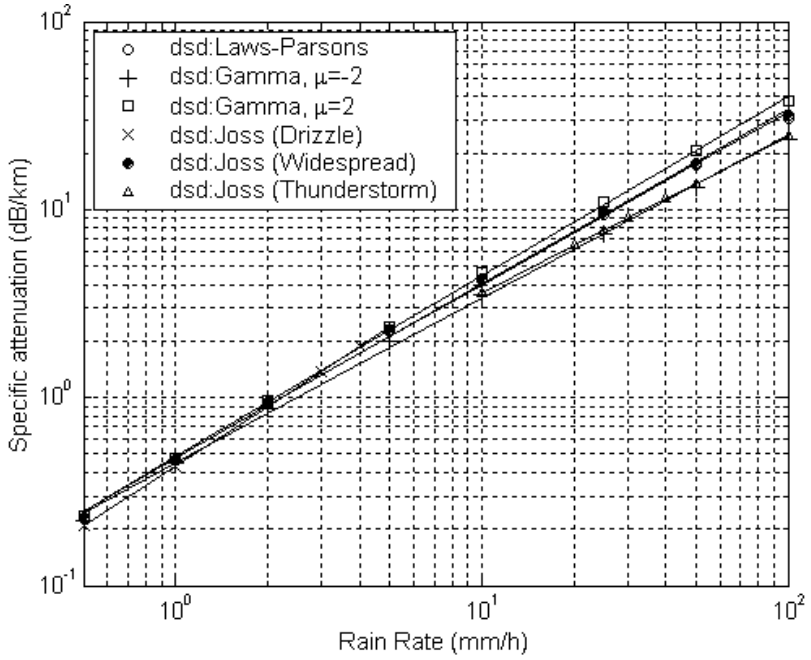

Fig. 2-8. Specific attenuation at 49.5 GHz: comparison among 6 analytical DSDs.

2.1.4. Melting layer effects

As already mentioned, two distinct rain regimes are schematically considered in radio propagation, although this subdivision is not used by meteorologists: stratiform (or widespread/large-scale) rain and convective (or shower-type) rain. The former type of rain events are associated to the presence of a melting layer (or bright band in radar terminology), located below the 0 °C isotherm [Raynaud et al., 2000]. It consists in a slab about 600 m thick where the ice particles aloft melt during their fall to the ground. Above and below the melting layer there are dry snowfall and liquid rainfall, respectively. The altitude of the melting layer is very variable from event to event being associated to the 0 °C isotherm height: roughly, the melting layer height ranges from less than 1 km in temperate regions up to 4 to 5 km in the tropics. On the other hand, convective rain is usually characterised by nearly vertical columnar cells. As a consequence, from the physical point of view, attenuation models for stratiform rain plus the associated melting layer and for convective rain should be developed separately, though it is not trivial to identify appropriate input parameters for the two types of rain. Fig. 2-9 shows a schematic view of the vertical profile for stratiform events and Fig. 2-10 shows a typical profile of specific attenuation (f = 30 GHz, rain intensity below the melting layer of 1 mm/h), estimated by the physically-based simulator of the effects of the melting layer on electromagnetic waves (ESA/POLIMI model, [D'Amico et al., 1998]).

DISTRIBUTION A: Distribution approved for public release. Distribution unlimited

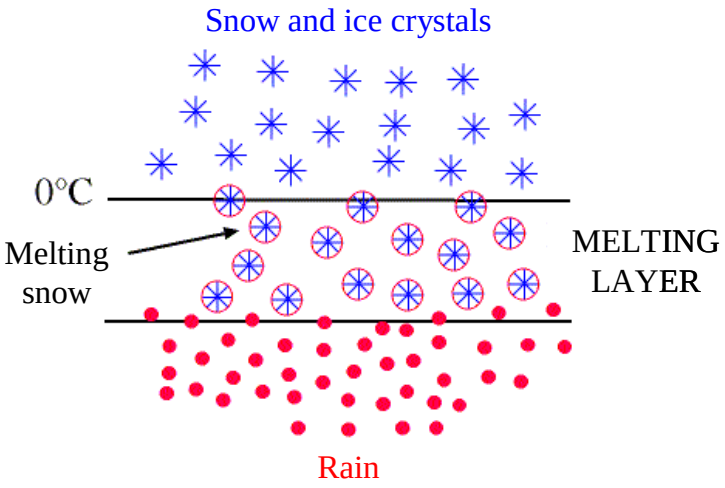

Fig. 2-9. Schematic view of the vertical profile for stratiform rain with the melting layer in evidence.

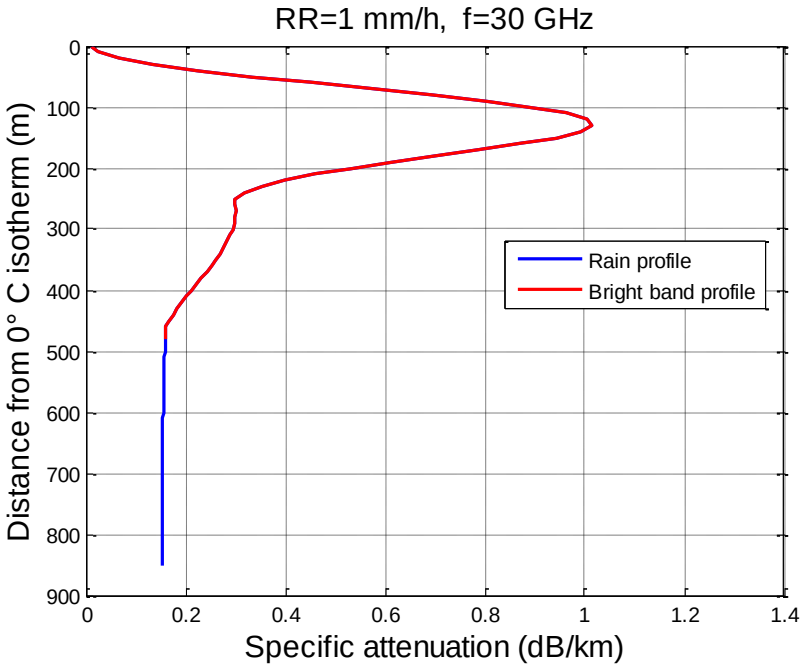

Fig. 2-10. Typical average vertical profile of specific attenuation, estimated using the physically-based simulator of the effects of the melting layer on electromagnetic waves (ESA/POLIMI model, [D'Amico et al., 1998]).

DISTRIBUTION A: Distribution approved for public release. Distribution unlimited

3. THE ALPHASAT ALDO PARABONI PROPAGATION EXPERIMENT

This Chapter gives an overview of the Alphasat Aldo Paraboni propagation experiment and of the participation of NASA and AFRL in such an experiment. Though the present research activity covers the period 2017-2020, this Chapter includes the results on all the propagation data that have been collected since the installation and operation of the NASA experimental equipment (June 2014). However, some information on data processing are not included, especially regarding the period prior to the installation of the radiometer (January 2017): all the details can all be found in [EOARD, 2017].

3.1. Introduction and scientific motivation

Future broadband satellite communication systems are expected to offer terabit capacity and very high data rates, as requested by the current market, both for broadcast and multimedia applications. The goal is to offer satellite-based solutions competitive to the ones provided by the terrestrial network, with, in addition, the ability to directly reach any end-user, regardless of their location. This challenging goal requires the use of high carrier frequencies, such as in the Ka band, Q/V bands and even beyond, in order to exploit the large bandwidth required to support the above-mentioned advanced services.

On the other hand, the utilization of electromagnetic waves in the EHF range (30-300 GHz) for satellite communications calls for the implementation of smart solutions, commonly referred to as Fade Mitigation Techniques (FMTs), to counteract severe atmospheric phenomena without excessive (or even unfeasible) power levels. Typical examples of FMTs are ACM (Adaptive Coding and Modulation), on-board reconfigurable antenna pattern, up/down link power control, site/frequency diversity, smart gateway reconfiguration, etc. The possibility to design and exploit profitably these techniques is based on the knowledge coming from the E.M. wave propagation science, i.e. on accurate models for the space-time distribution of attenuation and on measurements for their validation. For this reason, since the ‘70s, considerable efforts have been spent to set up satellite propagation experiments. Specifically:

- The first **US** satellite experiment to measure slant path signal fading statistics at frequencies above 10 GHz was performed with the NASA Applications Technology Satellite (ATS-5) operating at 15.3/31.625 GHz (downlink/uplink). The satellite was launched in August 1969. Afterwards, the ATS-6 20/30 GHz satellite (1974), the COMSTAR D1, D2, D3 and D4 (19.05/28.56 GHz) series satellites were launched between 1974 and 1981. In addition, a large scale Ka-band propagation experiment (at 20.2 and 27.5 GHz) was conducted with the Advanced Communications Technology Satellite (ACTS), successfully launched in September 1993.
- In **Japan**, early Ka-band satellite-based propagation experiments were performed with the Engineering Test Satellite Type II (ETS-II). These experiments were conducted at Kashima from May 1977 to April 1978, at 34.5 GHz. Large scale Ka-band propagation experiments were then conducted in several Japanese sites (Kashima, Sendai, Wakkanai, Yamagawa, Yokohama) for 2, 3 or 4 years (1978 to 1982) using Japan’s domestic Medium Capacity Communication satellite for Experimental Purpose (CS) at 19.5 GHz (downlink). After the CS propagation experiments, satellites CS-2a,b and CS-3a,b were launched in 1983 and 1989, respectively, with a propagation payload operating at 19.45 GHz.

DISTRIBUTION A: Distribution approved for public release. Distribution unlimited

- In **Europe**, the European Space Agency (ESA) experimental telecommunication satellite OLYMPUS was operational from mid-1989 to mid-1993. It was equipped with three propagation beacons at 12.50, 19.77 and 29.66 GHz. Co-polar and cross-polar attenuation measurements, along with radiometer and local meteorological data, were recorded in about 50 different locations in Western Europe. The research activity yielded high quality propagation statistics. The Politecnico di Milano experimental station of Spino d'Adda participated in the propagation experiment with a 3.5-m receiving station, which was managed by the National Research Council and the Politecnico di Milano.
- In **Italy**, the ITALSAT satellite, owned by the Italian Space Agency (ASI), was launched in January 1991 from the Kourou basis in French Guyana, with the purpose of experimenting advanced digital transmissions at high data rate and of conducting propagation experiments in the 18.7, 39.6 and 49.5 GHz frequency bands. Higher frequencies were chosen in order to ensure the continuous spectral coverage of the experimental results, from the Ka band to the V band. During the ITALSAT propagation experiment a new 3.5-m ground station was installed at Spino d'Adda, where 9 years of data were collected. Data processing and analysis at Spino d'Adda were followed by an intense modelling activity also in the frame of numerous ESA contracts, which led to several models being accepted as standards of the ITU-R (International Telecommunication Union – Radiocommunication Sector).

3.2. The Alphasat Aldo Paraboni experiment

3.2.1. System architecture

The Alphasat Aldo Paraboni experiment was conceived to collect propagation measurements across a wide area, such as Europe, and to directly assess the advantages obtainable from FMTs like ACM.

The **space segment** of the system consists in the Alphasat satellite, which was successfully launched in July 2013; the experiment officially started in November 2013 after the positive closure of the In-Orbit Validation (IOV) phase. The satellite, owned by Inmarsat and flying along a geosynchronous orbit (orbital position at 25° E) with variable inclination not exceeding ±3°, hosts several payloads (some of them with piggy-back configuration), both commercial and scientific ones. Among them, the TDP#5 (Technology Development Payload number 5) was selected by ESA to conduct research activities on radio wave propagation and space telecommunications in the framework of the ARTES 8 Telecom program. Specifically, the TDP#5 payload, developed by Thales Alenia Space Italy, consists of two self-standing elements:

- The communication experiment payload, composed of two transparent transponders operating in the Q/V bands (48 GHz for the uplink and 38 GHz for the downlink) with cross-strapping capabilities. The payload can radiate three beams, two of which are always simultaneously active: a fixed beam always covers the ground station located in Tito Scalo, Italy, while the second beam can switch between the stations located at Spino D'Adda, Italy, and Graz, Austria. The antennas gain is 38.3 and 37.5 dBi EOC (End Of Coverage) when used to receive and transmit, respectively. The nominal output of the transponders is 10 W. No redundancy is foreseen for the communication experiment payload due to mass and power requirement constraints. The Principal Investigator (PI) of the communication experiment is Università di Roma Tor Vergata, Italy.

DISTRIBUTION A: Distribution approved for public release. Distribution unlimited

- The propagation experiment payload, consisting of two continuous wave (CW) beacons operating in the Q and Ka bands, at 39.4 GHz and 19.7 GHz, respectively. The propagation experiment payload is fully redundant. The Principal Investigator (PI) of the propagation experiment is Politecnico di Milano.

The propagation payload, whose Q-band horn antenna is shown in Fig. 3-1 (courtesy of Space Engineering), was commissioned by the Italian Space Agency to ESA, which was responsible for its design, development, manufacturing and testing. Table 3-1 lists the main features of the propagation experiment beacons, which shows that both waves are linearly polarized (90° and 45° for Ka and Q band, respectively). Fig. 3-2 provides additional details on the beacons features by illustrating the calculated and measured coverage (gain): the Ka-band antenna boresight points to the Northern coast of Africa (see details in Table 3-1), while, for the Q-band antenna, the boresight is set to Spino d'Adda.

Fig. 3-1. Q-band horn antenna of the propagation payload onboard the Alphasat satellite (curtesy of Space Engineering).

Table 3-1. Main characteristics of propagation experiment beacons.

Ka band frequency	19.701 GHz	Q band frequency	39.402 GHz
Ka band polarization	Linear V	Q band polarization	Linear tilted 45°
Ka band antenna boresight	32.5° N, 20° E	Q band antenna boresight	45.4° N, 9.5° E
Ka band EIRP	19.5 dBW	Q band EIRP	26.5 dBW

DISTRIBUTION A: Distribution approved for public release. Distribution unlimited

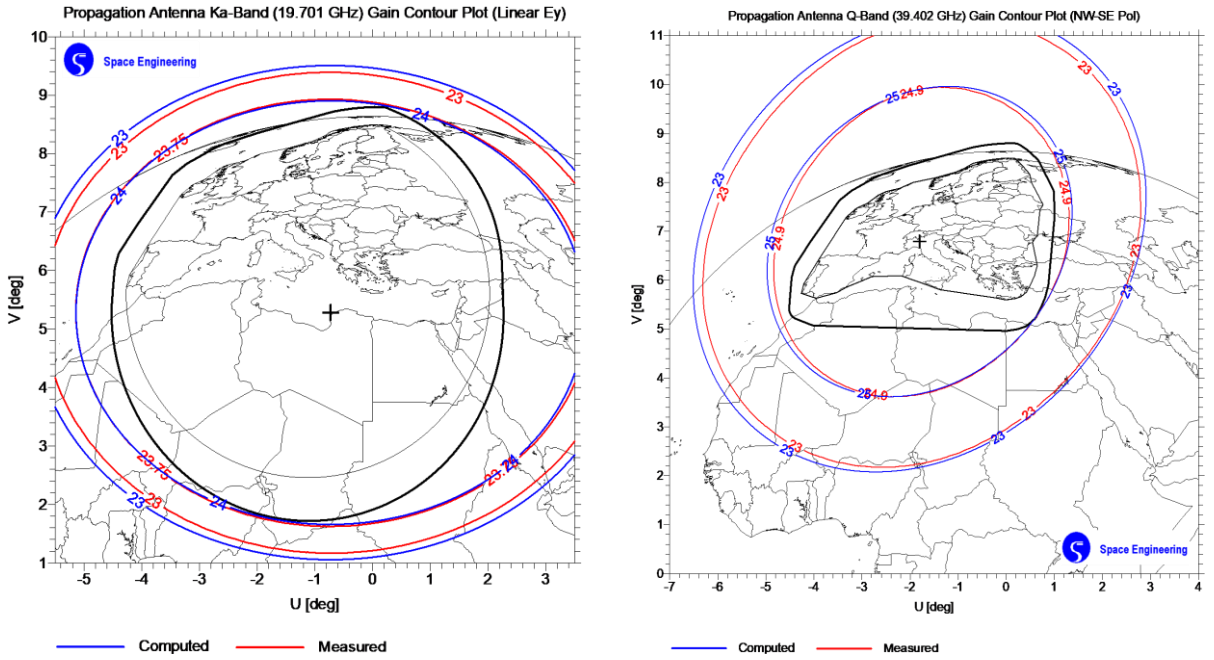

Fig. 3-2. TDP#5 Aldo Paraboni propagation experiment: calculated and measured coverage (gain) of the Ka band (left) and Q band (right) beacons.

As for the **ground segment**, ASI committed the development and deployment of the Italian ground terminals to Space Engineering. As mentioned above, one of these terminals is installed at the experimental station of Spino d'Adda (see Fig. 3-3 depicting an overview of the Spino d'Adda experimental station) where the Experimental Control Center (ECC) for the propagation experiment is also located. Another terminal, identical to the one of Spino d'Adda, is installed in Tito Scalo (see Fig. 3-4) which also hosts the ECC for the communication experiment. In addition, in order to enhance the significance of the experiment, ESA supported the development of additional propagation ground terminals such as the one installed in Graz, Austria.

Table 3-2 lists the main technical characteristics of the Spino d'Adda and Tito Scalo ground stations, including ancillary instruments: besides the beacon receivers sampling power data at 16 Hz and a classic weather station (not mentioned in the table) measuring pressure (*P*), relative humidity (*RH*) and temperature (*T*) data on the ground, the station also hosts RPG-HATPRO multi-channel profiling radiometers to monitor the sky noise temperature, from which the integrated liquid water and water vapor contents can be retrieved, as well as temperature and humidity profiles.

DISTRIBUTION A: Distribution approved for public release. Distribution unlimited

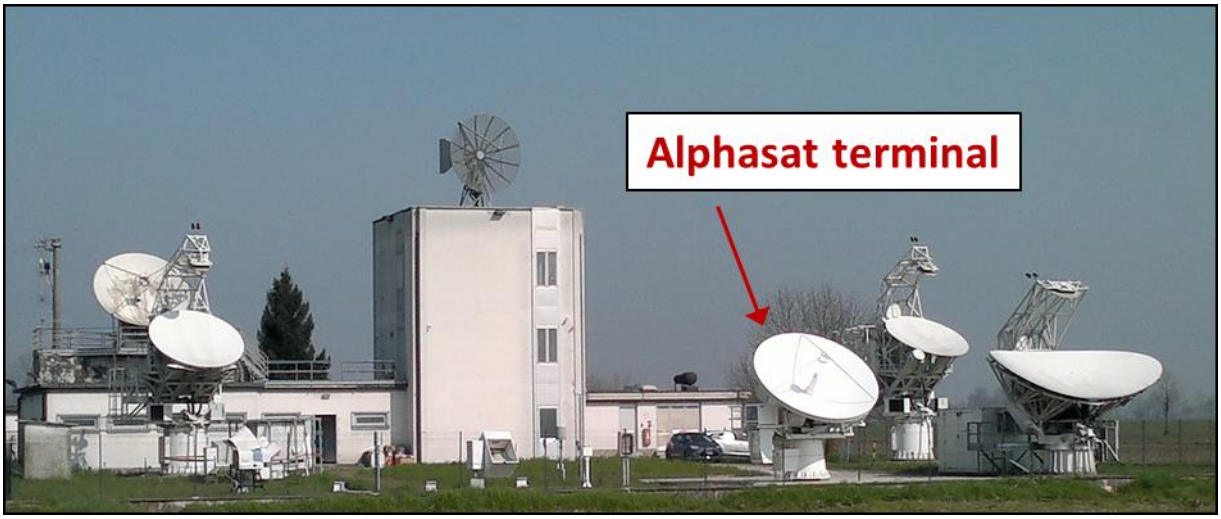

Fig. 3-3. Overview of the Spino d'Adda experimental station hosting the Alphasat terminal.

Fig. 3-4. Alphasat terminal installed at Tito Scalo.

DISTRIBUTION A: Distribution approved for public release. Distribution unlimited

Table 3-2. Main technical characteristics of the Spino d'Adda and Tito Scalo ground stations.

	Spino d'Adda	**Tito Scalo**
Site coordinates (latitude, longitude, altitude)	45.4°N 9.5° E 84 m a.m.s.l.	40.6°N 15.7°E 765 m a.m.s.l.
Foreseen period of measurements	2013-2019	
Path elevation angle (assuming satellite orbital inclination = 0°)	35.5°	42.1°
Receiver antenna	Cassegrain 4.2 m diameter	
Data acquisition rate	16 Hz	
Attenuation type **Dynamic Range**	Excess and total attenuation About 40 dB	
Radiometer	RPG-HATPRO Tropospheric temperature- and humidity-profiler (7 channels between 22.234 GHz and 31.4 GHz for tropospheric humidity profiling and 7 channels between 51.26 GHz and 58.5 GHz for temperature profiling up to 10 km)	
Rain gauge	SIAP+MICROS t028 TP500R (bucket capacity 0.2 mm)	

More in detail, Fig. 3-5 shows the architecture of the Spino d'Adda and Tito Scalo ground stations, which consist in the following sub-system:

- The Ground Station Front-End Subsystem (GSFS) composed of the antenna reflector, inclusive also of the mono-pulse tracking system, of the RF passive hardware and of the Ka and Q band LNAs (Low Noise Amplifiers). Furthermore, the GSFS includes the Infrastructure Element (IE) consisting in the Antenna Basement, and Inter-facility Link.
- The Ground Station Back-End Subsystem (GSBS), which mainly includes the V band High Power Amplifier Element (HPAE) for the communication experiment, the down and up converters, named Intermediate Frequency Equipment Element (IFEE), and the Frequency Generator Element (FGE).
- The Baseband Subsystem (BBS), that basically includes the baseband equipment performing all the required measurements to gather the experimental data.
- The Ancillary Equipment Subsystem (AES) consisting, as main parts, in the radiometer, the software elements to manage the ground station equipment and the data exchange among the Ground Stations and the centers (Mission Control Center, Experiment Control Center/Communication, Experiment Control Center/Propagation). Furthermore, the AES also includes all the cables to interconnect the equipment (IF/RF, Data) and to provide power supply, respectively named Signal Harness Element (SHE) and Electrical Harness Element (EHE).

DISTRIBUTION A: Distribution approved for public release. Distribution unlimited

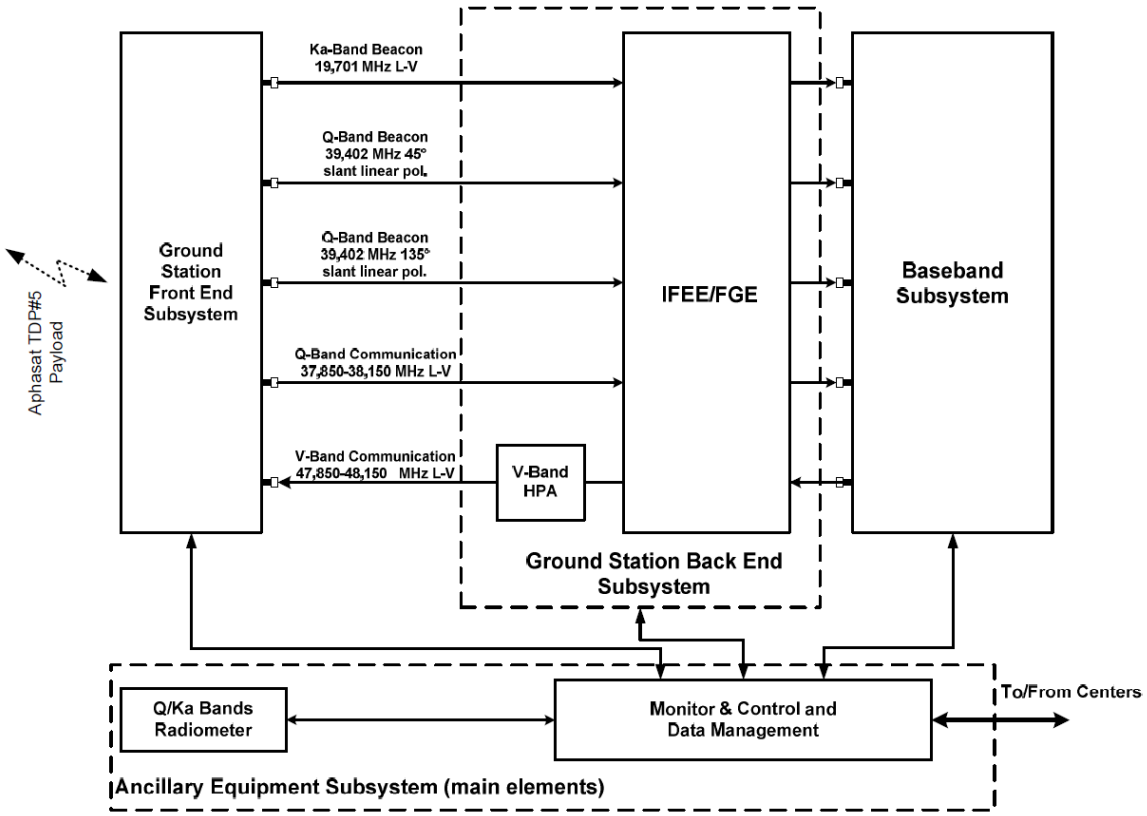

Fig. 3-5. Architecture of the Alphasat grounds station installed at Spino d'Adda and Tito Scalo.

Fig. 3-6 illustrates the overall system architecture of the Alphasat Aldo Paraboni experiment. Besides the main ground stations in Spino d'Adda, Graz and Tito Scalo, enabling both communication and propagation measurements, additional stations (equipped only with beacon receivers, i.e. taking part only in the propagation experiment) have been deployed in several sites across Europe (refer to Fig. 3-7 and Table 3-3 for details) to be coordinated by Politecnico di Milano. This not only increases the significance of the experiment but also paves the way to a fruitful international collaboration between experimenters to produce valuable joint results such as site diversity statistics. Fig. 3-7 and Table 3-3 also include the ground station deployed by NASA at Politecnico di Milano premises (roof of the Dipartimento di Elettronica, Informazione e Bioingegneria) and funded by EOARD. Details on the installation and operation of the NASA/EOARD station are given in section 3.3.

DISTRIBUTION A: Distribution approved for public release. Distribution unlimited

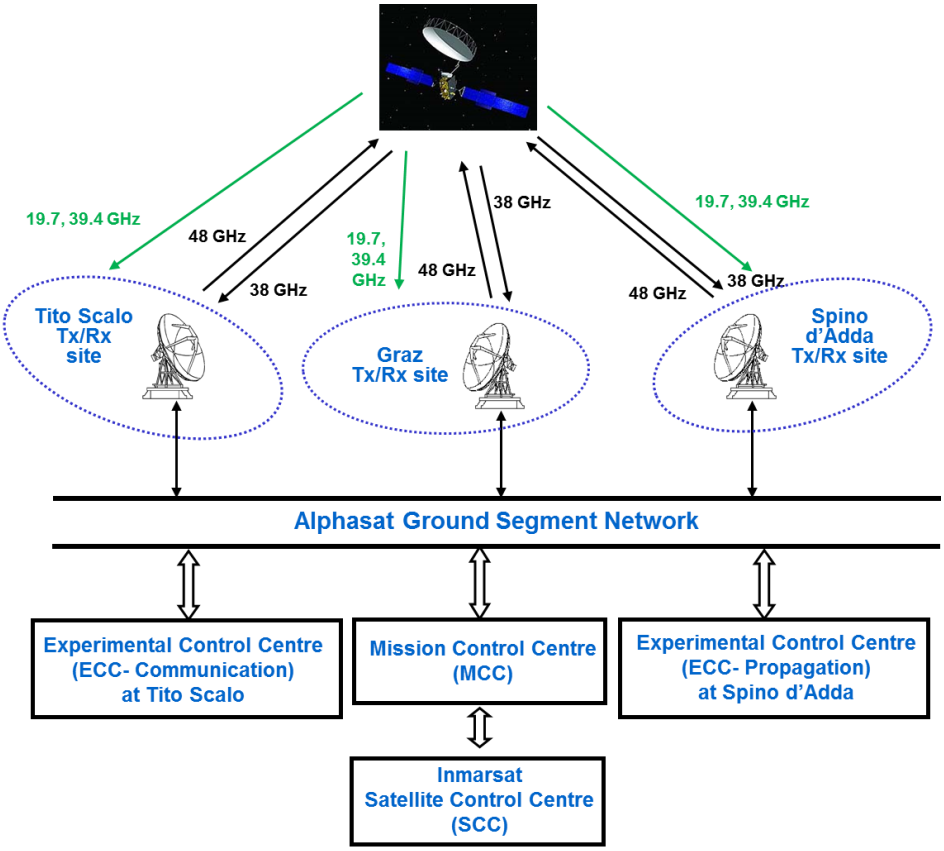

Fig. 3-6. System architecture of the Alphasat Aldo Paraboni experiment. Green and black arrows refer to the channels for the propagation and communication experiments, respectively.

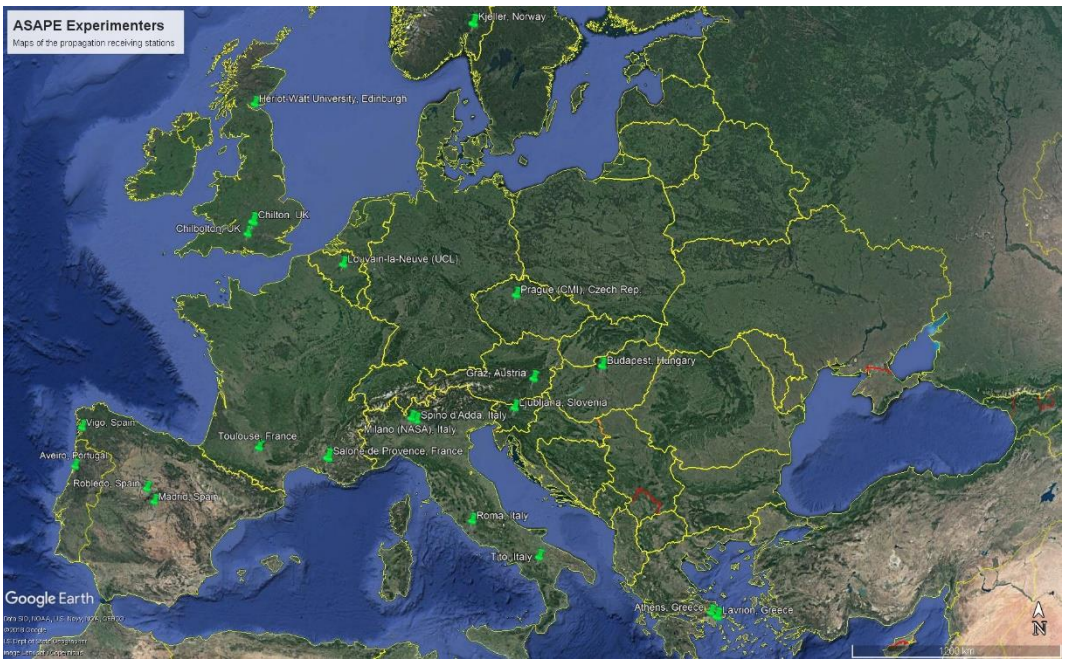

Fig. 3-7. Location of the current receiving stations for the Alphasat propagation experiment (May 2020).

Table 3-3. List of receiving stations for the Alphasat propagation experiment (May 2020).

Site	Country	Experimenter	Latitude	Longitude
Tito	Italy	Politecnico di Milano	40°35'55"N	15°43'23"E
Spino d'Adda	Italy	Politecnico di Milano	45°24'48"N	9°29'40"E
Graz	Austria	Joanneum Research	47°05'07"N	15°27'54"E
Milan	Italy	EOARD/NASA	45°28'43"N	9°13'58"E
Rome	Italy	University La Sapienza Rome	41°53'37"N	12°29'38"E
Toulouse	France	ONERA	43°34'14"N	1°28'19"E
Salon de Provence	France	CNES	43°37'12"N	5°7'12"'E
Chilbolton	U.K.	STFC	51°09'00"N	1°25'36'W
Chilton	U.K.	STFC	51°34'12"N	1°17'24'W
Aveiro	Portugal	University of Aveiro	40°37'48"N	8°39'36"W
Ljubljana	Slovenia	Jozef Stefan Institute	46°02'31"N	14°29'16"E
Madrid	Spain	Universidad Politecnica de Madrid	40º27'10"N	3º43'40"W
Vigo	Spain	University of Vigo	42°10'9"N	8°41'6"W
Athens	Greece	National Technical University	37°58'12"N	23°46'48"E
Lavrion	Greece	National Technical University	37°43'12"N	24°03'00"E
Prague	Czech Rep.	Institute of Atmospheric Physics	50°4'14"N	13°50'22"E
Budapest	Hungary	Budapest University of Technology	47°30'7"N	19°2'52"E
Louvain-la-Neuve	Belgium	Université Catholique de Louvain	50°40'09"N	4°36'52"E
Edinburgh	Scotland	Heriot-Watt University	55°54'43"N	3°19'21"W
Robledo	Spain	NASA/EOARD	40°52'12"N	4°15'00"W
Kjeller	Norway	FFI	59°58'48"N	11°00'00"E

3.2.2. The Communication Experiment

3.2.2.1. Mission objectives

The main goal of the Alphasat communication experiment is to directly verify the effectiveness of FMTs in the Q/V bands. The system was conceived considering practical, operational and technological constraints of future satellite broadband communication systems that will operate in the Q/V bands. The main objective of the telecommunication experiment is to demonstrate the feasibility of broadband satellite communications in Q/V band optimizing and assessing, over-the-air, the performance of the necessary adaptive access techniques.

As mentioned above, the communication experiment service area covers Italy and Austria with three beams. The system allows to establish and maintain full-duplex communication links between the ground terminal in Tito Scalo, also referred as TLC Experiment "Main Station", and:

- the equipment installed at Spino d' Adda, also referred as TLC Experiment "Secondary Station 1";

DISTRIBUTION A: Distribution approved for public release. Distribution unlimited

- or alternatively, the equipment installed at Graz, also referred as TLC Experiment "Secondary Station 2".

The payload transponder can be configured as follows:

- the cross-mode, in which each channel is received and transmitted on different antenna beams, i.e. the full-duplex link between two different stations is established.
- the loop-back-mode, in which each channel is received and transmitted on the same antenna beam, i.e. the same ground station transmit data to and receive data from the satellite.

The Earth to space communication is performed in the V-band range (specifically, channels centered at 47.9 and 48.1 GHz), while the space to Earth link operates in the Q-band range (specifically, channels centered at 37.9 and 38.1 GHz).

3.2.2.2. Experiment plan

The communication experiment relies on the use of the DVB-S2 standard for the forward channel of a fixed broadband satellite communication system [DVB-S2]. The Physical Layer (PL) structure is composed of a regular sequence of frames (PLFRAME), in each of which the modulation and coding scheme is homogeneous. When Adaptive Coding and Modulation (ACM) is used, schemes may change on a frame by frame basis depending on the channel condition. Every frame consists of a payload of 64800 bits in the "normal frame" configuration or 16200 bits in the "short frame" option. A frame corresponds to a FEC (Forward Error Correction) code block. A header of 90 binary modulation symbols containing synchronization and signaling information is included before the payload to allow receiver synchronization (carrier and phase recovery and frame synchronization) and detect the modulation and coding parameters before demodulation and FEC decoding. The FEC used in DVB-S2 is based on a very powerful concatenated scheme using a LDPC (Low-Density Parity Check) inner code with parameters (nLDPC, kLDPC) concatenated with a BCH (Bose-Chaudhuri-Hocquenghem) outer code with parameters (nBCH, kBCH). Four modulation modes can be selected for the transmitted payload: QPSK, 8PSK, 16APSK, 32APSK with modulation order respectively $M = 4$, $M = 8$, $M = 16$, $M = 32$. QPSK and 8PSK are typically proposed for broadcast applications, since they are virtually constant envelope modulations and can be used in nonlinear satellite transponders driven near saturation. Gray mapping of constellations shall be used for QPSK and 8PSK. The 16APSK and 32APSK modes are mainly targeted at professional applications, due to the higher requirements in terms of available SNR, but they can also be used for broadcasting. A combination of a FEC scheme and a modulation scheme is named as ACM mode (or MODCOD); the DVB-S2 standard includes 28 different ACM modes.

The communication experiment is divided into four categories:

- the channel estimation experiment;
- the ACM experiment;
- the ULPC experiment;
- the site diversity experiment.

The channel estimation experiment

The objective of the channel estimation experiment is to select the most useful metric which will be used to trigger the ACM and ULPC algorithms. The experiment considers the following

DISTRIBUTION A: Distribution approved for public release. Distribution unlimited

channel estimation parameters for driving FMTs: Received Signal Strength (RSS), Carrier to Noise Ratio (CNR), data aided Signal to Noise Ratio (SNR), Error Vector Magnitude (EVM), Bit Error Rate (BER) and Frame Error Rate (FER). The data gathered from ancillary equipment such as radiometric data and meteorological data or coming from the Q-band beacon receiver can be used to drive FMTs both in open-loop and in closed-loop configurations. The availability of different link quality metrics is an important feature, which allows identifying the reason of the link performance degradation, e.g. interference (in particular for multi-beam satellites [Loreti and Luglio, 2002]), amplifier distortions, rain fading, and depolarization. However, in a typical future commercial system these data will not be easily available. An unencoded QPSK transmission is an option of the experiment, which will be used to analyze the mathematical relation between time-varying attenuation and time-varying BER; in particular this option will be useful for the development of a Q/V band channel model (at bit or packet level) based on Markov chains.

The Adaptive Coding and Modulation (ACM) experiment

The objective of the ACM experiment is to design and optimize ACM algorithms for the specific 40-50 GHz communication channel. The ACM mode for the transmission of each individual PLFRAME is selected by the receiver through the ACM algorithm on the basis of the selected channel estimation metric and the current and/or predicted channel conditions. A trade-off exists between spectral efficiency and power efficiency for the selection of the best ACM mode [Stallo et al., 2009], [Mukherjee et al., 2010a], [Mukherjee et al., 2010b]. The ACM mode switching algorithm should optimize this trade-off, thus providing the best combination of spectral efficiency and BER/FER. A hysteresis loop is usually included in the ACM mode switching algorithm to prevent undesired oscillations of the transmitting ACM mode in case of SNR jitter between adjacent SNR thresholds.

The Alphasat TDP5 experiment will also provide the opportunity to test and validate a proper combination of the ACM and ULPC experiments.

The up-link power control (ULPC) experiment

The objective of up-link power control (ULPC) is to adaptively change the power transmitted by a ground terminal on the basis of link attenuation in order to maintain a constant power flux density at the satellite input. ULPC goals are: to improve system capacity, to compensate for fade, to reduce power consumption, to reduce interference (mainly for mobile applications), to compensate for antenna gain roll-off and mispointing. The ULPC implementation strategy should be coupled with on-board amplifiers to prevent transponders saturation; as a matter of fact, transmission of excessive power can cause harm to the space segment and to adjacent satellites.

Several strategies of power control can be experimented exploiting the TDP#5: open-loop ULPC and closed-loop ULPC.

Open loop ULPC relies on the possibility to estimate the uplink attenuation at the transmitter ground station using some independent means, as downlink beacon measurement or radiometric measurements. In the case of the Alphasat experiment, the open loop ULPC can take advantage of the downlink beacon signals in Q and Ka bands, hence uplink attenuation shall be extrapolated on the basis of some frequency scaling technique (this will introduce uncertainties that have to be carefully evaluated).

DISTRIBUTION A: Distribution approved for public release. Distribution unlimited

Closed-loop ULPC is based on the possibility to evaluate the up-link attenuation on the basis of the self-transmitted down-link signal or the feedback coming from the received ground station (the latter technique is also referred as "feedback-loop" power control).

Performance of ULPC will be evaluated using different metrics as power control accuracy and maximum level of fade that can be compensated.

The site diversity experiment

The basic principle underpinning site diversity is the use of multiple stations allowing the exclusion of the one subject to the deepest fade. This concept takes advantage of the strong spatial and temporal inhomogeneity of tropospheric phenomena, mainly rain.

The performance gain achieved by means of site diversity is dependent on the space correlation of precipitation, i.e. on the separation distance, which is the key parameter for system design.

Two parameters should be measured to evaluate the effectiveness of such a technique: the diversity improvement factor, defined as the ratio between the multiple- and single-site availability time (at the same attenuation level), and the diversity gain, defined as the difference (dB) between the single- and multiple-site attenuation values (for the same availability time). While a good choice for site separation distance might be around 20-30 km, the distance between the TDP#5 main ground station (Spino d'Adda, Tito Scalo, Graz) is much higher (hundreds of kilometers). As a result, in this context, it is not possible to obtain a meaningful diversity gain but, nevertheless, the TDP#5 spatial diversity experiment allows to verify and test the station switching control procedure, as well as diversity management logic and stations synchronizations issues. The experimental set-up includes a closed-loop payload configuration on one ground station that will be considered the site diversity "master station". One of the other two ground stations plays the role of "slave station". In this configuration different site diversity control loop and management logics can be investigated [Rossi et al., 2011].

3.2.3. The Propagation Experiment

3.2.3.1. Mission objectives

The Alphasat TDP#5 Scientific (Propagation) Experiment (renamed Alphasat Aldo Experiment in memory of prof. Aldo Paraboni [Rossi et al., 2009]) aims at collecting additional Ka- and Q-band propagation data needed for the optimization of modern satellite system design and at assessing the system level impact of propagation data.

More in detail, the objectives of the experiment are:

- The calculation of the first- (e.g. CCDFs, typically useful to identify the system power margin) and second order-statistics of attenuation (e.g. fade durations to dimension on board buffer memories; fade slope to determine the dynamic properties of adaptive mechanisms; spatial correlation to design site diversity systems) at the two frequencies of 19.7 (Ka band) and 39.4 GHz (Q band).
- The collection of depolarization and sky noise measurements.
- The investigation of the correlations between the measured parameters of the communication and propagation experiments.

DISTRIBUTION A: Distribution approved for public release. Distribution unlimited

- The acquisition of the concurrent meteorological measurements (rain-gauges, radiometers, radiosoundings, Meteorological Radar, Numerical Weather Products, Meteosat, etc.).
- The theoretical assessment of the gain originating from a satellite system able to partition the power available onboard among the various spot beams illuminating the service area.
- The development of prediction models to be possibly submitted to the international regulatory bodies such as the ITU-R, the ETSI, etc.
- The opportunity of cooperation between European experimenters, inherent to the realization of multisite experiments.

3.3. The NASA/EOARD propagation experiment station

3.3.1. System architecture

As shown in Table 3-3, the National Aeronautics and Space Administration (NASA) joined the Alphasat experimental activity with a set of Ka- and Q-band beacon receivers (and ancillary instruments) that are installed on the rooftop of the Dipartimento di Elettronica, Informazione e Bioingegneria (DEIB), Politecnico di Milano, Italy. The equipment is hosted at Politecnico di Milano premises under the international agreement between NASA and DEIB expressing the mutual interest in conducting research activities in the frame of the Alphasat experiment, with the main goal of producing joint scientific results and developing propagation models based on the data collected by the NASA station and by the Spino d'Adda terminal. As an example, being 22.6 km the separation distance between the two sites (refer to Fig. 3-8), the advantages of site diversity can be explored by calculating joint attenuation statistics.

Fig. 3-8. Sites in Milan and Spino d'Adda where the NASA and ASI experimental equipment is installed, respectively.

The installation of NASA equipment was complete by NASA personnel in one week (from April 14th to April 18th, 2014), with the support of Politecnico di Milano technical staff. Fig. 3-9 shows the exact position of the NASA equipment on the rooftop of the Dipartimento di Elettronica, Informazione e Bioingegneria (DEIB). The figure also shows a partial view of the NASA instruments and the position of the Alphasat satellite with respect to DEIB: as listed in

Table 3-4, the station coordinates are 45.47867° N (latitude), 9.232760° E (longitude) and its altitude is 0.138 km a.m.s.l.; Alphsat's orbital position on the equatorial plane is 25° E, which corresponds to the following nominal look angles from the NASA station: elevation = 35.42° and azimuth = 158.38°. In fact, due to Inmarsat's plan to minimize orbital maneuvers in order to extend the satellite lifetime as much as possible, the orbital plane inclination of Alphasat is expected to increase approximately with a rate of 0.46°/year, up to a maximum value of 3°, when the spacecraft equatorial orbit will be restored by Inmarsat. This oscillation has a (daily) twofold effect on the receiving equipment: a variation of the elevation and azimuth angles (as shown in Table 3-4, up to ±3.17° and ±1.08°, respectively) and a Doppler shift of the beacon frequencies.

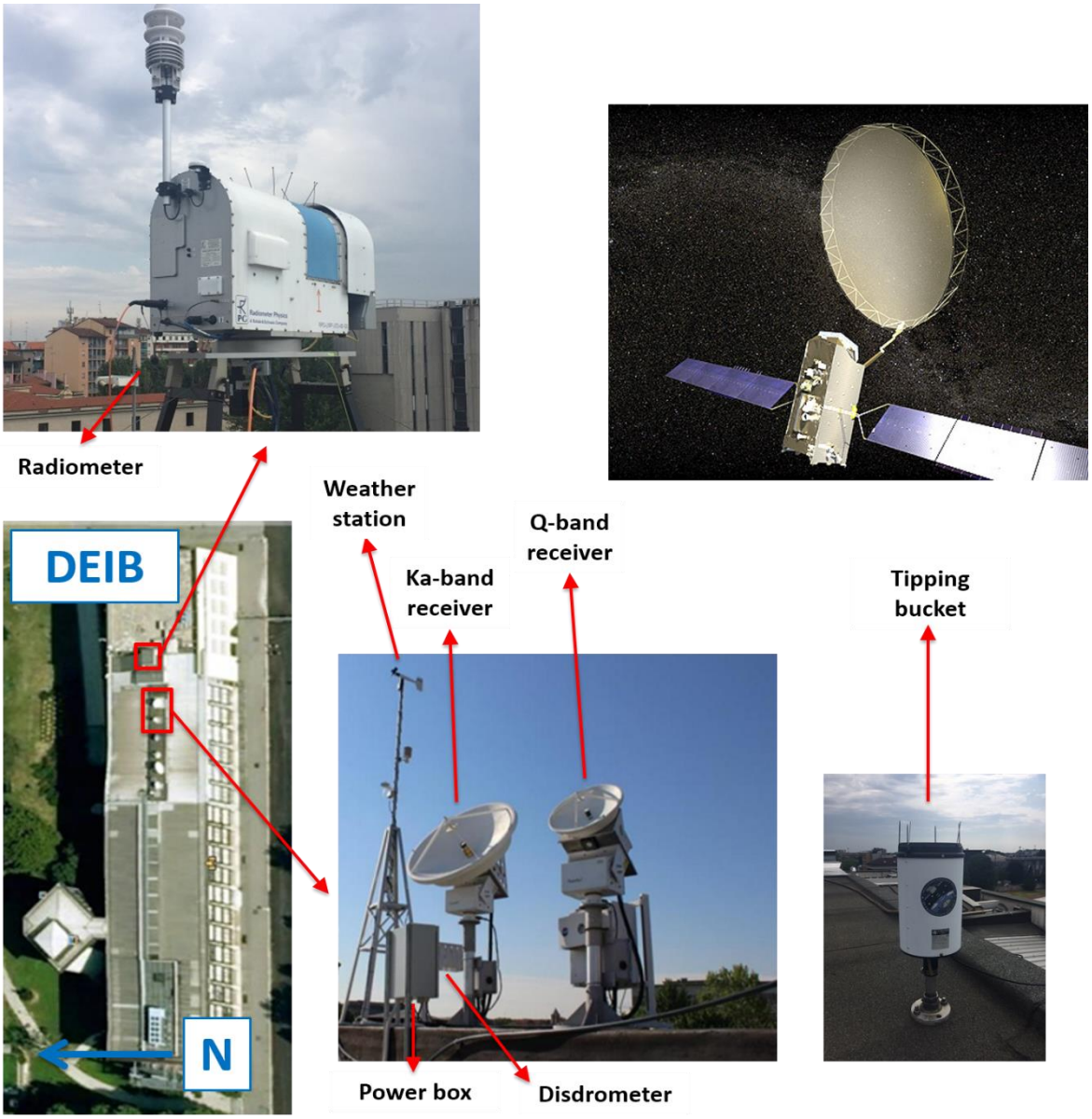

Fig. 3-9. NASA equipment on the rooftop of the Dipartimento di Elettronica, Informazione e Bioingegneria (DEIB), Politecnico di Milano.

Table 3-4. Details on the NASA station site and geometrical features of the link.

Alphasat	
Alphasat orbital plane inclination	0°+3°
Alphasat orbital position	25° E
NASA station	
Latitude	45.47867° N
Longitude	9.232760° E
Altitude	0.138 km a.m.s.l.
Geometrical characteristics of the link	
Elevation	35.42°±3.17°
Azimuth	158.38±1.08°

Fig. 3-10 shows the complete system architecture of the NASA equipment, which consists in the following instruments:

- *Ka-band and Q-band receiver front ends*, that include 1.2-m and 0.6-m Cassegrain antennas, respectively, and RF boxes containing Low Noise Amplifiers (LNAs) together with a chain of mixers, filters and amplifiers to minimize the noise and to down-convert both signals from the carrier frequencies to 70 MHz.
- *The Intermediate Frequency (IF) box*, whose main purpose is to further down-convert the received signal to 455 kHz (band approximately from 452 kHz to 462 kHz) after proper filtering and amplification.
- *Ka-band and Q-band Quicksets*, that enable to dynamically change the antenna pointing (azimuth and elevation) to track the satellite, whose relative position with respect to the station follows a daily pattern due to the slight inclination of the orbital plane (as discussed above). This is performed in open-loop configuration, i.e. taking as reference the spacecraft ephemerides, which, in turn, are estimated from the TLE (Two-Line Element) files regularly made available by Inmarsat on a weekly basis.
- *The weather station*, equipped with sensors of: pressure, temperature, relative humidity, rain rate (tipping bucket with 0.1 mm/tip), wind speed and direction. All the data are gathered by the Weather Tracker connected to the PC.
- *The disdrometer*, that accurately measures precipitation by classifying hydrometeors according to their physical state and by their diameter; outputs of this instrument are Drop Size Distributions (DSDs) and the rain rate.
- *The PC*, that includes the data acquisition cards (DAQ) for the two beacon channels, and the QuickSet control cards. The main tasks of the PC are to digitalize the beacon signal and to store all the data (also meteorological ones collected by the Weather Tracker) in separate text files for easy inspection, and to control the antenna pointing via the QuickSets on the basis of the predicted satellite ephemerides. In addition, the PC also stores health data for several elements of the instrumentation.
- *The UPS* (Uninterruptible Power Supply), that guarantees protection of the PC and all the receiving equipment from voltage spikes and power backup in case of temporary blackouts. The UPS is also coupled with a transformer to convert the local 220V voltage to 110V.

- *The radiometer*, installed at the end of 2016 to complement the set of measurements and mainly allow deriving the reference atmospheric attenuation (in non-rainy conditions) to calibrate the power levels acquired by the beacon receivers.

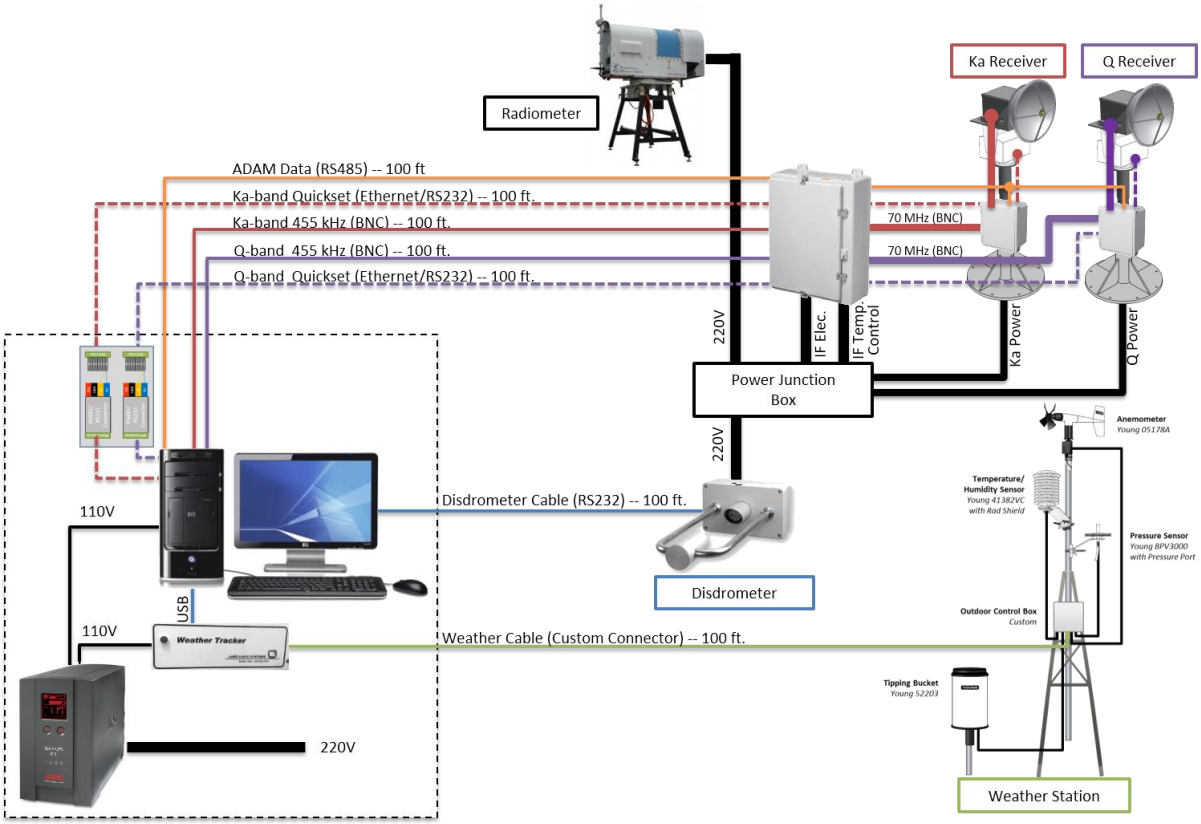

Fig. 3-10. Complete system architecture of the NASA station.

3.3.2. Measurements

This section provides details on the measurements collected using the NASA equipment.

3.3.2.1. Beacon receivers

Table 3-5 lists the quantities recorded by the NASA beacon receivers.

Table 3-5. Detailed list of the quantities recorded by NASA beacon receivers.

Instrument	Sampling time	Products
Beacon receivers	Variable (current = 8 samples/second)	- In-phase and quadrature components of the signal - Power levels (dBm) - Signal peak (down-converted) frequency (kHz)

The main outputs of these instruments are the in-phase and quadrature components of the received signal, which allows investigating both the phase and the amplitude (power) of the signal. Since the receivers are not equipped with Phase-Locked Loops (PLLs) to automatically track the beacon signal phase and frequency, power data collection is achieved by calculating the real-time Fast Fourier Transform (FFT) of the signal and by implementing an enhanced version of the Quinn-Fernandes estimation technique to identify the peak down-converted

frequency (f_{peak}) and, thus, to calculate the received power (P_{lev}) [Quinn and Fernandes, 1991]. Fig. 3-11 shows an example of the real-time FFT spectra (July 1st, 2014) for the Ka-band and Q-band signals (top side) as calculated by the NASA DRX data acquisition software; the bottom side of the figure reports time series of P_{lev} and f_{peak} for both channels. The sampling frequency is 8 Hz to allow the characterization of the fast signal variations associated to scintillations.

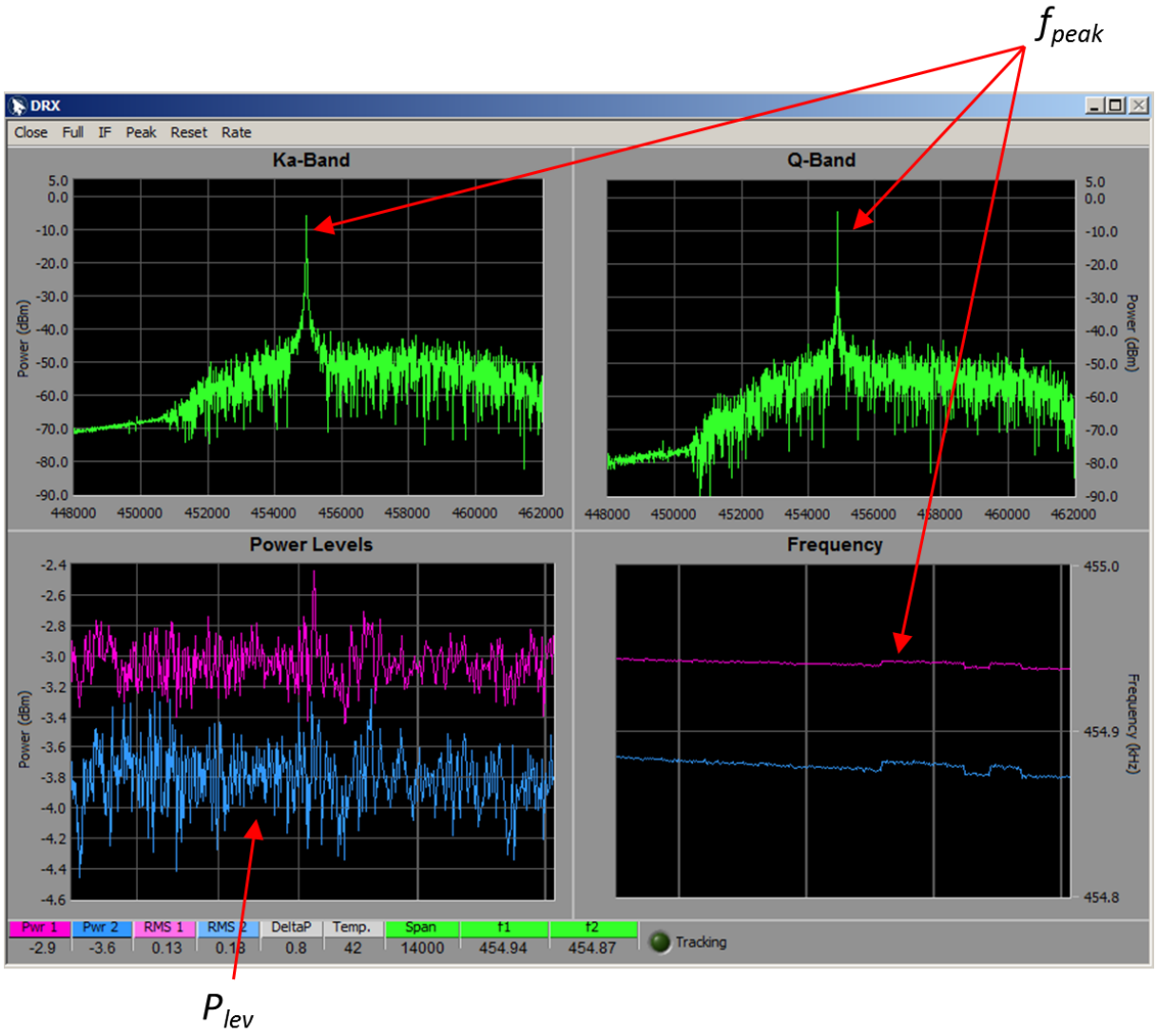

Fig. 3-11. Sample screenshot (July 1st, 2014) of the NASA DRX data acquisition software: real-time FFT spectra of the Ka-band and Q-band signals (top side) and time series of P_{lev} and f_{peak} for both channels (bottom side).

Fig. 3-12 depicts an example of the received power levels (red line for the Ka-band and blue line for the Q-band). Data refer to the 29th of June 2014, when several short rain events occurred. This is clearly pointed out by the marked decrease in the power levels, for example around 8 and 14:30 UTC, due to the strong scattering and absorption effects induced by rain drops at these frequency bands. Fig. 3-12 also allows appreciating the fast signal fluctuations due to scintillations, in turn caused by small-scale inhomogeneity in the atmosphere and by

DISTRIBUTION A: Distribution approved for public release. Distribution unlimited

turbulence. Fig. 3-13 provides additional information on the data collected by the beacon receivers by reporting the temporal trend of the peak signal frequency, f_{peak} (same day). As mentioned above, the apparent beacon signal frequency oscillates due to the slight inclination of Alphasat orbital plane, which introduces a radial relative velocity component.

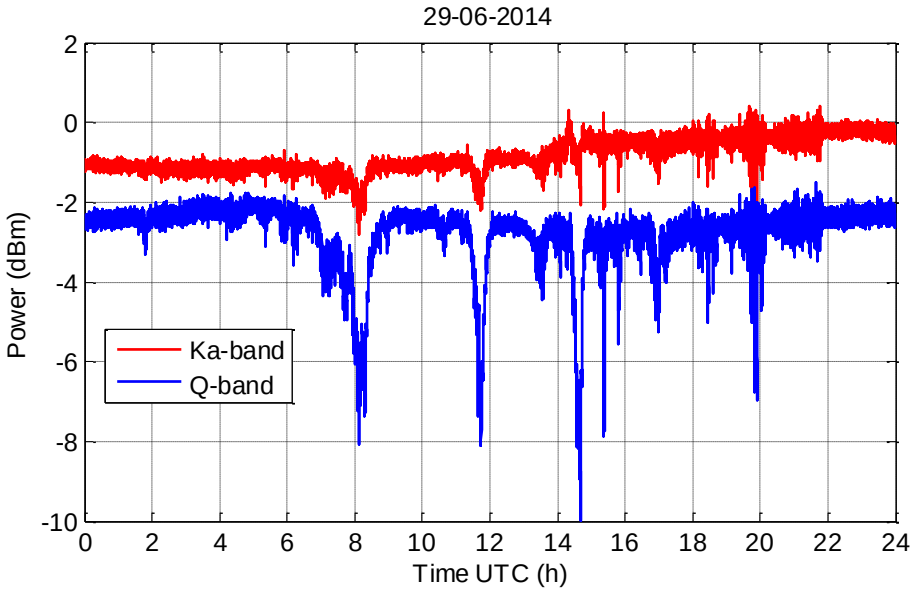

Fig. 3-12. Example of the power levels received on the 29th of June, 2014.

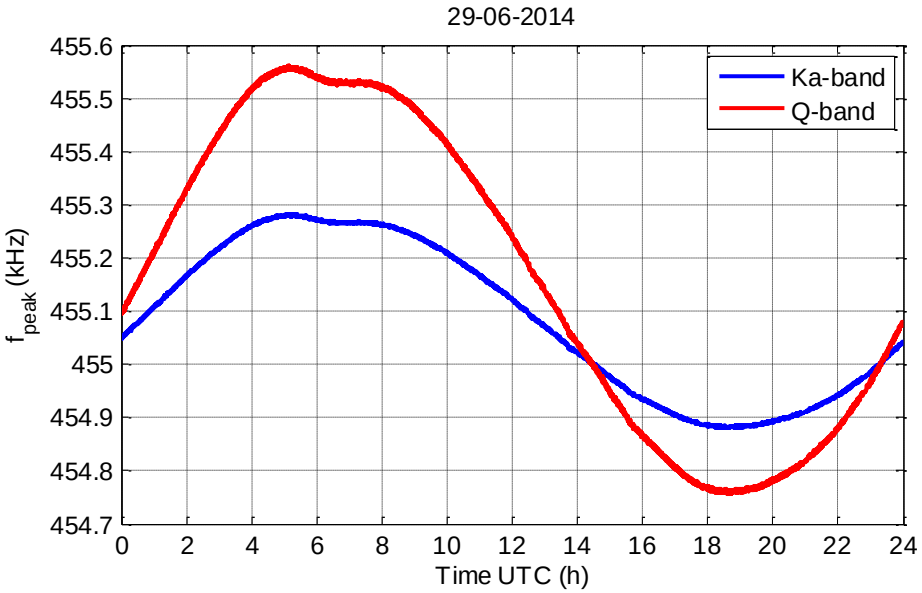

Fig. 3-13. Temporal trend of f_{peak} associated to signal reported in Fig. 3-12.

3.3.2.2. Weather station

Table 3-6 lists all the quantities recorded by the NASA Young Weather Station.

DISTRIBUTION A: Distribution approved for public release. Distribution unlimited

Table 3-6. Detailed list of the quantities recorded by NASA Young Weather Station.

Instrument	Sampling time	Products
Young Weather Station	1 sample/minute	- Wind gust (m/s) - Wind speed (m/s) - Wind direction (°) - Air temperature (°C) - Relative humidity (%) - Pressure (hPa) - Rain gauge tips in a 1 minute - Rain rate (mm/h) - Rain accumulation (mm)

Fig. 3-14 shows a sample screenshot of the Young Weather Station data acquisition software (14th of July, 2014) whose main aim is to show real-time measurements and to store them into text files. In this case, the sampling frequency is 1 sample/minute which allows to adequately catch the temporal variability of the atmospheric quantities, definitely lower than that of the received beacon signals.

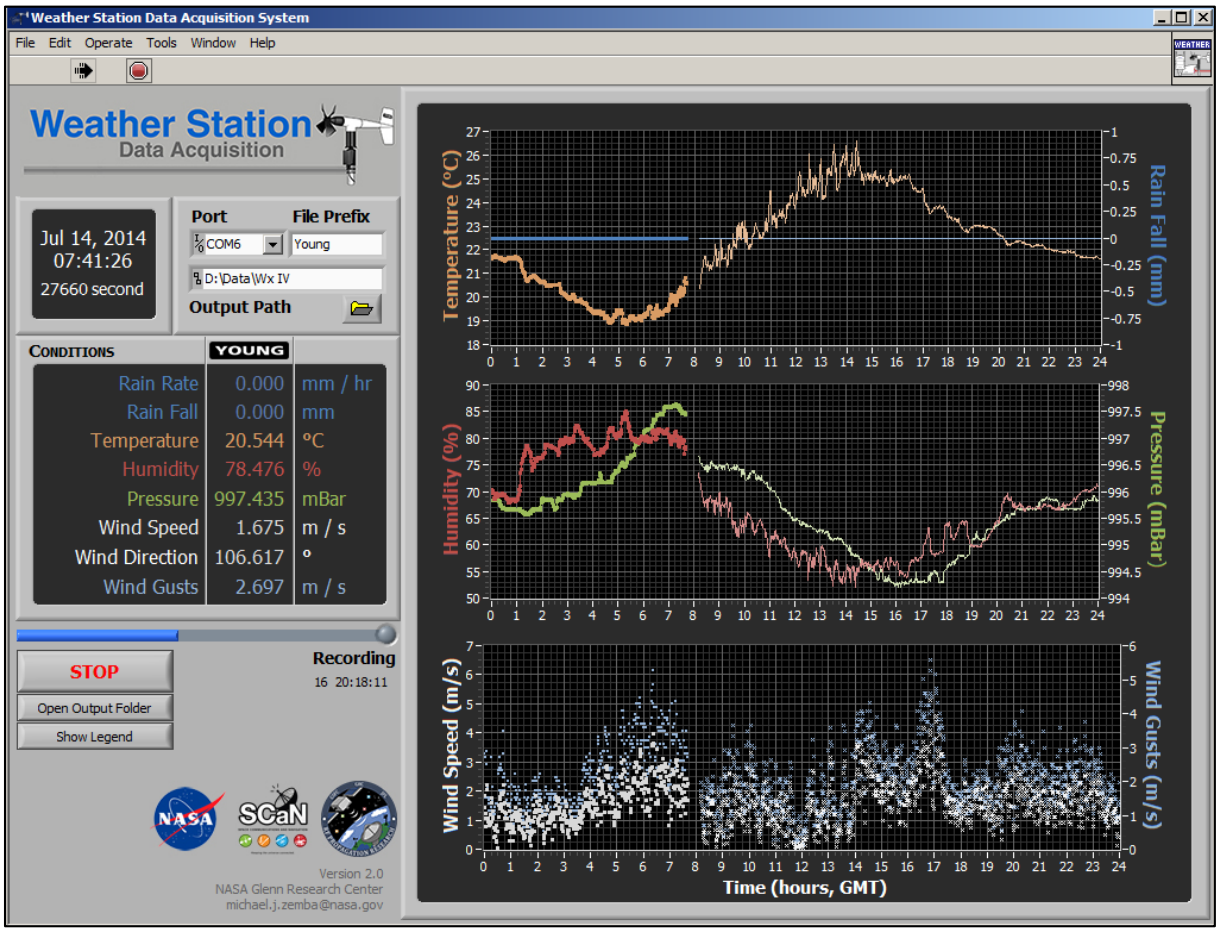

Fig. 3-14. Sample screenshot of the Young Weather Station data acquisition software (14th July, 2014).

Fig. 3-15 shows the time series of the data collected by the weather station on the 29th of June, 2014 (the same day which the data in Fig. 3-12 and Fig. 3-13 refer to). The wind gust is

calculated as the maximum wind speed value within each minute, while, as for the wind direction, the 0° corresponds to South. The rain rate data collected by the tipping bucket rain gauge confirms the presence of rain on the site around 8, 12 and 14 UTC, while no precipitation is detected around 20 UTC; nevertheless, the beacon receivers show a sudden drop in the signal (Fig. 3-12), due to a rain cell along the propagation path. As it is often the case, large attenuations due to rain are associated to the increase in the wind intensity, which is visible around 14 UTC. These are only few examples of how ancillary meteorological data collected on the ground can aid the understanding of the physical processes impairing the link, as well as the development of propagation models. In this sense, rain rate data are of key importance for models predicting rain attenuation statistics (e.g. [Capsoni et al., 2009a]), while temperature, pressure, relative humidity and wind are more related to models aimed at estimating gaseous absorption [ITU-R P.676-12] and scintillations (e.g. [Karasawa et al., 1988]).

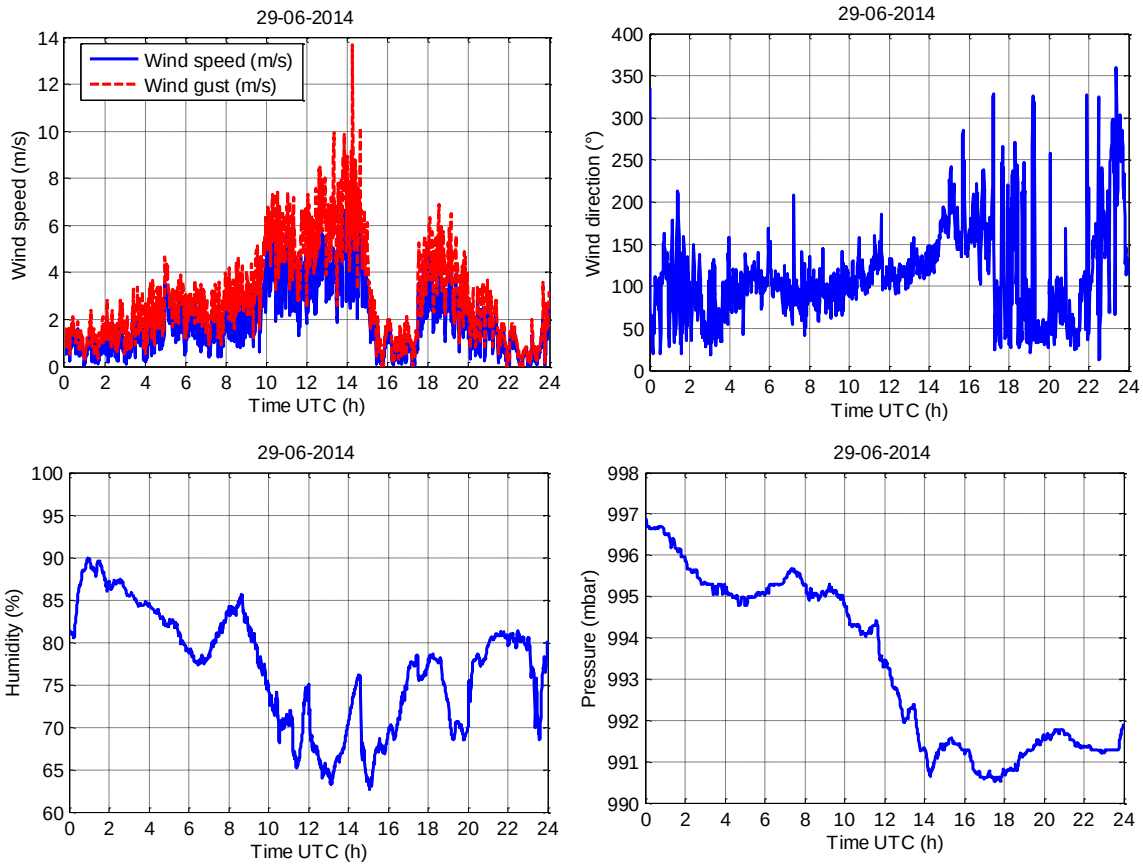

DISTRIBUTION A: Distribution approved for public release. Distribution unlimited

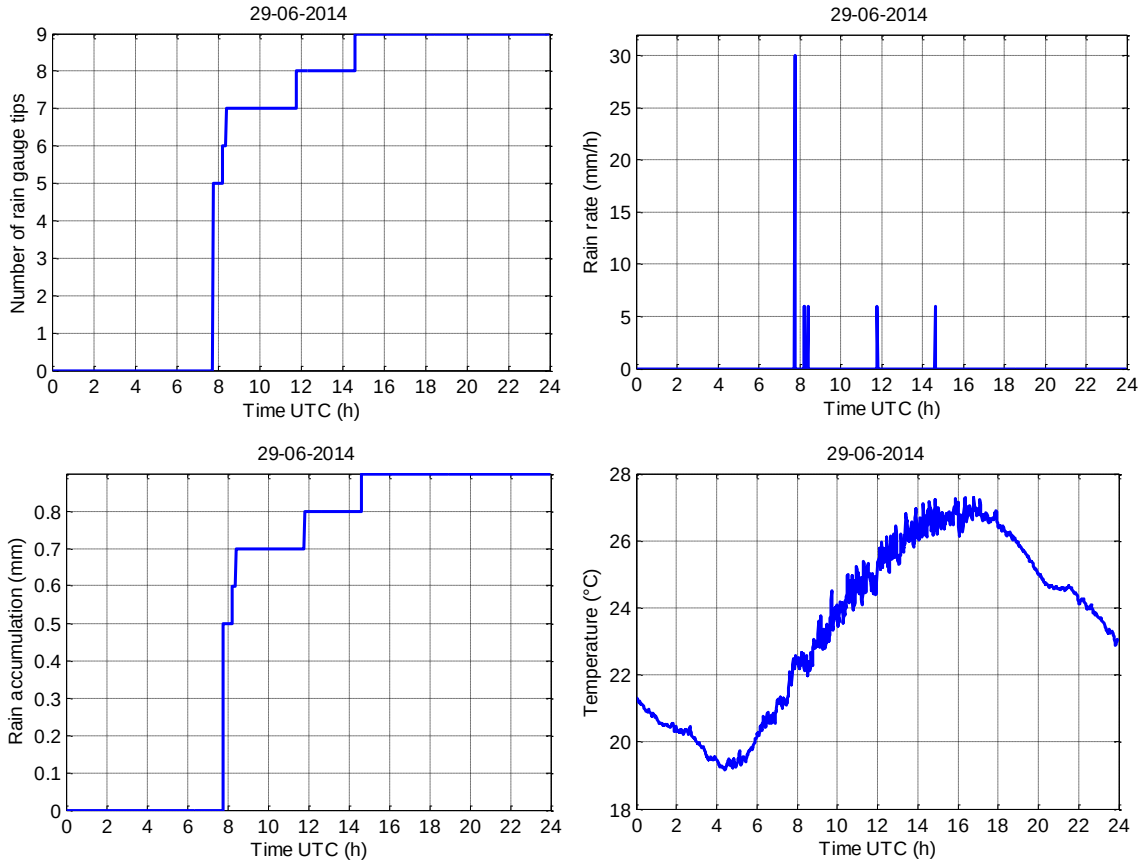

Fig. 3-15. Time series of the meteorological quantities collected by the Young weather station (29th June, 2014).

3.3.2.3. Disdrometer

Table 3-7 lists the quantities recorded by the NASA disdrometer.

Table 3-7. Detailed list of the quantities recorded by NASA disdrometer.

Instrument	Sampling time	Products
Disdrometer (Thies Clima Laser Precipitation Monitor)	1 sample/minute	- Rain rate (total, liquid, solid) (mm/h) - Total rain accumulation (mm) - Visibility (m) - Radar reflectivity (dBz) - Max diameter hail (mm) - Number of measured particles - Drop Size Distribution - Drop Velocity Distribution

Fig. 3-16 shows a sample screenshot of the disdrometer data acquisition software (2nd July, 2014) whose main aims are to show real-time measurements of hydrometeors and to store them into text files. Like for the weather station, the sampling frequency is 1 sample/minute, a good compromise between the data amount to be stored and the temporal variability of precipitation events.

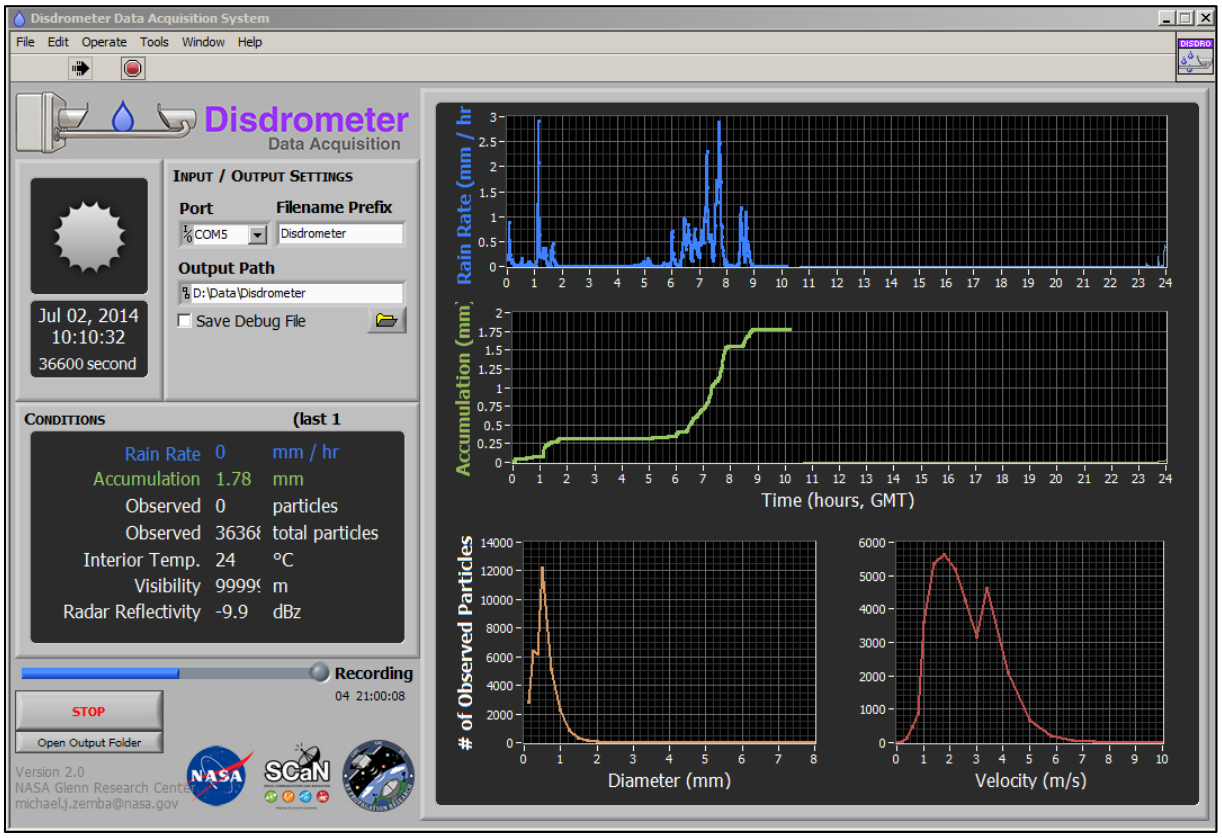

Fig. 3-16. Sample screenshot of the disdrometer data acquisition software (2nd July, 2014).

Fig. 3-17 shows the time series of some of the data collected by the disdrometer, again on the 29th of June 2014. The main outputs of the instruments are the Drop Size Distribution (DSD) and the distribution of the particles fall velocity (top side of Fig. 3-17), from which both the rain accumulation and the rain intensity can be calculated. A comparison of the graphs in Fig. 3-17 with the data collected by the rain gauge (shown in Fig. 3-15 above) immediately points out the limitations inherent to the latter; indeed the discrepancy in the rain rate R measured by the two instruments (particularly marked around 8 UTC) reflects the different processes lying at the basis of the disdrometer and the rain gauge. The former combines multiple microphysical information (dimension and number of particles and fall velocity) to derive R (see e.g. [Lam et al., 2012]), while the latter only rely on the number of tips occurred in a minute to estimate the same quantity, i.e.:

$$R = \frac{N\,r}{\Delta T} \quad \text{(mm/h)} \tag{3-1}$$

where N is the number of tips occurred, r is the rain amount accumulated in each tip (0.1 mm for the NASA rain gauge) and ΔT is the sampling time (1 minute in this case). The main consequence of (3-1) is the limited resolution in measuring rain rate: in fact, according to (3-1), 1 tip in a minute corresponds to 6 mm/h. This limitation clearly emerges from the comparison of the rain rate time series depicted in Fig. 3-15 and Fig. 3-17. On the other hand, the disdrometer accuracy is definitely higher and, for this reason, these data will be privileged throughout the whole experiment to estimate R.

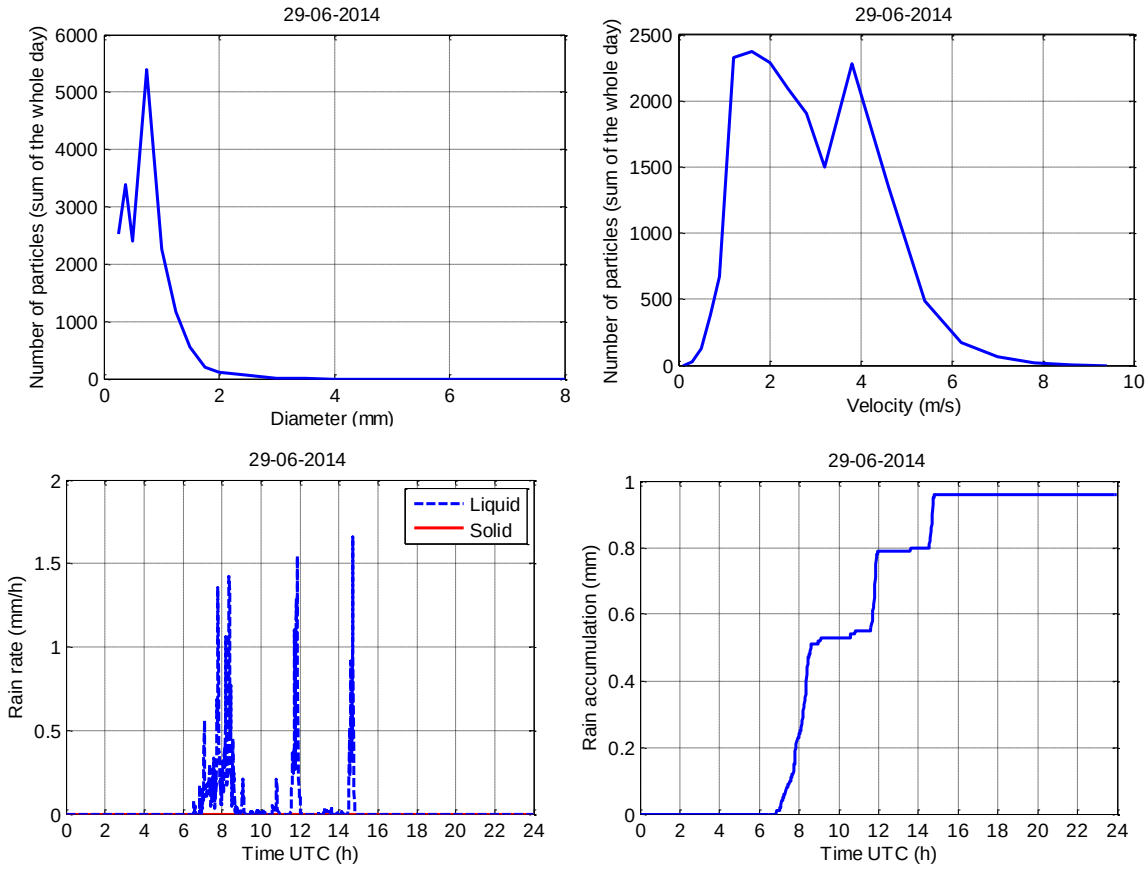

Fig. 3-17. Time series of the some of the data collected by the disdrometer (29^{th} June, 2014).

Another key advantage of the disdrometer is the possibility to observe the type (dimension and physical state) and number of particles in precipitation events. Indeed, the DSD is tightly linked to frequency scaling techniques that aim at estimating the rain attenuation at a target frequency f_2 from the rain attenuation measured at a lower frequency f_1 (e.g. useful to apply ULPC).

3.3.2.4. Radiometer

Table 3-8 lists the quantities collected by the radiometer installed at Politecnico di Milano and manufactured by Radiometer Physics GmbH (RPG).

Table 3-8. Detailed list of the quantities recorded by the radiometer.

Instrument	Sampling time	Products
Radiometer (RPG-LWP + 72.5/82.5 GHz)	1 sample/second	- Brightness temperature at 23.84, 31.4, 72.5 and 82.5 GHz - Rain flag - Pressure, temperature, relative humidity

Fig. 3-18 shows sample time series of brightness temperature collected by the radiometer on the 19^{th} of December 2016, along the path to Alphasat (35.42° elevation).

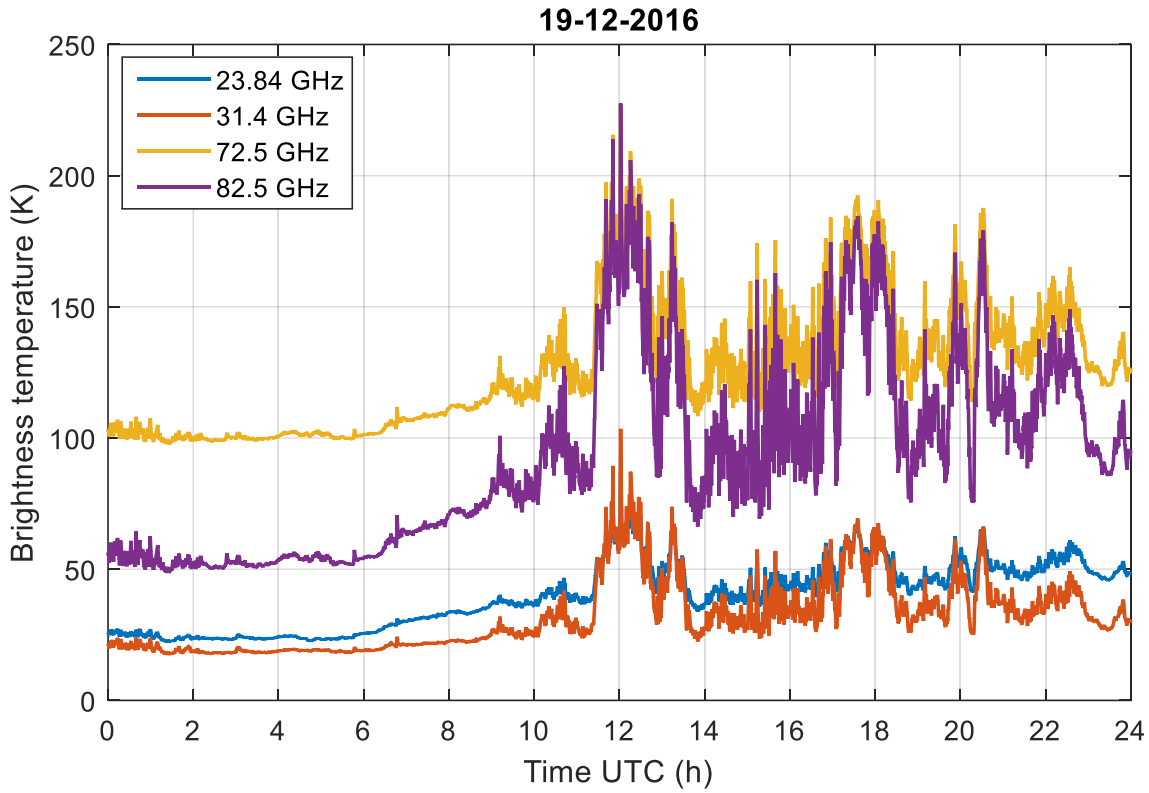

Fig. 3-18. Sample time series of the brightness temperature collected by the radiometer (19th December, 2016) along the path to Alphasat (35.42° elevation).

3.3.3. Beacon data calibration

The derivation of the absolute tropospheric attenuation starting from the received power levels is of key importance to achieve a comprehensive set propagation data.

In principle, the tropospheric attenuation could be inferred from the knowledge of all the elements involved in the Earth-satellite link budget (e.g. path length, frequency, gain of the antennas, overall attenuation/gain introduced by the receiver gain, …); in practice, this is hardly feasible because of the limited accuracy with which some of the quantities mentioned above are actually known, such as: oscillation in the nominal power transmitted by the beacons, modification of the gain/attenuation levels in the electronic components, small pointing errors, etc.

The typical approach employed to solve this problem is the use of a radiometer collocated with the beacon receiver with the same elevation and azimuth angles of the receiver antenna. As a result, the atmospheric attenuation level can be estimated from the brightness temperature data collected by the (calibrated) radiometer (this is only possible in non-rainy conditions due to the scatter-free assumption in the radiometric inversion model [Luini et al., 2007]) and this knowledge can help the calibration of the received power levels. This approach is explored (and its application described) in Section 3.3.3.1 below.

When a radiometer is not available (as in the case of the NASA station until December 2016), the same reference attenuation levels can be estimated by means of well-known mass absorption models such as those proposed by Liebe *et al.* [Liebe et al., 1993] and Rosenkranz [Rosenkranz, 1998]. To this aim, this kind of models needs as input vertical profiles of pressure

(*P*), temperature (*T*) and relative humidity (*RH*), in turn obtainable from RAOBS or Numerical Weather Prediction (NWP) products (e.g. forecasts data made available by the ECMWF every 6 hours on a regular latitude/longitude grid with 0.1°×0.1° spatial resolution). This approach, described and applied in [EOARD, 2013] to estimate the atmospheric attenuation prior to the installation of the radiometer (December 2016), is not reported here: indeed the present research activities cover the period 2017-2020, when the radiometer can be used to obtain the atmospheric attenuation.

3.3.3.1. Calibration with radiometers

The RPG (Radiometer Physics GmbH) radiometer (model RPG-LWP + 72.5/82.5 GHz) was installed at the end 2016 to collected brightness temperature data (4 channels centered around the frequencies listed in Table 3-9), with the main objectives of improving the accuracy in converting the received beacon signals into total tropospheric attenuation, as well as of providing an accurate estimate of the attenuation to be expected in the W band (non-rainy conditions). Both goals rely on preliminary steps, the main one being the derivation of site dependent radiometric coefficients. This is thoroughly explained in the next subsections.

Table 3-9. Frequency channels of the MWR (GHz).

f_{MWR}	23.84	31.4	72.5	82.5

Theoretical background

For a non-scattering atmosphere in local thermodynamic equilibrium, the atmospheric brightness temperature T_B (K) measured by microwave radiometers at frequency f and elevation angle θ is related to the absorptive and emissive processes of the medium by the linearized form of the Radiative Transfer Equation (RTE), under Rayleigh approximation:

$$T_B(f,\theta) = T_C(f)e^{-\tau_f(0,\infty)\cdot\frac{1}{\sin\theta}} + \frac{1}{\sin\theta}\int_0^\infty T(z)\alpha(f,z)e^{-\tau_f(0,z)\sin\theta}dz \tag{3-2}$$

where T_c is the cosmic background emission, commonly assumed to be 2.73 K in the EHF range, $T(z)$ is the absolute physical temperature of air (K), z is the spatial position of the emitting air volume (km), $\alpha(f, z)$ is the atmospheric volume absorption coefficient (Np/km) at frequency f, and $\tau_f(0, z)$ (Np) is the optical depth of the atmospheric layer between 0 and z. The latter is referred to as atmospheric opacity when z tends to infinity:

$$\tau(f,\theta) = \tau_f(0,\infty)\cdot\frac{1}{\sin\theta} = \frac{1}{\sin\theta}\cdot\int_0^\infty\alpha(f,z)dz \tag{3-3}$$

The atmospheric opacity $\tau(f,\theta)$ can be expressed in terms of brightness temperature T_B after introducing the atmospheric mean radiating temperature T_{mr} (K), defined as:

$$T_{mr}(f,\theta) = \frac{\int_0^\infty T(z)\alpha(f,z)e^{-\tau_f(0,z)\frac{1}{\sin\theta}}dz}{\int_0^\infty \alpha(f,z)e^{-\tau_f(0,z)\frac{1}{\sin\theta}}dz} \tag{3-4}$$

Thus:

$$T_B(f,\theta) = T_C e^{-\tau(f,\theta)} + T_{mr}(f,\theta)(1-e^{-\tau(f,\theta)}) \tag{3-5}$$

In turn, this leads to the following expressions for the atmospheric opacity and for the attenuation A [Luini et al., 2007]:

$$\begin{aligned}\tau(f,\theta) &= \ln\left[\frac{T_{mr}(f,\theta)-T_C}{T_{mr}(f,\theta)-T_B(f,\theta)}\right] \quad \text{(Np)} \\ A(f,\theta) &= 10\log_{10}\left[\frac{T_{mr}(f,\theta)-T_C}{T_{mr}(f,\theta)-T_B(f,\theta)}\right] \quad \text{(dB)}\end{aligned} \tag{3-6}$$

Equation (3-6) shows that the radiometer enables to estimate the atmospheric attenuation at frequency f from the measured brightness temperature. Equations (3-2) to (3-6) rely on the parallel-plane approximation for which the atmosphere is considered as horizontally homogeneous. Under this approximation, which holds in non-rainy conditions, the following equation is valid:

$$A(f,\theta) = A_{zen}(f)\cdot m(\theta) = A_{zen}(f)\cdot\frac{1}{\sin(\theta)} \tag{3-7}$$

based on which the attenuation at the elevation angle of interest $A(f,\theta)$ can be computed from the attenuation obtained along the zenithal direction $A_{zen}(f)$ according to the corresponding air mass $m(\theta)$. As already stated, the key assumption underpinning the validity of this expression is that the atmosphere is non-scattering or, equivalently, that the scattering coefficient of water/ice particles is much smaller than the correspondent absorption coefficient. This is acceptable in rain-free conditions and for cloud particles up to 300 GHz. Under these assumptions [Luini et al., 2007]:

$$A(f,90°) = A_{ox}(f,90°) + a_W(f)\cdot L + a_V(f)\cdot V \tag{3-8}$$

where a_W and a_V are frequency-dependent path-averaged mass absorption coefficients of liquid water and water vapor, respectively, A_{ox} is the dry absorption due to the presence of oxygen (zenithal direction), while V and L are the integrated water vapor and integrated liquid water, respectively, defined as (v and w are the water vapor content and cloud liquid content in g/m^3):

$$V = \int_0^\infty v(l)dl \quad \text{and} \quad L = \int_0^\infty w(l)dl \tag{3-9}$$

The mass absorption coefficients can be calculated as:

$$a_V = \frac{\int_0^\infty \alpha_V(l)dl}{V} = \frac{A_V(f,90°)}{V} \quad \text{and} \quad a_W = \frac{\int_0^\infty \alpha_L(l)dl}{L} = \frac{A_L(f,90°)}{L} \tag{3-10}$$

where α_V and α_L are specific attenuations (dB/km) due to water vapor and liquid water, respectively.

If measurements of T_B are performed at frequencies f_1 and f_2, leading to estimates of A_{f1} and A_{f2} by means of equation (3-8), then the values of V and L can be estimated as:

$$\begin{aligned}V &= a_1\left[A(f_1,90°) - A_{ox}(f_1,90°)\right] + a_2\left[A(f_2,90°) - A_{ox}(f_2,90°)\right] \\ L &= b_1\left[A(f_1,90°) - A_{ox}(f_1,90°)\right] + b_2\left[A(f_2,90°) - A_{ox}(f_2,90°)\right]\end{aligned} \tag{3-11}$$

where a_1, a_2, b_1 and b_2 are function of A_{ox}, a_V and a_W at the two frequencies.

DISTRIBUTION A: Distribution approved for public release. Distribution unlimited

Besides the integrated water vapor and liquid water contents, radiometers enables the prediction of total tropospheric attenuation A in non-rainy conditions at frequencies different from the radiometric ones, including those of interest for the Alphasat propagation experiment (19.7 and 39.4 GHz). Indeed, A at a reference frequency f can be estimated using (3-8), in which the oxygen attenuation and the mass absorption coefficients all refer to f. This involves the use of V and L, obtained from (3-9). An alternative simpler approach to estimate $A(f)$, employed in here, relies on the following simple model:

$$A(f, 35.4°) = a_0 + a_1 A_{23.84}(35.4°) + a_2 A_{31.4}(35.4°) + a_3 A_{82.5}(35.4°) \quad (3\text{-}12)$$

Equation (3-12) indicates that the slant path tropospheric attenuation at 19.7 and 39.4 GHz, in rain-free conditions, can be obtained as a linear combination of the radiometric attenuation at 23.84, 31.4 and 82.5 GHz. In principle, only the channels at 23.84 and 31.4 GHz would be sufficient to provide an accurate estimate of $A(f)$, as they are respectively more sensitive to water vapor and liquid water extinction; the 82.5 GHz line is added to increase the sensitivity to clouds along the path, as their effect is still relatively limited at 31.4 GHz. On the other hand, the 72.5 GHz channel is not included to avoid weighting excessively the contribution of clouds in the inversion process.

Calculation of propagation quantities and parameters at radiometric frequencies from vertical atmospheric profiles

Equations (3-11) and (3-12) require, directly or indirectly and for all the radiometric frequencies involved, the calculation of the mass absorption coefficients (a_V and a_W), mean oxygen attenuation values (A_{ox}) and mean radiating temperature (T_{mr}) starting from local vertical profiles of temperature, pressure, and humidity in the atmosphere, in turn commonly derived from radiosonde observations (RAOBS) and/or Numerical Weather Prediction (NWP) data. Indeed, such data are typically used as input to mass absorption models, such as those developed by Liebe *et al.* [Liebe et al., 1993] and Rosenkranz [Rosenkranz, 1998], in order to calculate the above mentioned quantities. In this research effort, T_{mr}, A_{ox}, a_V and a_W have been calculated by resorting to the RAOBS data collected at Milano-Linate airport. Table 3-10 gives specific information on the RAOBS data used to derive the radiometric coefficients.

Table 3-10. RAOBS data used to derive radiometric coefficients.

Database	University of Wyoming (http://weather.uwyo.edu/upperair/sounding.html)
Selected years	2011-2015
Number of profiles	2/day at 0, and 12 UTC
Site	Milano-Linate airport, Italy

First, liquid water profiles were calculated using the TKK model [Salonen and Uppala, 1991] (as slightly modified in [Martellucci et al., 2002]), which identifies clouds and quantifies the liquid and ice water contents from the knowledge of pressure, temperature and relative humidity at each vertical layer. Afterwards, the MPM93 mass absorption model [Liebe et al., 1993] was employed to calculate, for each radiosonde launch:

- The attenuation due to liquid water in clouds, A_L

- The attenuation due to water vapor, A_V
- The attenuation due to oxygen, A_{ox}
- The total tropospheric attenuation (except for the contribution from rain), A
- The integrated liquid water and water vapor contents, L and V, respectively
- The brightness temperature, T_B
- The mean radiating temperature, T_{mr}.

Fig. 3-19 summarizes the procedure for the calculation of all the quantities listed above from RAOBS vertical profiles for a given elevation angle (average elevation angle for the NASA Alphasat beacon receivers in Milan, θ = 35.42°) and given radiometric frequencies (23.84, 31.4 and 82.5 GHz, as indicated in (3-12)).

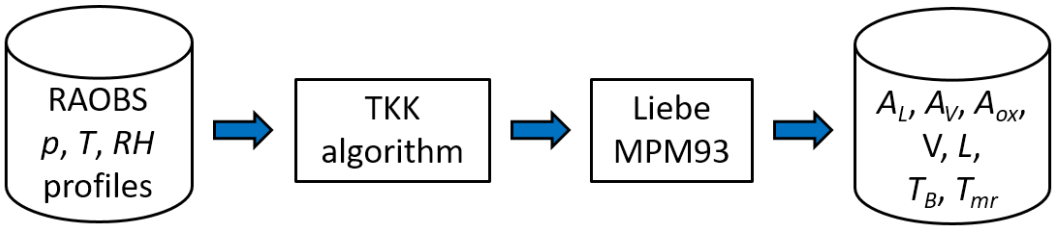

Fig. 3-19. Procedure for the calculation of propagation parameters. T is the temperature; p is the pressure; RH is the relative humidity; A_L, A_V and A_{ox} are the path attenuations due to clouds, water vapor and oxygen, respectively; V and L are the integrated water vapor and integrated liquid water, respectively; T_B is the brightness temperature and T_{mr} is the mean radiating temperature.

Table 3-11 reports the mean yearly average and standard deviation (σ) values of T_{mr}, while Table 3-12 and Table 3-13 focus on monthly average and standard deviation values of T_{mr}, respectively.

Table 3-11. Yearly average and standard deviation (σ) values of T_{mr} (K) as a function of frequency (GHz).

f	Yearly average T_{mr}	Yearly σ of T_{mr}
23.84	274.4	7.8
31.4	270.7	8.0
72.5	270.4	8.0
82.5	274.0	8.4

Table 3-12. Monthly average values of T_{mr} (K) as a function of frequency (GHz).

		Month											
		1	**2**	**3**	**4**	**5**	**6**	**7**	**8**	**9**	**10**	**11**	**12**
f	**23.84**	265.7	265.3	268.2	271.9	276.4	280.3	284.3	284.0	281.4	277.1	270.9	267.7
	31.4	262.0	261.5	264.1	267.8	272.6	276.8	281.1	280.9	278.1	273.6	267.2	263.9
	72.5	261.7	261.2	263.7	267.4	272.5	276.5	280.8	280.7	277.8	273.1	266.8	263.6
	82.5	264.8	264.4	267.3	271.2	276.2	280.4	284.7	284.5	281.7	277.0	270.3	266.8

DISTRIBUTION A: Distribution approved for public release. Distribution unlimited

Table 3-13. Monthly standard deviation (σ) values of T_{mr} (K) as a function of frequency (GHz).

		Month											
		1	**2**	**3**	**4**	**5**	**6**	**7**	**8**	**9**	**10**	**11**	**12**
f	**23.84**	4.6	4.1	4.4	3.7	3.4	4.0	3.2	3.4	3.3	3.5	4.0	4.4
	31.4	4.6	4.1	4.5	3.7	3.5	4.0	3.4	3.5	3.4	3.7	4.1	4.6
	72.5	4.5	4.0	4.4	3.7	3.7	3.8	3.3	3.4	3.2	3.8	4.1	4.5
	82.5	4.9	4.3	4.8	3.9	3.6	4.2	3.5	3.6	3.5	3.8	4.3	4.8

The regression coefficients a_0, a_1, a_2 and a_3 in (3-12) for the two Alphasat propagation experiment operational frequencies are listed in Table 3-14.

Table 3-14. Coefficients for the estimation of the atmospheric attenuation at operational frequencies of the Alphasat propagation experiment (GHz).

f	a_0	a_1	a_2	a_3
19.7	0.015265	0.431025	0.169472	-0.00172
39.4	0.137625	-0.17903	1.403818	0.043795

Finally, though not directly employed in this work to estimate the tropospheric attenuation at 19.7 and 39.4 GHz, for the sake of completeness, Table 3-15 lists the mean yearly values of A_{ox} and Table 3-16 reports the mass absorption coefficients a_V and a_W.

Table 3-15. Yearly average values of A_{ox} (dB) as a function of frequency (GHz).

f	**Mean yearly A_{ox}**
23.84	0.124
31.4	0.203
72.5	1.295
82.5	0.392

Table 3-16. Yearly average mass absorption coefficients a_V and a_W (dB/mm) as a function of frequency (GHz).

f	a_V	a_W
23.84	0.0241	0.5333
31.4	0.009	0.8803
72.5	0.0302	3.2432
82.5	0.0389	3.8263

The following figures show an example of the usefulness of radiometric measurements. Specifically, Fig. 3-20 depicts the trend of the brightness temperature (path to Alphasat) collected by the instrument at 23.84, 31.4 and 82.5 GHz, used to estimate *V* and *L* (zenithal path), as shown in Fig. 3-21 and Fig. 3-22, respectively. The data clearly indicate a constant increase in the water vapor throughout the day, as well as the presence of heavy clouds along the path, especially around midday, when the zenithal integrated liquid water content *L* exceeds 1 mm. This is confirmed by Fig. 3-23, which depicts the trend of the MWR-derived total

DISTRIBUTION A: Distribution approved for public release. Distribution unlimited

tropospheric attenuation A_{MWR} at 19.7 and 39.4 GHz: around 12 UTC, A_{MWR} exceeds 1 dB and 3 dB, respectively for the two frequencies.

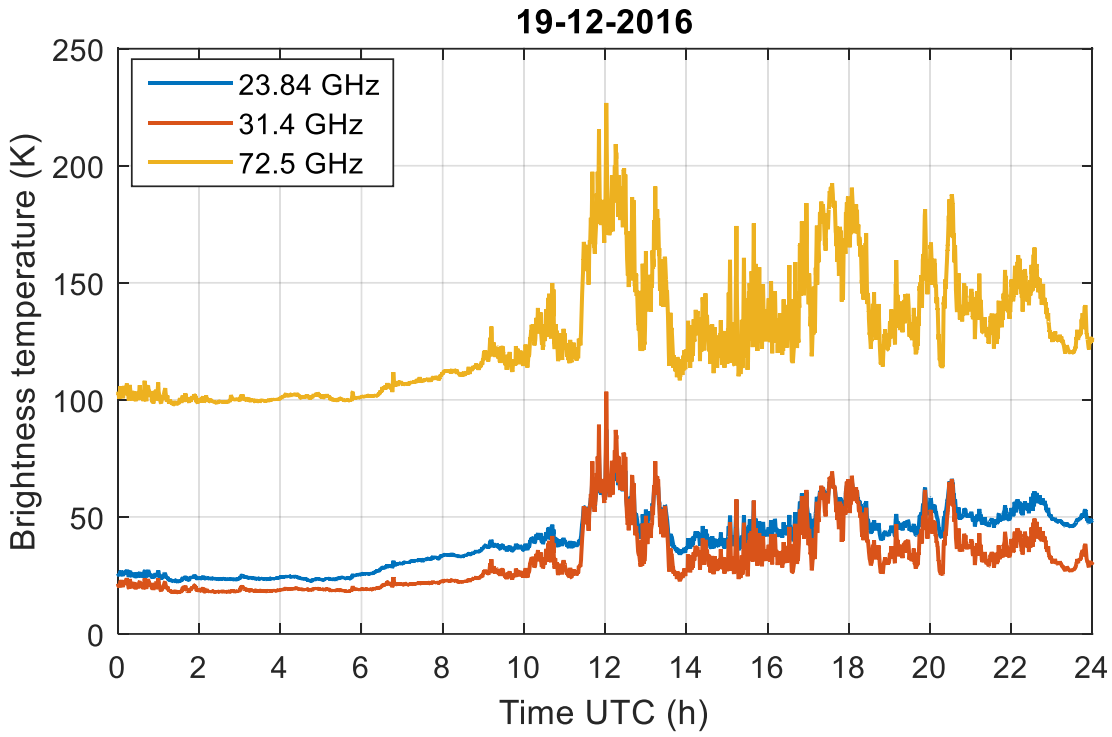

Fig. 3-20. Time series of the brightness temperature collected by the radiometer (19th December, 2016).

DISTRIBUTION A: Distribution approved for public release. Distribution unlimited

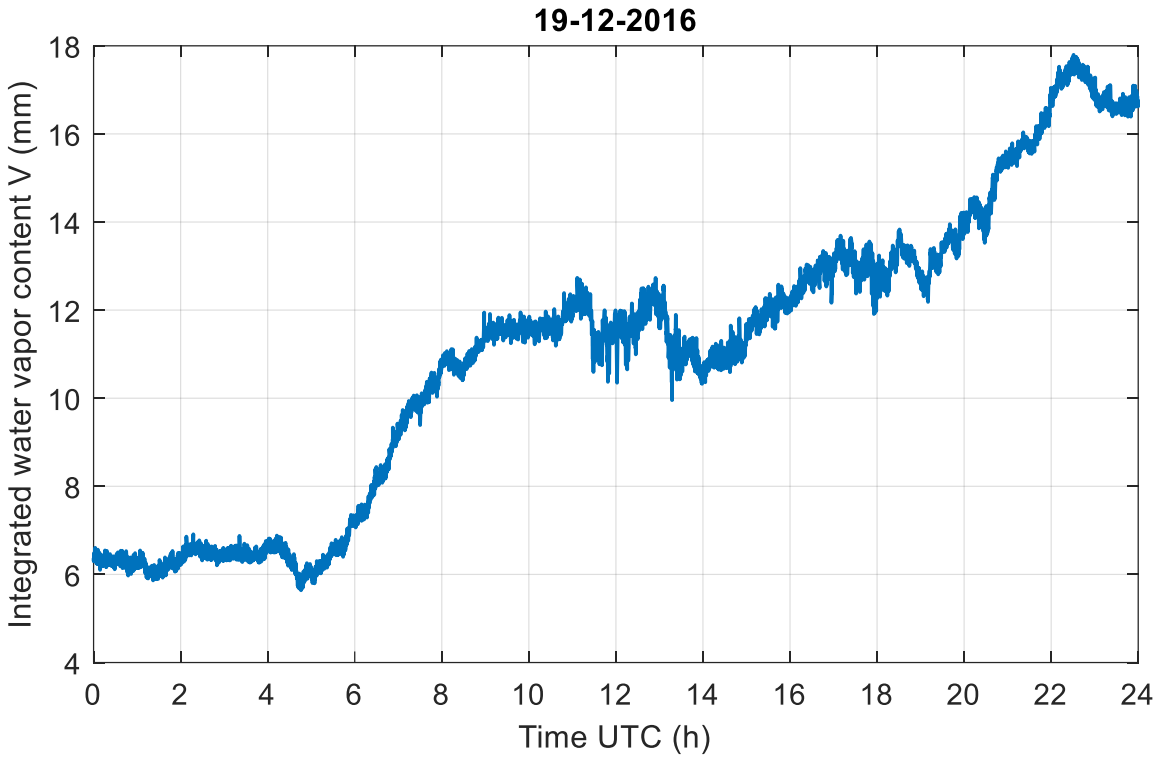

Fig. 3-21. Time series of the integrated water vapor content V estimated from the radiometric measurements (19th December, 2016).

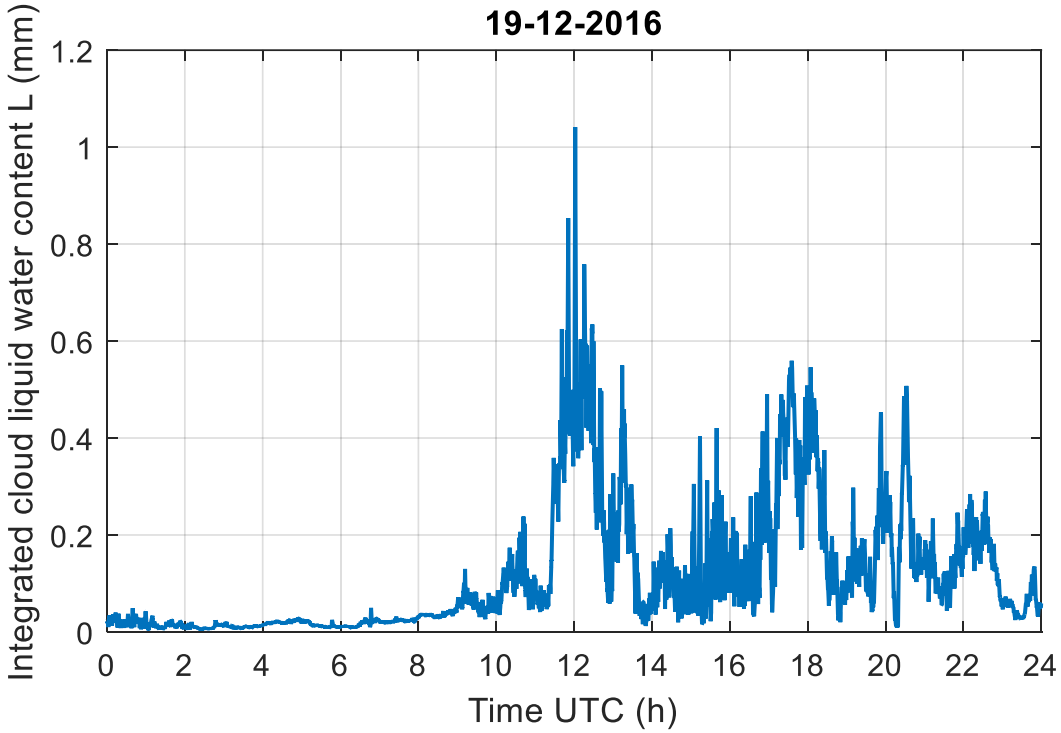

Fig. 3-22. Time series of the integrated liquid water content L estimated from the radiometric measurements (19th December, 2016).

DISTRIBUTION A: Distribution approved for public release. Distribution unlimited

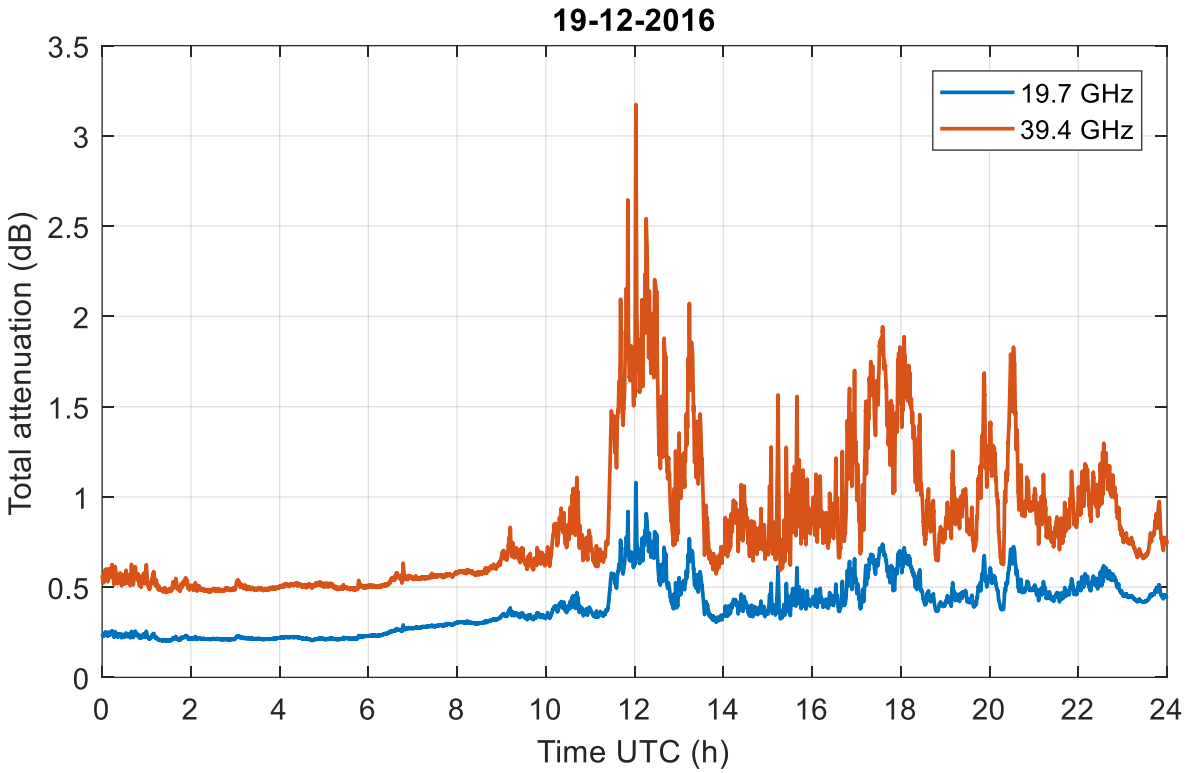

Fig. 3-23. Time series of the total tropospheric attenuation estimated from the radiometric measurements (19th December, 2016).

Calibration of beacon signals using MWR-derived attenuation

The calibration of the received beacon signals (P_B) using radiometric data is achieved by using as reference the MWR-derived total tropospheric attenuation at 19.7 and 39.4 GHz (A_{MWR}). A key point of the calibration procedure is to identify the presence of rain along the path: as already mentioned, A_{MWR}, as estimated according to the equations (3-2)-(3-12), is reliable only in nonrainy conditions.

In order to identify rain events, we have employed a procedure that exploits the brightness temperature data at 23.84 and 31.4 GHz collected by the radiometer, which, as reported in [Luini et al., 2007], can give a preliminary indication on the presence of rain along the path. Specifically, no rain is assumed to affect the link if:

$$SSI = \frac{T_B(31.4) - 11.9}{T_B(23.84)} < 0.95 \tag{3-13}$$

The "first-guess" rain event identified through equation (3-13) is afterwards verified and "adjusted" by visually inspecting the rain rate time series collected by the disdrometer and the received beacon signals. The procedure is clarified below in Fig. 3-24, Fig. 3-25 and Fig. 3-26, which report, for the same day, A_{MWR} at 39.4 GHz, the rain rate and the beacon power levels, respectively. In all figures, the yellow line represents the duration of the rain even as identified by visual inspection of all the data mentioned above. In fact, as is clear from Fig. 3-24, the application of equation (3-13) marks as rainy (red asterisks) some samples that, based on the

DISTRIBUTION A: Distribution approved for public release. Distribution unlimited

trend of P_B in Fig. 3-26, are likely associated to clouds. On the contrary, equation (3-13) fails to identify the final part of the rain event, as indicated by the disdrometer.

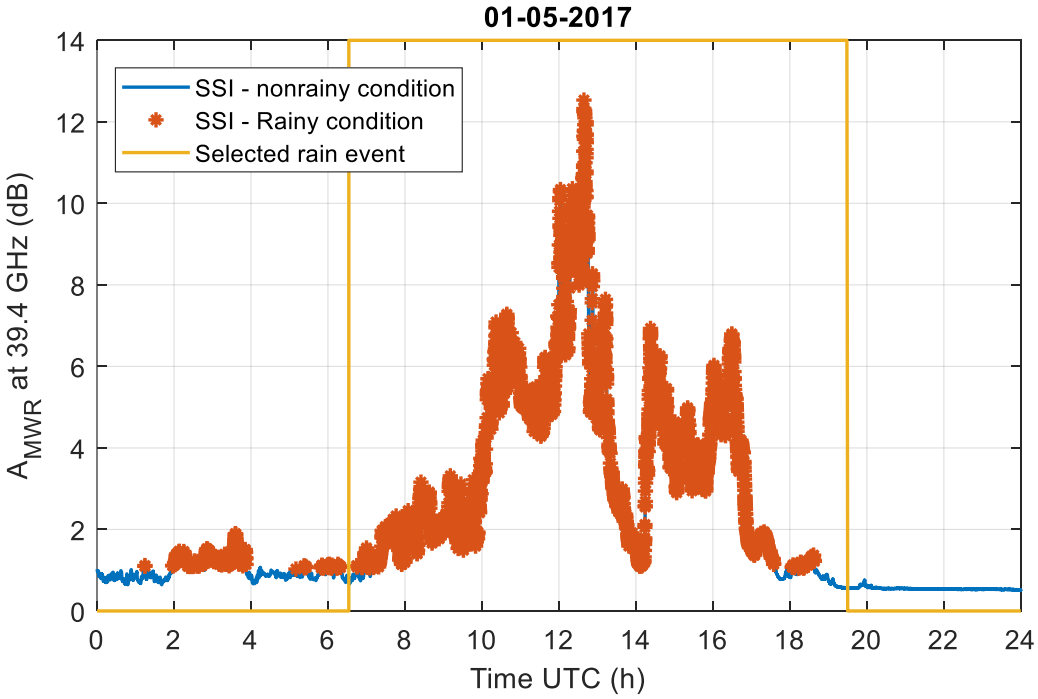

Fig. 3-24. Time series of A_{MWR} temperature at 31.4 GHz, with preliminary identification of rainy periods (1st May, 2016).

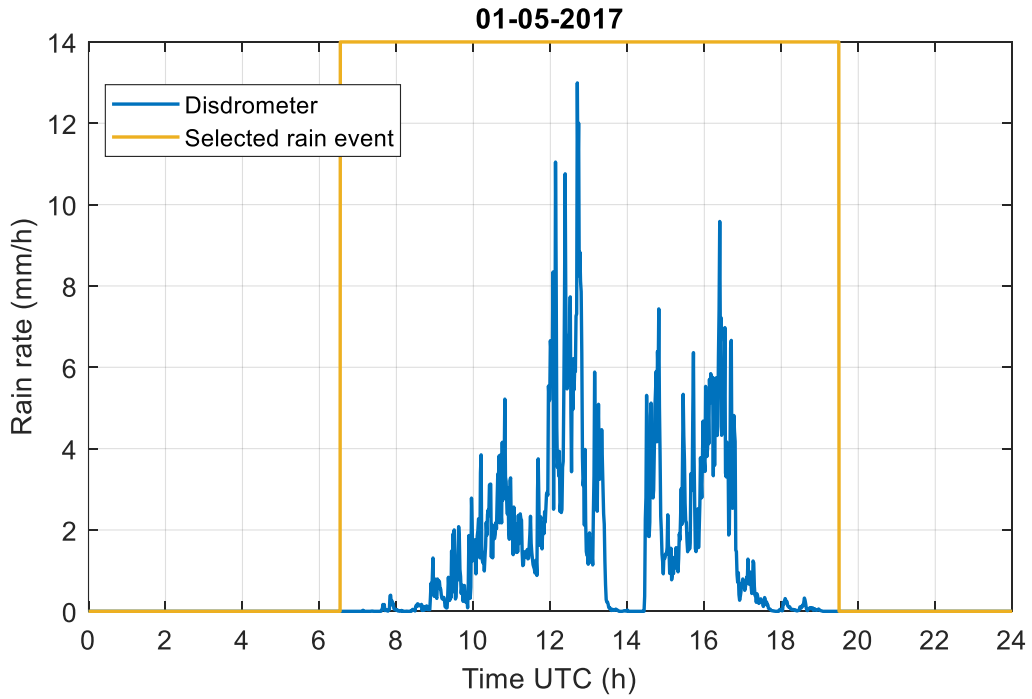

Fig. 3-25. Time series of the rain rate derived from the disdrometer (1st May, 2016).

DISTRIBUTION A: Distribution approved for public release. Distribution unlimited

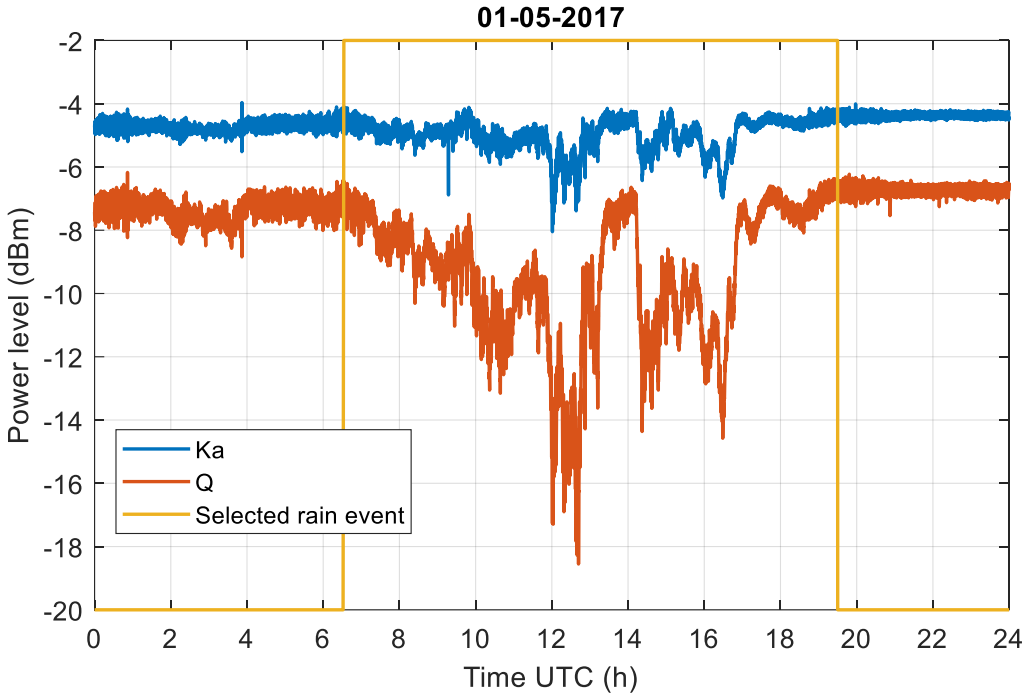

Fig. 3-26. Power levels derived from the beacon receivers (1st May, 2016).

The steps of the calibration procedure are:

1. Calculate A_B by low-pass filtering (to remove scintillations) and changing the sing of P_B
2. Calculate the difference between A_B and A_{MWR}:

$$A_{diff} = A_B - A_{MWR} \tag{3-14}$$

3. Define A'_{diff}
   - In absence of rain, $A'_{diff} = A_{diff}$
   - During rain event, A'_{diff} is calculated as the linear interpolation between the A^b_{diff} and A^e_{diff}, respectively defined as the last sample of A_{diff} before the start of the rain event and the first sample of A_{diff} after the rain event.
4. Calculate the beacon-derived total attenuation A as:

$$A = A_B - A'_{diff} \tag{3-15}$$

The steps above are clarified in Fig. 3-27, which shows A_B, A_{MWR} and A'_{diff} for the 1st May, 2016, while the final step of the calibration process, i.e. the application of equation (3-15), is reported in Fig. 3-28. As expected, during the rain event, there is no perfect agreement between A and A_{MWR}: while the latter is unreliable in presence of scattering effects along the path, the beacon receiver can measure with high accuracy the effects induces by rain. This is the reason why beacon receivers and radiometers should always be combined in electromagnetic wave propagation experiments.

DISTRIBUTION A: Distribution approved for public release. Distribution unlimited

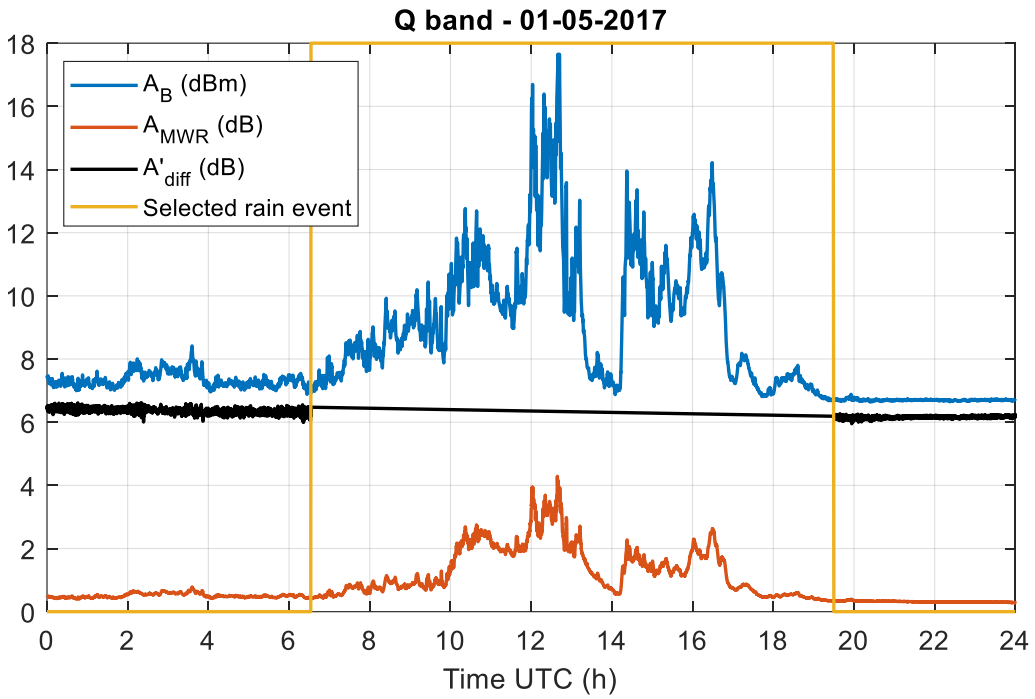

Fig. 3-27. Time series of A_B, A_{MWR} and A'_{diff} (1st May, 2016).

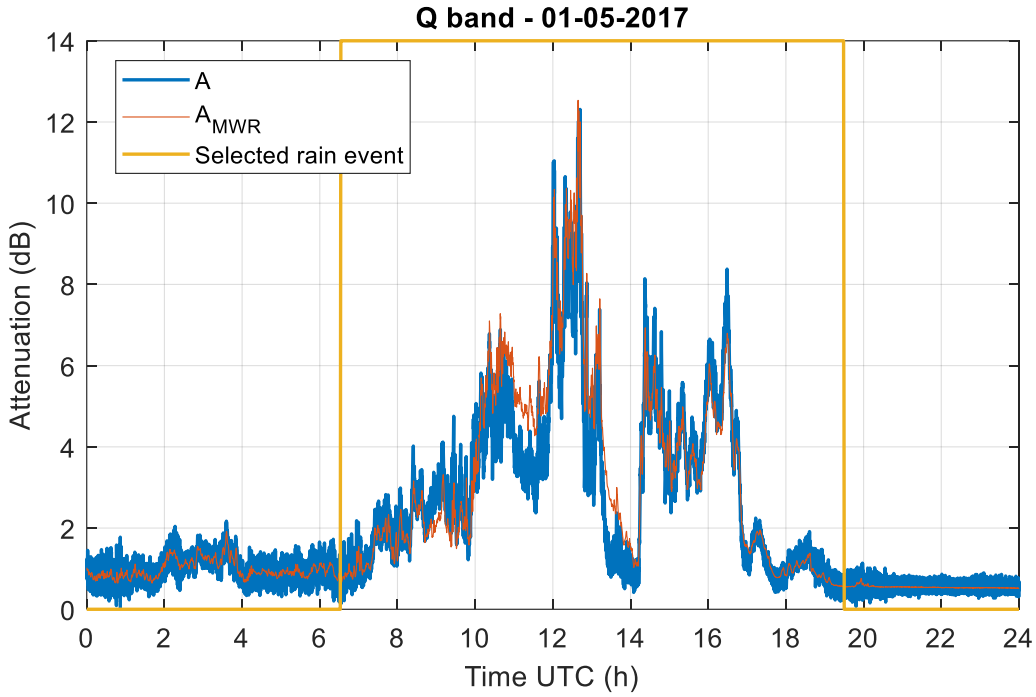

Fig. 3-28. Time series of the calibrated total attenuation derived from the beacon power levels and estimated by the radiometer (1st May, 2016).

DISTRIBUTION A: Distribution approved for public release. Distribution unlimited

3.3.4. Statistics of attenuation

3.3.4.1. Total attenuation from beacon data

Fig. 3-29 and Fig. 3-30 depict the yearly CCDFs of total tropospheric attenuation obtained by processing all the beacon data collected from June 2014 to May 2019. More specifically, all data between June 2014 to December 2016 were calibrated using the RAOBS-derived clear sky reference levels [EOARD 2017], while the remaining data (January 2017 to May 2019) were processed by exploiting radiometric measurements (see section 3.3.3.1). No additional results are included because of a major hardware failure (motherboard) in the NASA PC collecting the data, which occurred on the 7th of July 2019 and lasted till the 19th of February 2020. Results are provided separately for year 1 (June 2014-May 2015, blue line), year 2 (June 2015-May 2016, red line), year 3 (June 2016-May 2017, yellow line), year 4 (June 2017-May 2018, violet line), and year 5 (June 2018-May 2019, green line), as well as for the full 5-year period (black dashed line). These latter curves are also reported in Fig. 3-31, for a more convenient comparison between the data collected at the two frequencies. As it turns out, the year-to-year variability is rather limited (with year 1 and year 5 showing the worse and best propagation conditions, respectively).

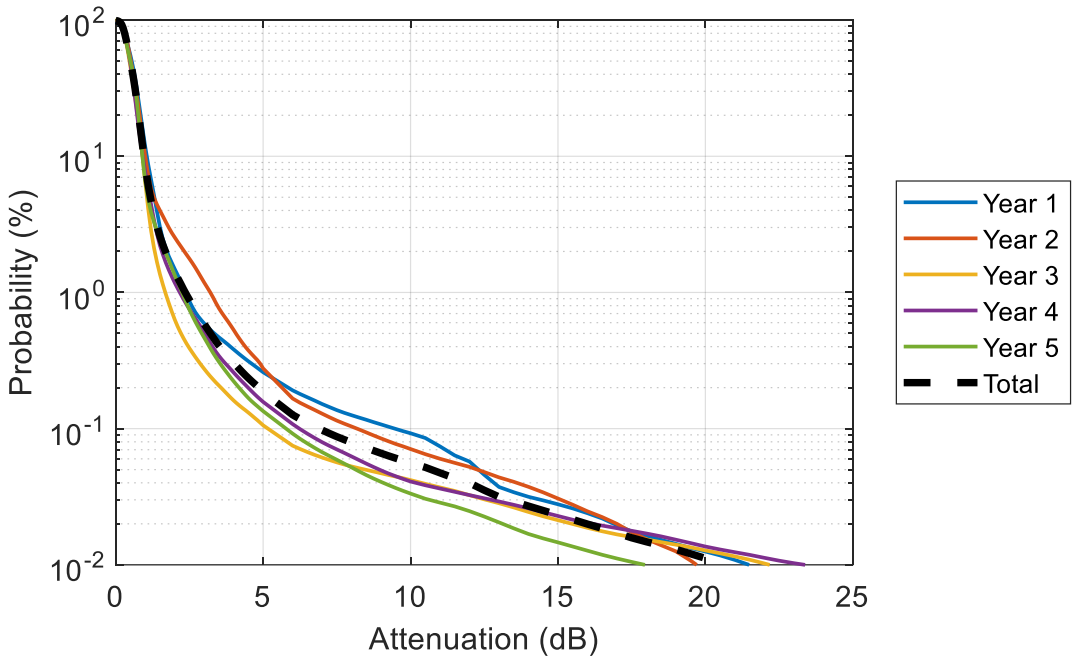

Fig. 3-29. Yearly CCDFs of total attenuation (separate years, Ka band).

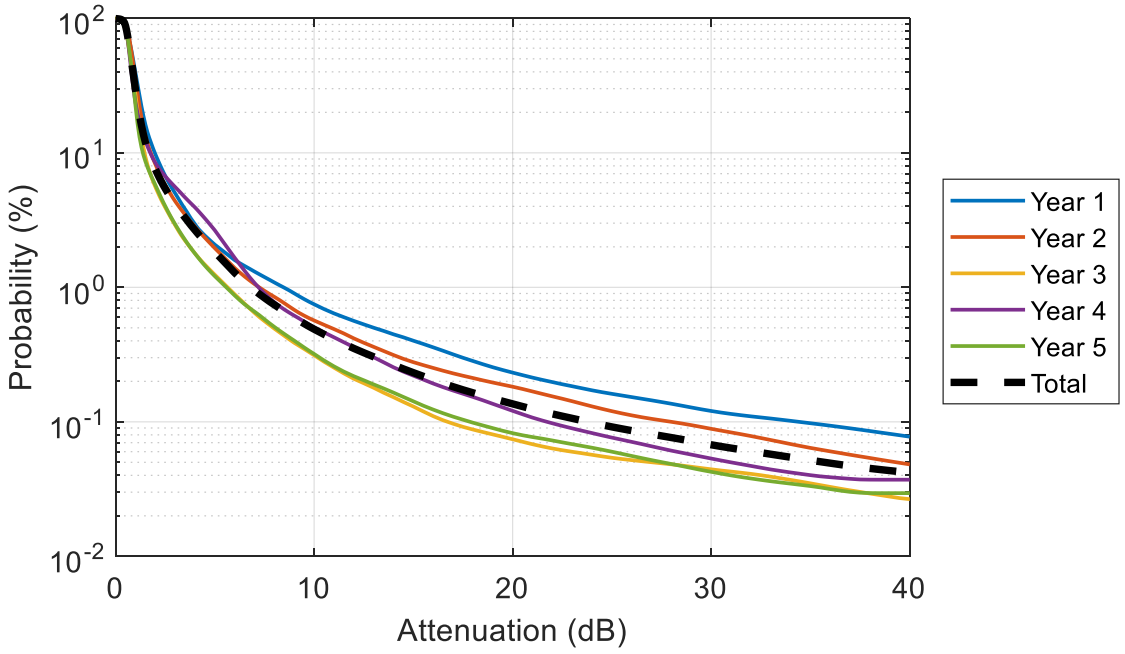

Fig. 3-30. Yearly CCDFs of total attenuation (separate years, Q band).

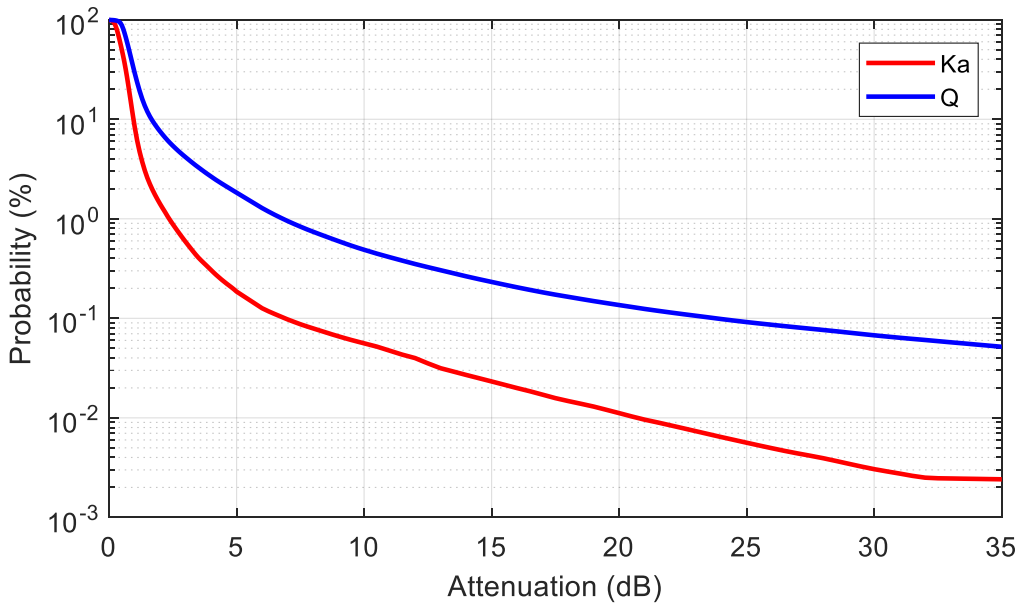

Fig. 3-31. Yearly CCDFs of total attenuation (full 5-year period, Ka band and Q band).

Fig. 3-32 and Fig. 3-33 provide additional information by showing the monthly attenuation CCDFs (each month refer to data extracted from all years). The figures also include again the full 5-year statistics (black dashed lines) for convenience.

DISTRIBUTION A: Distribution approved for public release. Distribution unlimited

Table 3-17, Table 3-18 and Table 3-19 list the beacon data availabilities for each month, on a monthly basis, and on a yearly basis, respectively: results indicate quite an overall satisfactory performance of the beacon receivers (the whole period availability is around 89% and 91% for the Ka band and the Q band, respectively).

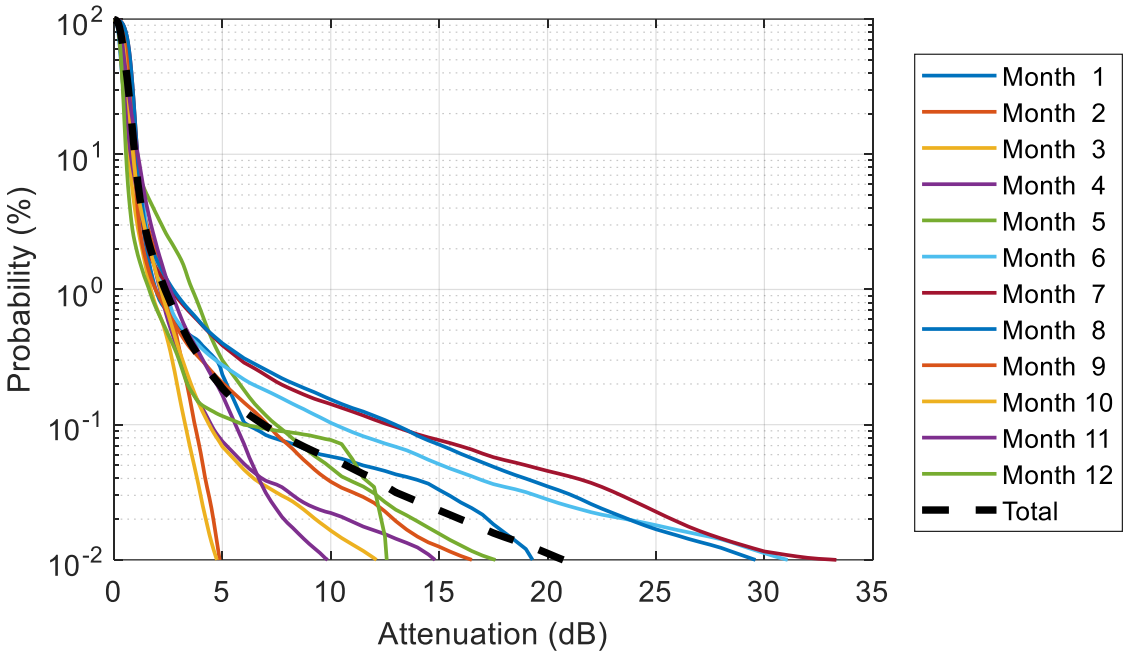

Fig. 3-32. Monthly CCDFs of total attenuation (full 5-year period, Ka band).

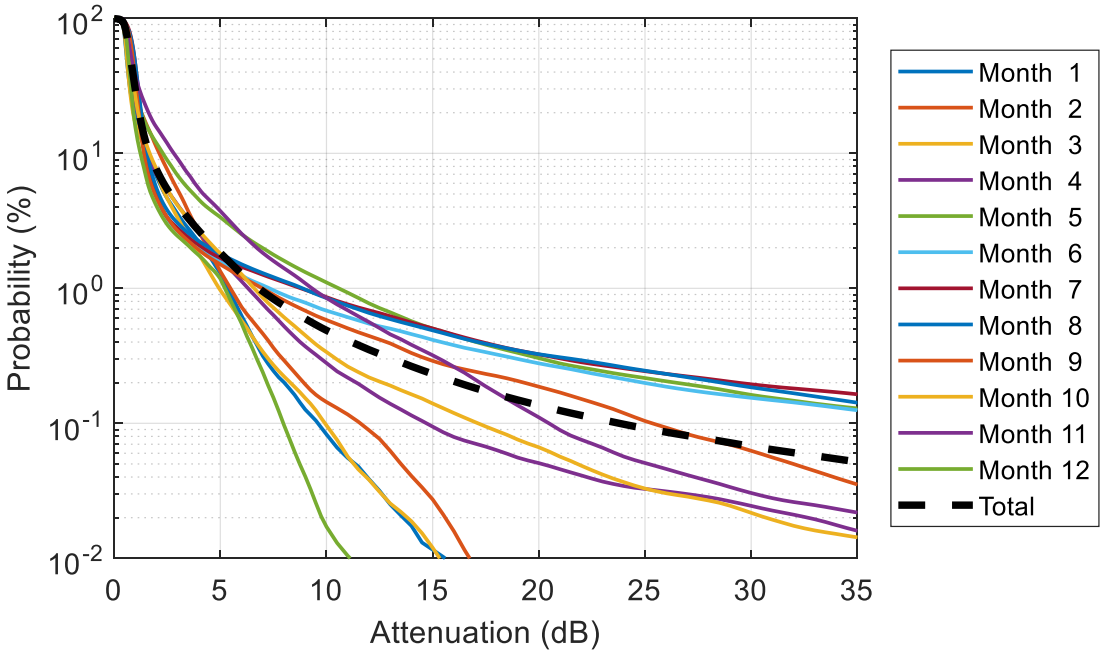

Fig. 3-33. Monthly CCDFs of total attenuation (full 5-year period, Q band).

Table 3-17. Beacon data availability: all months, full 5-year period.

Month	Ka band	Q band	Month	Ka band	Q band
June 2014	75.8	70.8	June 2016	26.5	26.5
July 2014	75.2	78.7	July 2016	100	99.9
August 2014	92.9	94.3	August 2016	85.1	85
September 2014	84.3	86.1	September 2016	100	100
October 2014	92.1	98.5	October 2016	72.1	70.1
November 2014	93.7	99.9	November 2016	80	80
December 2014	98.8	100	December 2016	100	96.8
January 2015	86.3	89.5	January 2017	96.5	99
February 2015	74.1	87.1	February 2017	99.9	99.9
March 2015	71.2	99.8	March 2017	79.3	80.5
April 2015	91.8	100	April 2017	97.9	99.6
May 2015	92.3	94.2	May 2017	99.4	99.7
June 2015	98.6	100	June 2018	99.8	99.7
July 2015	96.8	96.7	July 2018	98.2	99.1
August 2015	100	99.9	August 2018	99.7	99.7
September 2015	100	99.9	September 2018	92.9	92.2
October 2015	100	99.9	October 2018	80.5	80.4
November 2015	99.4	99.3	November 2018	98.3	99.6
December 2015	100	100	December 2018	90.2	91.9
January 2016	79.2	79.2	January 2018	92.9	93.5
February 2016	90.6	91.2	February 2018	92.1	92.0
March 2016	99	99.9	March 2018	81.8	81.7
April 2016	94.9	88.2	April 2018	94.2	94.0
May 2016	66.9	80.1	May 2018	95.7	95.6

June 2018	97.5	97.5
July 2018	70.2	70.1
August 2018	71.1	71
September 2018	100	100
October 2018	91.3	91.2
November 2018	100	99.9
December 2018	90	93.1
January 2019	61	65
February 2019	89.1	90.9
March 2019	83.4	87.6
April 2019	98.8	99.4
May 2019	100	99.9

DISTRIBUTION A: Distribution approved for public release. Distribution unlimited

Table 3-18. Average monthly beacon data availability, full 5-year period.

Month	Ka band	Q band
January	83.2	84.9
February	89.2	92.2
March	82.9	89.9
April	95.4	96.2
May	90.9	93.9
June	79.6	78.9
July	88.1	88.9
August	89.8	90
September	95.4	95.6
October	87.2	88
November	94.3	95.8
December	95.8	96.3

Table 3-19. Yearly beacon data availability, full 5-year period.

Year	Ka band	Q band
Year 1 (June 2014-May 2015)	85.7	91.6
Year 2 (June 2015-May 2016)	93.8	94.5
Year 3 (June 2016-May 2017)	86.4	86.4
Year 4 (June 2017-May 2018)	93	93.3
Year 5 (June 2018-May 2019)	87.7	88.8
5 years (June 2014-May 2019)	89.3	90.9

For the sake of completeness, Fig. 3-34 and Fig. 3-35 show the yearly and monthly CCDFs of the rain rate.

DISTRIBUTION A: Distribution approved for public release. Distribution unlimited

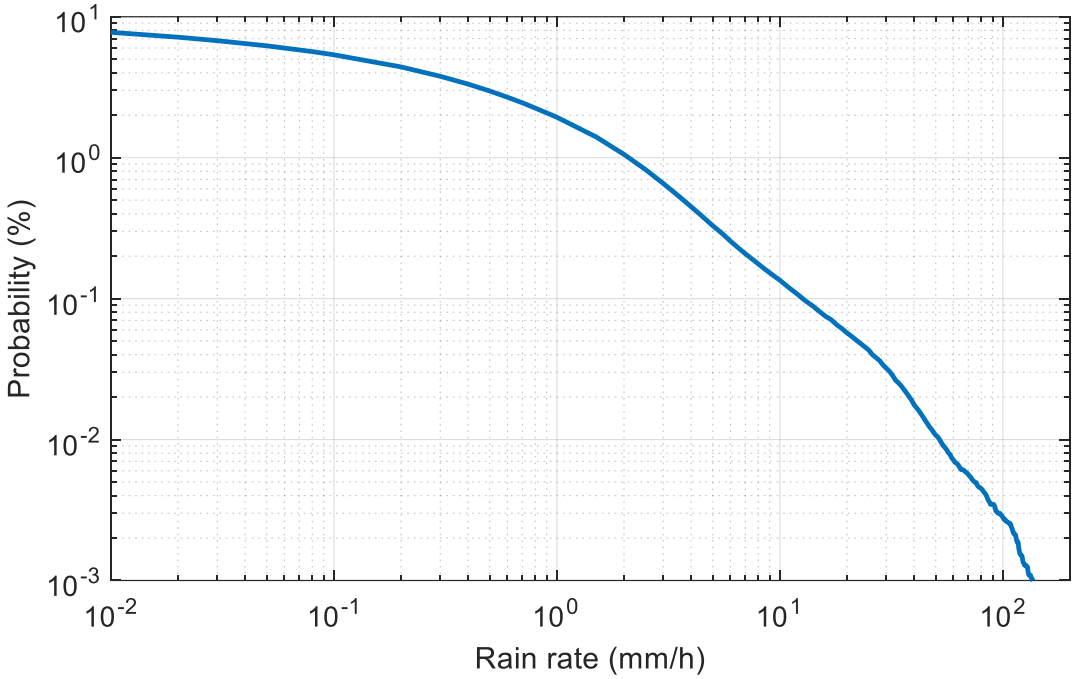

Fig. 3-34. Yearly CCDF of the rain rate derived from the disdrometer (full 5-year period).

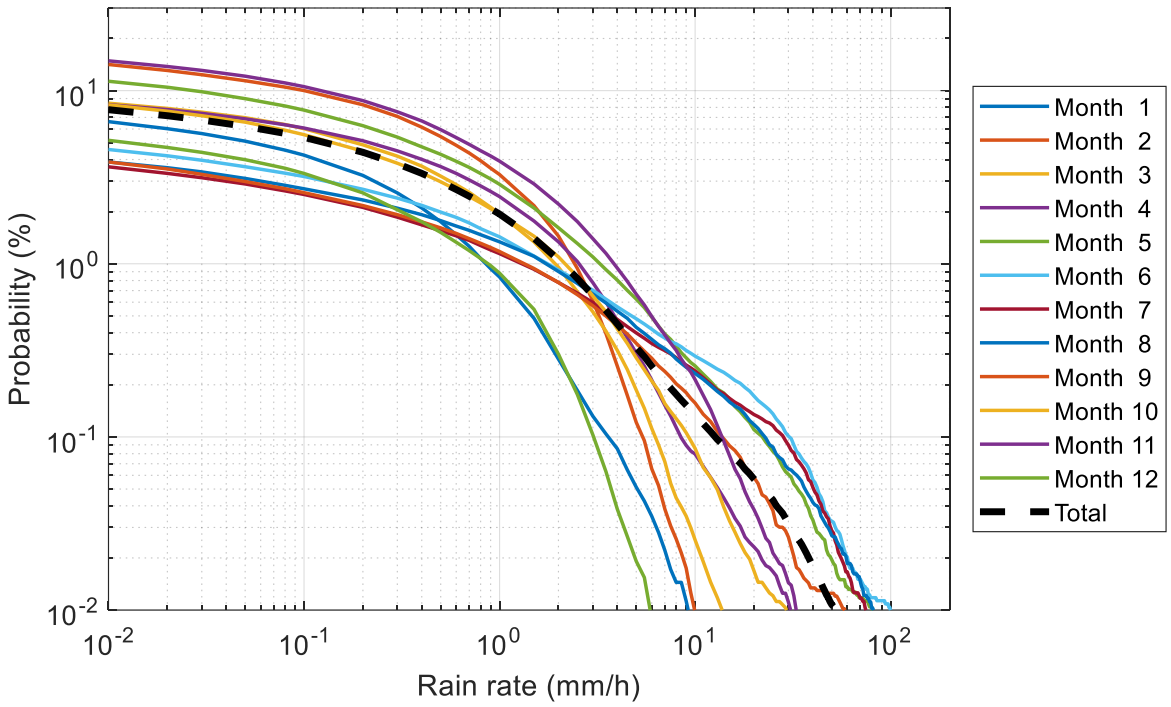

Fig. 3-35. Monthly CCDF of the rain rate derived from the disdrometer (full 5-year period).

3.3.4.2. Total attenuation from radiometric data

In addition to the attenuation results presented in the previous section, brightness temperature data were processed to derive directly the path attenuation at the two radiometric

frequencies in the W band, i.e. 72.5 and 82.5 GHz. To this aim, equation (3-6) was used, which, besides T_B, also requires the knowledge of T_{mr}. In order to maximize the attenuation retrieval accuracy, instead of relying on the yearly and monthly values of T_{mr} reported in Table 3-11 and Table 3-12, respectively, we have opted for using instantaneous values of T_{mr} obtainable from ground meteorological measurements. Specifically, using again the same RAOBS dataset described in the previous section and the prediction methodology explained in Fig. 3-19, we have investigated the relationship between the T_{mr} and the ground temperature T_G, the ground pressure P_G and the ground relative humidity RH_G. Fig. 3-36, Fig. 3-37 and Fig. 3-38 show the associated scatter plots, which indicate quite a high linear correlation between T_{mr} and T_G, while this is not the case for P_G, nor for RH_G.

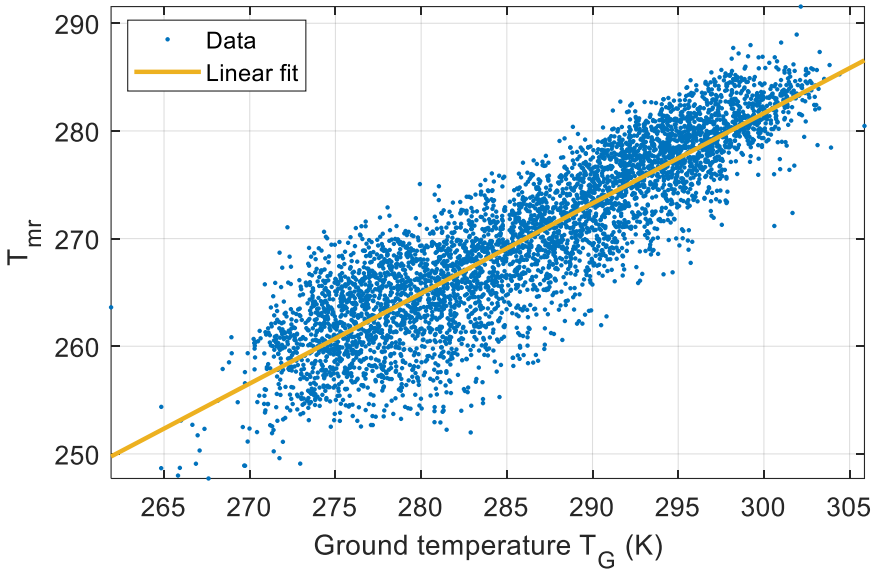

Fig. 3-36. Scatterplot between T_{mr} and the ground temperature T_G, along with fitting linear expression (f = 72.5 GHz).

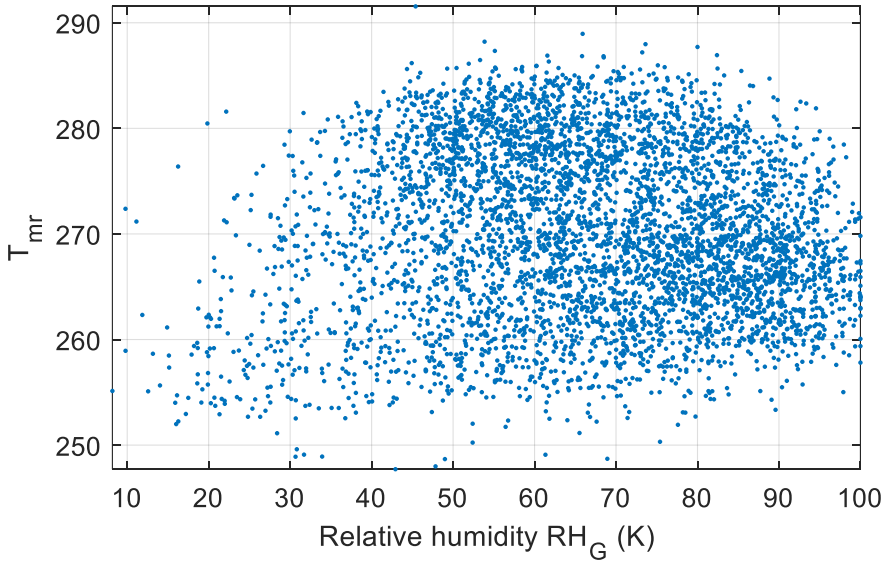

Fig. 3-37. Scatterplot between T_{mr} and the ground relative humidity RH_G (f = 72.5 GHz).

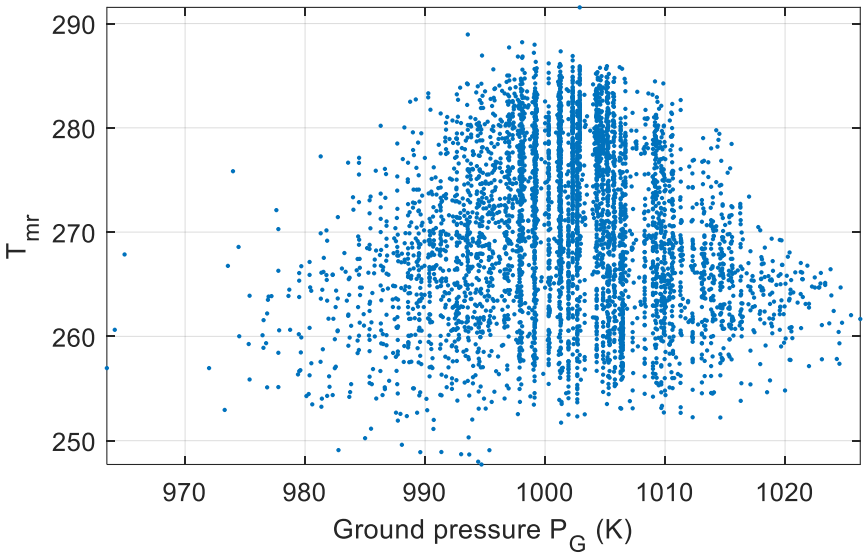

Fig. 3-38. Scatterplot between T_{mr} and the ground pressure P_G (f = 72.5 GHz).

As a result, we have selected the following expression to estimate T_{mr} from ground measurements:

$$T_{mr}(f) = c_1(f)T_G + c_2(f) \tag{3-16}$$

where c_1 and c_2 are the frequency dependent coefficients reported in Table 3-20.

Table 3-20. Coefficients in (3-16).

Frequency	c_1	c_2
23.84 GHz	0.82	38.49
31.4 GHz	0.84	29.3
72.5 GHz	0.84	30.53
82.5 GHz	0.88	21.51

As an example, Fig. 3-39 shows the comparison between T_{mr} as calculated from RAOBS data plus the Liebe MPM93 model and as estimated from the ground temperature through (3-16) (f = 72.5 GHz): the agreement is satisfactory as indicated by the average value (close to 0 K) and the root mean square value (3.8 K) of the prediction error. Similar results were found for the other radiometric channels, including the one at 82.5 GHz.

DISTRIBUTION A: Distribution approved for public release. Distribution unlimited

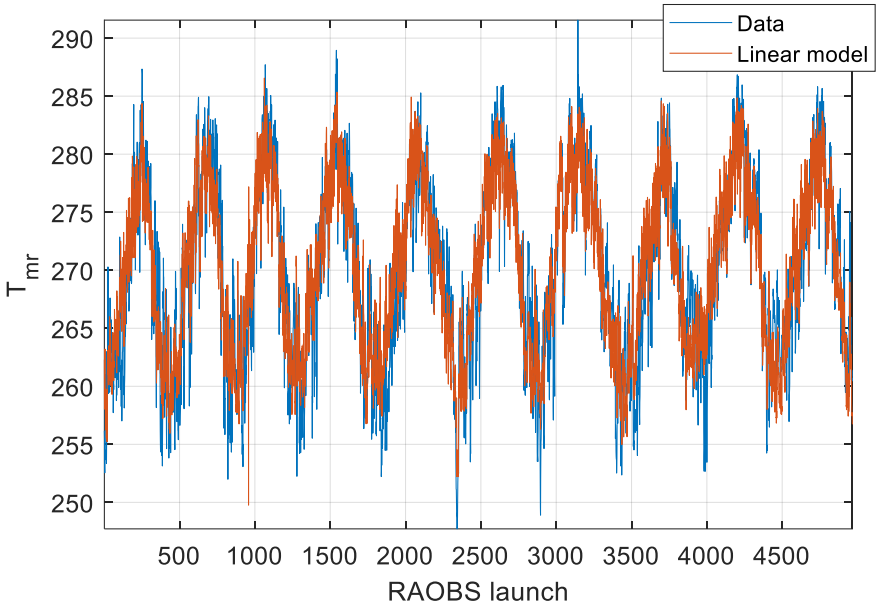

Fig. 3-39. Comparison between T_{mr} as calculated from RAOBS data plus the Liebe MPM93 model and as estimated from the ground temperature through (3-16) (f = 72.5 GHz).

As equation (3-16) is valid under the assumption of scattering-free atmosphere, we have employed the same Sky Status Indicator (SSI) in (3-13) as an attempt to filter out brightness temperature data collected in presence of rain.

Fig. 3-40 compares the CCDFs of the attenuation derived from the radiometer (2 full years, from June 2017 to May 2019), obtained on the one side using only the data in nonrainy conditions as indicated by the SSI, on the other side using the full dataset: as expected, a huge difference between the two sets of curves emerges. Fig. 3-41 shows the same comparison as in Fig. 3-40, but for in terms of brightness temperature.

DISTRIBUTION A: Distribution approved for public release. Distribution unlimited

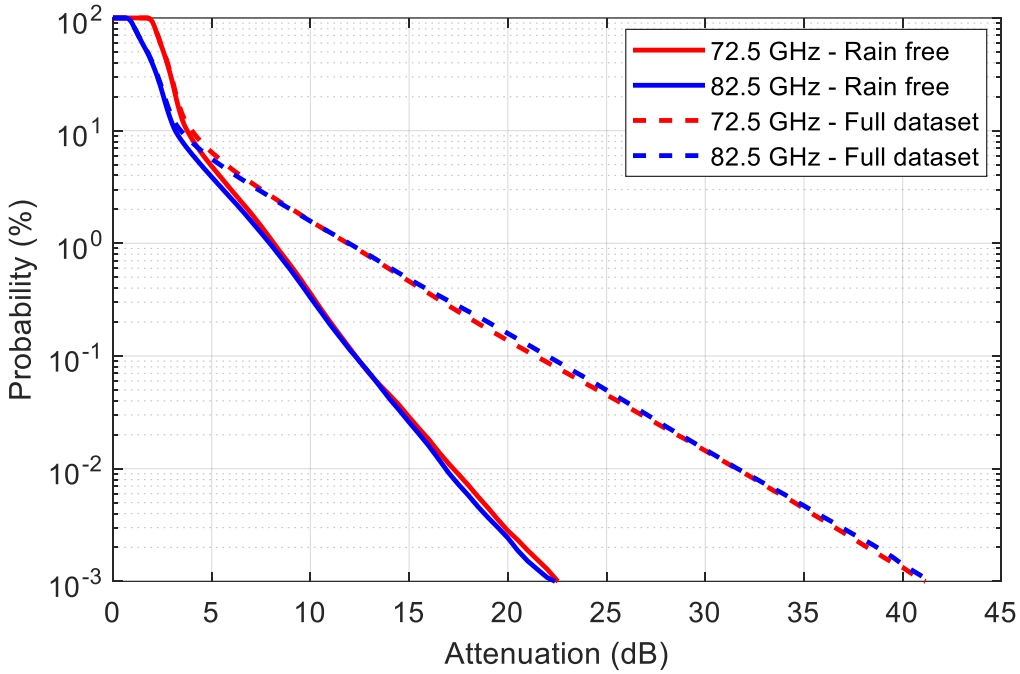

Fig. 3-40. CCDFs of the attenuation derived from the radiometer: comparison between the data filtered using the SSI and the full dataset.

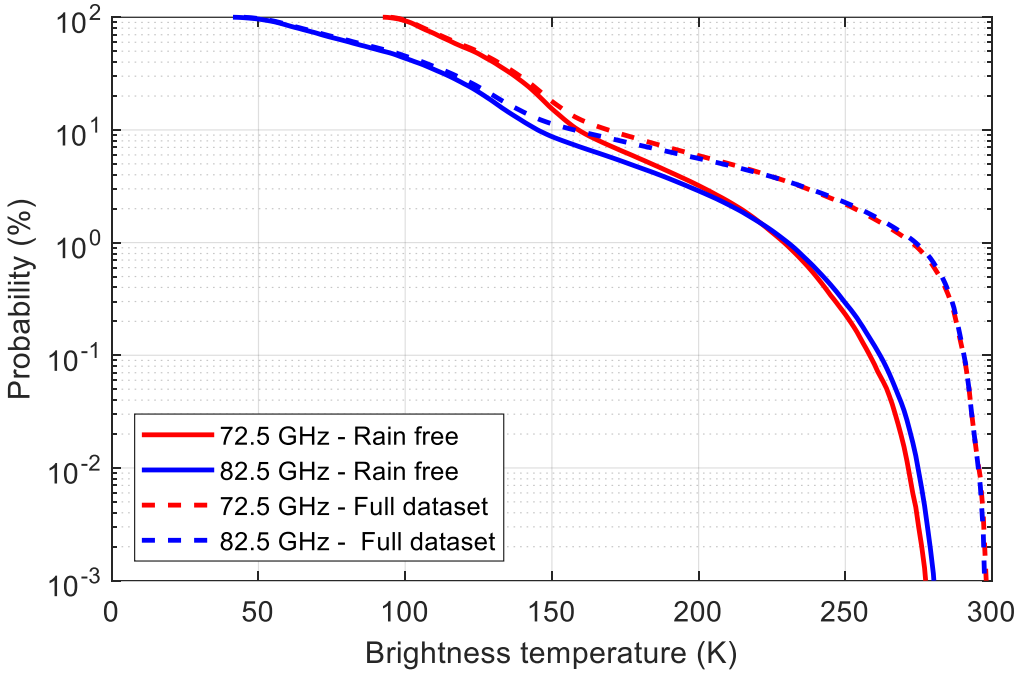

Fig. 3-41. CCDFs of the brightness temperature: comparison between the data filtered using the SSI and the full dataset.

3.3.5. Site diversity

Given the availability of two Alphasat receivers installed in Spino d'Adda and Milano (22.6 km apart, as indicated in Fig. 3-8), the advantage of using a two-site diversity system was

explored. As a hint of this, Fig. 3-42 shows an example of the total attenuation data collected in the same (rainy) day (5th of November, 2014) in both station (top for Spino d'Adda, bottom for Milan): the spatial variability of rain is such that when high attenuation is experienced in one site (e.g. between 0 and 2 UTC in Spino d'Adda), much lower values are often recorded in the other site. This is even clearer in Fig. 3-43, which compares the sample signals collected at the two sites during another rainy day (Ka band on the top, Q band in the middle; red and green lines associated to Spino d'Adda and Milan receivers, respectively), together with the attenuation level that a site diversity system would experience, i.e. the minimum level between the two stations (black dashed line). Fig. 3-44 shows the rain rate time series as measured by the 1-minute integration time raingauge installed at Spino d'Adda and by the 1-minute integration time disdrometer installed in Milan.

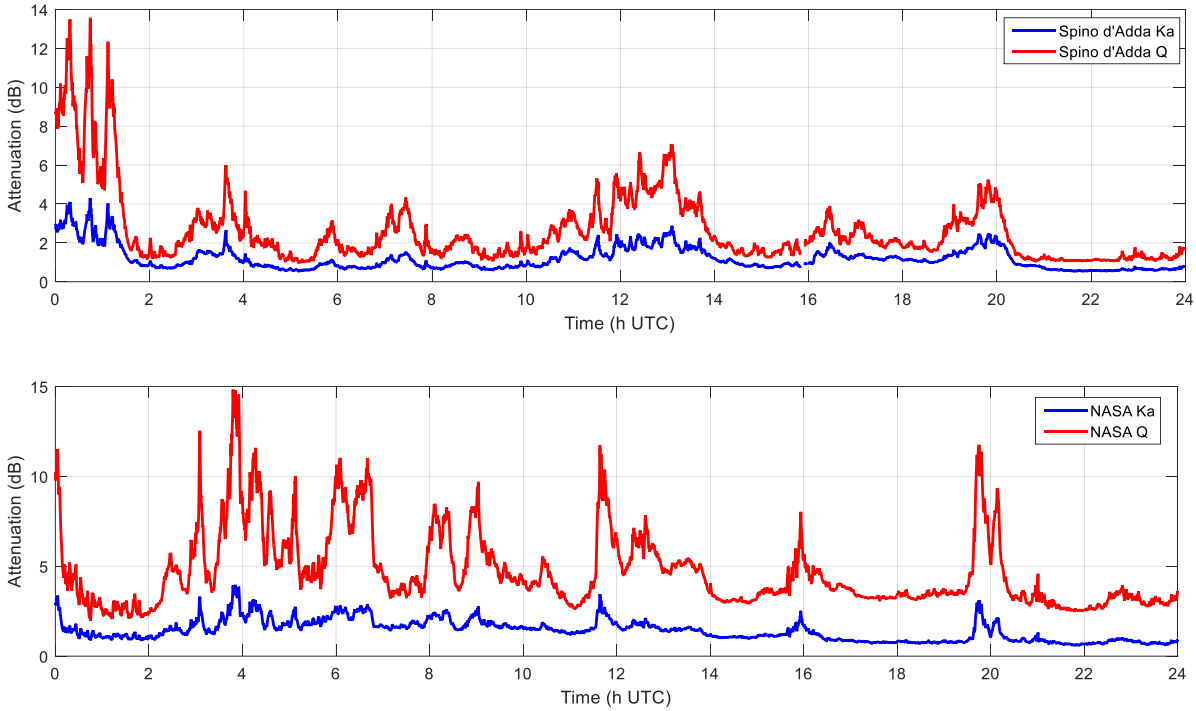

Fig. 3-42. Example of total attenuation data (5th of November, 2014) for Spino d'Adda (top) and for Milan (bottom).

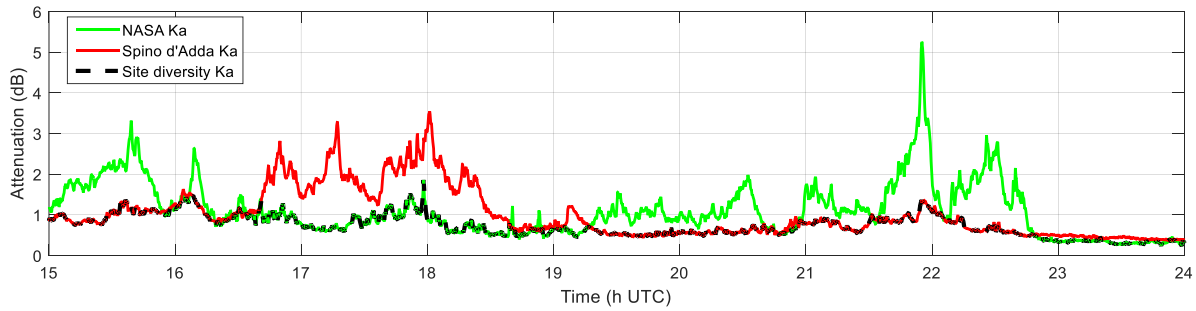

DISTRIBUTION A: Distribution approved for public release. Distribution unlimited

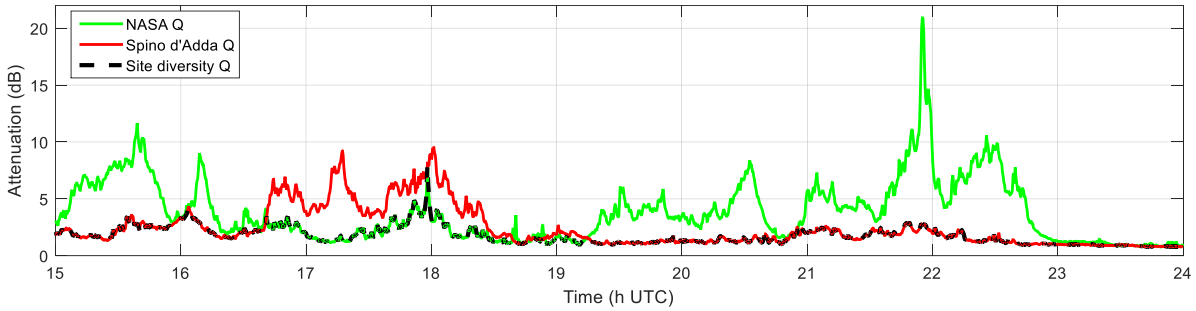

Fig. 3-43. Sample signals collected at the two sites during a rainy day (Ka band on the top, Q band on the bottom); red and green lines are associated to Spino d'Adda and Milan receivers, respectively, while the black line represents the site diversity attenuation level.

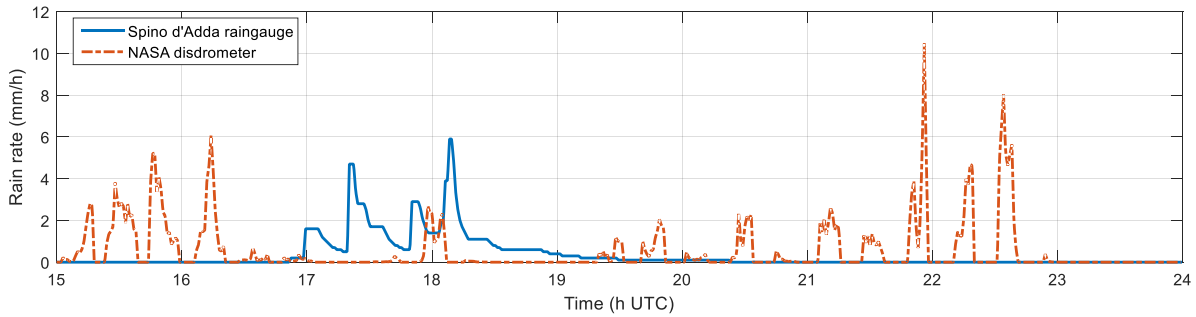

Fig. 3-44. Rain rate time series as measured by the 1-minute integration time raingauge installed at Spino d'Adda and by the 1-minute integration time disdrometer installed in Milan (same day as in Fig. 3-43).

Fig. 3-43 gives a hint about the advantage of the site diversity scheme exploiting the two stations: as an example, considering the Q band and the NASA station as the master, the peak attenuation during the day turns out to be higher than 20 dB, while a diversity system would experience only 8-dB maximum attenuation during the same measurement period.

A more comprehensive information on the performance of a two site diversity systems is shown in Fig. 3-45 and Fig. 3-46, which compare the attenuation CCDFs obtained separately for the two sites (Ka band and Q band, respectively), as well as for the diversity system (label = 'Joint'), the latter calculated by selecting, for each second, the lowest attenuation value. The attenuation statistics for Milan and Spino d'Adda are in good agreement, not only because both sites are subject to the same climate and lie in the same large flat area (Padana Valley), but also because the CCDFs in this case consist of fully concurrent measurements. More specifically, in this case, only measurements collected during 2015 were selected because of the current limited availability of processed attenuation data for the Spino d'Adda site.

Results in Fig. 3-45 and Fig. 3-46 clearly point out how effective is to use site diversity to increase the system availability and/or quality of service: as an example, the power margin to guarantee a system availability of 99.99% at Q band shifts from approximately 40 dB using a single link to roughly 22.5 dB using the diversity scheme. Such a margin would drop to 5 dB

DISTRIBUTION A: Distribution approved for public release. Distribution unlimited

(violet curve) in case of statistical independence between the two stations, i.e. with very large separation distances (order of hundreds of kilometers) between the two receivers.

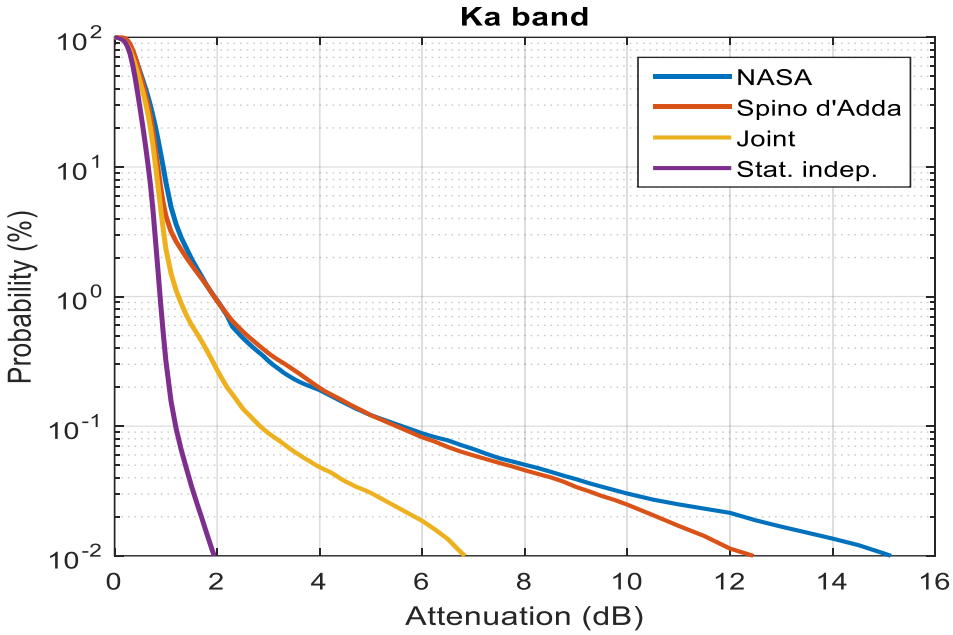

Fig. 3-45. CCDFs of total total attenuation at 19.7 GHz for the two receivers installed in Spino d'Adda and in Milan. Also the two-station site diversity CCDF is reported in the figure, as well as the curve that would be obtained by a two-site diversity scheme with statistical independent stations.

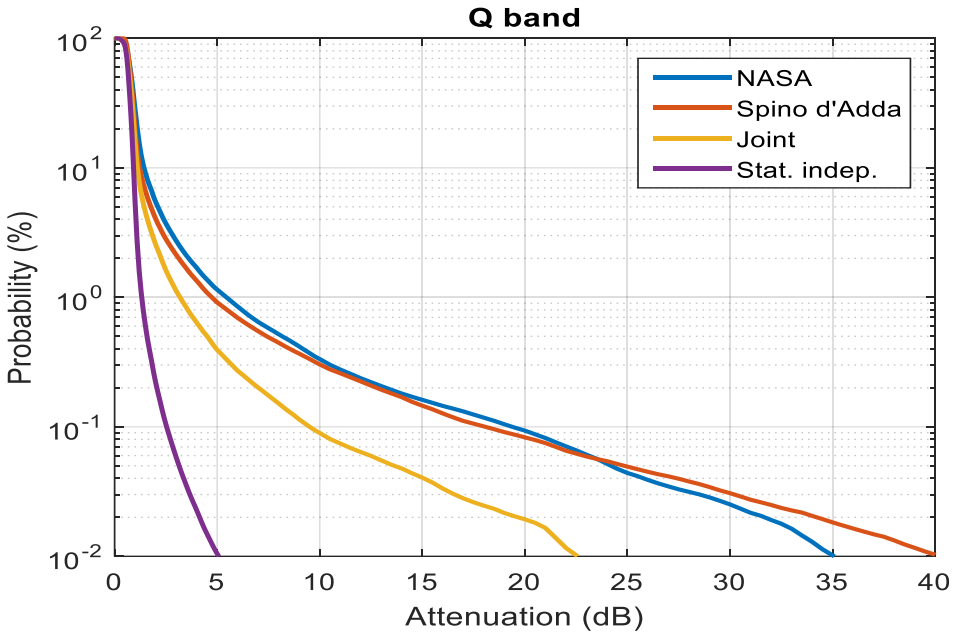

Fig. 3-46. CCDFs of total tropospheric attenuation at 39.4 GHz for the two receivers installed in Spino d'Adda and in Milan. Also the two-station site diversity CCDF is reported in the figure, as well as the curve that would be obtained by a two-site diversity scheme with statistical independent stations.

DISTRIBUTION A: Distribution approved for public release. Distribution unlimited

3.3.6. Time diversity

Among Fade Mitigation Techniques (FMTs), time diversity may represent a simple viable choice. Such a technique consists in retransmitting the same information after a suitable time delay Δt in order to take advantage of the time decorrelation of the rainfall process. The obvious advantage derives from the possibility to select, at the receiver side, the copy of the transmitted information carried by the signal with the highest Signal-to-Noise Ratio (SNR). In addition, this solution is economically advantageous since it does not require duplicating the network equipment (as for site diversity), although at the cost of a reduced effective data rate.

Starting from the time series of total attenuation A collected by the NASA beacon receivers in the full 2014-2019 period, we have investigated the advantage originating from implementing time diversity. Specifically, for each instant t, the minimum attenuation value between $A(t)$ and $A(t+\Delta t)$ is always selected (as shown in of Fig. 3-47 for a sample time series). By cumulating the results over all time series, one can compute the joint probability $P(A^*) = P\left(\left[A(t), A(t+\Delta t)\right] > A^*\right)$, from which, in turn, the gain originating from the implementation of the time diversity technique (for example in terms of reduction in the power margin required to achieve the same service level) can be deduced. Formally, the gain G offered by a time diversity system, with retransmission delay Δt, is calculated as (refer to Fig. 3-48):

$$G\left(\Delta t, A_s\right) = A_s(P) - A_j(\Delta t, P) \tag{3-17}$$

where A_s and A_j are the attenuation values of the complementary cumulative distribution functions (CCDFs) (both for the same probability level P), respectively relative to a simple receiver (no FMT implemented) and to a time diversity system.

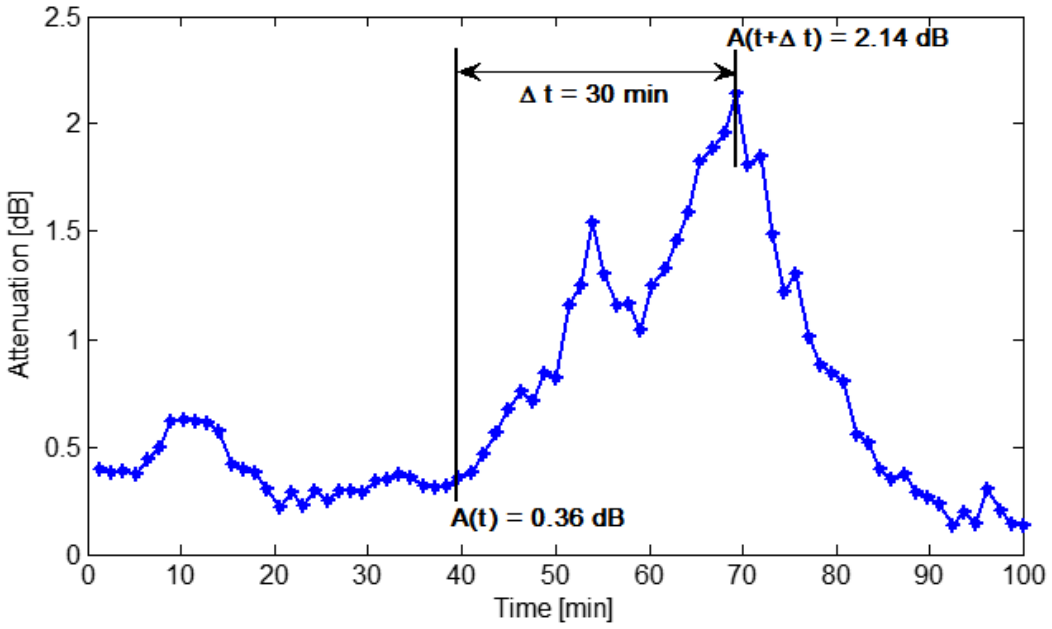

Fig. 3-47. Procedure to estimate the time diversity gain from attenuation time series: selection of the minimum attenuation value between A(t) and A(t+Δt) for each instant t.

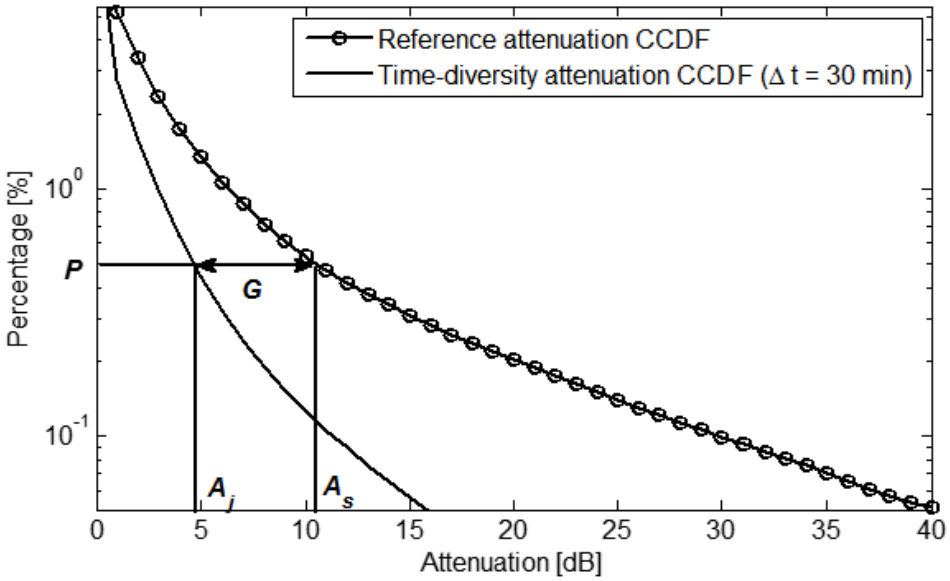

Fig. 3-48. Calculation of time diversity gain from the reference and the time diversity CCDFs.

Fig. 3-49, Fig. 3-50, Fig. 3-51 and Fig. 3-52 report the results on time diversity for both beacon frequencies. Specifically, Fig. 3-49 (f = 19.7 GHz) shows the CCDFs of attenuation obtained from the original beacon measurements (i.e. no FMT, sampling frequency equal to 8 Hz), as well as the attenuation statistics achieved by implementing time diversity, for different retransmission delays Δt = 1, 5, 10, 20 and 30 minutes. As expected, the longer Δt, the higher will be the advantage deriving from time diversity, which is tightly linked to the temporal decorrelation of rain.

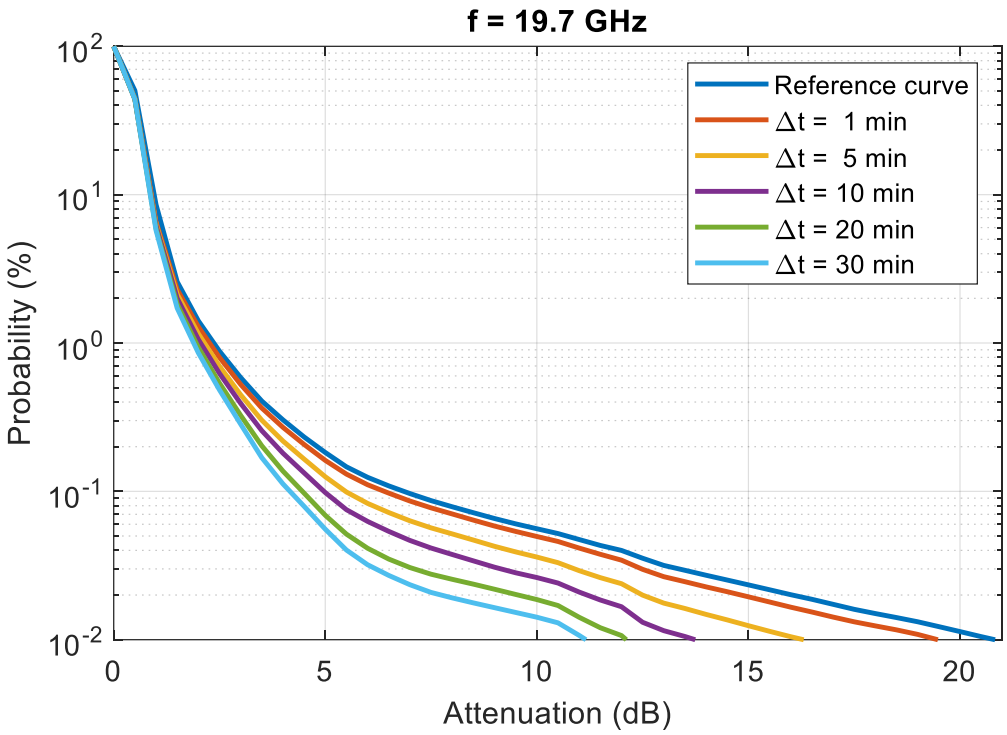

Fig. 3-49. CCDFs of attenuation (f = 19.7 GHz), obtained from the original beacon measurements (i.e. no FMT, sampling frequency equal to 8 Hz), as well as the attenuation statistics achieved by implementing time diversity, for different retransmission delays. Full 2014-2019 period.

Such an advantage is clarified more in Fig. 3-50 (f = 19.7 GHz), which depicts the trend of the gain G in equation (3-17), both as a function of the retransmission delay and of the exceedance probability P (i.e. to the reference attenuation value A_s – see Fig. 3-48): as an example, for P = 0.01% and Δt = 30 minutes, time diversity would allow to reduce the power margin to cope with atmospheric attenuation at 19.7 GHz, A_s = 20.5 dB, to $A_j = A_s - G \approx 11$ dB.

DISTRIBUTION A: Distribution approved for public release. Distribution unlimited

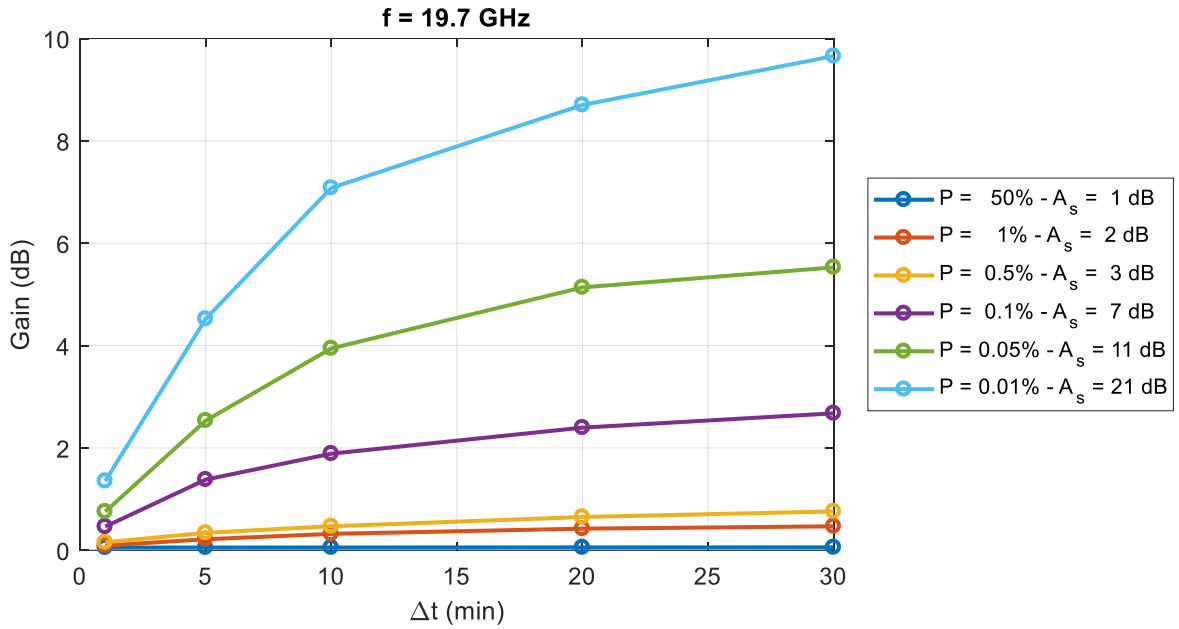

Fig. 3-50. Time diversity gain G as a function of the retransmission delay and of the exceedance probability P (f = 19.7 GHz). Full 2014-2019 period.

The same results, but for *f* = 39.4 GHz, are reported in Fig. 3-51 and Fig. 3-52: results show an even higher advantage from implementing time diversity.

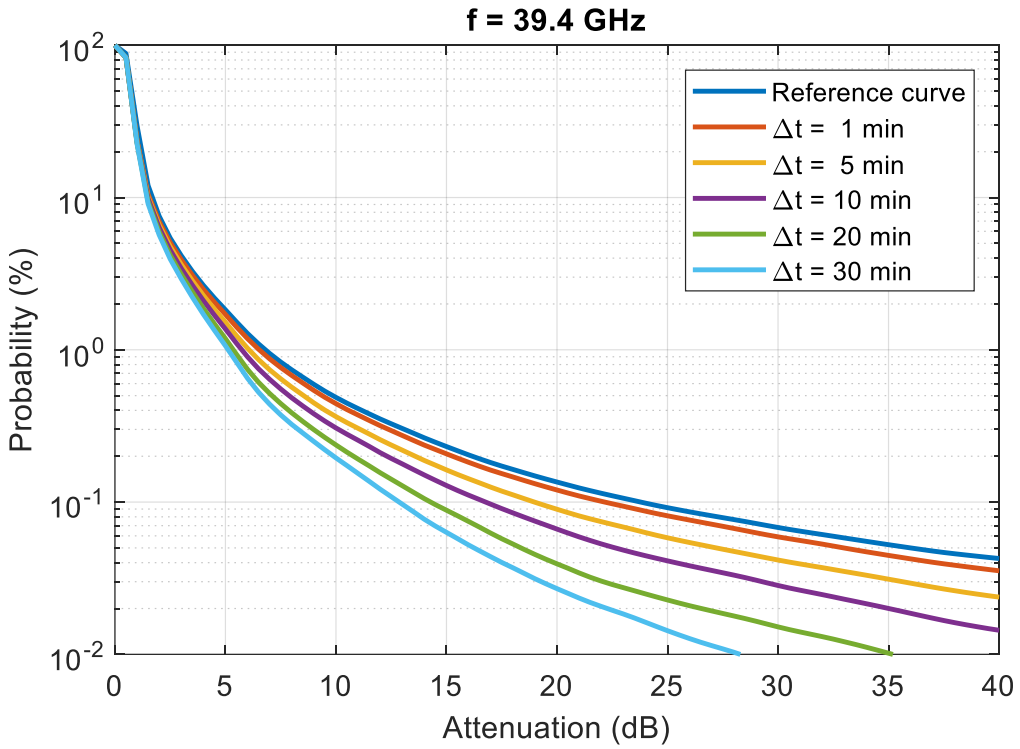

Fig. 3-51. CCDFs of attenuation (f = 39.4 GHz), obtained from the original beacon measurements (i.e. no FMT, sampling frequency equal to 8 Hz), as well as the attenuation statistics achieved by implementing time diversity, for different retransmission delays. Full 2014-2019 period.

DISTRIBUTION A: Distribution approved for public release. Distribution unlimited

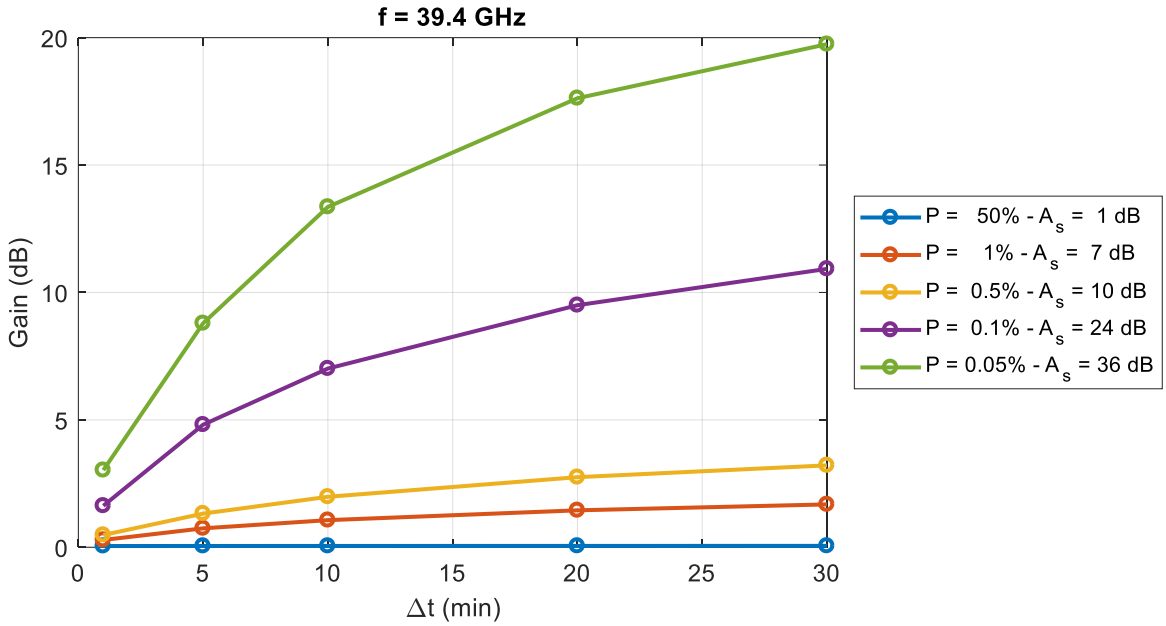

Fig. 3-52. Time diversity gain G as a function of the retransmission delay and of the exceedance probability P (f = 39.4 GHz). Full 2014-2019 period.

3.3.7. Fade duration

The design and operation of the Fade Mitigation Techniques (FMTs) cannot be based only on the instantaneous atmospheric fade level, but it should also consider the characterization of the temporal evolution of the attenuation, i.e. the so-called fade dynamics; specifically, fade duration and the fade slope statistics. More in detail, this sub-section focuses on fade duration, defined as the time interval for which a certain attenuation threshold is exceeded, as depicted in Fig. 3-53.

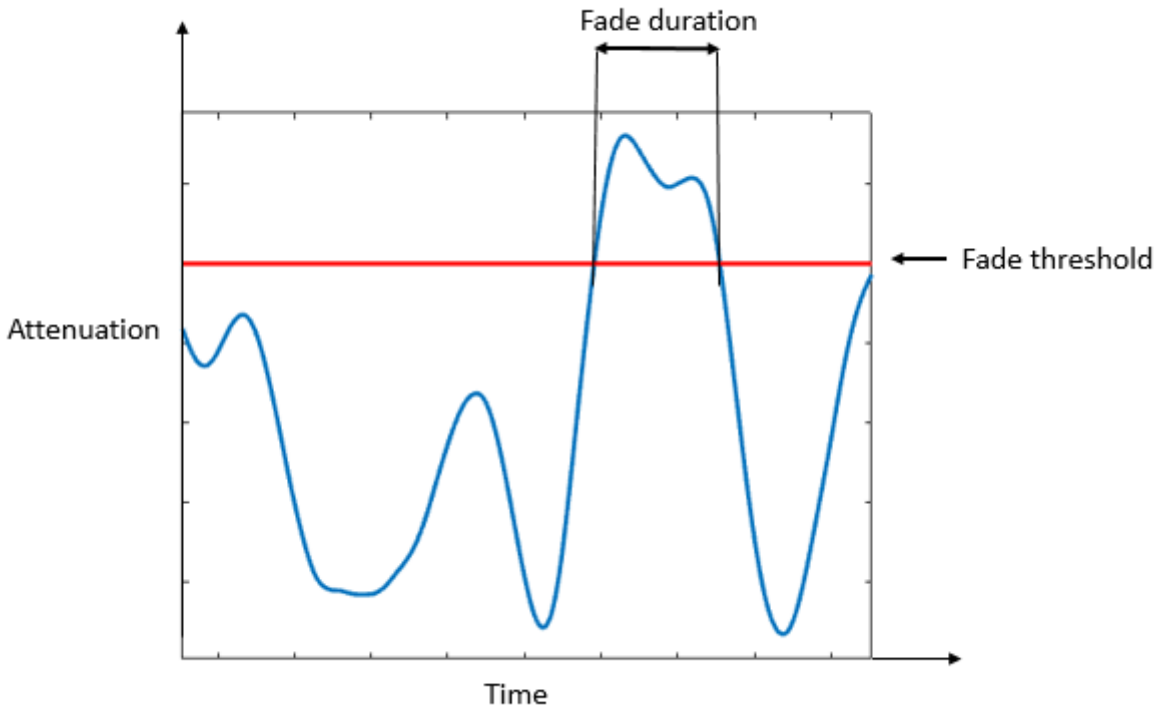

Fig. 3-53. Definition of fade duration, i.e. the duration for which a certain attenuation threshold is exceeded.

Fade duration statistics are conditional distributions of the number of fade events exceeding given durations, where a fade event is defined for a given attenuation threshold: the number of the outages, the system availability and the fade margin are all factors that can be merged to achieve a more comprehensive system design. The conditional fade duration CCDFs derived from the beacon data collected in Milan at the Ka- and Q- band are shown in Fig. 3-54 and Fig. 3-55 for a set of attenuation thresholds (e.g. 5, 7, 10, 12, 15, 18, 20, 22, 25, 30, 35 dB). For each curve, the statistics are normalized to the case of 1-second fade duration.

DISTRIBUTION A: Distribution approved for public release. Distribution unlimited

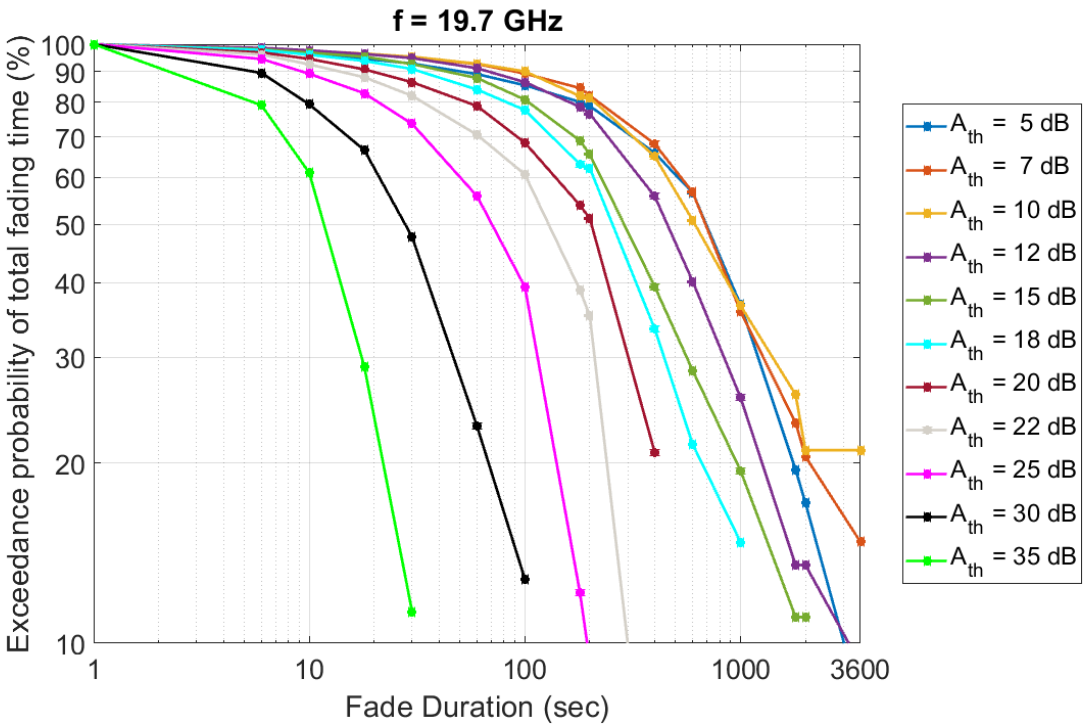

Fig. 3-54. CCDFs of the fade duration (f = 19.7 GHz), obtained from the beacon measurements collected in Milan (full 5-year period).

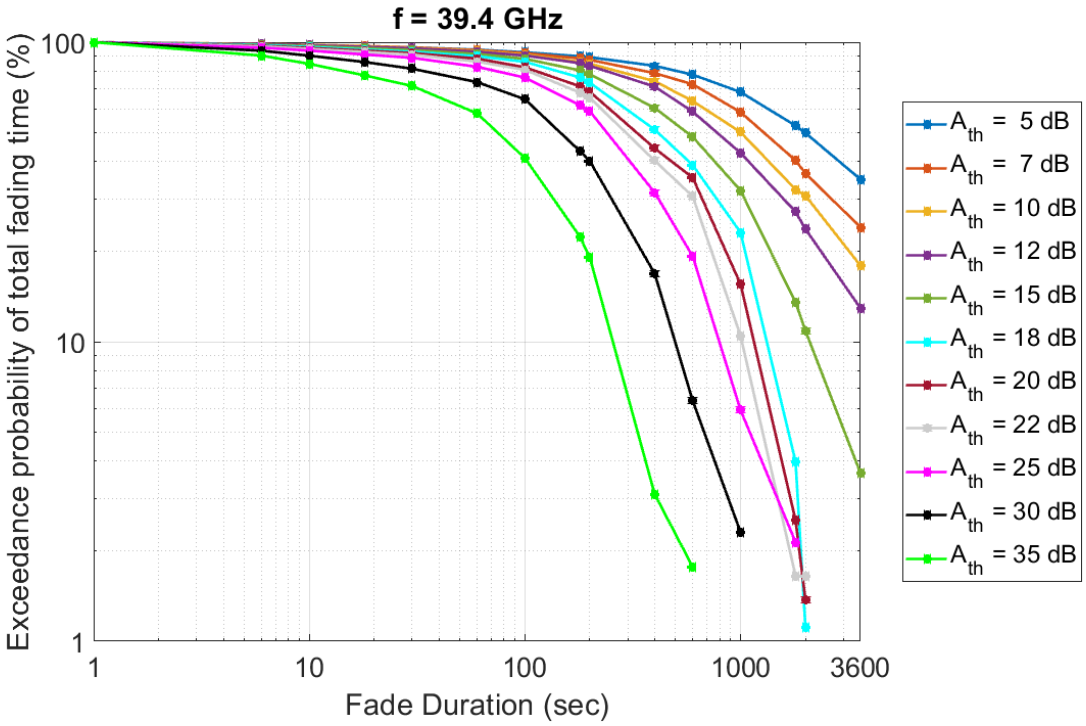

Fig. 3-55. CCDFs of the fade duration (f = 39.4 GHz), obtained from the beacon measurements collected in Milan (full 5-year period).

DISTRIBUTION A: Distribution approved for public release. Distribution unlimited

Besides the temporal distribution of fade events, the number of the fade events completes the analysis: the associated CCDFs are reported in Fig. 3-56 and Fig. 3-57, at 19.7 GHz and 39.4 GHz, respectively.

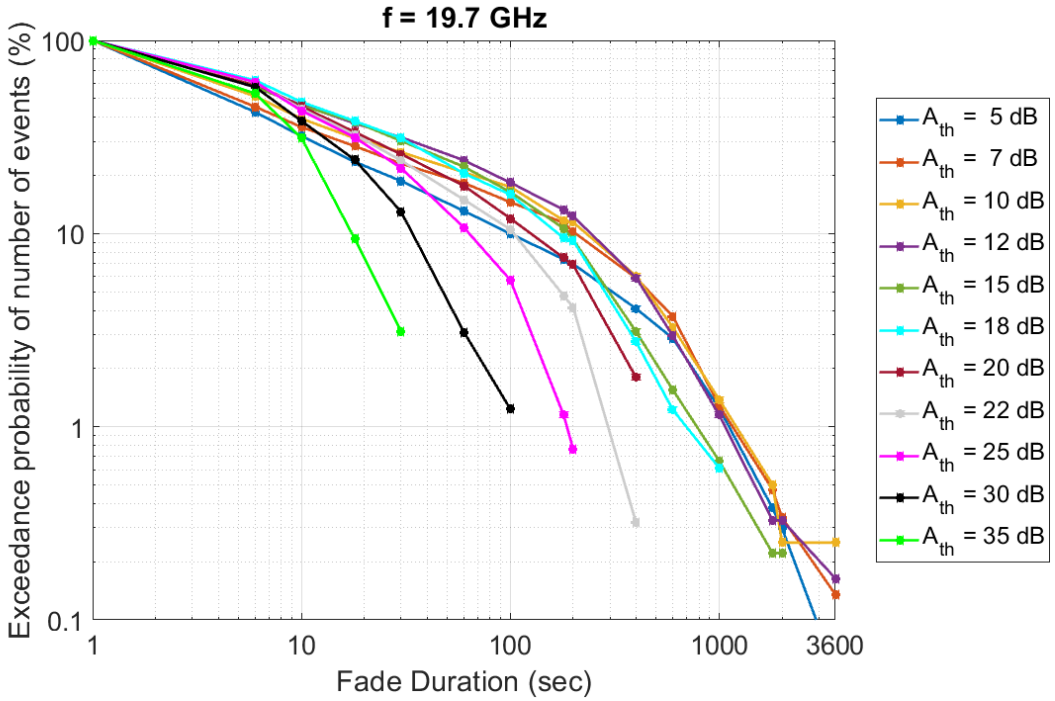

Fig. 3-56. CCDFs of the number of fades (f = 19.7 GHz), obtained from the beacon measurements collected in Milan (full 5-year period).

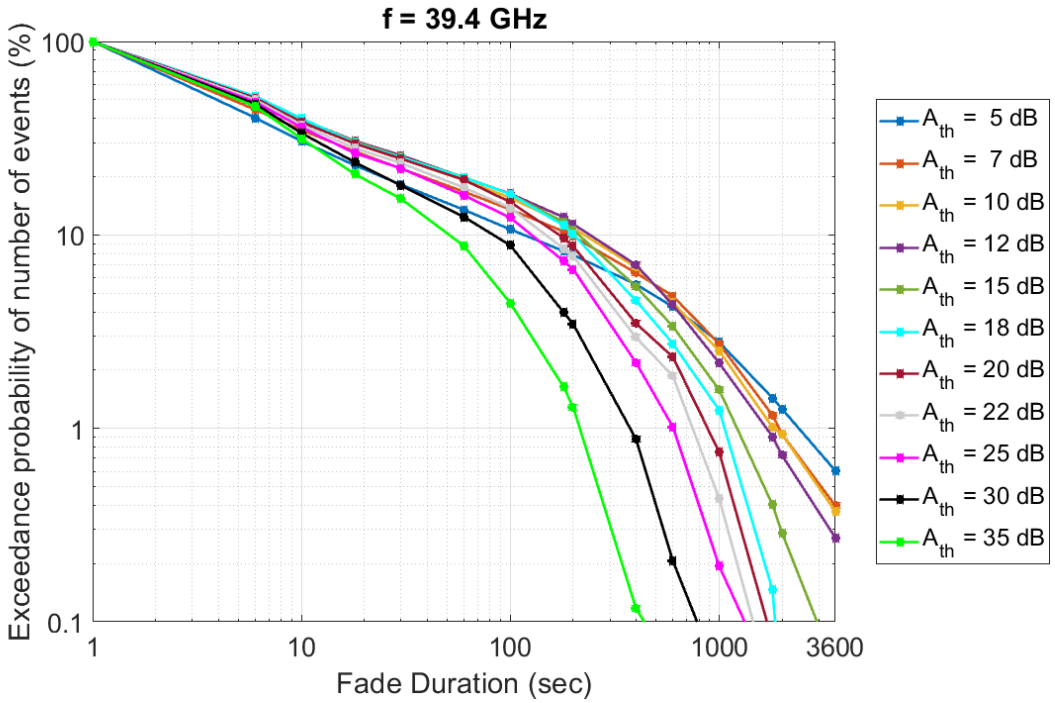

Fig. 3-57. CCDFs of the number of fades (f = 39.4 GHz), obtained from the beacon measurements collected in Milan (full 5-year period).

DISTRIBUTION A: Distribution approved for public release. Distribution unlimited

As expected, the results indicate that at higher frequency longer fades will affect the channel.

3.3.8. Fade slope

Fade slope is a key factor in the analysis of the second-order statistics, as it is strictly related to the operation of FMT; more in detail, fade slope represents the rate of attenuation change in time, measured in dB/s. After definition of the fade time interval by setting an attenuation threshold, the fade slope is calculated as the attenuation variation in such a temporal slot: this is clarified in Fig. 3-58, which shows the fade slope associated to time t_1.

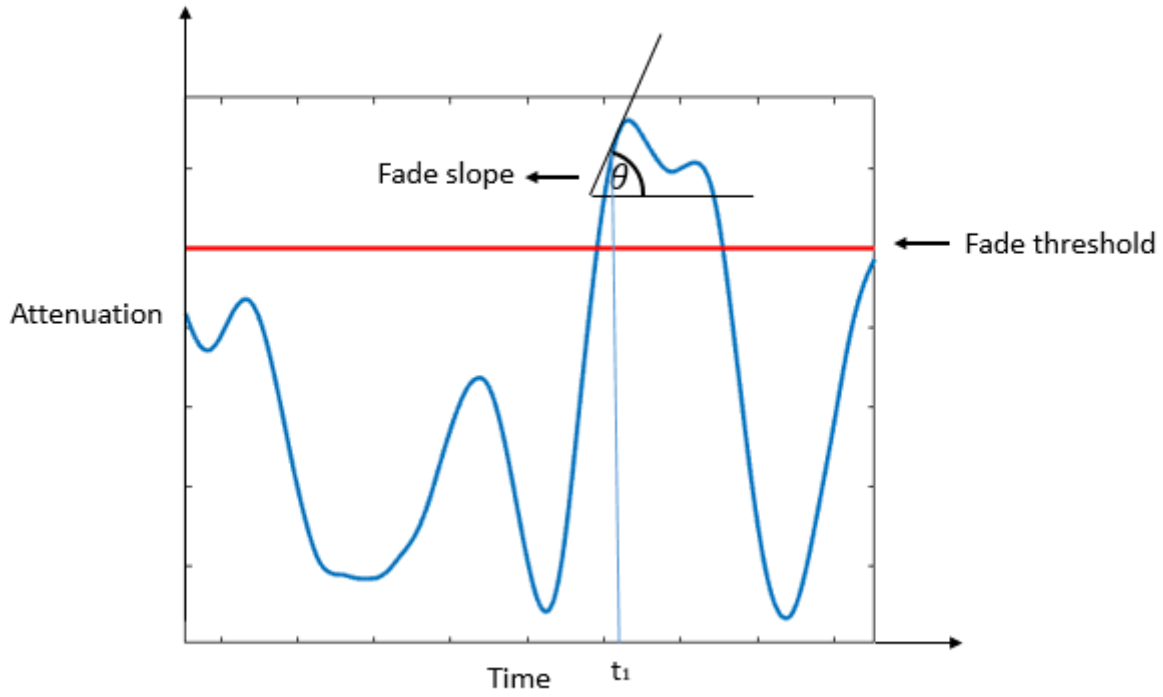

Fig. 3-58. Definition of fade slope, i.e. the rate of attenuation change in time (dB/s).

Similarly to fade duration, fade slope statistics are conditioned to a fixed fade level: Fig. 3-59 and Fig. 3-60 report the conditional probability density functions obtained from the attenuation data collected in Milan, at 19.7 GHz and 39.4 GHz, respectively, for attenuation thresholds equal to 1, 3, 5, 10, 15, 20, 25, 30, 35 dB. Also, Fig. 3-61 and Fig. 3-62 depict the probability density function of the fade slope. In this analysis, the time interval considered for the calculation of the fade slope is 60 seconds.

DISTRIBUTION A: Distribution approved for public release. Distribution unlimited

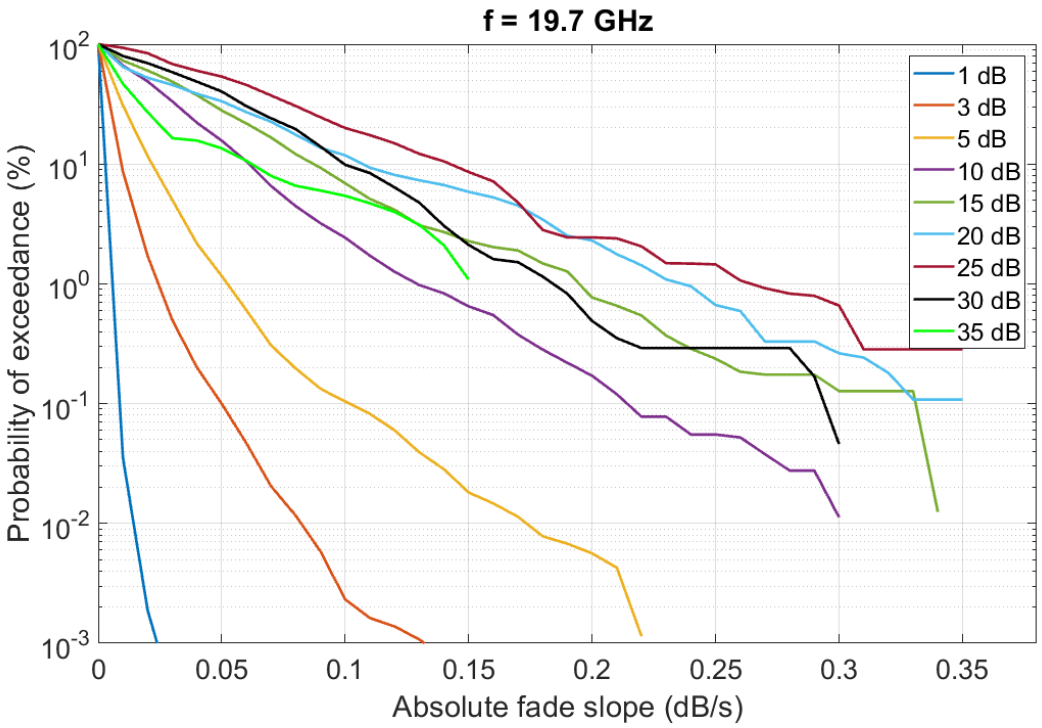

Fig. 3-59. CCDFs of the fade slope (f = 19.7 GHz), obtained from the beacon measurements collected in Milan (full 5-year period).

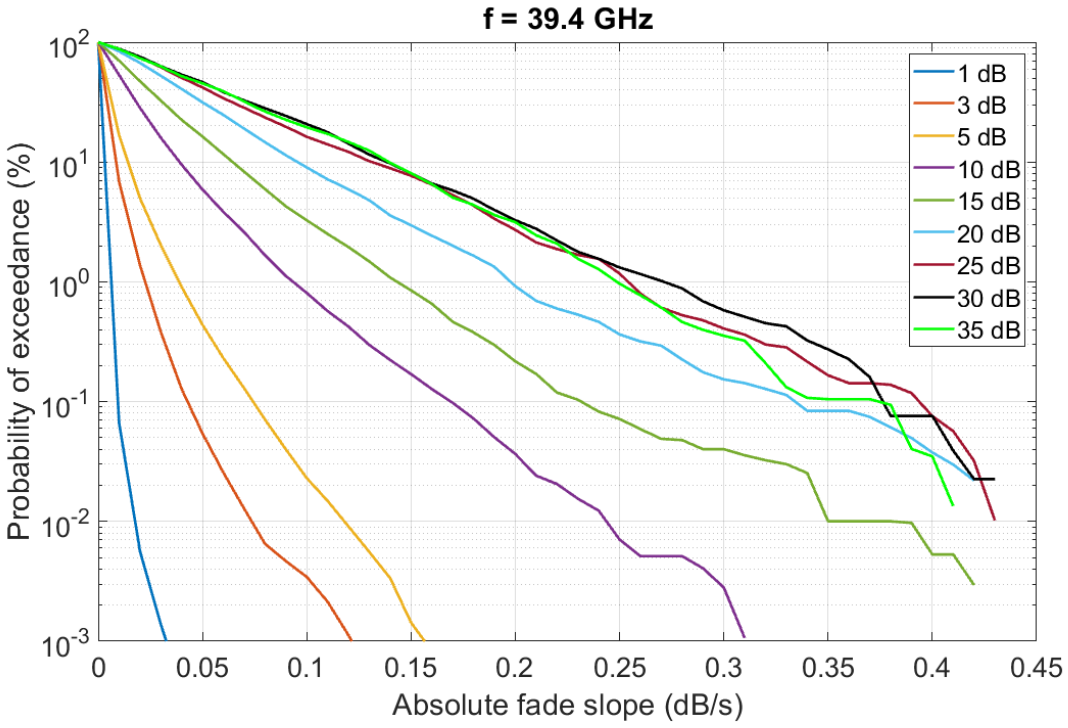

Fig. 3-60. CCDFs of the fade slope (f = 39.4 GHz), obtained from the beacon measurements collected in Milan (full 5-year period).

DISTRIBUTION A: Distribution approved for public release. Distribution unlimited

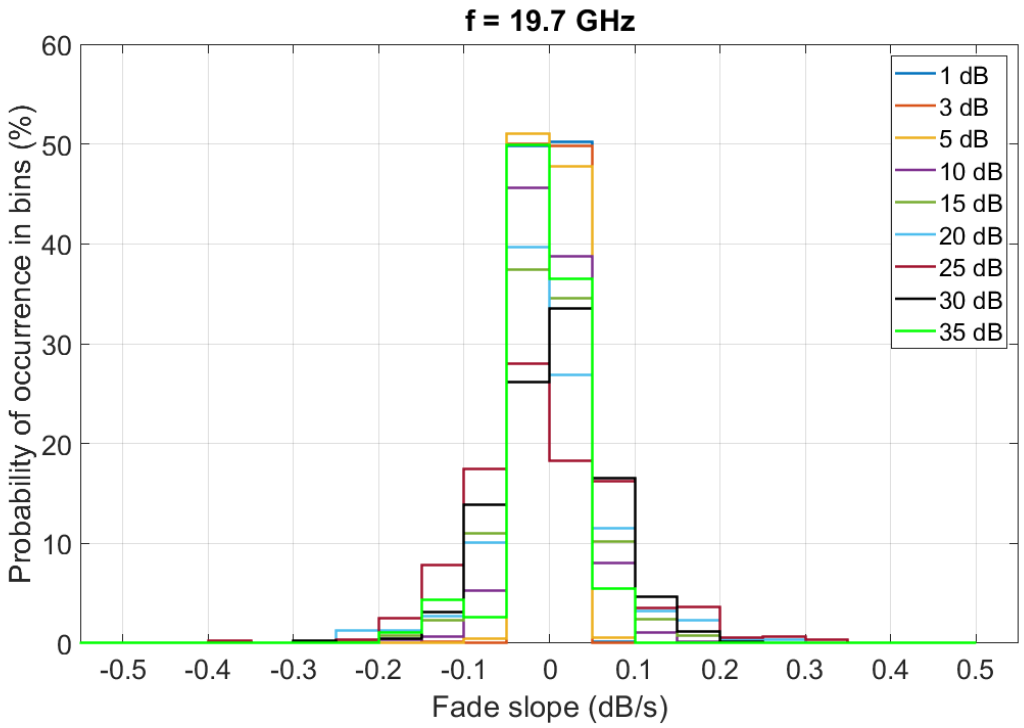

Fig. 3-61. Probability density function of the fade slope (f = 19.7 GHz), obtained from the beacon measurements collected in Milan (full 5-year period).

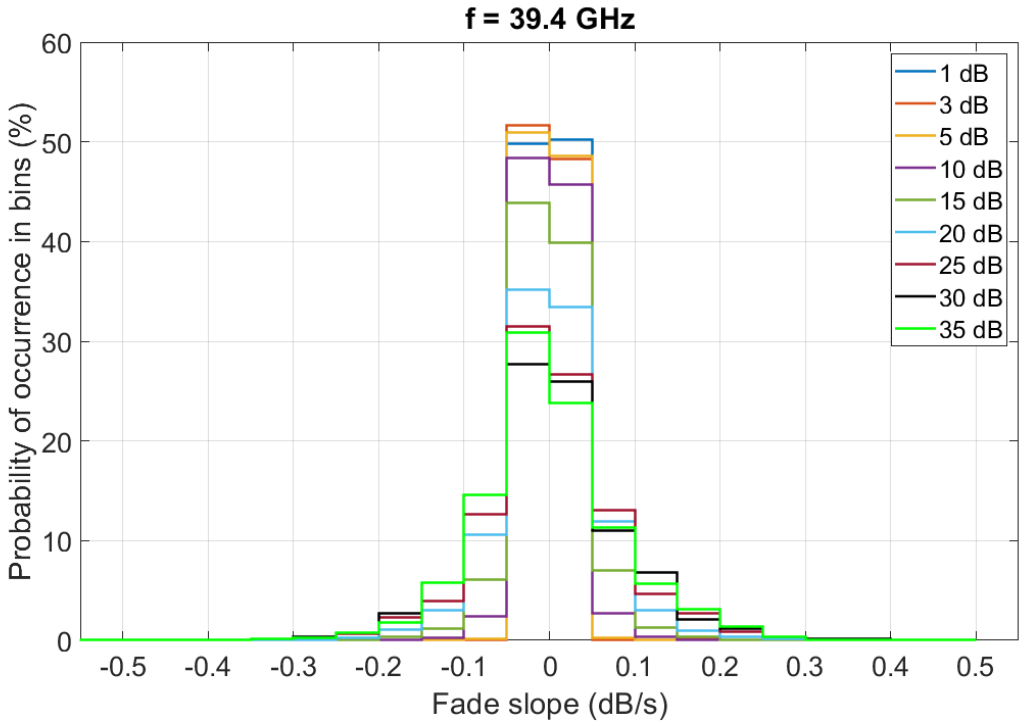

Fig. 3-62. Probability density function of the fade slope (f = 39.4 GHz), obtained from the beacon measurements collected in Milan (full 5-year period).

DISTRIBUTION A: Distribution approved for public release. Distribution unlimited

4. SPACE-TIME MULTIEXCELL

4.1. Introduction

This Chapter presents the development of a physically-based model for the synthesis of space-time correlated rain attenuation time series at any frequency in the millimeter-wave range. The methodology relies on (and extends) the MultiEXCELL model, which generates realistic rain maps by combining several exponentially-shaped rain cells, of different peak intensity and size, according to the natural aggregative process observed in a large database of rain maps. The time evolution of the rain maps is achieved by considering the structural modification of single rain cells, which occurs according to simple yet effective analytical expressions, as well as their displacement due to the wind. As a result, the model offers the chance to generate realistic synthetic rain maps reflecting both the spatial and temporal correlation of the rain rate, which, in turn, can be used to simulate the interaction of precipitation with wireless systems of any complexity working at frequencies higher than 10 GHz (from single terrestrial/satellite links to more complex systems distributed in space).

4.2. Rain attenuation modeling

As discussed in Chapter 2, rain attenuation is well known to represent the major atmospheric impairment to wireless communication systems operating at frequencies higher than 10 GHz [Riva et al., 2014]. Indeed, the high extinction properties of rain drops (causing scattering and absorption of the electromagnetic power impinging on them) can induce quite long outage periods, particularly impairing high-availability systems (e.g. higher than 99.9%). Luckily, rain is associated to a large spatial and temporal variability, such that the use of simultaneous multiple receivers with proper separation distance (some tens of kilometres) allows to significantly increase the overall system availability and/or quality of service [Luini and Capsoni, 2013b]. In order to design such complex systems and to estimate the advantage originating from site diversity, significant efforts have been devoted to developing models able to reproduce realistic rain fields [Jeannin et al., 2012], [Féral et al., 2003]. Some of them, particularly appreciated for their flexibility, reliability and accuracy, rely on the description of the meteorological environment through an ensemble of rain cells [Féral et al., 2003]. EXCELL (EXponential CELL) [Capsoni et al., 1987], and its extension, MultiEXCELL (Multi EXponential CELL) [Luini and Capsoni, 2011], belong to this class of models, and have been successfully used for the analysis of several propagation impairments in different scenarios (rain attenuation [Capsoni et al., 2009a] and interference due to hydrometeor scattering [Capsoni et al., 2010], just to cite a couple of them). MultiEXCELL was devised by taking advantage of a large database of rain maps (regular Cartesian grid of 0.5 km×0.5 km) collected in some years by the meteorological radar located at Spino d'Adda, Italy. Such maps were investigated to identify single rain cells, characterize them in terms of basic integral parameters (e.g. the area, the average rain rate and the ellipticity), and model their aggregative process (e.g. distance between cells in a cluster). Details on the development of MultiEXCELL are fully provided in [Luini and Capsoni, 2011].

Besides the spatial distribution of the rain rate, knowledge of its temporal evolution is of key importance for a more comprehensive design of wireless systems: as an example, information on the duration of rain events would provide additional details on the expected quality of service, as well as the chance to devise proper switching algorithms in site diversity

DISTRIBUTION A: Distribution approved for public release. Distribution unlimited

systems. To this aim, further studies on the same database of rain maps, collected approximately every 77 seconds, were performed to investigate also the temporal evolution of rain cells: the final aim, pursued in this Chapter, is to extend the potentiality of MultiEXCELL by enabling the generation of space-time correlated rain fields. This effort, initiated in [Capsoni and Luini, 2009] and continued in [Ghirardin et al., 2016], is extended here by investigating and modelling the temporal evolution of clusters of cells, hence, of full rain maps.

4.3. Single rain cell temporal evolution

As explained in [Capsoni et al., 1987] and [Luini and Capsoni, 2011], the spatial distribution of the rain rate R (mm/h) in a circular rain cell can be conveniently modelled using the following exponential profile:

$$R = R_M e^{-\rho/\rho_0} \tag{4-1}$$

where ρ is the distance from the cell center, while R_M and ρ_0 are the peak rain rate and the equivalent radius of the cell, respectively, which univocally define the cell itself. Note that the profile in (4-1) is intended to preserve the main integral features of real rain cells (namely, the area at 5 mm/h and the mean rain rate) rather than aiming to mimic exactly the spatial distribution of the rain cell.

The analysis of rain cells evolving in time, presented in [Capsoni and Luini, 2009], has shown that the peak intensity of a cell changes according to:

$$R_M(t) = R_P \exp\left(-0.024 R_P^{0.299} |t|\right) \tag{4-2}$$

where R_P is the maximum R_M value throughout a cell's "life".

Another key finding reported in [Capsoni and Luini, 2009] is that when the peak rain intensity of the equivalent synthetic cell increases, the cell size gets smaller, i.e. that it is possible to define a constant value k throughout the life of a cell, defined as the:

$$k = R_M(t)\rho_0(t) \tag{4-3}$$

As a result, k and R_P (the latter ranging from 5 to 250 mm/h) are sufficient to completely define the structural evolution of a rain cell in time. As an example, Fig. 4-1 shows a rain cell evolving in time (specifically $R_M(t)$ and $\rho_0(t)$) for k = 30 and R_P = 50 mm/h.

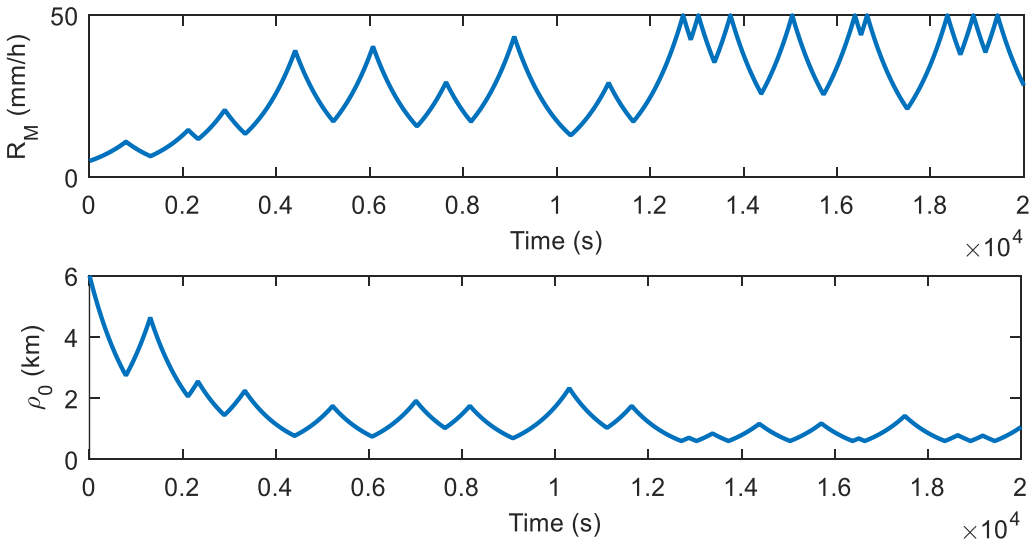

Fig. 4-1. Example of temporal evolution for a rain cell (i.e. $R_M(t)$ and $\rho_0(t)$) with R_P = 50 mm/h and k = 30.

4.4. Rain field temporal evolution: single event

A key information required to model rain fields is how the rainy area η evolves in time, which was investigated and reported in [Ghirardin et al., 2016]. As is clear from Fig. 4-2, which depicts the statistics of the temporal trend of the rainy area η (calculated over 81 rain events), normalized to the maximum value η_P reached within the event, such value approximately follows a linear trend whose slope varies depending on the duration of the event and on the main type of precipitation occurring (i.e. stratiform or convective rain).

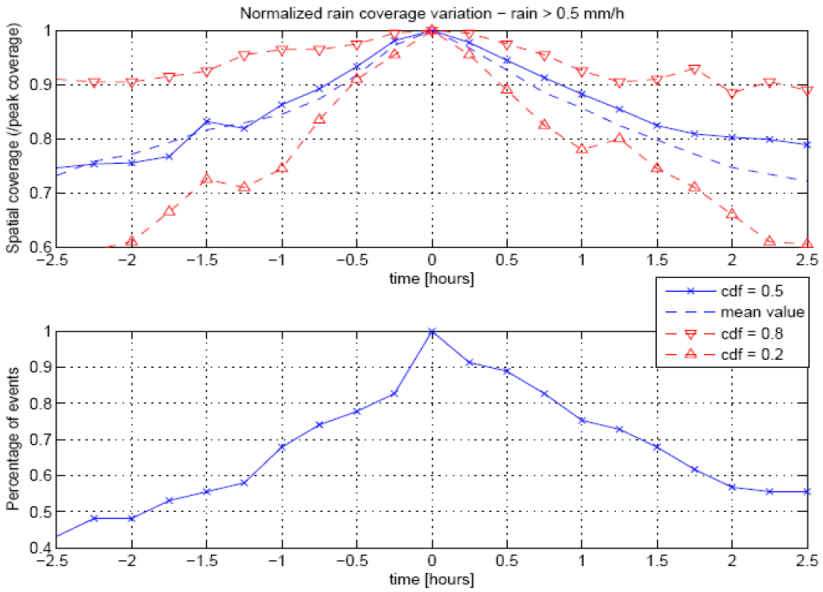

Fig. 4-2. Top graph: temporal evolution of the rainy area, normalized to the maximum value reached during a rain event η_P (calculated over 81 rain events). Results expressed in terms of mean and median values, and percentiles (0.2 and 0.8). Bottom graph: percentage of the events used to produce the statistics in the top graph.

As investigated and thoroughly discussed in [Luini and Capsoni, 2011], and clearly shown in Fig. 4-3 as well, rain cells do not randomly distribute within the rainy area, but they rather tend to aggregate to form larger clusters, whose ensemble, in turn, gives rise to a full rain field. As a result, in order to generate spatially-correlated rain fields, the distance between the cells must be maintained. As explained in [Luini and Capsoni, 2011] for MultiEXCELL, this is achieved by randomly extracting the intercellular distance NNICD (red arrow in Fig. 4-3) and the interaggregate distance NNIAD (green arrow in Fig. 4-3) from the empirical Probability Density Functions (PDFs) reported in Fig. 4-4 (NNICD on the left and NNIAD on the right).

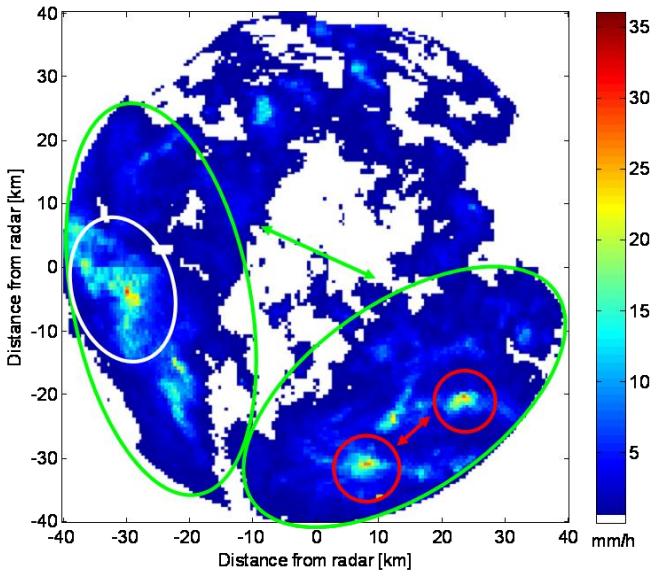

Fig. 4-3. Sample radar-derived rain map showing different rain cells forming larger clusters.

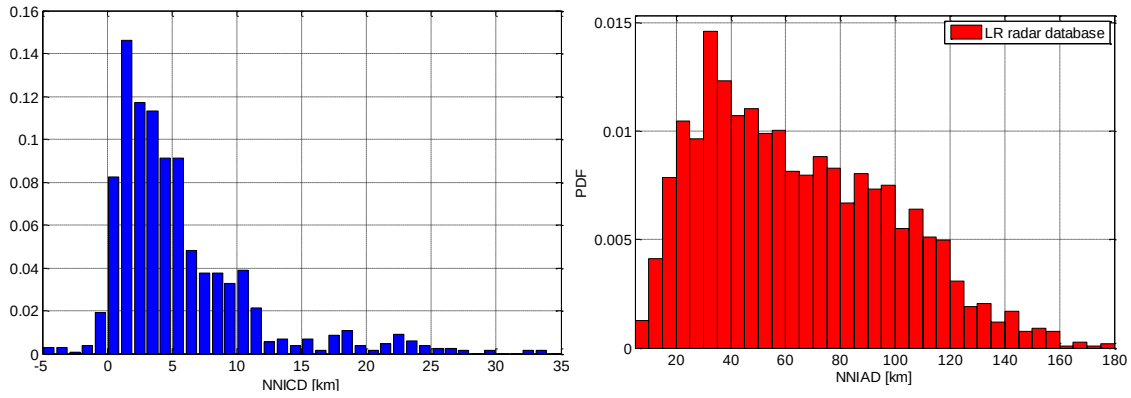

Fig. 4-4. PDF of the intercellular distance NNICD and of the interaggregate distance NNIAD used to produce realistic rain fields with MultiEXCELL [Luini and Capsoni, 2011].

All the elements above (temporal evolution of each single rain cell and of the rainy area, spatial distribution of rain cells) must be combined to generate rain events of given duration *T*. As MultiEXCELL already relies on input data extracted from NWP datasets, specifically

on the ERA40 database for which data are organized in 6-hour slots, T = 6 h is a suitable choice. The full procedure to generate a rain event consists in the following steps:

1. Define the maximum rainy area occurring during the whole 6-hour period, η_{max}.
2. Define the rate of change in time of the normalized rainy area η_P, i.e. choose s_η the slope of the linear expression modeling the change of η_P, ranging between 0.06 and 0.55 h^{-1}.
3. Sample the linear trend of η_P with sampling time Δt = 1 minute, assuming that η_{max} is reached at $T/2$ = 3 hours. Knowing the dimension of the map, the trend of η is obtained (see the blue line in Fig. 4-5).
4. Start the generation of the rain event from $t_0 = T/2$: generate a MultiEXCELL rain map with rainy area equal to η_{max} by randomly picking only rain cells whose area is smaller than η_{max}.
5. For every cell i selected at step 4, calculate the associated value of k_i according to (4-3):

$$k_i = R_M^i(t_0)\,\rho_0^i(t_0) \tag{4-4}$$

   k_i will remain constant throughout the cell's life.
6. Considering that, as observed in rain fields using weather radar data, the peak rain rate R_M is constrained between 5 and 250 mm/h and that ρ_0 ranges between 0.6 and 20 km [Capsoni et al., 1987], every cell i will be limited in the possible values that R_M and ρ_0 can assume. Specifically, the maximum R_M of cell i, defined as R_P in (4-2), is given by:

$$R_P^i = k_i / 0.6 \tag{4-5}$$

7. Once R_P^i is known, the temporal rate of change of $R_M^i(t)$ is fully defined according to (4-2), and so is the one of $\rho_0^i(t)$, obtained by combining (4-2) and (4-4).
8. The rain map at $t = t_0+\Delta t$ is synthesized by modeling the temporal evolution of each cell in the map at $t = t_0$. Specifically, through Δt, the R_M of each cell can increase or decrease following the trend in (4-2), as also shown in Fig. 4-1. All the cells must evolve in such a way that the summation of their area matches $\eta(t_0+\Delta t)$. According to Fig. 4-5, $\eta(t_0+\Delta t)$ will be smaller than $\eta(t_0)$, therefore smaller cells might be dropped in the synthesis of the new map. The red dashed line in Fig. 4-5 shows the actual fractional rainy area η obtained from the synthetic maps, which closely follows the target η.

DISTRIBUTION A: Distribution approved for public release. Distribution unlimited

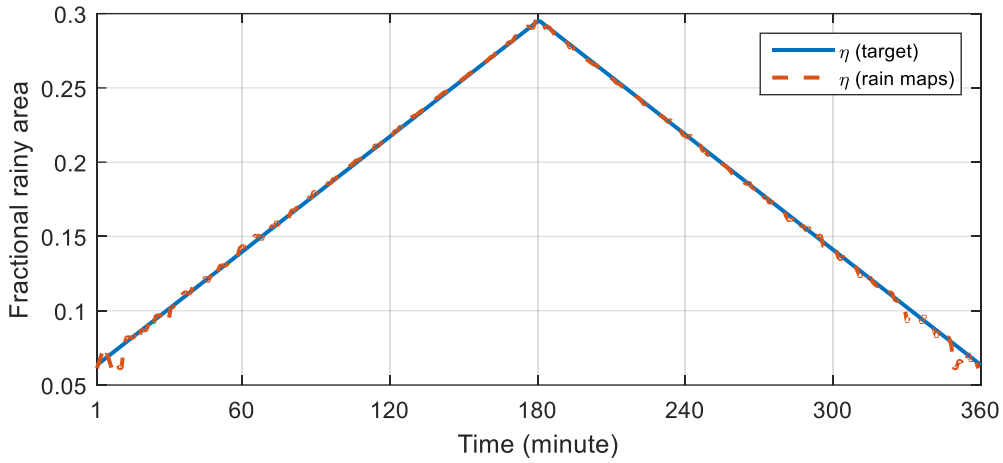

Fig. 4-5. Sample temporal trend of the normalized rainy area η_P.

9. Besides structural evolution, all the cells are also subject to displacement with a fixed velocity v, whose value is randomly selected between 10 and 50 km/h: this range is derived from typical values of the wind intensity blowing at the altitude corresponding to 700-mbar, which, in [Luini et al., 2011b], was found to be the most correlated to the movement of rain fields.
10. The process at step 8 is iterated until either all cells are dropped (i.e. the target η is zero) or the end of the event is reached ($t = t_0 + T/2$).
11. The values of $R_M(t)$ and $\rho_0(t)$ determined for $T/2 \leq t \leq T$ are flipped in time and used also for the interval $1 \leq t \leq T/2$, such that, for example, if one cell with R_M = 10 mm/h and ρ_0 =2 km is found for t = 360 - 50 = 310 min, the same cell is used for the map at t = 50 minutes. However, the cell will not be in the same position, but in a different one depending on the selected displacement velocity.

As an example, Fig. 4-6 shows how one of the synthetic maps evolves from t = 250 min to t = 280 min. In this case, v = 18 m/s (westward horizontal wind) and the rain field evolution leads to dropping 3 cells and to a general reduction in the rain intensity.

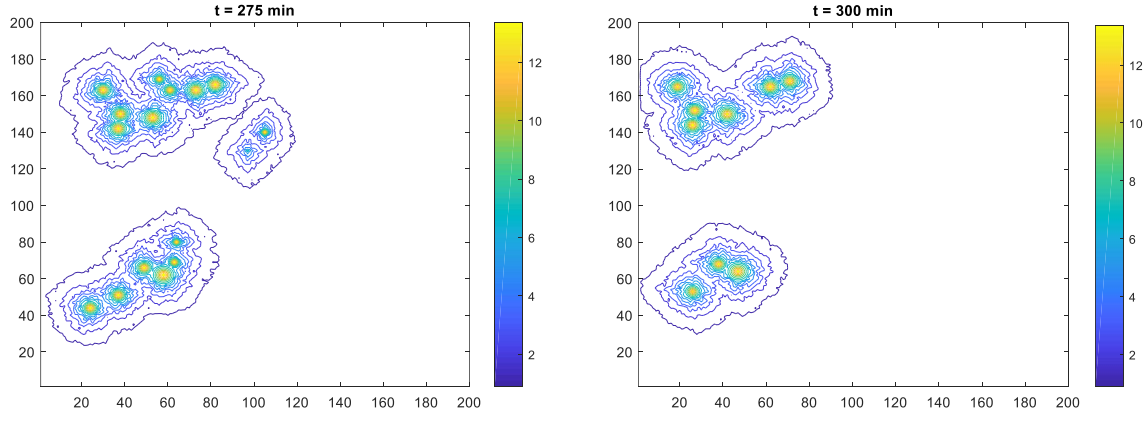

Fig. 4-6. Example of map evolution with v = 18 m/s (westward horizontal wind).

4.5. Combination of rain events: ST MultiEXCELL

The main constraint of any rain field model is to reproduce the rain rate statistics of the site, which are usually provided as input to the model itself in terms of Complementary Cumulative Distribution Function (CCDF) of the rain rate, also referred to as $P(R)$. This is also the case for ST MultiEXCELL, which, in addition, also aims at maintaining the spatial and temporal correlation of the rain rate observed in real rain fields. The spatial correlation is already preserved by distributing rain cells on the map at the proper distance [Luini and Capsoni, 2011], while the temporal correlation is achieved on the one side, by taking into accounting the evolution of single rain cells (hence, of the whole rain field) in 6 hours (henceforth referred to as "rain event" for the sake of simplicity), as explained in Section 4.4, and, on the other side, by relying on the NWP data extracted from the ERA40 database to identify rainy slots during the period of interest.

The rationale of ST MultiEXCELL is to generate as many rain events as the number of ERA40 rainy 6-hour slots in a year, N_{6h}, each of which will contribute to reproducing the target $P(R)$. To this aim, each rain event will be constrained to include only rain cells whose peak rain rate is lower than a given threshold and to a reproduce a given temporal trend of the fractional rainy area η_P, in turn chosen so as to maintain the overall local yearly statistics of the η_P. The full procedure to generate space-time correlated rain fields consists in the following steps:

1. Extract from the ERA40 database the values of the total rain amount accumulated in 6 hours (M_t) for a full year, as well as the wind intensity and direction associated to the 700-mbar isobar height (W_s and W_d, respectively). The yearly probability that a 6-hour slot is rainy, P_{r6h}, is calculated from M_t, while the latter values are used to calculate the Probability Density Functions (PDFs) of W_s and W_d.
2. Obtain the local $P(R)$ and the probability to have rain P_0, either from measurements or by using recommendation ITU-R P.837-7 [ITU-R P.837-7].
3. Calculate the target yearly PDF of the rainy area η_P, which, according to the findings obtained from radar-derived rain maps, is modelled as an exponential random variable [Luini and Capsoni, 2011], [Jeannin et al., 2012]. The yearly average value of η_P, the only value needed to define the exponential PDF, is calculated as $\eta_{AV} = P_0/P_{r6h}$: indeed, according to the quasi-ergodicity principle of rain fields (time and space are statistically equivalent), the temporal probability to have rain corresponds to the portion of the map area covered by rain [Luini and Capsoni, 2011], [Jeannin et al., 2012]. As an example, Fig. 4-7 depicts the PDF of the target fractional rainy area η_P for Spino d'Adda, Italy, which is associated to $P_0 \approx 4\%$ and $P_{r6h} \approx 28\%$.

DISTRIBUTION A: Distribution approved for public release. Distribution unlimited

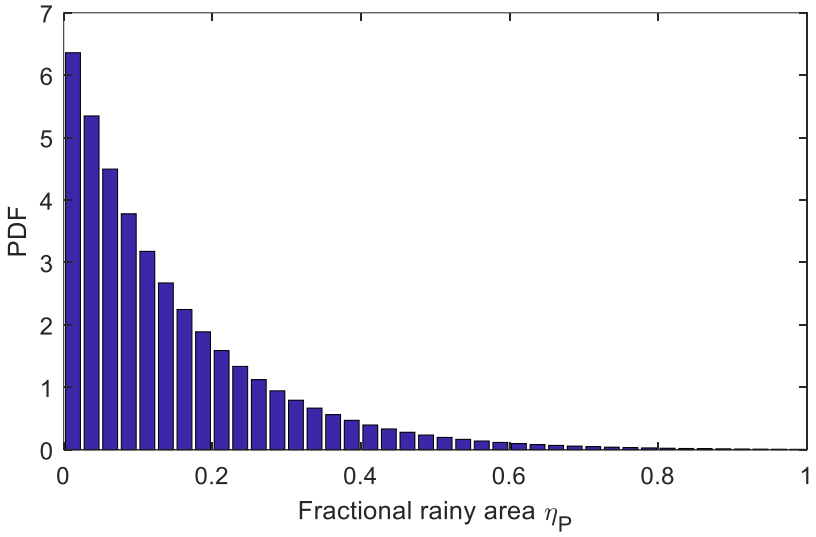

Fig. 4-7. PDF of the target fractional rainy area η_P for Spino d'Adda, Italy.

4. Start the generation of rain events, according to the procedure defined in Section 4.4, by defining, for each of them:
    - W_s and W_d for the rain cell translation speed and direction, which are randomly extracted from the respective PDFs.
    - The maximum fractional rainy area $\eta_P^{\max}$, which is progressively chosen so as to preserve the target PDF of η_P defined at step 3.
    - s_η, the slope of the linear expression modeling the change in η_P within the 6-hour rain event (see Fig. 4-5), which is calculated as follows:

$$s_\eta = (0.06 - 0.55)\eta_P^{\max} + 0.55 \tag{4-6}$$

Equation (4-6), which is shown in Fig. 4-8 for convenience, reflects the main features of stratiform and convective events: the former cover large areas (large $\eta_P^{\max}$) and vary slowly in time (low rate of change s_η), while the latter, conversely, are of limited horizontal extent (small $\eta_P^{\max}$) but with a quick temporal evolution (high rate of change s_η). The coefficients in (4-6) were chosen partially based on the information obtained from radar-derived rain maps (see Fig. 4-2) and partially by checking the temporal correlation of the rain rate in the synthetic maps against the same information extracted from the local rain gauge installed in Spino d'Adda (more details are provided in Section 4.6).

DISTRIBUTION A: Distribution approved for public release. Distribution unlimited

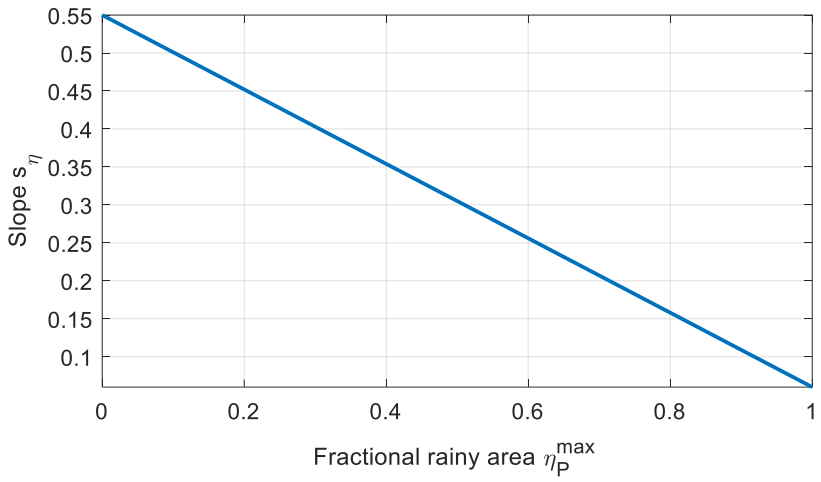

Fig. 4-8. Fractional rainy area rate of change s_η as a function of the maximum fractional rainy area within the event, η_P^{max}

- The maximum peak rain rate value R_M^{max}, which limits the selection of rain cells only to those for which $R_M < R_M^{max}$.

The last bullet above highlights a key point of the procedure defined to generate rain events while matching the input $P(R)$. At the beginning, only cells with high peak rain intensity R_M are selected (i.e. convective ones), until the $P(R)$ calculated from the synthetic maps, $P(R)_M$, starts matching the target $P(R)$ for rain rate values higher than a given value R^*. Afterwards, for the generation of the following events, R_M^{max} is set to R^*, such that the rain cells in the new events will contribute only to the portion of the $P(R)_M$ not matching the input $P(R)$ yet. This process, which is repeated iteratively until the whole $P(R)_M$ coincides with the input $P(R)$, is clarified in Fig. 4-9, which shows two sample stages of the rain event generation method: the green curve is obtained after synthesizing 10 events (out of 404), whose ensemble provides a good agreement between the input $P(R)$ and $P(R)_M$ for $R > 170$ mm/h (therefore, for the generation of the following events, R_M^{max} is set to 170 mm/h); the red curve refers to the generation of 320 events and to $R_M^{max} = 14$ mm/h. The data refer to the site of Spino d'Adda, Italy, where a long-term $P(R)$ is available, as measured locally by a rain gauge.

DISTRIBUTION A: Distribution approved for public release. Distribution unlimited

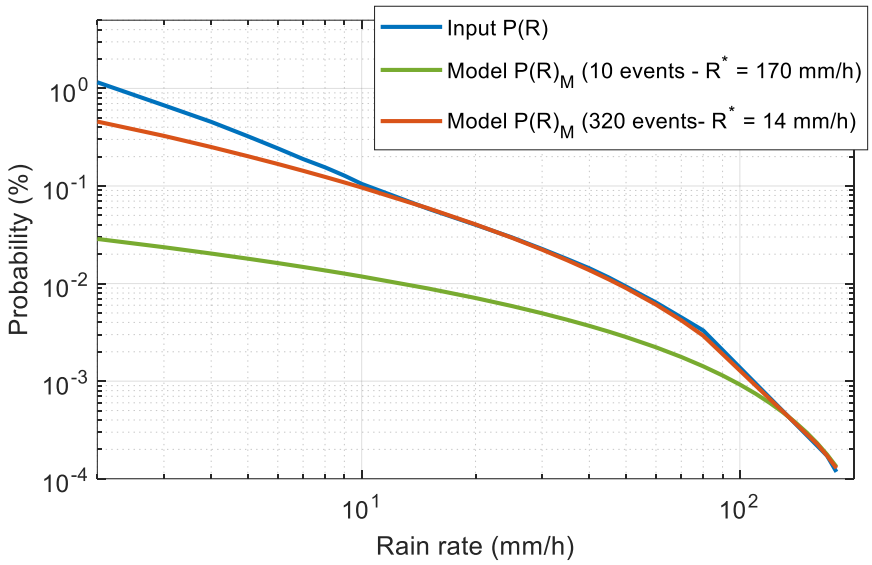

Fig. 4-9. Progressive generation of the rain events and associated P(R).

5. Keep on generating rain events until $P(R)_M$ reproduces the input $P(R)$ and the number of rain events N_{ev} matches N_{6h}, the number of 6-hour rainy slots as derived from the ERA40 database. These two conditions might be difficult to meet concurrently: this issue is discussed in more detail at the end of this numbered list.

6. For each synthetic rain event *i*, calculate M_t^M, i.e. the total rain amount accumulated in 6 hours, and sort the rain events such that the order of M_t^M matches the temporal trend of M_t extracted from the ERA40 database. In fact, the goal is to retain the 6-hour rainfall time correlation (i.e. the duration of rainy and dry periods) and the percentage contribution of the rain accumulated in each 6-hour slot on the total yearly rain amount (i.e. the likelihood to have more rain accumulated in a given season/month) indicated by the ERA40 database, but not to reproduce exactly the ERA40 values of M_t: in fact, NWP models are more likely to correctly identify rainy and dry periods rather than providing an accurate estimate of the accumulated rain amount. This finding was reported, for example, in [ESA 18278], in which the ERA40 database was found to show a general global tendency to poorly match the yearly accumulated rain amount M_Y, and it is also confirmed in this work: using ERA40 data, for Spino d'Adda, $M_Y = \sum_{t=1}^{1460} M_t \approx 500$ mm, while $M_Y \approx 760$ mm, as measured by the local rain gauge. As a result, given the constraint to match the input $P(R)$, for Spino d'Adda, M_t^M will generally tend to exceed M_t (see Fig. 4-10), such that $M_Y^M = \sum_{t=1}^{1460} M_t^M$ will eventually reach the M_Y value measured by the rain gauge: in fact, if the synthetic $P(R)_M$ matches the target $P(R)$, so does M_Y^M with M_Y (indeed, $M_Y = -\int_0^\infty R \, dP(R)/dR \, dR$, as reported in [Luini and Capsoni, 2012]).

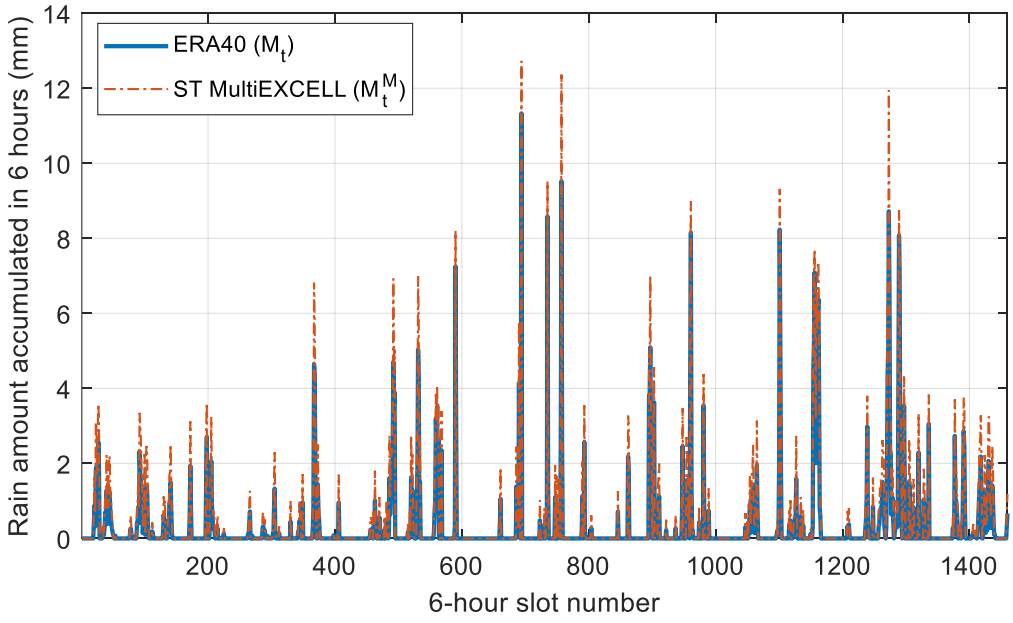

Fig. 4-10. Trend of the rain amount accumulated in 6 hours for a sample year in Spino d'Adda: ERA40 database and ST MultiEXCELL.

A clarification on step 5 is necessary. As mentioned above, the main constraint imposed on the generation of rain events is that $P(R)_M$ matches the input $P(R)$. However, this might occur with a number of rain events N_{ev} significantly higher or smaller than the target number of available rainy slots, N_{6h}. In fact, this would somehow considerably modify the rain rate temporal correlation embedded in the ERA40 time series of M_t (several rain events would be added or dropped, respectively, according to step 6 above). However, both cases can be avoided by tuning η_{AV}, i.e. by increasing its value if N_{ev} is considerably lower than N_{6h} and vice versa. On the other hand, obtaining slightly different values of N_{ev} and N_{6h} does not represent an issue: in the reference case of Spino d'Adda, N_{ev} = 404 and N_{6h} = 408. As a result, four 6-hour rain slots were not matched with any rain event, but, according to the sorting process described at step 6 (ERA40 rain slots are matched to rain events in decreasing order for M_t), those are all associated to negligible values of M_t (lower than 0.06 mm/6h).

4.6. Preliminary validation of ST MultiEXCELL

Fig. 4-11 shows the comparison between the $P(R)$ calculated from the rain gauge data (with label 'Input $P(R)$') and the one obtained by considering all the rainy pixels of the synthetic rain events (with label 'Model $P(R)_M$'): as expected, the agreement between the curves is very good.

A good agreement is also shown in Fig. 4-12, which compares the PDF of the fractional rainy area η_P as calculated from ERA40 data (see step 3 in Section 4.5) and as obtained from all the rain maps composing the synthetic rain events.

DISTRIBUTION A: Distribution approved for public release. Distribution unlimited

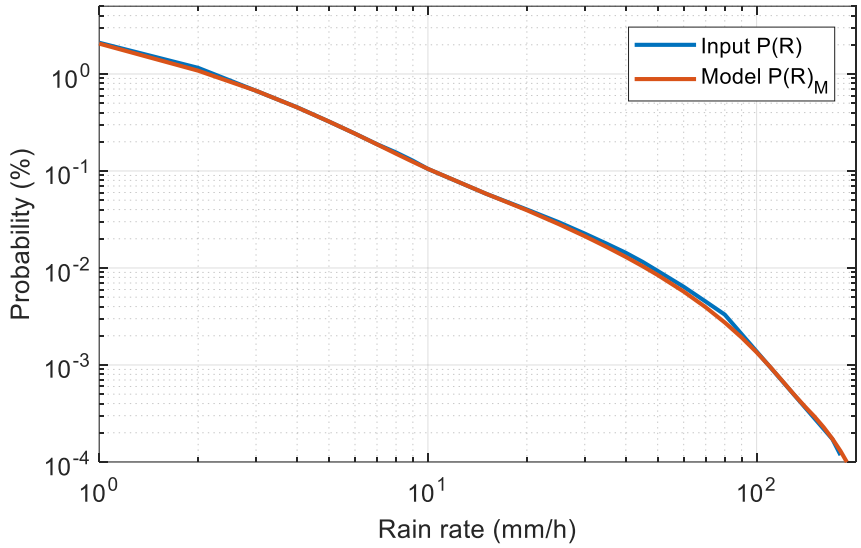

Fig. 4-11. P(R) calculated from the rain events generated by ST MultiEXCELL and from rain gauge data (Spino d'Adda, Italy).

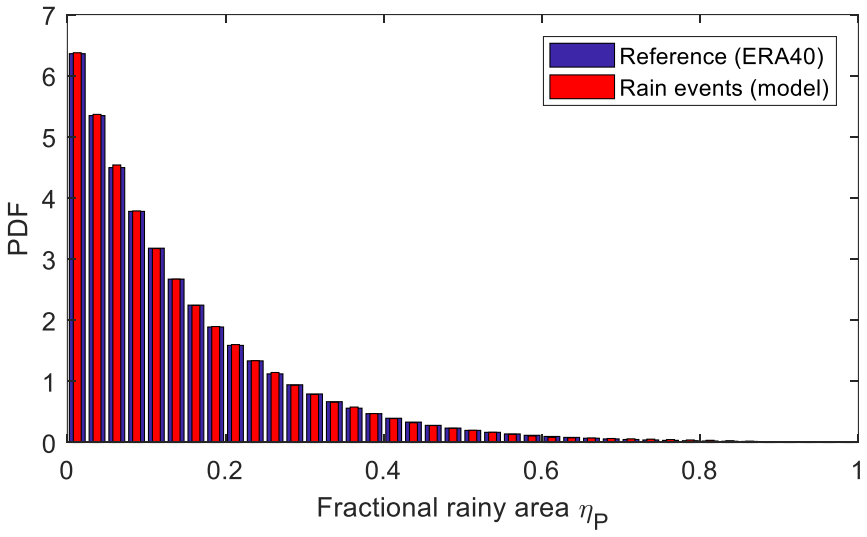

Fig. 4-12. Reference and model-derived PDF of the fractional rainy area η_P (Spino d'Adda, Italy).

Besides first-order statistics, ST MultiEXCELL also aims at reproducing the correct spatial and temporal correlation of the rain rate. As an example, Fig. 4-13 depicts the rain rate time series extracted from one of the 404 rain events synthesized for Spino d'Adda; the data refer to a "virtual rain gauge" being located in three different positions on the map (with coordinate x_{RG} and y_{RG}), which are indicated by the black squares in Fig. 4-14: besides showing a realistic rain event affecting each of the three positions on the map, the three curves in the figure also indicate that, as expected, the correlation between the time series decreases as the distance among the points increases.

DISTRIBUTION A: Distribution approved for public release. Distribution unlimited

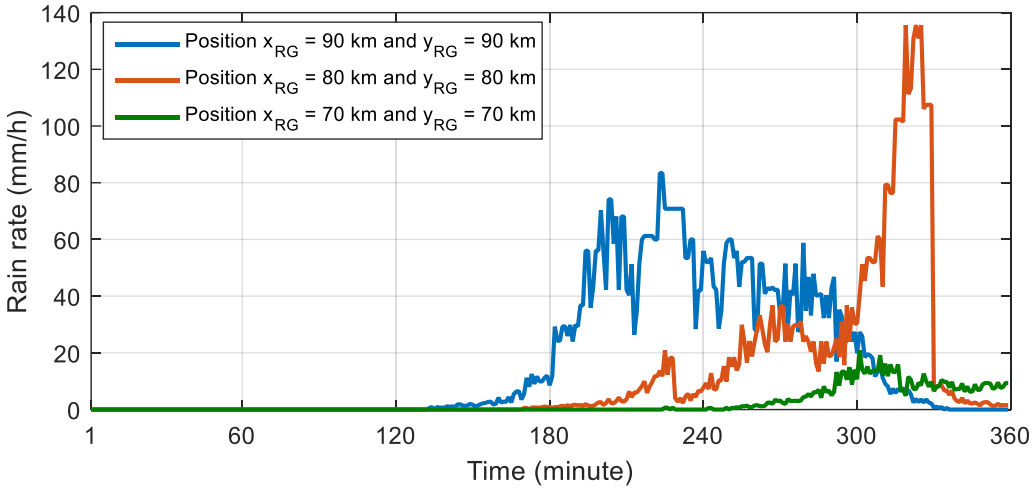

Fig. 4-13. Sample time series of the rain rate for three different positions of the "virtual rain gauge" on the map (Spino d'Adda, Italy).

A much larger pool of virtual rain gauges was considered (red crosses in Fig. 4-14) to better assess the spatial and temporal correlation of the rain maps synthesized by ST MultiEXCELL.

The temporal correlation of the rain rate was evaluated by concatenating the time series associated to each position on the map reported in Fig. 4-14 into a single time series, and afterwards by calculating the temporal correlation index ρ_T defined as [Luini and Capsoni, 2013c]:

$$\rho_T(\tilde{t},\Delta t)=\frac{\mathrm{E}\left[R(\tilde{t})R(\tilde{t}+\Delta t)\right]-\mathrm{E}\left[R(\tilde{t})\right]E\left[R(\tilde{t}+\Delta t)\right]}{\sigma\left[R(\tilde{t})\right]\sigma\left[R(\tilde{t}+\Delta t)\right]} \tag{4-7}$$

In (4-7), E[•] and σ[•] are the mean and standard deviation operators, while $R(\tilde{t})$ and $R(\tilde{t})$ are the rain rate time series, respectively relative to time $\tilde{t}$ and $\tilde{t}+\Delta t$. Fig. 4-15 shows the mean value of ρ_T as a function of the time lag Δt, regardless of the time instant $\tilde{t}$, calculated both from the synthetic rain events and from the rain gauge data: overall, the agreement between the two curves is quite satisfactory.

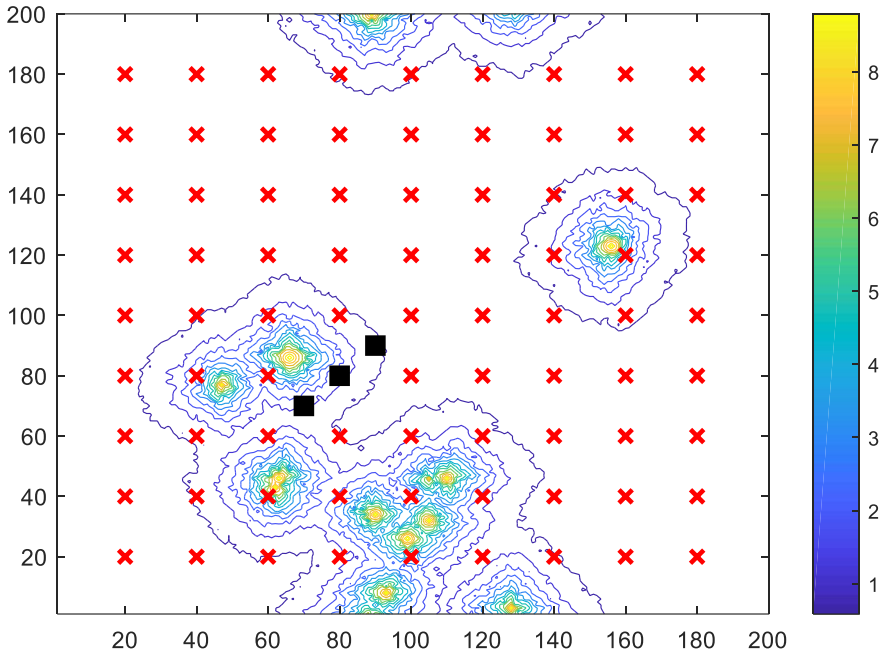

Fig. 4-14. Sample ST MultiEXCELL rain map and positions of the virtual rain gauge.

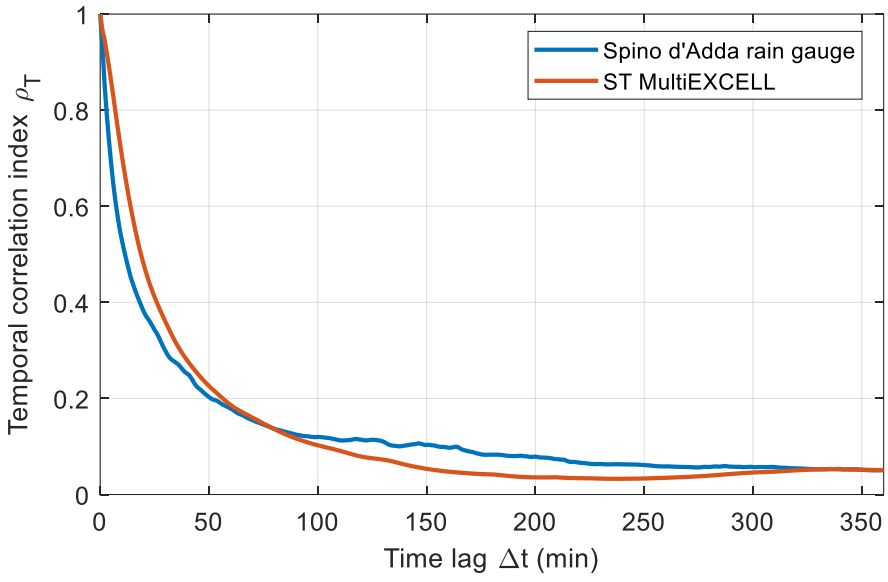

Fig. 4-15. Trend of the temporal correlation coefficient ρ_T as a function of the time lag Δt, derived from the rain events generated by ST MultiEXCELL and from rain gauge data (Spino d'Adda, Italy).

The spatial correlation of the rain rate was assessed by resorting again to the same pool of positions indicated in Fig. 4-14, i.e. by calculating, for each pair of positions, the spatial correlation index ρ_S [Luini and Capsoni, 2013c]:

$$\rho_S(\mathrm{x},\mathrm{y}) = \frac{\mathrm{E}\left[R(\mathrm{x})R(\mathrm{y})\right] - \mathrm{E}\left[R(\mathrm{x})\right]E\left[R(\mathrm{y})\right]}{\sigma\left[R(\mathrm{x})\right]\sigma\left[R(\mathrm{y})\right]} \tag{4-8}$$

In (4-8), $R(\mathrm{x})$ and $R(\mathrm{y})$ are the rain rate time series, respectively relative to pixels x and y. Similarly to ρ_T, the spatial correlation index between two points was assumed to depend (mostly) on their distance d and only marginally on their position, i.e.:

$$\rho_S(\mathrm{x},\mathrm{y}) = \rho_S(d = |\mathrm{x}-\mathrm{y}|) \tag{4-9}$$

Fig. 4-16 shows the mean value of ρ_S as a function of the distance d, regardless of the position of the two pixels on the map, calculated both from the rain events synthesized by ST MultiEXCELL and from the rain maps generated by MultiEXCELL, which are not correlated in time [Luini and Capsoni, 2011]. This satisfactory agreement between the curves is a hint of the fact that ST MultiEXCELL correctly preserves the spatial correlation of the rain rate, as MultiEXCELL was in turn proven to do so when applied to achieve predictions in propagation oriented applications (e.g. rain attenuation along the terrestrial links [Luini and Capsoni, 2010], site diversity gain [Luini and Capsoni, 2013b], interference due to hydrometeor scattering [Capsoni et al., 2010]).

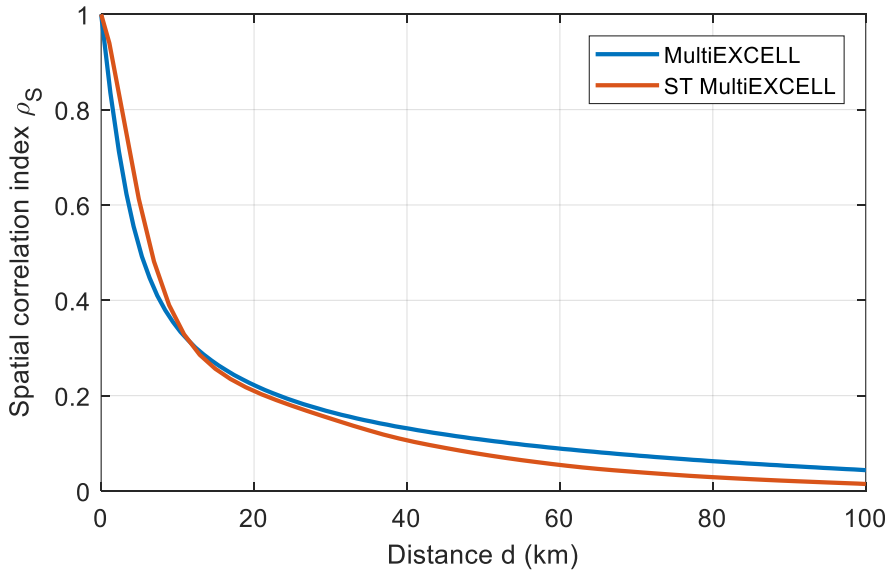

Fig. 4-16. Trend of the spatial correlation coefficient ρ_S as a function of the distance d, derived from the ST MultiEXCELL rain events and from MultiEXCELL rain maps (Spino d'Adda, Italy).

The results reported above offer a preliminary validation of ST MultiEXCELL regarding the preservation of first-order ($P(R)$) and second-order statistics (the temporal and spatial correlation) of the rain rate; notwithstanding this, additional data collected in other sites are needed to corroborate these results.

DISTRIBUTION A: Distribution approved for public release. Distribution unlimited

4.7. Reference application scenario: Rome, NY (USA) and V/W band SatCom system

The key advantage of ST MultiEXCELL is the change to simulate, in a comprehensive way, the performance of a site diversity system.

The reference scenario is the main ground station located in Rome, NY (USA): the selected frequencies are in the V-band and in the W-band, specifically 50, 70, 80, 90 GHz. The main geometrical and electrical characteristics of the reference Earth-space link considered in Rome, NY, are presented in Table 4-1.

Table 4-1. Main geometrical and electrical characteristics of the Earth-space link in Rome, NY (USA).

Site	Rome, NY (USA)
Latitude	43.22° N
Longitude	75.41° W
Altitude	150 m a.m.s.l.
Satellite orbital position	100° W
Link elevation	34.4°
Link orientation	146.2°
Frequency	50, 70, 80, 90 GHz
Wave polarization	Vertical

The simulation of the interaction between the rain maps generated by ST MultiEXCELL and the Earth-space link allows estimating the rain attenuation; this is achieved by using recommendation ITU-R P.838-3 [ITU-R P.838-3], according to which the specific attenuation due to rain is obtained as $\gamma = kR^{\alpha}$, where R is the rainfall rate in mm/h, while the coefficients k and α, extracted from recommendation ITU-R P.838-3, are listed in Table 4-2.

Table 4-2. Values of the k and α coefficients extracted from recommendation ITU-R P.838-3 for the prediction of rain attenuation statistics

Frequency (GHz)	***k***	***α***
50	0.6492	0.7906
70	1.0263	0.7236
80	1.1674	0.7036
90	1.2797	0.6887

The rain height H_r, required to estimate rain attenuation, is retrieved from recommendation ITU-R P.839-4 [ITU-R P.839-4]; specifically, $H_r = h_0 + 0.36$ km, where h_0 is the mean yearly 0 °C isotherm height derived from the digital maps attached to recommendation ITU-R P.839-4 and the increment of 0.36 km is used to model, in an equivalent way, the presence of the bright band. The mean yearly value of H_r for Rome, NY, is 3.85 km. Starting from the rainfall

DISTRIBUTION A: Distribution approved for public release. Distribution unlimited

rate maps provided by ST MultiEXCELL, the k and α coefficients, and the rain height, the rain attenuation can be easily computed by numerically integrating the specific attenuation along the link.

Site diversity is one of the most effective techniques to counteract tropospheric fades, taking advantage of the strongly uneven spatial distribution of rain attenuation. Site diversity involves the use of at least two ground stations, which simultaneously receive the signal emitted by the same satellite, thus allowing to always select the station less affected by attenuation, ideally on an instantaneous basis. This concept is implemented in the simulations carried out using ST MultiEXCELL synthetic maps, by defining couple of points across each maps with the same baseline distance D (both horizontally and vertically). The results of the simulations, in terms of yearly CCDFs of rain attenuation, are shown in for 50, 70, 80 and 90 GHz from Fig. 4-17 to Fig. 4-20; each figure depicts the reference single site curve, and the joint ones for different baselines ranging from 2 to 50 km.

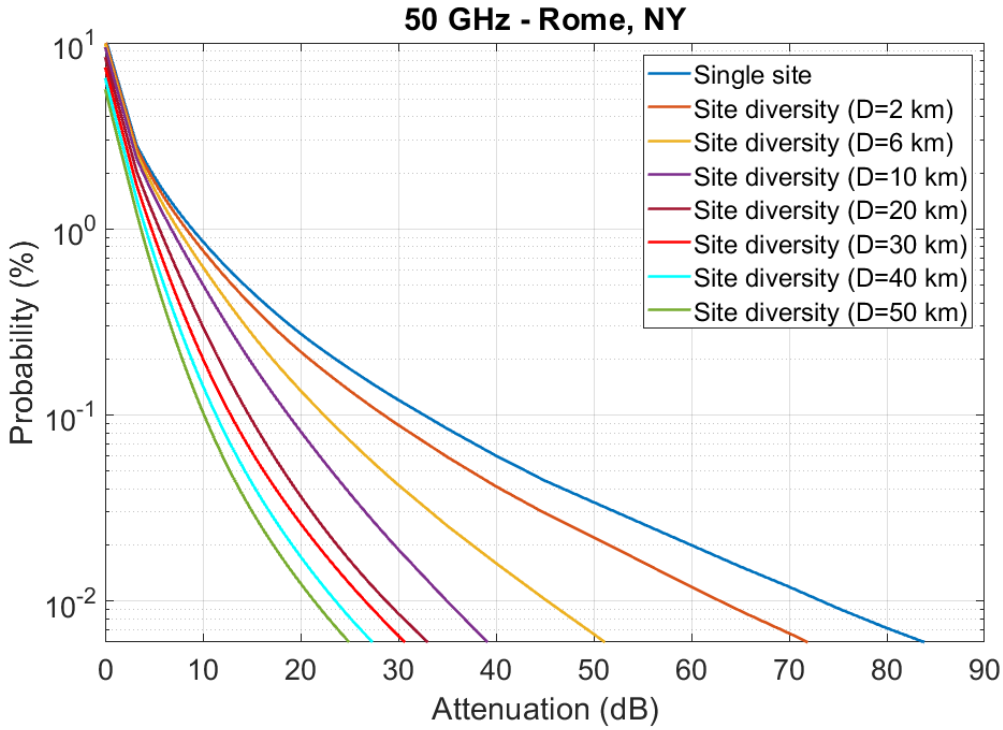

Fig. 4-17. Rain attenuation statistics at 50 GHz for Rome, NY, obtained from the ST MultiEXCELL synthetic maps: single site (blue line) and two-site (several baseline values) system.

DISTRIBUTION A: Distribution approved for public release. Distribution unlimited

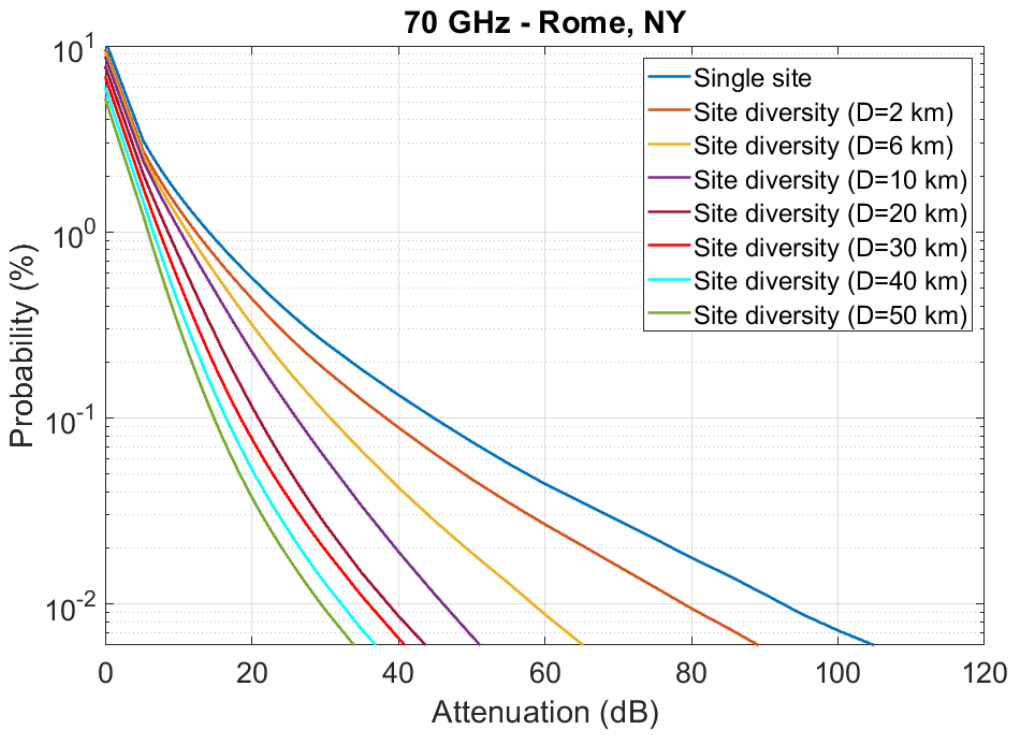

Fig. 4-18. Rain attenuation statistics at 70 GHz for Rome, NY, obtained from the ST MultiEXCELL synthetic maps: single site (blue line) and two-site (several baseline values) system.

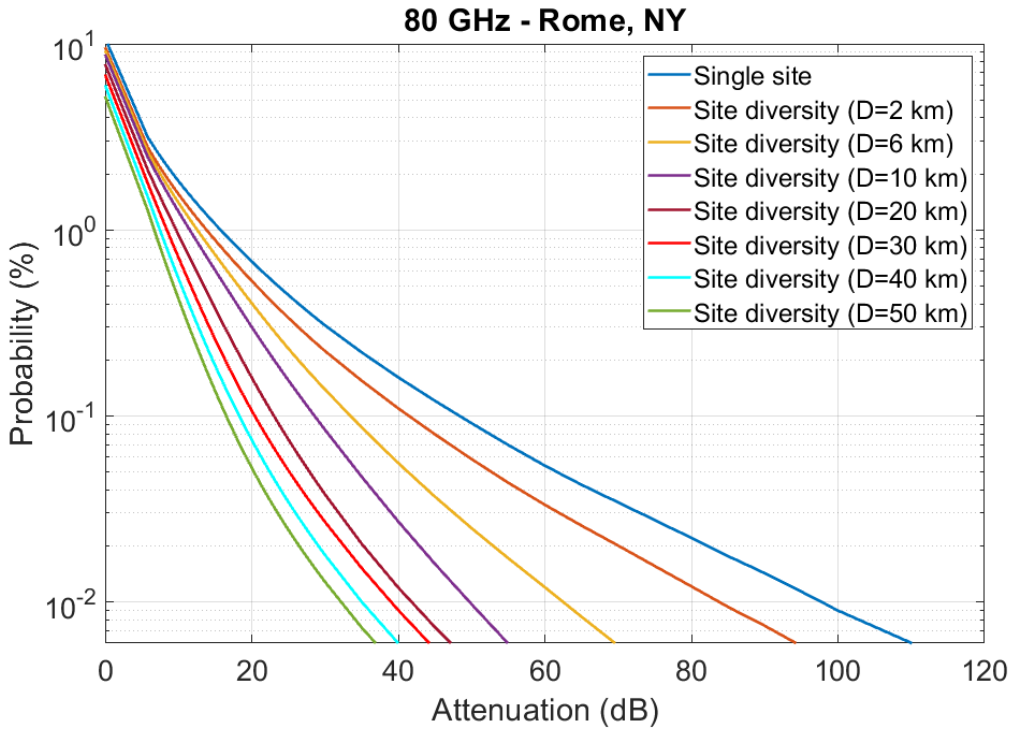

Fig. 4-19. Rain attenuation statistics at 80 GHz for Rome, NY, obtained from the ST MultiEXCELL synthetic maps: single site (blue line) and two-site (several baseline values) system.

DISTRIBUTION A: Distribution approved for public release. Distribution unlimited

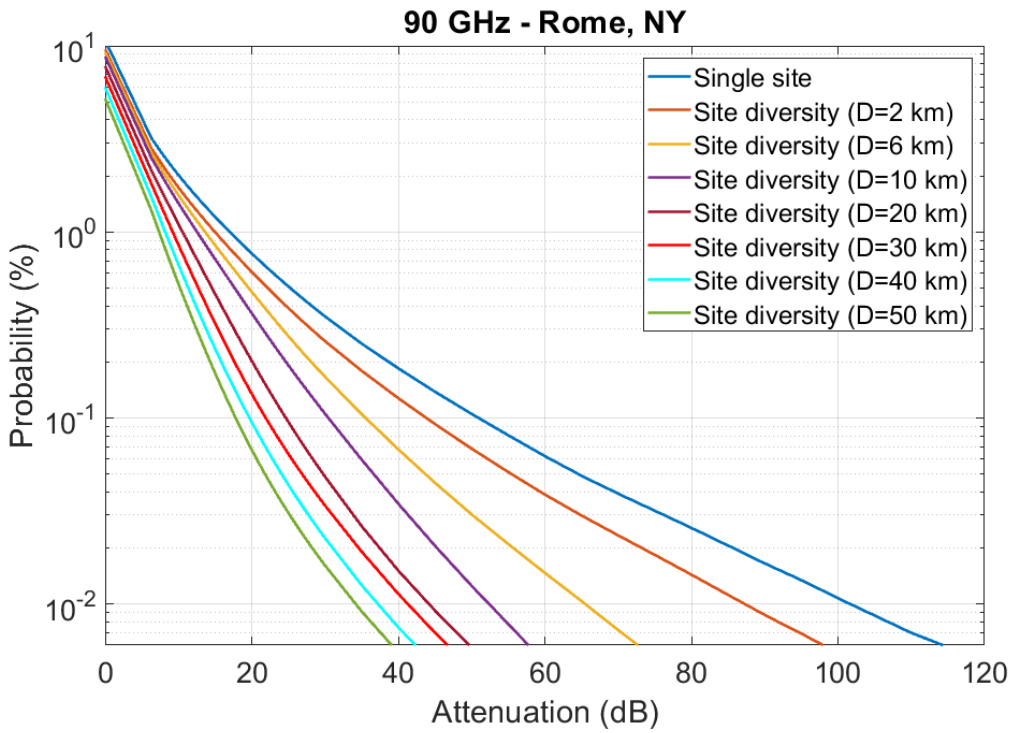

Fig. 4-20. Rain attenuation statistics at 90 GHz for Rome, NY, obtained from the ST MultiEXCELL synthetic maps: single site (blue line) and two-site (several baseline values) system.

The site diversity gain is defined as

$$G(D, A_S) = A_S(P) - A_j(D, P) \tag{4-10}$$

where A_S and A_j are the attenuation values of the CCDF (both for the same outage probability level P), respectively relative to the single station and to the diversity scheme, for which the minimum attenuation value is always selected. The site separation distance D has a significant impact on the gain: the trend of the site diversity gain, calculated from the CCDFs reported above, is depicted from Fig. 4-21 to Fig. 4-24.

DISTRIBUTION A: Distribution approved for public release. Distribution unlimited

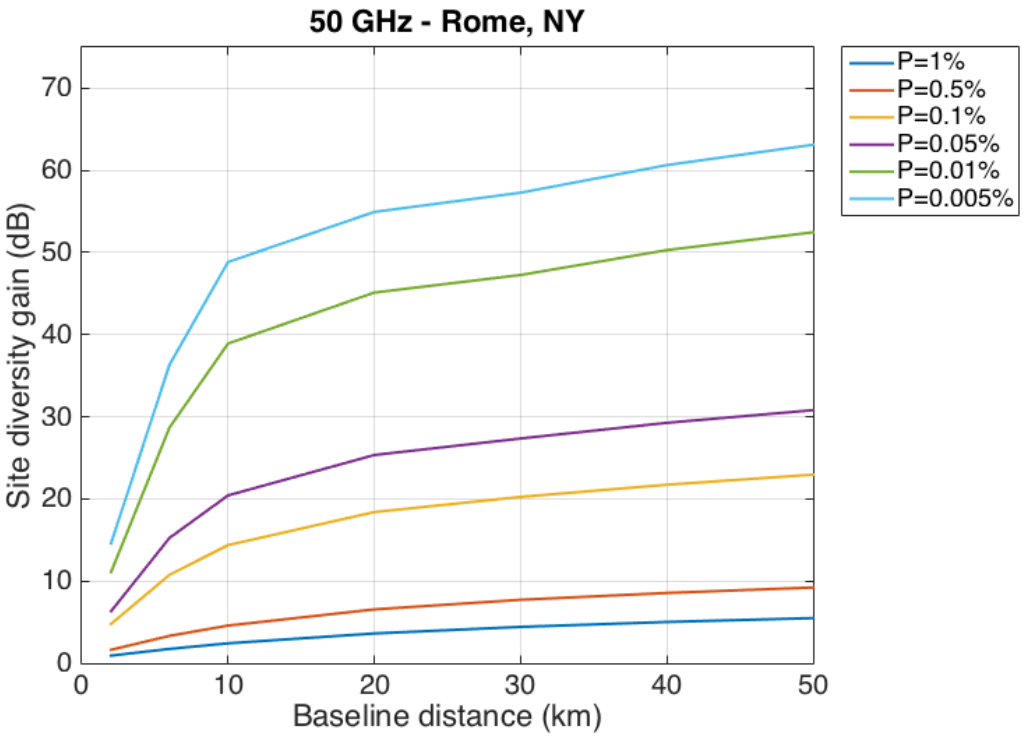

Fig. 4-21. Site diversity gain at 50 GHz for Rome, NY, obtained from the ST MultiEXCELL rain maps: two-site diversity scheme.

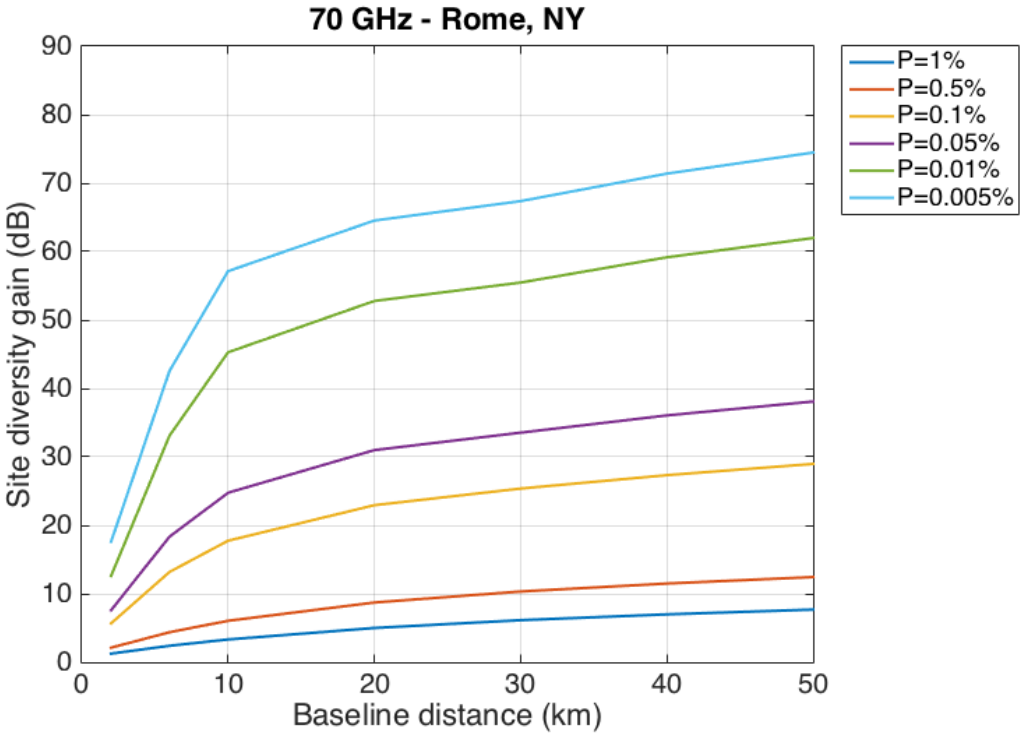

Fig. 4-22. Site diversity gain at 70 GHz for Rome, NY, obtained from the ST MultiEXCELL rain maps: two-site diversity scheme.

DISTRIBUTION A: Distribution approved for public release. Distribution unlimited

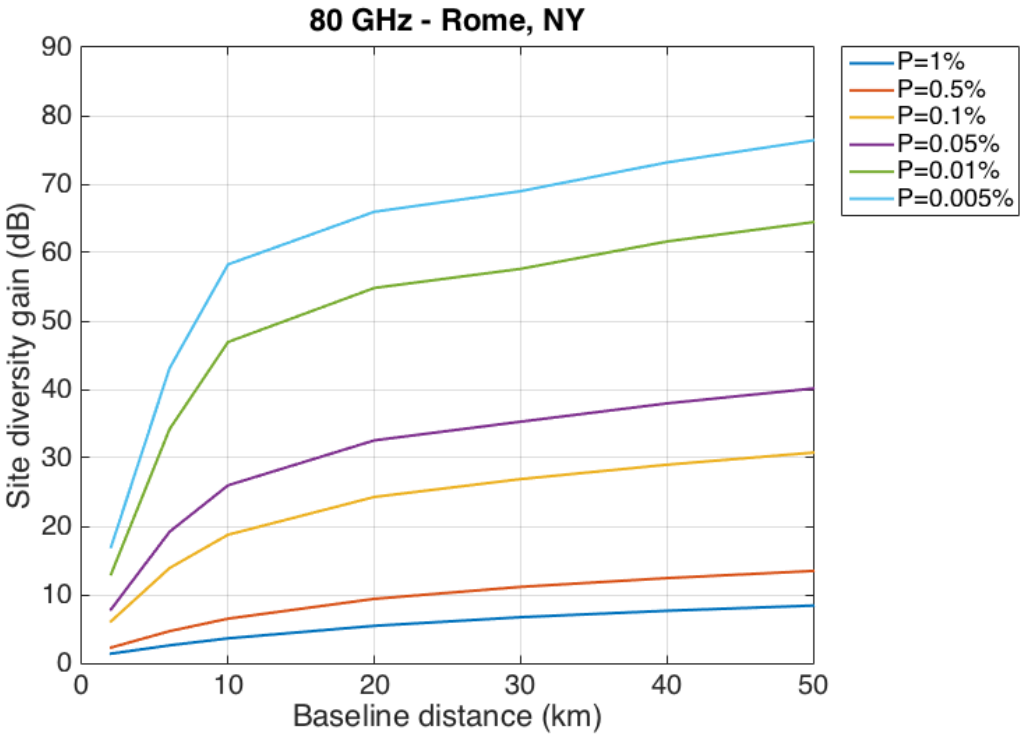

Fig. 4-23. Site diversity gain at 80 GHz for Rome, NY, obtained from the ST MultiEXCELL rain maps: two-site diversity scheme.

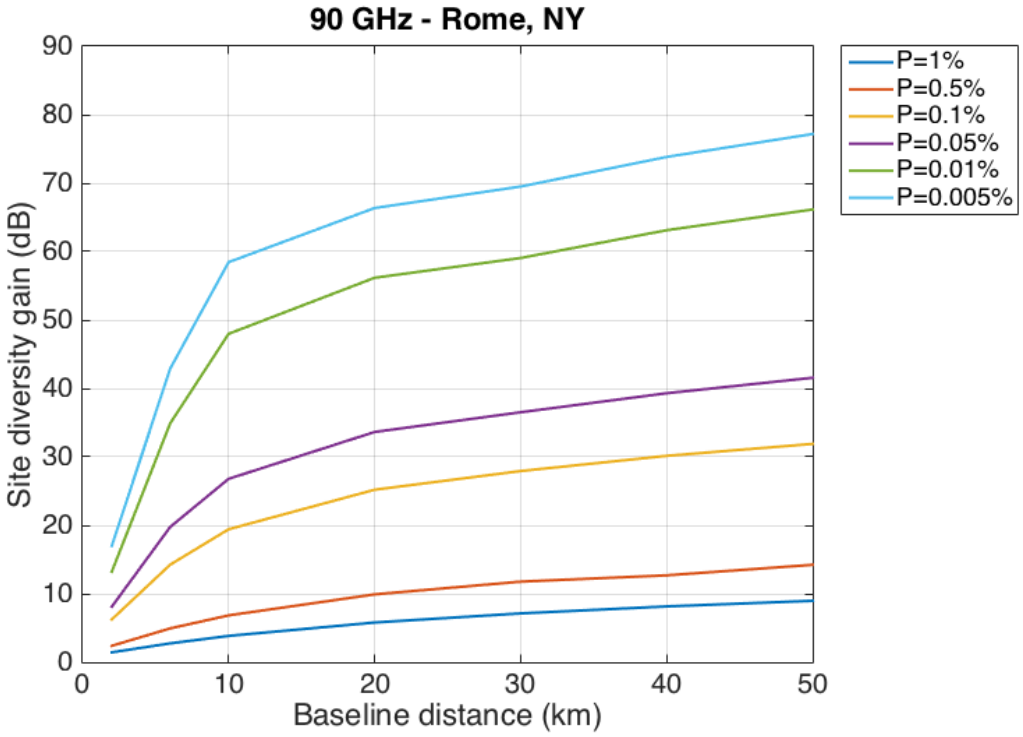

Fig. 4-24. Site diversity gain at 90 GHz for Rome, NY, obtained from the ST MultiEXCELL rain maps: two-site diversity scheme.

DISTRIBUTION A: Distribution approved for public release. Distribution unlimited

The results shown above clearly point out that site diversity is effective in counteracting rain attenuation. In fact, considering the typical outage probability of 0.01%, a large part of the attenuation can be compensated for by using two stations (e.g. at 70 GHz, $A_S(0.01\%) = 90$ dB, while $A_j(50$ km,$0.01\%) = 25$ dB). The results also indicate that the diversity gain increases steeply for separation distances shorter than 20 km because of the fast decorrelation characterizing rain fields in that range of distances. Afterwards, the site diversity gain increases more slowly for $D > 20$ km. Moreover, keeping the same probability level P, the gain increases with frequency, and so does the single-site attenuation: for $D = 20$ km, the diversity gain is 45 dB at 50 GHz, and is more than 50 dB at higher frequencies. For $D = 50$ km, $G = 53$ dB at 50 GHz and $G > 60$ dB for 70, 80 and 90 GHz.

The results presented so far were obtained by assuming an ideal site diversity system, able to switch instantaneously from one station to the other: in a real system, this assumption is unrealistic because of the latency time that is intrinsic to the system; as a matter of fact, the switch will occur with a certain delay. As a consequence, too many switches between the stations, if very close one to the other, might limit the system performance. A possible way to avoid this is to associate a proper attenuation threshold A_{th} to one station (e.g. the slave one in a master-slave system) such that the switch will occur only if the differential attenuation between the two stations exceeds A_{th}. This switching strategy will obviously reduce the number of switches, at the expenses of a reduction in the site diversity gain: as a matter of fact, the choice of A_{th} is a tradeoff between the number of switches and the diversity gain. Given the space-time correlation of the maps generated by ST MultiEXCELL, it is possible to assess the effect of applying the threshold A_{th} to the diversity system. Results, i.e. number of switches in a year and CCDFs of attenuation for the diversity system, are shown in the following figures for two reference baseline distances: $D = 20$ and 50 km.

DISTRIBUTION A: Distribution approved for public release. Distribution unlimited

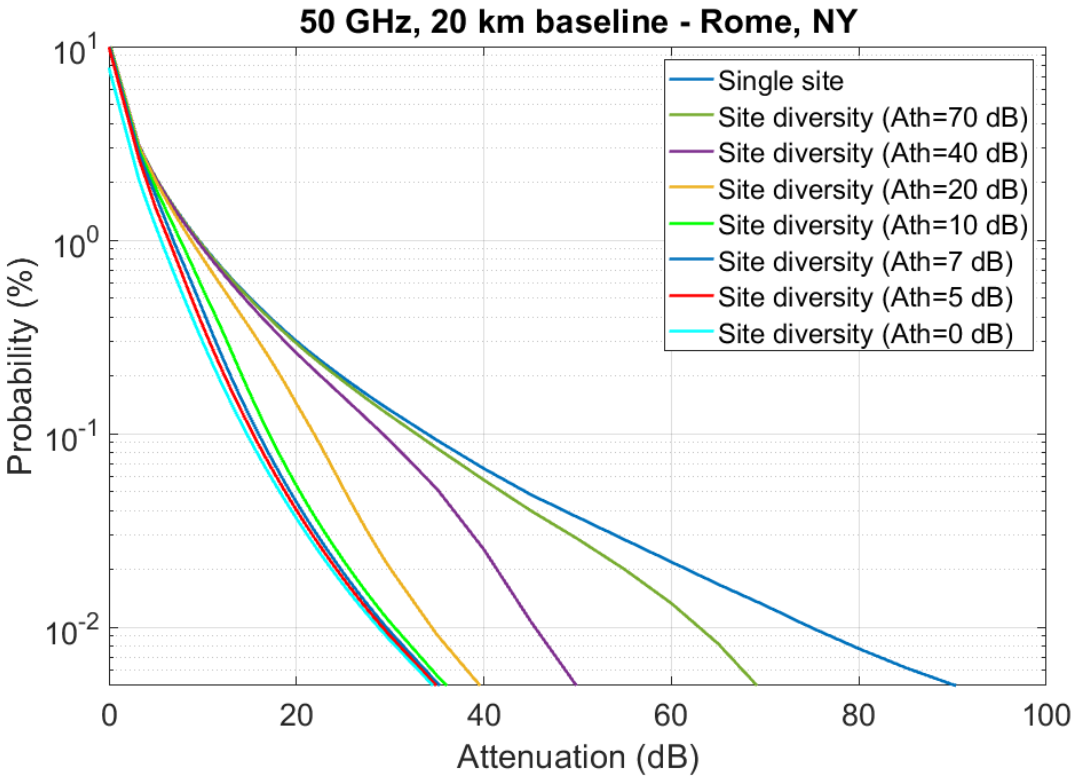

Fig. 4-25. Rain attenuation statistics at 50 GHz for Rome, NY, obtained from ST MultiEXCELL maps: single site (blue line) and two-site system (several values of A_{th} for fixed baseline of 20 km).

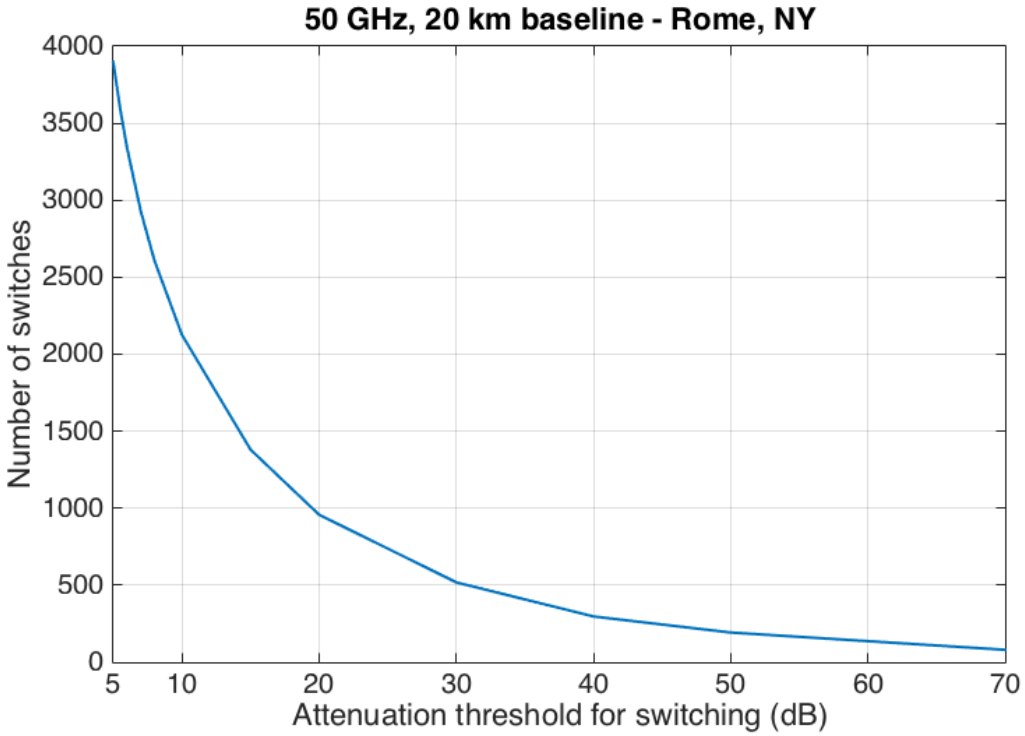

Fig. 4-26. Number of switches in a year between the stations as a function of the threshold A_{th} (50 GHz, 20 km baseline in Rome, NY).

DISTRIBUTION A: Distribution approved for public release. Distribution unlimited

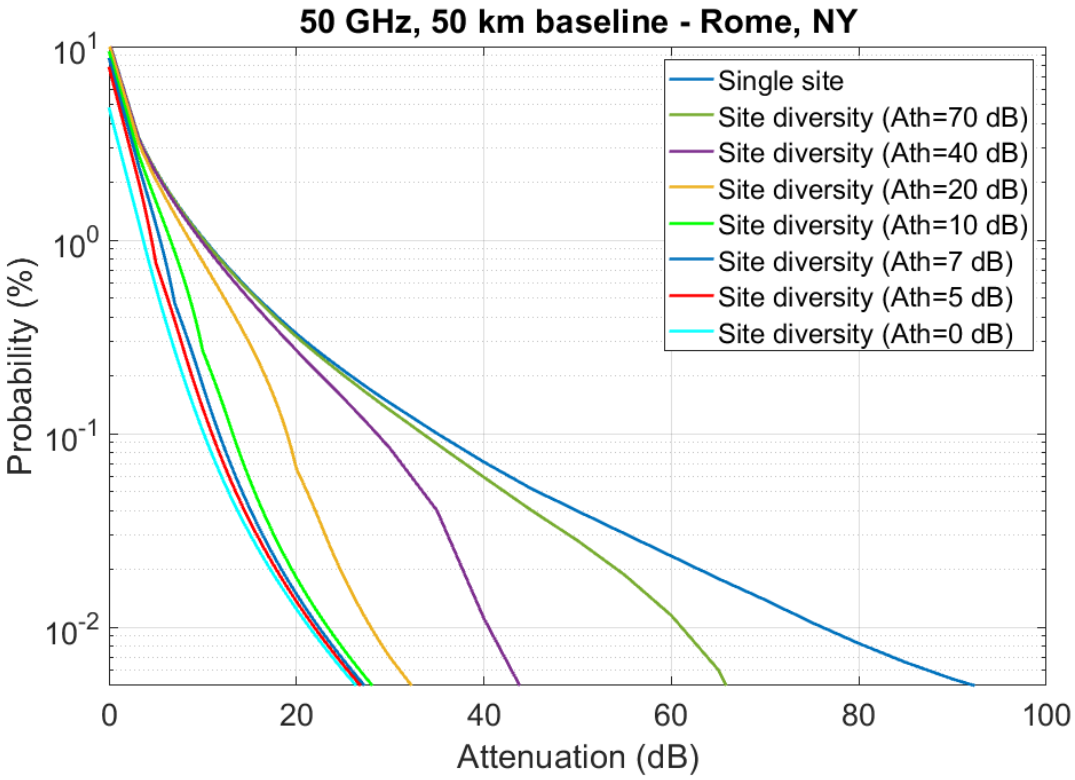

Fig. 4-27. Rain attenuation statistics at 50 GHz for Rome, NY, obtained from ST MultiEXCELL maps: single site (blue line) and two-site system (several values of A_{th} for fixed baseline of 50 km).

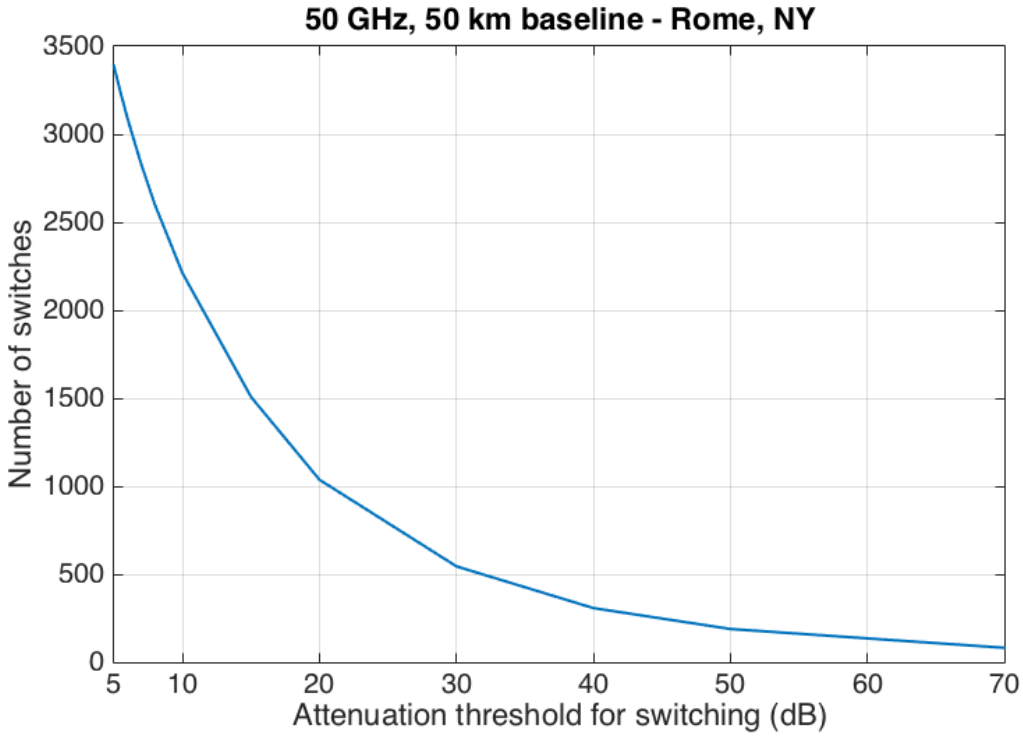

Fig. 4-28. Number of switches in a year between the stations as a function of the threshold A_{th} (50 GHz, 50 km baseline in Rome, NY).

DISTRIBUTION A: Distribution approved for public release. Distribution unlimited

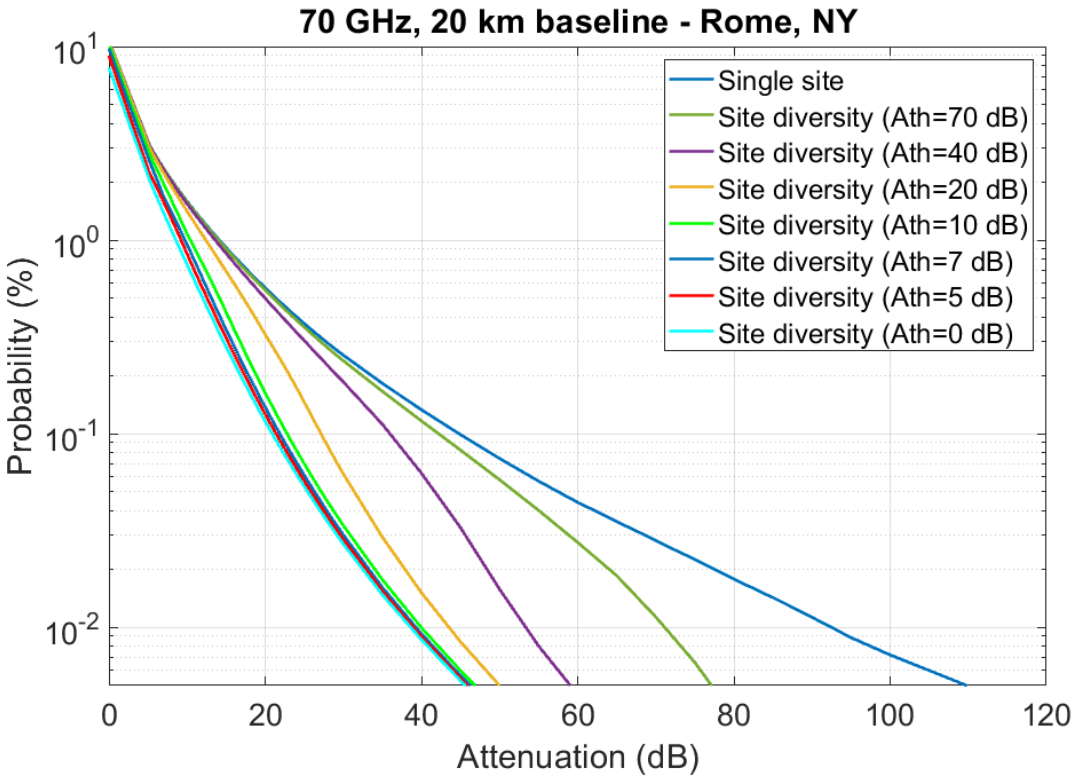

Fig. 4-29. Rain attenuation statistics at 70 GHz for Rome, NY, obtained from ST MultiEXCELL maps: single site (blue line) and two-site system (several values of A_{th} for fixed baseline of 20 km).

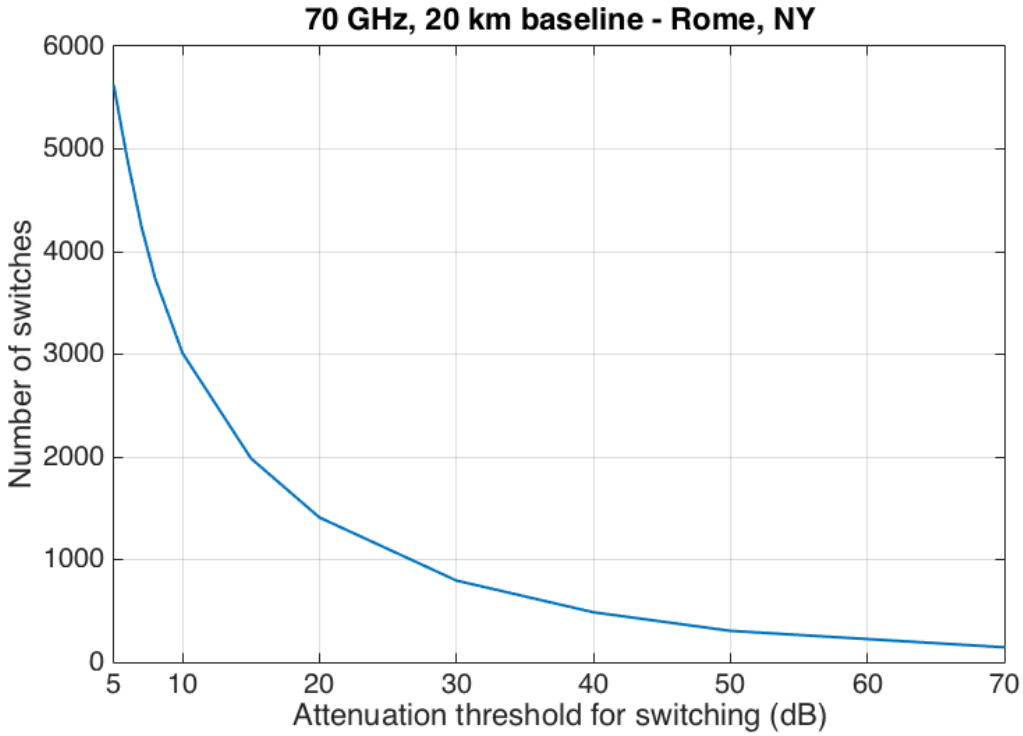

Fig. 4-30. Number of switches in a year between the stations as a function of the threshold A_{th} (70 GHz, 20 km baseline in Rome, NY).

DISTRIBUTION A: Distribution approved for public release. Distribution unlimited

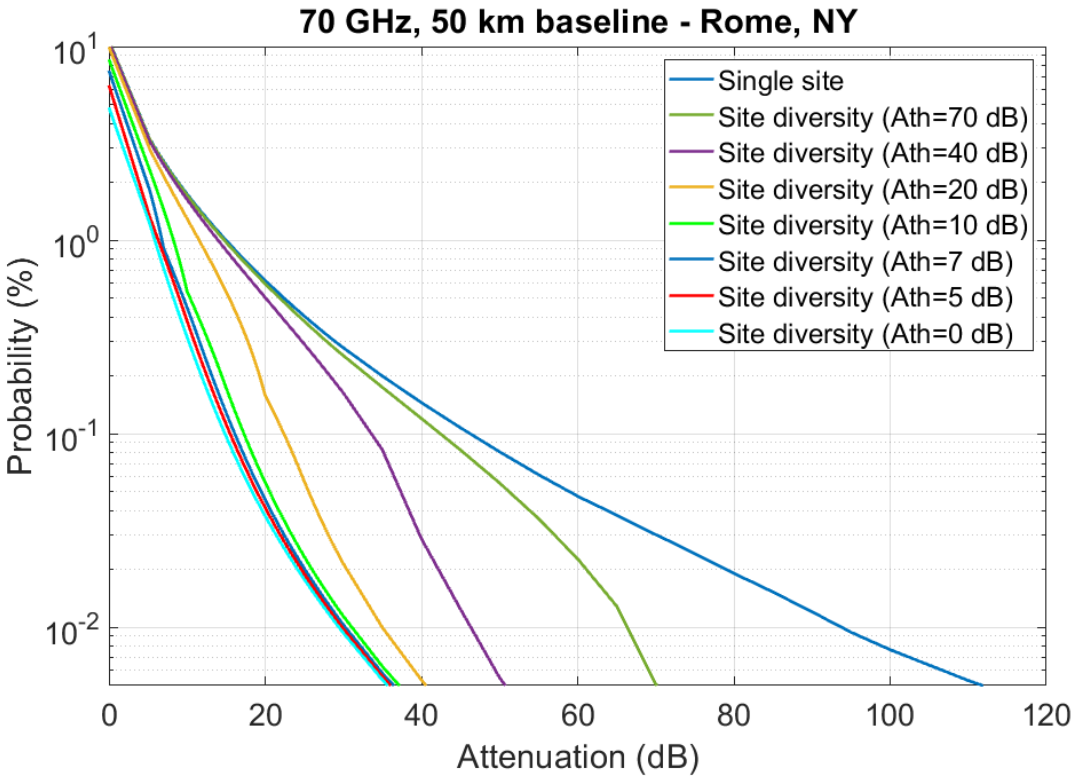

Fig. 4-31. Rain attenuation statistics at 70 GHz for Rome, NY, obtained from ST MultiEXCELL maps: single site (blue line) and two-site system (several values of A_{th} for fixed baseline of 50 km).

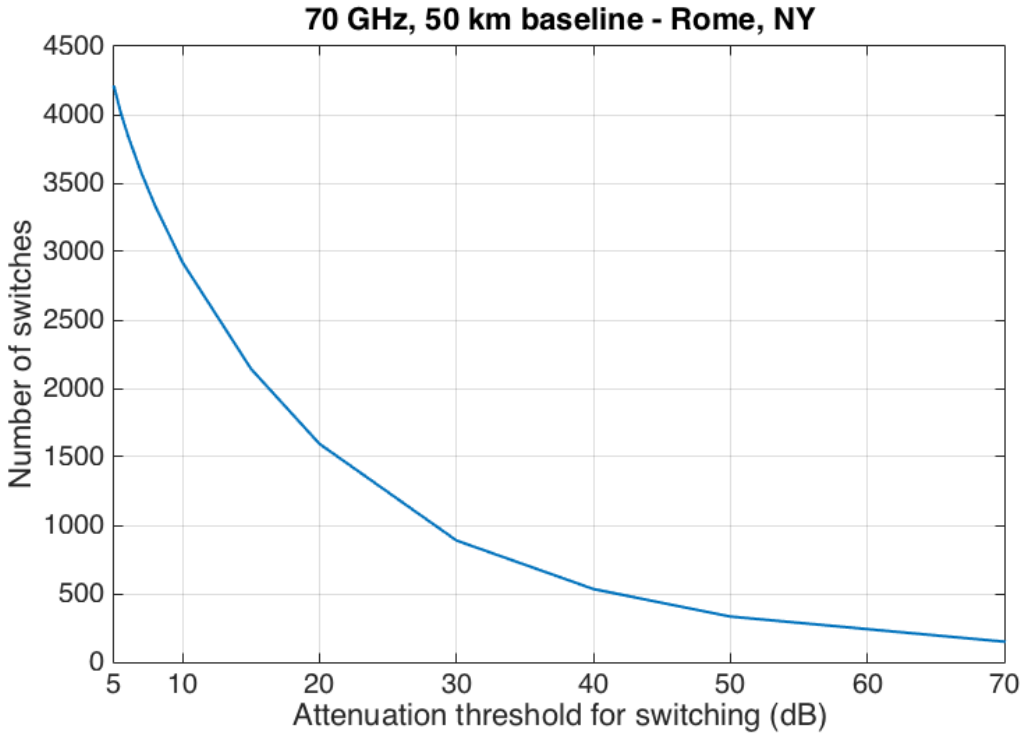

Fig. 4-32. Number of switches in a year between the stations as a function of the threshold A_{th} (70 GHz, 50 km baseline in Rome, NY).

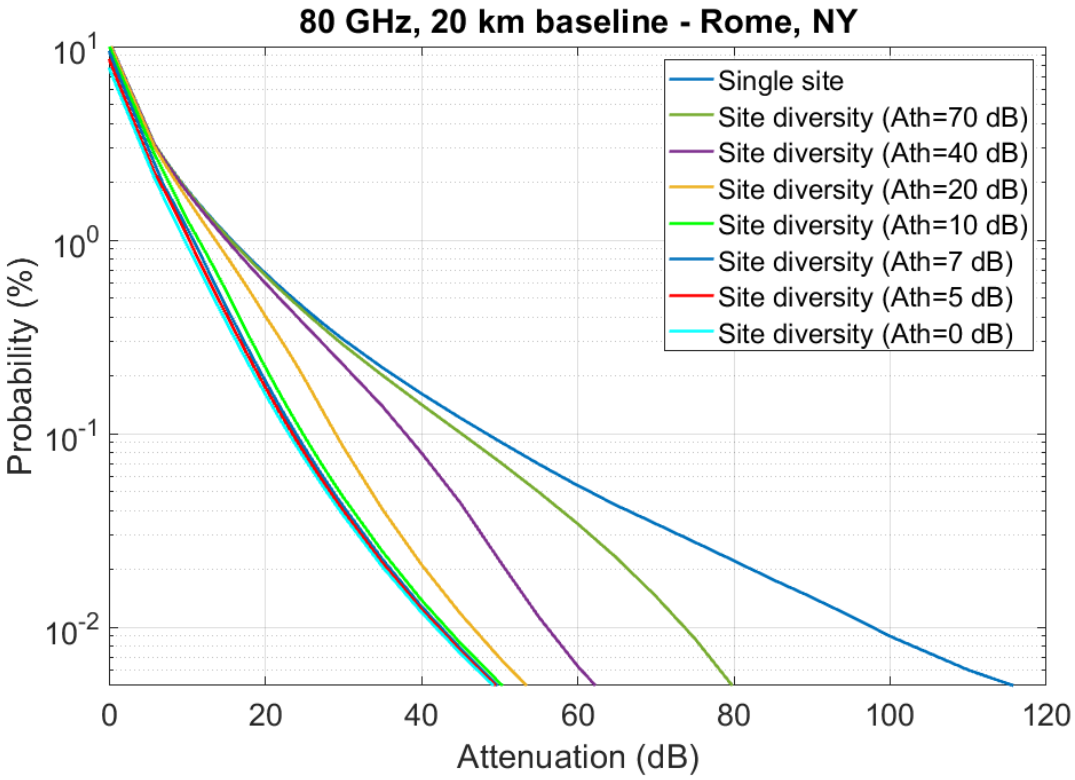

Fig. 4-33. Rain attenuation statistics at 80 GHz for Rome, NY, obtained from ST MultiEXCELL maps: single site (blue line) and two-site system (several values of A_{th} for fixed baseline of 20 km).

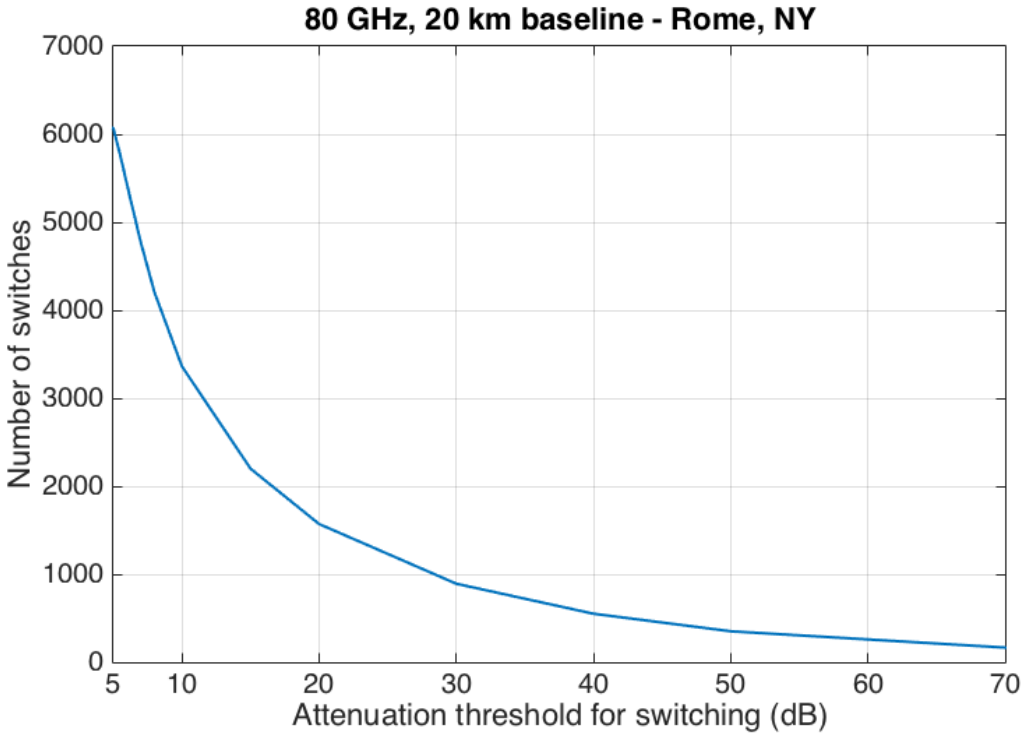

Fig. 4-34. Number of switches in a year between the stations as a function of the threshold A_{th} (80 GHz, 20 km baseline in Rome, NY).

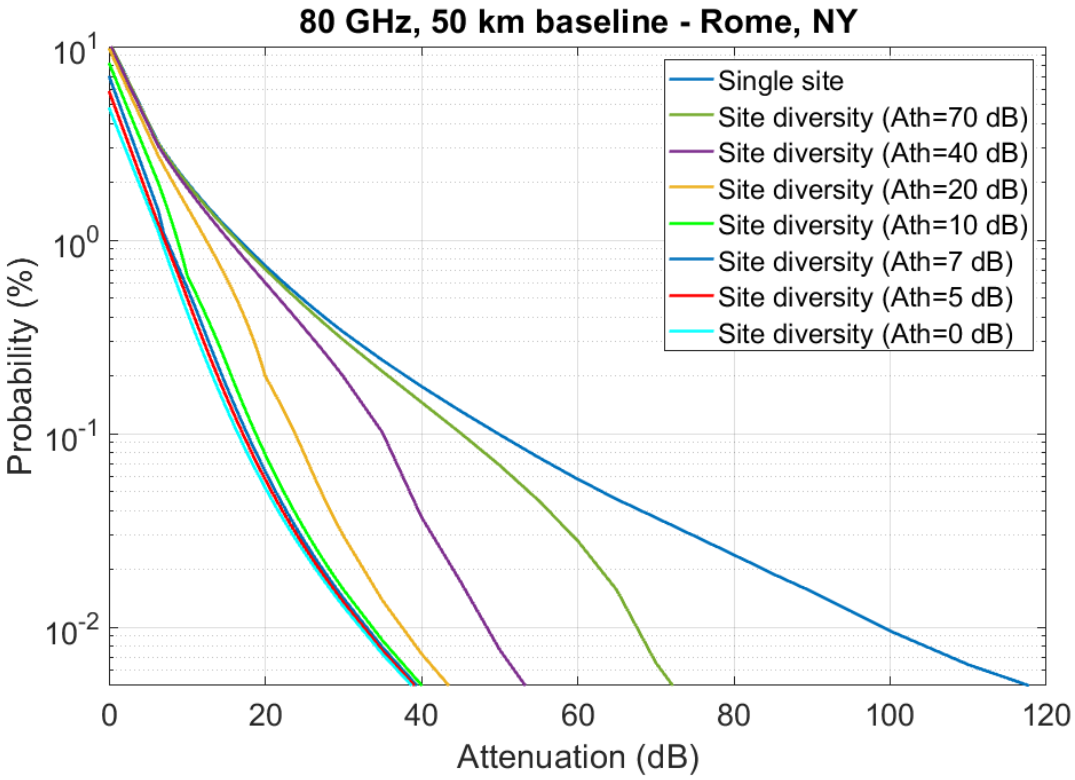

Fig. 4-35. Rain attenuation statistics at 80 GHz for Rome, NY, obtained from ST MultiEXCELL maps: single site (blue line) and two-site system (several values of A_{th} for fixed baseline of 50 km).

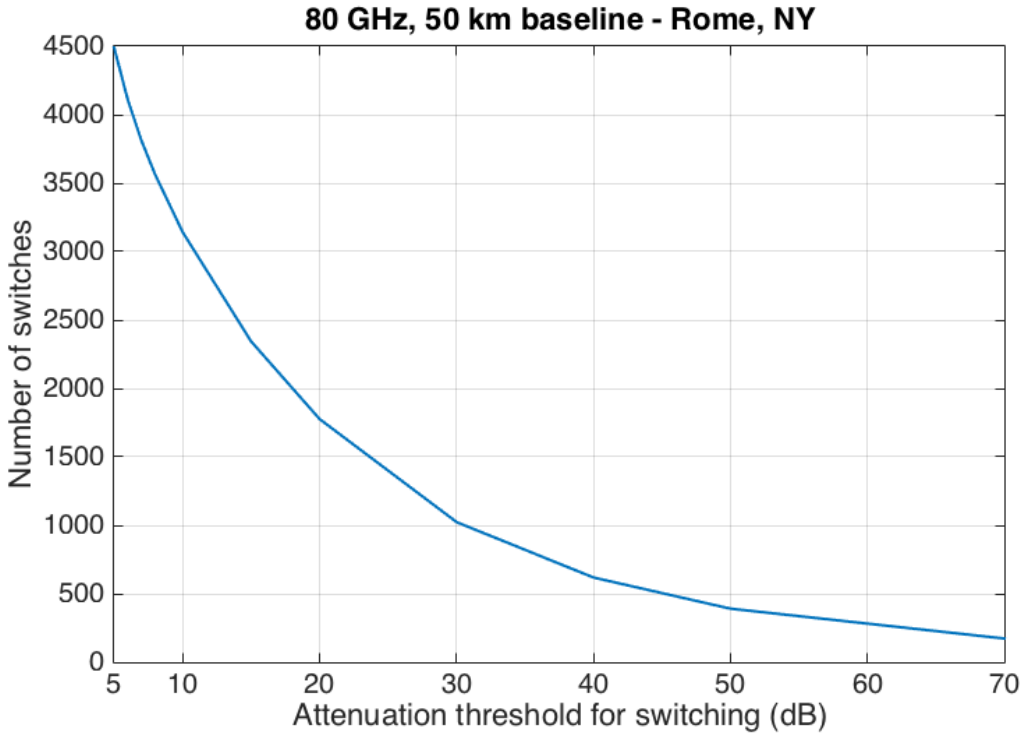

Fig. 4-36. Number of switches in a year between the stations as a function of the threshold A_{th} (80 GHz, 50 km baseline in Rome, NY).

DISTRIBUTION A: Distribution approved for public release. Distribution unlimited

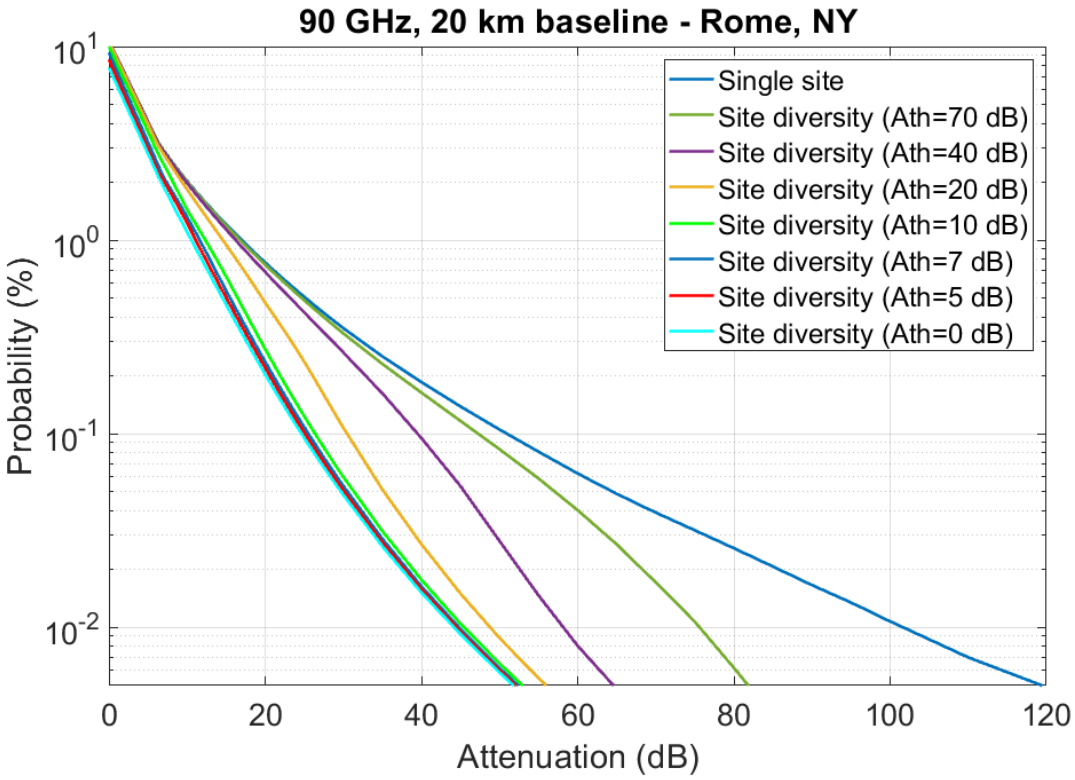

Fig. 4-37. Rain attenuation statistics at 90 GHz for Rome, NY, obtained from ST MultiEXCELL maps: single site (blue line) and two-site system (several values of A_{th} for fixed baseline of 20 km).

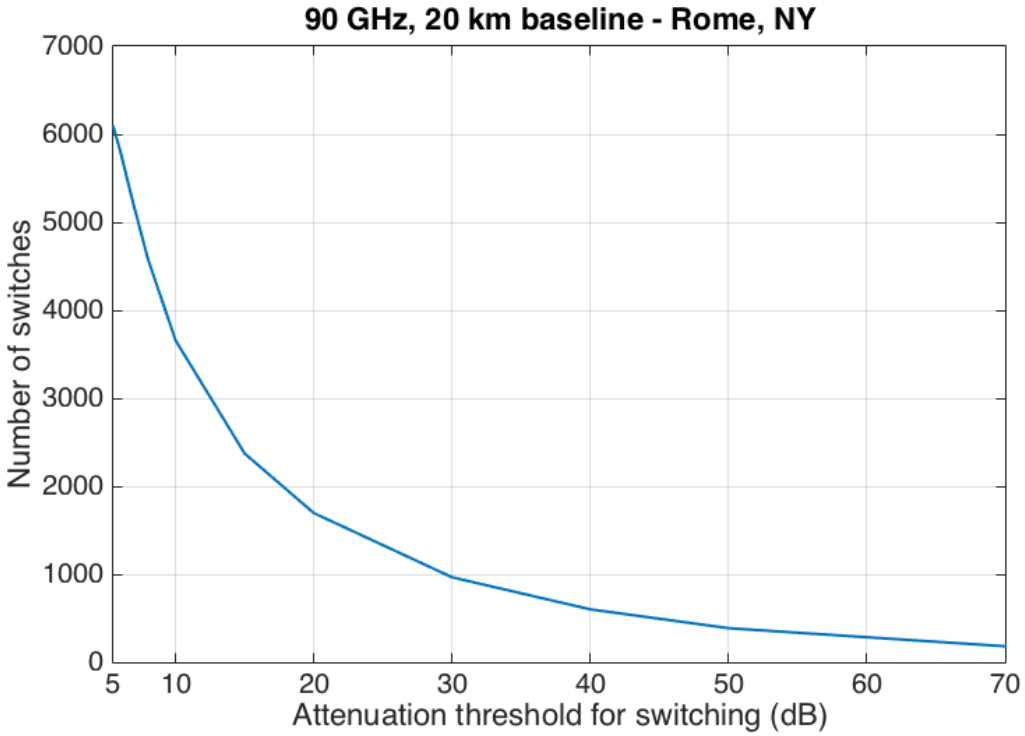

Fig. 4-38. Number of switches in a year between the stations as a function of the threshold A_{th} (90 GHz, 20 km baseline in Rome, NY).

DISTRIBUTION A: Distribution approved for public release. Distribution unlimited

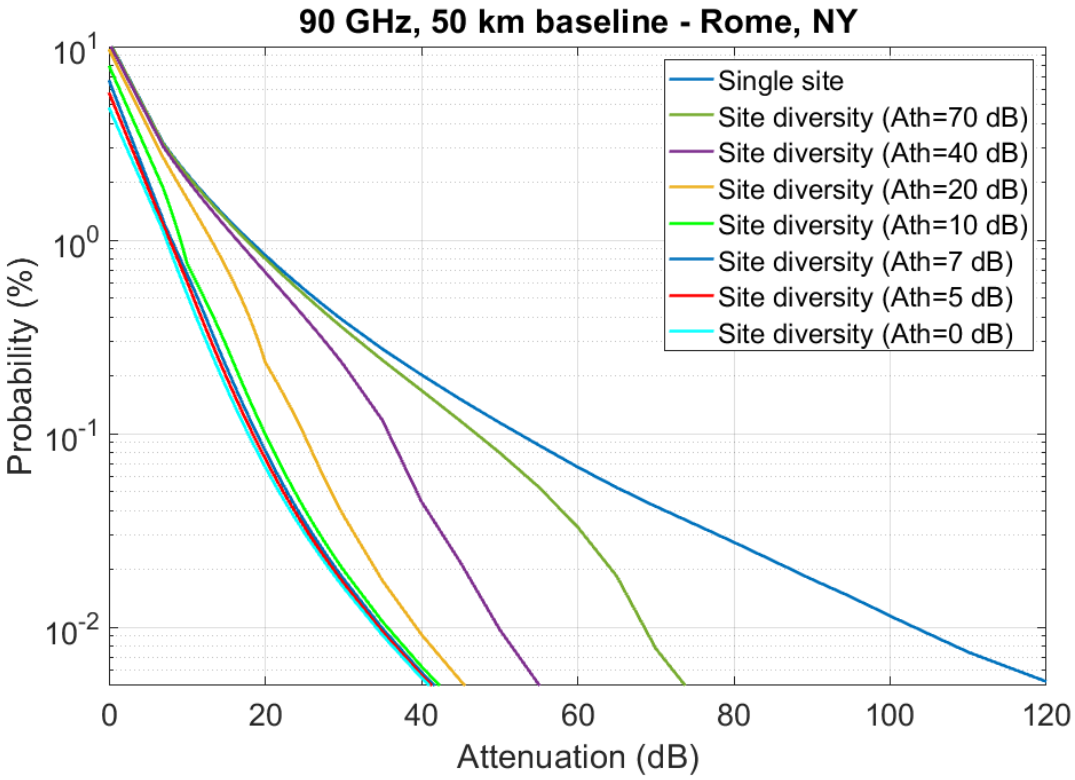

Fig. 4-39. Rain attenuation statistics at 90 GHz for Rome, NY, obtained from ST MultiEXCELL maps: single site (blue line) and two-site system (several values of A_{th} for fixed baseline of 50 km).

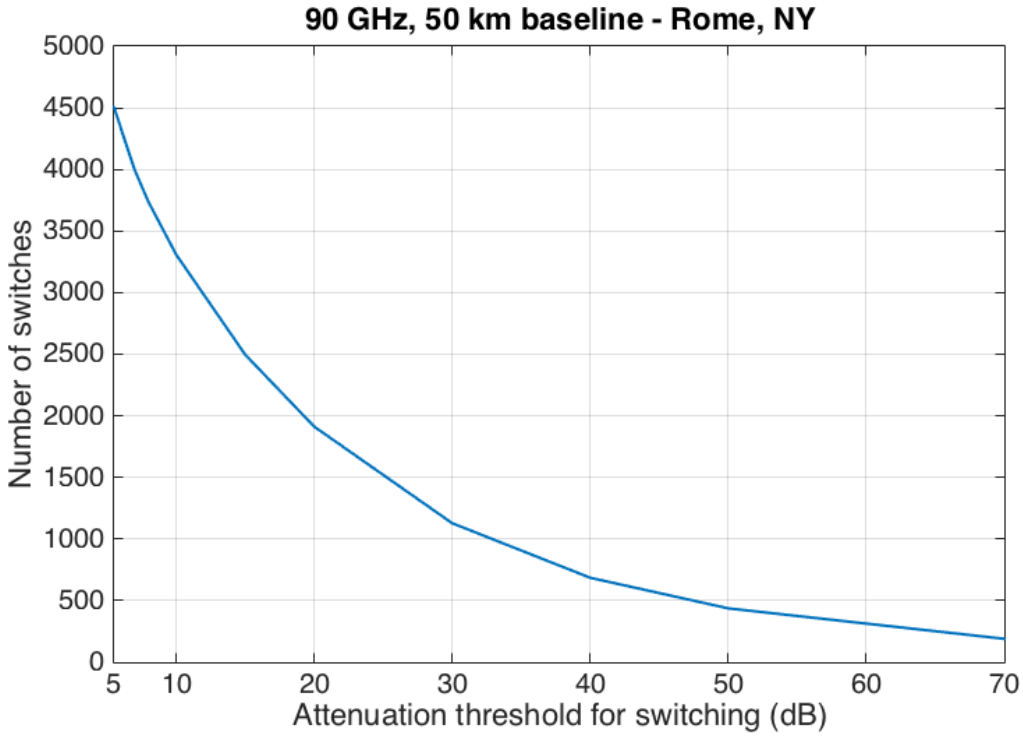

Fig. 4-40. Number of switches in a year between the stations as a function of the threshold A_{th} (90 GHz, 50 km baseline in Rome, NY).

DISTRIBUTION A: Distribution approved for public release. Distribution unlimited

The results indicate that a good tradeoff for the choice of A_{th} is 10 dB, which allows to reduce the number of switches to 2000-4000 – depending on the frequency and baseline distance – with a maximum gain loss of 1.3 dB at P = 0.01% if compared to the "perfect" case. Considering the 20 km-baseline and A_{th} = 10 dB, the attenuation with the two sites is 30.4 dB at 50 GHz, reaching 40, 43.15 and 45.4 dB respectively at 70, 80 and 90 GHz, again for P = 0.01 %. The associated yearly number of switches are 2125, 3010, 3350 and 3660, respectively. With the same threshold and same level of probability, for D = 50 km A_j ranges between 23.35 dB (50 GHz) and 35.6 dB (90 GHz), with the corresponding yearly number of switches between 2210 and 3310.

DISTRIBUTION A: Distribution approved for public release. Distribution unlimited

5. RAIN ATTENUATION FREQUENCY SCALING: DATA AND MODELS

5.1. Introduction

As pointed out in Chapter 2, tropospheric effects severely impair the propagation of centimetric and millimetric electromagnetic waves. Clouds, gases (namely water vapor and oxygen) and hydrometeors are the main atmospheric components interacting with EM waves in the 1-1000 GHz range [Riva et al., 2014]. The impact of precipitation becomes relevant and predominant above 10 GHz, as the wavelength is comparable with the dimension of rain drops, which cause absorption and scattering of the electromagnetic energy [Crane, 1996].

As a consequence, the accurate prediction of the attenuation induced by rain remains an essential task in order to properly design reliable Earth-space links in satellite communication (SatCom) systems, as well as in Earth Observation (EO) and in Space Exploration (SE) missions. In fact, rain attenuation prediction is becoming more and more critical in the light of the increase in the carrier frequencies that all the systems mentioned above are gradually facing (shift from the Ka to the Q/V/W bands for SatCom systems [Rossi et al., 2014] and from the X to the Ka band for EO and SE missions [Biscarini et al., 2016]), which calls for the need of even more accurate and reliable prediction models. On the one hand, the optimum prediction method should rely on a sound physical basis to guarantee a high level of reliability, especially when applied to achieve predictions at frequencies for which no experimental measurements are yet available (e.g. W band [EOARD, 2013]); on the other hand, such model should not just provide statistical results, but also enable to predict time series of the rain attenuation A_{rain} for the design and operation of the necessary fade mitigation techniques, such as site diversity [Luini and Capsoni, 2013b], whose effectiveness is tightly linked to the dynamics of A_{rain} (e.g. fade slope and fade duration).

Some physically-based rain attenuation models exist in the literature, but they can be typically applied only on a statistical basis (e.g. [Capsoni et al., 2009a], [Bryant et al., 2001] and [Dissanayake et al., 1997] to cite a few); on the other hand, time series synthesizers, such as [Boulanger et al, 2013], generate time series of A_{rain}, but they are of stochastic nature, i.e. with a limited physical soundness, and, moreover, they require as input the statistics of A_{rain}.

Among the plethora of the available rain attenuation prediction models, the Synthetic Storm Technique (SST), firstly presented in [Drufuca, 1974] and extended in [Matricciani, 1996] to Earth-space links, emerges as a unique methodology combining the advantages of a sound physical-mathematical framework, of the applicability on a statistical basis and on an event basis, and of the need of limited inputs (time series of the rain rate). Notwithstanding this, the SST presents a limitation associated to how the effect of the melting layer is modeled, which is addressed in this contribution with the aim of improving the model's prediction accuracy. This goal is achieved also by providing more refined data as input to SST (rain height and storm translation velocity). The proposed methodology, henceforth referred to as Enhanced SST (E-SST), is tested against the propagation data collected by the NASA equipment installed at Politecnico di Milano during the whole of 2017 in the frame of the Alphasat Aldo Paraboni propagation experiment [Rossi et al., 2016]. To this aim, a new methodology to isolate the contribution of rain attenuation from the received beacon power is devised by relying on the combination of multiple ancillary instruments and data.

DISTRIBUTION A: Distribution approved for public release. Distribution unlimited

The remainder of this chapter is structured as follows. Section 5.2 describes the methodology to derive rain attenuation from the received beacon signals (two frequency bands). Section 5.3 introduces E-SST by highlighting its key features adopted to enhance the performance of SST. Section 5.4 deals with the presentation, discussion and evaluation of the results obtained from the use of E-SST, both when applied directly and when embedded into an even more accurate frequency scaling approach.

5.2. Experimental setup and data processing

The E-SST model is developed and tested using a full year (2017) of propagation data collected by the experimental equipment described in detail in Chapter 3. The achieved results originate from the combination of the data collected by all the sensors and instruments available on the site, as explained hereinafter below.

5.2.1. Processing of disdrometer data

One of the paramount objectives of electromagnetic wave propagation experiments is to measure the attenuation due to rain, which can be extracted from the received beacon signal, once rain events are identified: to this aim, disdrometer data are key. As a first step, such data are combined to calculate the Drop Size Distribution (DSD) $N(D)$, which indicates the number of rain drops with given diameter D per m^3 [Luini et al., 2018b]:

$$N(D_i) = \frac{10^6 n_i}{S\, v(D_i) T \Delta D_i} \qquad (mm^{-1}m^{-3}) \tag{5-1}$$

In (5-1), n_i is the number of raindrops whose diameter falls in the i-th class (with mean diameter D_i), ΔD_i (mm) represents the width of each drop-size class, S (mm^2) is the disdrometer sampling area, T (seconds) is the instrument integration time, $v(D_i)$ (m/s) is the rain drop falling velocity. The rain rate R (mm/h) is then derived from the DSD as:

$$R = 600 \cdot 10^{-6} \pi \sum_{i=1}^{N} N(D_i) D_i^3 v(D_i) dD_i \tag{5-2}$$

5.2.2. Vertical atmospheric profiles

The vertical atmospheric profiles retrieved from the ERA5 database (0.28125°×0.28125° horizontal resolution, 137 vertical levels, data available every hour, latest reanalysis from ECMWF − European Centre for Medium-range Weather Forecast) are processed to extract the 0 °C isotherm height (h_0) and the wind speed associated to the 700-mbar isobar height (v): in fact, the former is typically considered as a good estimate of the rain height (especially during stratiform events) [Capsoni et al., 2009a], while the latter was proven to be well correlated to the precipitation translation velocity [Luini et al., 2011b]. Both h_0 and v represent key input information for E-SST. The information on the vertical structure of the atmosphere is completed by the radiosonde observations (RAOBS) data collected at Milano Linate Airport, 5 km from the experimental site (two launches per day).

5.2.3. Processing of beacon data to extract rain attenuation

Isolating the contribution of rain from the total attenuation induced by the atmosphere is not a trivial task.

The typical well-established approach to derive rain attenuation from the received beacon power P is to first low-pass filter P to remove scintillations with typical cut-off frequency of

0.03 Hz. Afterwards, rain events are identified, usually both by taking advantage of the local rain sensors (if present) and by inspecting the trend of *P*; finally, the rain attenuation A_{rain} is calculated by subtracting from *P* the power level that is the linear interpolation of *P* just before the beginning and the end of each event [Boulanger et al., 2019].

Though simple, this approach does not actually isolate A_{rain}, but rather the so called "excess attenuation", i.e. a combination of the attenuation due to rain and clouds; as a matter of fact, the cloud attenuation A_{cloud} is expected to increase during rain events, and this cannot be taken into account by the procedure mentioned above, which, in fact, limits A_{rain} to the values observed before and after the rain event, due to the interpolation procedure mentioned above. As the attenuation due to clouds becomes more and more relevant with frequency increasing from the Ku/Ka bands to Q/V bands, an alternative more accurate approach to separate rain attenuation and cloud attenuation is proposed hereinafter.

As a first step, the total atmospheric attenuation A_t is derived from the received beacon power *P* by taking advantage of the collocated microwave radiometer (MWR), which allows estimating, with very high accuracy, the total tropospheric attenuation in non-rainy conditions A^{MWR}, starting from brightness temperature data T_B collected at (at least) two channels. The full procedure to derive A_t from *P*, which is well established and has been employed in several propagation experiments (e.g. [Boulanger et al., 2015]) when radiometric data are available, is duly detailed in [Luini et al., 2018a].

The first step to derive rain attenuation is to remove scintillations from the total attenuation by low-pass filtering A_t, as already mentioned above. The next step is to subtract from A_t the contribution of atmospheric gases, i.e. oxygen and water vapour. To this aim, radiometric measurements can again be used. More specifically, the gaseous attenuation A_G^{MWR} is calculated by removing the cloud attenuation A_{cloud}^{MWR} from the MWR-derived total tropospheric attenuation A^{MWR}:

$$A_G^{MWR} = A^{MWR} - A_{cloud}^{MWR} = A^{MWR} - a_L L \tag{5-3}$$

Equation (5-3) indicates that the cloud attenuation is calculated by using the liquid water mass absorption coefficient $a_L(f)$ and the liquid water content integrated along the path *L*; the former is extracted from Recommendation ITU-R P.840-8 (equation (14) in [ITU-R P.840-8]), which provides a_L (19.7 GHz) = 0.391 dB/mm and a_L (39.4 GHz) = 1.338 dB/mm, while the latter is retrieved again from the radiometric measurements using the well-established simple linear inversion model reported in [Luini et al., 2007]. It is worth stressing that, as radiometric retrievals of *L* are reliable only in scatter-free conditions [Luini et al., 2007], during rain events, the value of A_G^{MWR} is interpolated between the beginning and the end of the event: this step is not expected to introduce a significant error because, differently from the attenuation due to clouds, A_G^{MWR} is likely to remain quite stable during rain events.

Taking advantage of A_G^{MWR}, the attenuation due to rain plus clouds A_{rc} is calculated as:

$$A_{rc} = A_t - A_G^{MWR} \tag{5-4}$$

As a final step, the cloud attenuation A_{cloud} and the rain attenuation A_{rain} are obtained as:

$$A_{cloud} = \begin{cases} R_{RC} A_{rc} & A_{rc} \le A_{rc}^{max} \\ A_{cloud}^{max} & A_{rc} > A_{rc}^{max} \end{cases} \quad (5\text{-}5)$$

$$A_{rain} = A_{rc} - A_{cloud} \quad (5\text{-}6)$$

where:

$$R_{RC} = a \exp(-b\, A_{rc}) + (1 - a)\exp(-c\, A_{rc}) \quad (5\text{-}7)$$

Fig. 5-1 shows the trend of R_{RC} for both frequencies, while Table 5-1 lists the coefficients *a*, *b*, *c*, and the values of A_{cloud}^{max} and A_{rc}^{max} in (5-5).

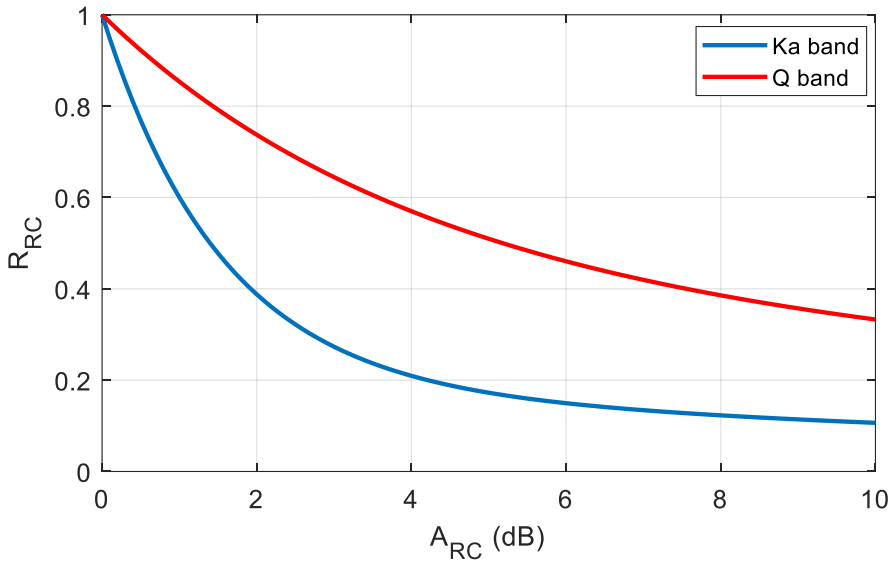

Fig. 5-1. Trend of R_{RC} as a function of A_{rc} for both frequencies.

Table 5-1. Coefficients in (5-7) and values in (5-5).

	a	b	c	A_{cloud}^{max}	A_{rc}^{max}
Ka band	0.8089	0.6552	0.05958	1.1 dB	11 dB
Q band	0.5689	0.2589	0.03963	3.85 dB	16.9 dB

As shown in Fig. 5-1, R_{RC} has a monotonic decreasing trend: in fact, at the very start of the rain event, i.e. when the link is about to enter into a rain cell, the attenuation will reasonably be induced only by clouds (R_{RC} = 1 and A_{rain} = 0); as the rain event translates more on the link, R_{RC} is expected to decrease (i.e. A_{rain} to increase) quickly, as most of the attenuation will be due to rain. The trend of R_{RC}, as well as the coefficients *a*, *b* and *c*, were derived by optimizing the agreement between the complementary cumulative distribution function (CCDF) of A_{cloud} as obtained from (5-5) using the full year of beacon-derived attenuation data A_t and as estimated from 10 years of the RAOBS mentioned in Section 5.2.2. Specifically, as performed in [Luini et al., 2007], vertical profiles of *P-RH-T* obtained from RAOBS were used first to derive the liquid water content by means of the TKK cloud detection algorithm [Salonen and Uppala, 1991], and, afterwards, to calculate the cloud attenuation through the Liebe MPM93 mass

absorption model [Liebe et al., 1993]. At the same time, as shown in (5-5), R_{RC} is used up to A_{rc}^{max}, which reflects the maximum value of cloud attenuation that can be obtained in the site A_{cloud}^{max} (1.1 dB and 3.8 dB, for the Ka band and Q band, respectively, as shown in Table 5-1), again calculated from RAOBS data.

Fig. 5-2 compares the CCDFs of A_{cloud} (Q band), while Fig. 5-3 shows an example of the separate contributions to total attenuation (gases, clouds, and rain), obtained using the procedure outlined above (Q band, 4th of February 2017).

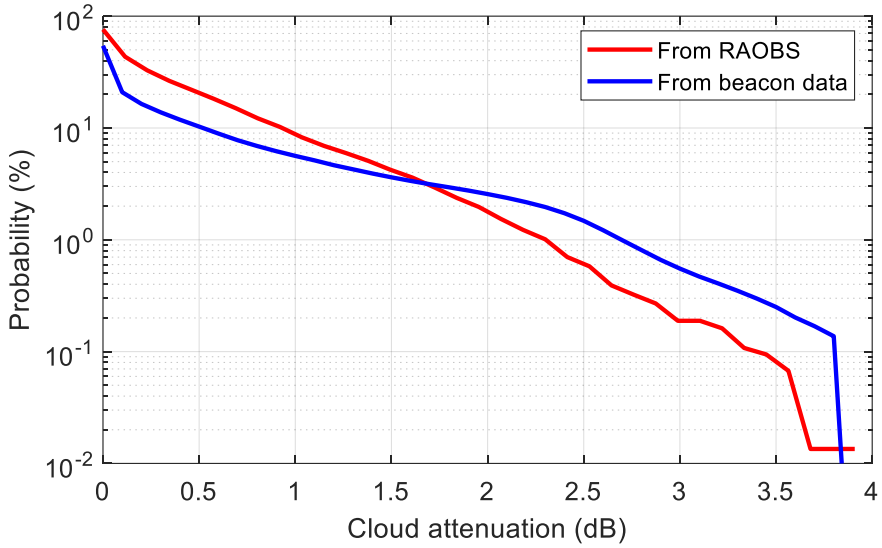

Fig. 5-2. CCDFs of the cloud attenuation obtained from RAOBS data (10 full years) and from the beacon data (one full year) by using equation (5-5) at Q band.

As is clear from the discussion above, the proposed procedure to isolate rain attenuation from the received power is more complex (but also more accurate) than the customary approach (it requires ancillary instruments, such as a MWR, and data, such as vertical atmospheric profiles) and it needs to be tailored to the available beacon data (e.g. the link frequency). Nevertheless, besides being key to properly derive the rain attenuation used in Section 5.4 as the reference to assess the accuracy of E-SST, the proposed procedure represents a novel approach to separate the different sources of tropospheric attenuation starting from beacon data; indeed, this task becomes more and more critical as the frequency raises due to the increasingly higher contribution of clouds.

DISTRIBUTION A: Distribution approved for public release. Distribution unlimited

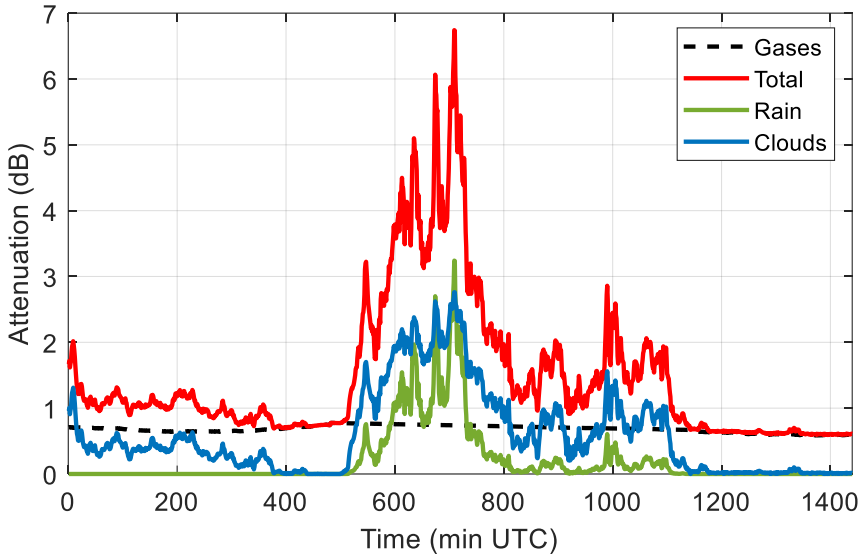

Fig. 5-3. Separation of the attenuation contributions due to gases, clouds and rain for a sample day (4th of February 2017) at Q band.

5.3. The Enhanced Synthetic Storm Technique (E-SST)

Firstly introduced in [Drufuca, 1974], the Synthetic Storm Technique (SST) is a methodology to synthesize rain attenuation time series (on terrestrial links) from local rain rate observations, which relies on the frozen storm hypothesis put forth in [Taylor, 1938]. The same concept was successfully extended to Earth-space links by Matricciani in [Matricciani, 1996] by modelling the vertical structure of precipitation with two layers (see the top side of Fig. 5-4): the first one (layer *A*, extending from the ground up to h_A) accounts for the attenuation induced by rain (whose intensity is R_A), while the second one (layer *B*, extending from h_A to $h_B = h_A + 0.4$ km) takes into account the impact of the melting layer, which is associated to the effective rain rate $R_B = 3.134\ R_A$. By virtue of the frozen storm hypothesis and by assuming a constant precipitation translation speed *v* [Taylor, 1938], the time *t* can be easily turned into the distance $d = v\ t$. Thus, making reference to Fig. 5-4, the rain attenuation A_{rain} at a given instant t_0 can be numerically calculated as:

$$A_{rain}(t_0) = \frac{1}{\cos(\theta)}\left[\int_{d_0}^{d_0+S_A} k_A R(l)^{\alpha_A}\, dl + \int_{d_0+S_A}^{d_0+S_A+S_B} k_B 3.134^{\alpha_B} R(l)^{\alpha_B}\, dl\right] \qquad (5\text{-}8)$$

In (5-8), θ is the link elevation angle, *k* and α are the power-law coefficients turning the rain rate into specific attenuation, which might differ for layers *A* and *B*, e.g. because of the different hydrometeor temperature and size. Finally *R* is the rain rate along the link, whose values are extracted from the rain intensity time series (after the conversion from time to space, $d = v\ t$) according to the geometry depicted in Fig. 5-4 (bottom side). The figure also clarifies how the same calculation is performed for different points in time (see t_0 and t_n).

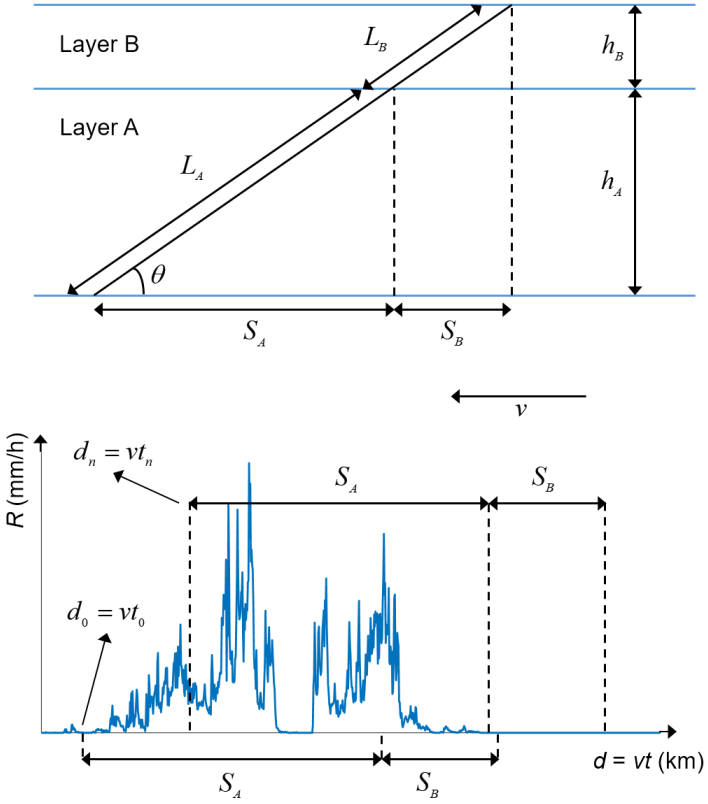

Fig. 5-4. Reference outline for the application of the SST: geometry of the link and of the vertical structure of precipitation (top side) and identification of the rain rate values for the calculation of A_{rain} (bottom side).

The SST has been widely used and tested, and represents a valuable tool to obtain rain attenuation time series from rain rate observations. However, the model presents a main shortcoming, which this contribution aims at overcoming. In fact, a limitation in the accuracy of the SST lies in layer *B*, which is intended to model the contribution to attenuation due to the melting layer [Matricciani, 1996]: as a matter of fact, a well-defined melting layer appears only in association to stratiform events, as the strong updrafts and downdrafts occurring during convective events create a mixture of ice, liquid water and melting particles. This point has been addressed in [Capsoni et al., 2006] by proposing an algorithm to discriminate between convective and stratiform events (based on whether the peak rain rate during the event exceeds 10 mm/h or not, respectively), which, in turn, allows not only including the effects of the melting layer only during the former type of events, but also employing different stratiform and convective rain heights [Capsoni et al., 2009a].

The SST prediction accuracy can be further improved by using as input, when available, "instantaneous" values of the rain height h_0 and of the wind speed v. The following list summarizes the key features introduced into the E-SST:

1. Starting from the rain rate time series, every event is classified as convective (stratiform) if its peak rain intensity exceeds (does not exceed) 10 mm/h [Capsoni et al., 2006]. Events are separated by dry periods lasting at least 1 hour.
2. Differently from the SST, the melting layer attenuation is taken into account only during stratiform events and in an equivalent way; in fact, a single layer is considered: the specific rain attenuation is calculated using the k and α coefficients

(see (5-8)) from Recommendation ITU-R P.838-3 [ITU-R P.838-3] and the equivalent rain height is calculated by adding 0.36 km to h_0, as suggested in Recommendation ITU-R P.839-4 [ITU-R P.839-4]. This choice is aimed at both simplifying and updating the model by relying on the most recent coefficients recommended by ITU-R to estimate the specific attenuation due to rain.

As a result, the equivalent rain height for stratiform events is:

$$H_S = h_0 + 0.36 \qquad \text{(km)} \tag{5-9}$$

while the equivalent rain height for convective events is:

$$H_C = h_0 \qquad \text{(km)} \tag{5-10}$$

Both in (5-9) and (5-10), h_0 is the 0 °C isotherm height derived from ERA5 vertical profiles of temperature. For each sample in the rain event time series, h_0 is obtained as the linear interpolation between the two closest ERA5 profiles.

3. Similarly to point 2, the precipitation translation velocity v is derived from ERA5 vertical profiles, specifically by selecting the wind speed associated to the 700-mbar isobar height [Luini et al., 2011b].

5.4. Results and discussion

This Section deals with the validation of the E-SST, whose results are compared with those obtained from the SST and against the reference experimental data collected in Milan in the framework of the Alphasat Aldo Paraboni propagation experiment. More specifically, first the E-SST is applied for the direct prediction of rain attenuation time series starting from rain rate data. Afterwards, the model is embedded into a more accurate frequency scaling technique. To the aim of testing the accuracy of the E-SST, we have used a full year of propagation data (2017) collected by the NASA experimental equipment installed at Politecnico di Milano, as described in Chapter 3.

5.4.1. Rain attenuation prediction: direct application of the E-SST

Similarly to what is proposed in [Matricciani, 1996], the most straightforward application of the E-SST consists in the prediction of rain attenuation time series starting from the 1-minute sampled rain rate data using (5-8) and the rain heights in (5-9) and (5-10).

The top side of Fig. 5-5 shows the results obtained for a stratiform event (peak rain rate $R <$ 10 mm/h) occurred on the 3rd of February 2017; the blue line represents the rain attenuation derived from the beacon measurement at 39.4 GHz, while the other curves indicate the predictions delivered by the SST (red dashed line) and the E-SST (dash-dotted green line). The bottom side of the figure reports the concurrent rain rate measured by the disdrometer.

DISTRIBUTION A: Distribution approved for public release. Distribution unlimited

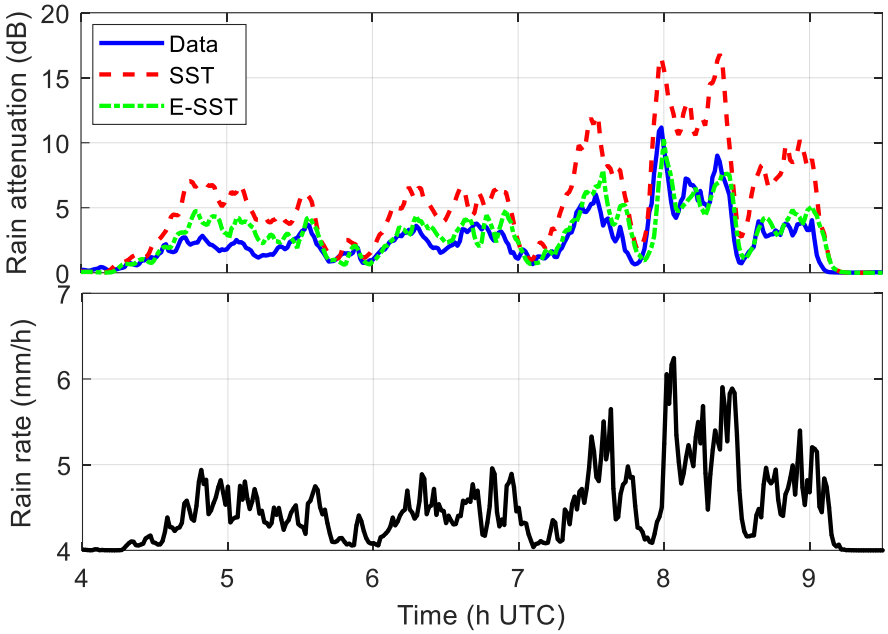

Fig. 5-5. Direct application of the SST and the E-SST to a stratiform rain event on the 3rd of February 2017 (peak rain rate R *< 10 mm/h), at Q band.*

Results indicate a higher prediction accuracy of E-SST compared to SST, which mainly results from using more precise input information. In fact, as input to the SST we have used the yearly mean value of the wind speed, $\overline{v} = 7.2$ m/s, and the yearly mean value of the 0 °C isotherm height, $\overline{h}_A = \overline{h}_0 = 3.061$ km (i.e. $\overline{h}_B = 3.461$ km), both derived from the ERA5 profiles of the whole of 2017; on the other hand, as input to E-SST, we have used the daily ERA5 values associated to the profiles ranging from 4 to 9 UTC, with v and h_0 in the 8.56-9.54 m/s range, and in the 1.783-1.845 km interval, respectively.

Another sample rain event is shown in Fig. 5-6, which depicts the outcomes of the application of the SST and the E-SST for a shorter but more intense convective event occurred on the 5th of May 2017 (Ka-band data). As is clear from Fig. 5-6, the E-SST provides significantly more accurate results than the SST: the large discrepancy between the two models is due both to the difference in the input rain height and storm velocity (in this case, during the event, h_0 ranges between 2.702 km and 2.841 km, while v varies in the 1.04-2.52 m/s range), but also to the inclusion of the melting layer effect in the SST, which is very unlikely during convective events. It is also worth noticing that, in this case, the predicted attenuation peaks appear a bit "delayed" with respect to those shown in the attenuation data likely due to the simplifying assumptions used in both models: for instance, the frozen storm hypothesis [Taylor, 1938] (which might be more questionable for very turbulent convective events) and the fact that the rain event is inherently assumed to reach the receiver along the direction of the link.

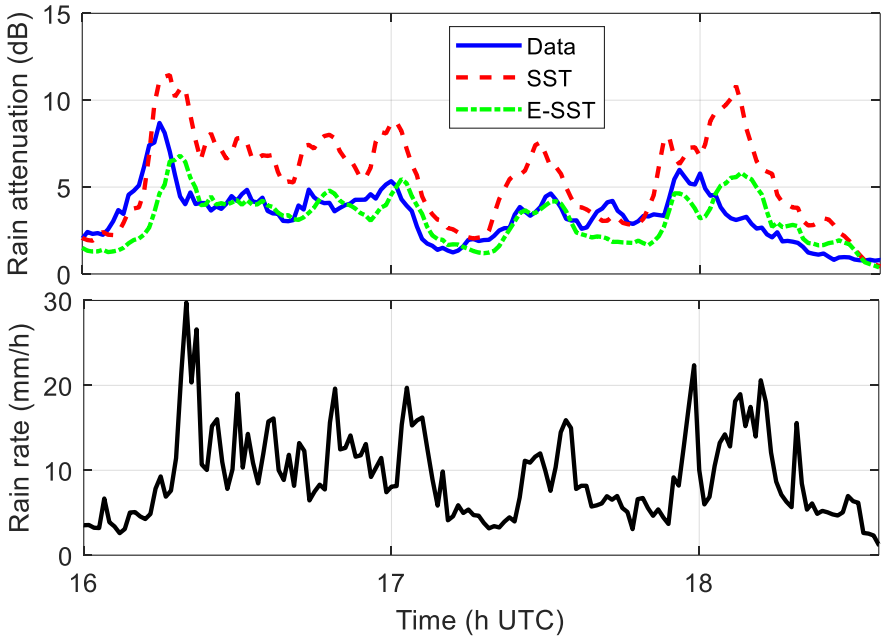

Fig. 5-6. Direct application of the SST and the E-SST: convective rain event on the 5th of May 2017 (peak rain rate R > 10 mm/h), Ka band data.

A more comprehensive picture of the models' prediction accuracy is given in Fig. 5-7 and Fig. 5-8, which show the complementary cumulative distribution functions (CCDFs) of rain attenuation including all events in 2017 (Ka band and Q band, respectively). The models' performance is quantified by using the following ITU-R-defined error figure [ITU-R P.311-14]:

$$\varepsilon(P) = \begin{cases} 100 \cdot \left(\frac{A_R(P)}{10}\right)^{0.2} \ln\left(\frac{A_P(P)}{A_R(P)}\right) & A_R(P) < 10 \text{ dB} \\ 100 \cdot \ln\left(\frac{A_P(P)}{A_R(P)}\right) & A_R(P) \geq 10 \text{ dB} \end{cases} \quad (5\text{-}11)$$

In (5-11), $A_R(P)$ and $A_P(P)$ represent rain attenuation, both correspondent to probability level P, extracted respectively from the reference (measured data) and the estimated (model) CCDFs. Table 5-2 lists the average (E) and root mean square (RMS) values of $\varepsilon(P)$ for both models: the results confirm the increase in accuracy of the E-SST.

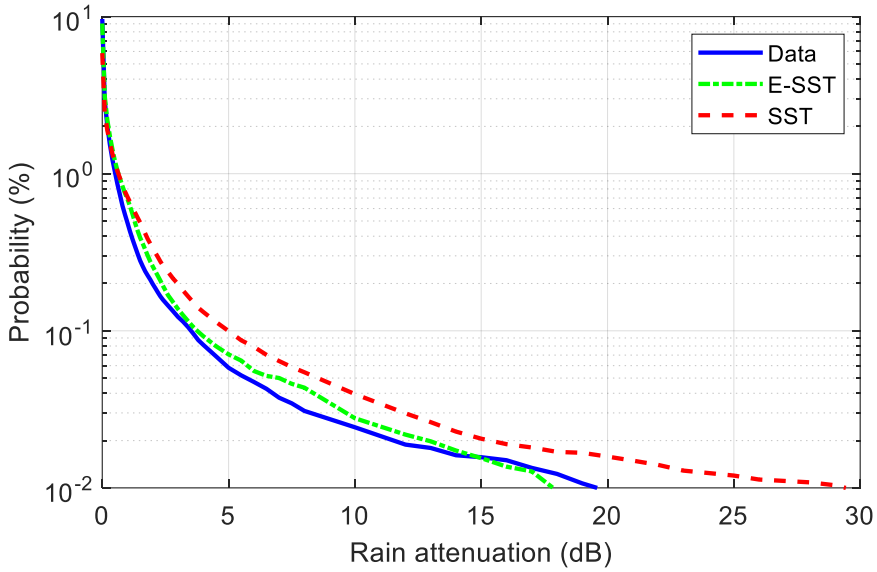

Fig. 5-7. Direct application of the SST and the E-SST at Ka band, whole year statistics.

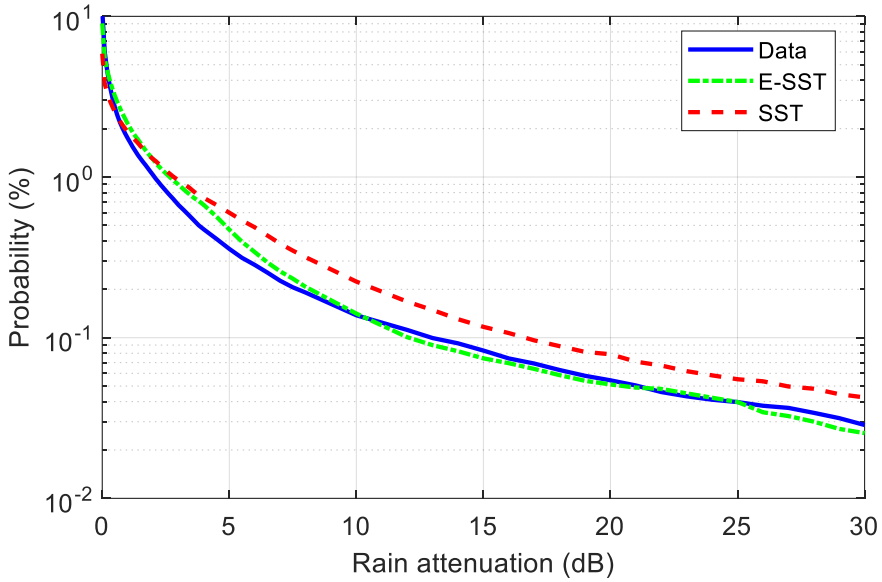

Fig. 5-8. Direct application of the SST and the E-SST at Q band, whole year statistics.

Table 5-2. Overall prediction accuracy of the SST and the E-SST (direct application): rain attenuation CCDFs (2017), both bands.

	E (%)		RMS (%)	
	Ka band	**Q band**	**Ka band**	**Q band**
SST	21.95	20.45	24.78	22.66
E-SST	4.65	2.85	8.14	5.2

5.4.2. Rain attenuation prediction: frequency scaling based on the E-SST

When measurements of rain attenuation A_{rain} along a link at frequency f_{DOWN} are available in a site, frequency scaling represents a simple yet accurate approach to predict A_{rain} along the same link, but at a different frequency f_{UP}. This is achieved by means of the frequency scaling

ratio R_{FS}:

$$A_{rain}{}^{(f_{UP})} = R_{FS}\, A_{rain}{}^{(f_{DOWN})} \tag{5-12}$$

The accuracy of frequency scaling techniques is generally higher than the one of prediction models, as rain attenuation measurements embed key information on the rain event (e.g. spatial distribution of the rain rate, both horizontally and vertically). Moreover, when the dynamics of rain attenuation are of interest, e.g. for the investigation of fade slope and fade duration (both of which are important, for example, to properly design site diversity techniques) or for the real-time scenarios involving the application of up-link power control, frequency scaling will provide more realistic time series of the predicted rain attenuation than the application of any prediction model.

Empirical frequency scaling models exist in the literature. They are typically valid on a statistical basis and are of limited accuracy as they define a fixed value for R_{FS}, dependent only on f_{DOWN} and f_{UP}. In fact, on the contrary, R_{FS} usually changes significantly from event to event (even more, within the same event). This aspect can be duly taken into account by resorting to DSD data, on which the specific attenuation due to rain γ_{DSD} depends on [Luini et al., 2018b]:

$$\gamma_{DSD}(f) = 4.343 \cdot 10^3 \frac{\lambda^2}{\pi} \sum_{i=1}^{N} \mathrm{Re}[S_0(D_i, f)] N(D_i) \Delta D_i \tag{5-13}$$

In (5-13), $N = 22$ is the number of diameter classes measured by the disdrometer, while the forward scattering coefficient S_0 is calculated using the T-matrix approach [Mishchenko et al., 2002], assuming the axial ratio defined by Beard and Chuang in [Beard and Chuang, 1987]. As a result, the frequency scaling ratio R_{FS} is defined as:

$$R_{FS}^{DSD}(t_0) = \frac{\gamma_{DSD}(t_0, f_{UP})}{\gamma_{DSD}(t_0, f_{DOWN})} \tag{5-14}$$

Though this approach offers a very good frequency scaling accuracy [Nessel et al., 2015], the availability of DSD data is usually quite rare. As an alternative, the frequency scaling ratio R_{FS} can be defined by taking advantage of the E-SST:

$$R_{FS}^{E-SST}(t_0) = \frac{A_{rain}(t_0, f_{UP})}{A_{rain}(t_0, f_{DOWN})} \tag{5-15}$$

where both $A_{rain}(t_0, f_{UP})$ and $A_{rain}(t_0, f_{DOWN})$ are calculated according to the mathematical framework of the E-SST.

Fig. 5-9 and Fig. 5-10 show the variability of the frequency scaling ratio for the two events reported in Fig. 5-5 and Fig. 5-6, respectively, both as derived from the E-SST and from DSD data. Moreover, as a term of comparison, also included in Fig. 5-9 and Fig. 5-10 is the frequency scaling ratio defined by the statistical model of Recommendation [ITU-R P.618-13] (blue solid line), for which R_{FS} marginally depends also on A_{rain} (f_{DOWN}), besides on f_{DOWN} and f_{UP}.

As is clear from Fig. 5-9 and Fig. 5-10, R_{FS}^{DSD} is highly variable even within the same event: while R_{FS}^{E-SST} tends to follow the same trend as R_{FS}^{DSD}, the frequency scaling ratio defined by the ITU-R is much more stable and thus unable to provide an accurate frequency scaling.

DISTRIBUTION A: Distribution approved for public release. Distribution unlimited

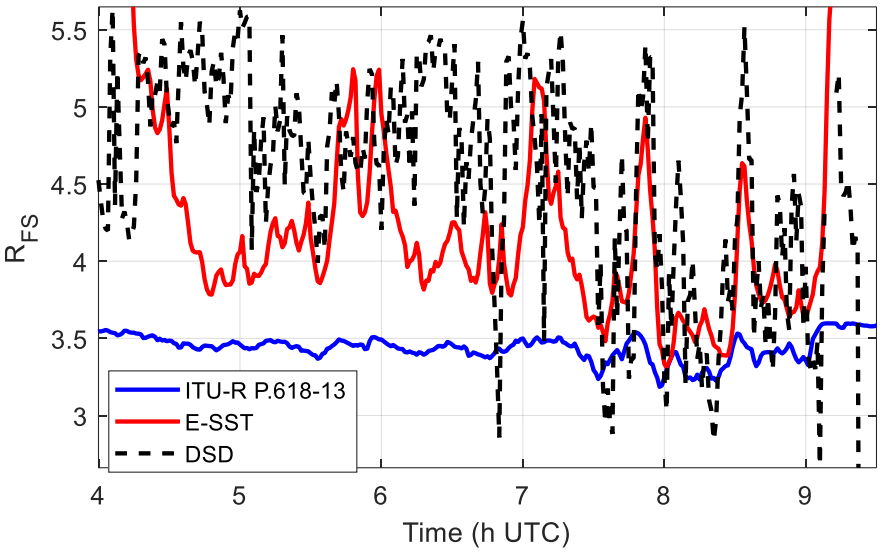

Fig. 5-9. Frequency scaling ratio R_{FS} for the same stratiform event in Fig. 5-5 as calculated using the E-SST model and DSD data, as well as derived from the model included in Recommendation ITU-R P.618-13.

Fig. 5-11 and Fig. 5-12 show the time series obtained by scaling the attenuation measured at 19.7 GHz to 39.4 GHz, using the E-SST and DSD data. As expected, results indicate that both methods provide a further prediction improvement achieved by using the frequency scaling approach, if compared to the direct application of the E-SST. More importantly, results show that an accurate frequency scaling can be obtained even by just using the E-SST, i.e. without the need of DSD data, which, as already mentioned, are seldom available and are used in this work as the reference upper limit of the prediction accuracy using frequency scaling techniques.

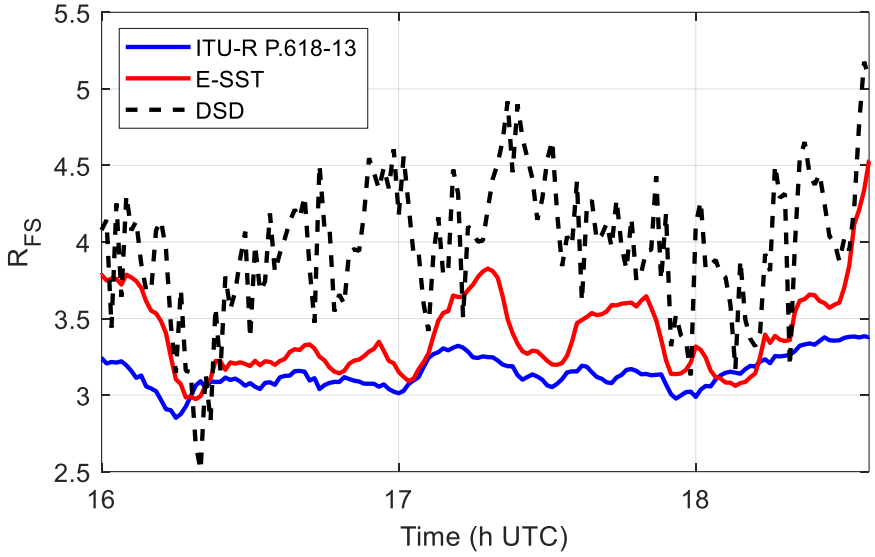

Fig. 5-10. Frequency scaling ratio R_{FS} for the same convective event in Fig. 5-6 as calculated using the E-SST model and DSD data, as well as derived from the model included in Recommendation ITU-R P.618-13.

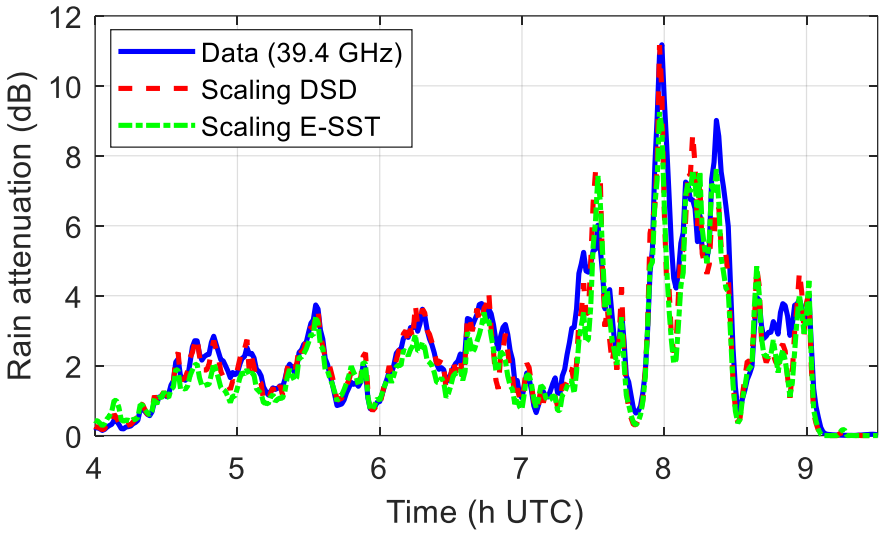

Fig. 5-11. Scaling of the attenuation measured at 19.7 GHz to 39.4 GHz for the stratiform rain event on the 3rd of February 2017 (peak rain rate R < *10 mm/h) in Fig. 5-5.*

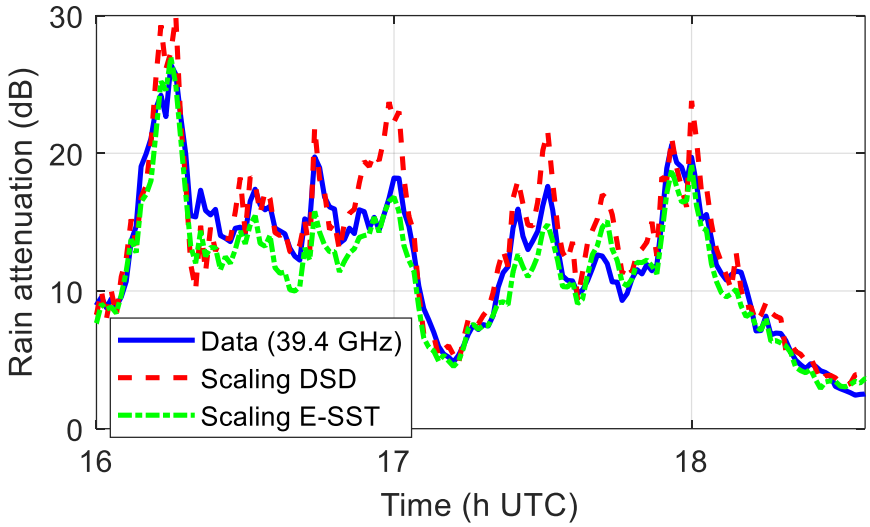

Fig. 5-12. Scaling of the attenuation measured at 19.7 GHz to 39.4 GHz for the convective rain event on the 5th of May 2017 (peak rain rate R > 10 mm/h) in Fig. 5-6.

In line with the results reported in Fig. 5-11 and Fig. 5-12, as expected, the frequency scaling approach offers an overall enhancement in the prediction of the CCDF of A_{rain}(39.4 GHz): the bias improves and the RMS of the error figure in (5-11), reported in Table 5-3, lowers to 4.8% and 3.9%, using the E-SST and DSD data, respectively (values to be compared with the results listed in Table 5-2).

DISTRIBUTION A: Distribution approved for public release. Distribution unlimited

Table 5-3. Overall prediction accuracy using the frequency scaling approach: rain attenuation CCDFs (2017), Q Band.

	E (%)	RMS (%)
	Q band	Q band
E-SST (frequency scaling)	-3.5	4.83
DSD (frequency scaling)	1.5	3.89

Even more marked is the decrease in the prediction error on the time series of the attenuation, which is quantified by using E and RMS of the absolute error figure between the predictions and the measurements in (5-16).

$$\emptyset(t) = A_P(t) - A_R(t) \tag{5-16}$$

Results, reported in Table 5-4, confirm the improvement associated to the frequency scaling approach using the E-SST, if compared to the direct application of the model. Included in the table is also the performance of the reference frequency scaling technique relying on DSD data.

Table 5-4. Overall prediction accuracy of the E-SST (both direct application and frequency scaling approach) on rain attenuation time series (2017), Q band. Included is also the performance of the reference frequency scaling using DSD data.

	E (dB)	RMS (dB)
E-SST (direct application)	-0.11	2.99
E-SST (frequency scaling)	-0.05	1.77
DSD (frequency scaling)	-0.05	1.72

DISTRIBUTION A: Distribution approved for public release. Distribution unlimited

6. TOTAL ATTENUATION FREQUENCY SCALING: FROM KA BAND TO W BAND

6.1. Introduction

Besides rain attenuation, also the other tropospheric constituents have a significant impact at higher frequencies such as in the Q/V and W bands. This Chapter presents two models aiming to predict the total tropospheric attenuation at frequency bands for which no experimental data are currently available (e.g. W band).

The models rely on frequency scaling to predict the attenuation at a higher frequency starting from the time series of the tropospheric attenuation measured at a lower frequency. To this aim, the models embed methodologies to first separate the impact of each atmospheric constituents contributing to the total tropospheric attenuation (one of which is included in Chapter 5); afterwards, the attenuation due to each constituent is scaled separately. Both models require as input the tropospheric attenuation time series at the lower frequency (e.g. Ka band), as well as ancillary meteorological information collected at the receiver site. The first model, more complex and accurate, requires additional inputs such as radiometric measurements, instantaneous information on the DSD, the vertical profiles of the wind speed, temperature and pressure. The second model, of easier implementation and showing a slight decrease in the prediction accuracy, relies on fewer inputs and consists of simplified procedures.

Similarly to what is done in Chapter 5, the models are tested against the data collected at Politecnico di Milano within the Alphasat Aldo Paraboni Propagation experiment, both in terms of first-order statistics (i.e. complementary cumulative distribution function) and in terms of time series. Finally, both models are applied to predict the time series of total tropospheric attenuation at frequencies in the W band, hence to evaluate the gain of a system implementing time diversity.

6.2. Frequency scaling of total tropospheric attenuation: model development

The frequency scaling model presented in this Section, hereinafter referred to as Total Attenuation Frequency Scaling (TAFS), relies on the same methodology already presented in Chapter 5 (see Section 5.2.3) to isolate the contributions to the total tropospheric attenuation at lower frequency f_{DOWN}, which are then separately scaled to a higher frequency f_{UP} by using different approaches, which are summarized in Fig. 6-1.

DISTRIBUTION A: Distribution approved for public release. Distribution unlimited

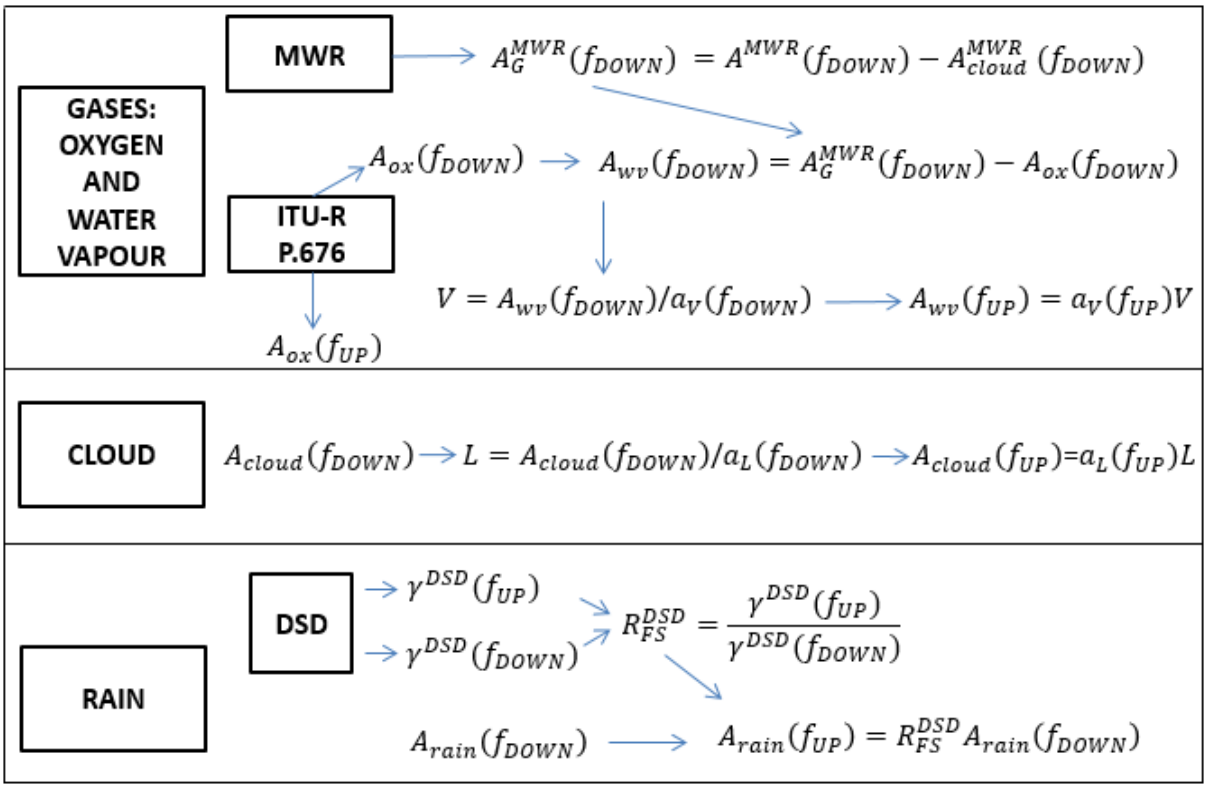

Fig. 6-1. Workflow of the the Total Attenuation Frequency Scaling (TAFS) model.

The step-by-step TAFS procedure first considers the contribution of gases, i.e. oxygen and water vapor in the 10-100 GHz frequency band [Nebuloni et al., 2017]. Specifically, oxygen attenuation is predicted directly by applying the approximate (yet accurate) model in Annex 2 of Recommendation [ITU-R P.676-12] at the desired frequencies (by using as input the ground measurements of temperature and pressure), thus obtaining $A_{ox}(f_{UP})$ and $A_{ox}(f_{DOWN})$. Afterwards, $A_{ox}(f_{DOWN})$ is subtracted from $A_G^{MWR}(f_{DOWN})$ (see Chapter 5 for the detailed explanation on how $A_G^{MWR}(f_{DOWN})$ is derived from radiometric data) to obtain the water vapor attenuation component at f_{DOWN}.

6.2.1. Water vapor attenuation

Water vapor attenuation is calculated as

$$A_{wv}(f_{UP}) = a_V(f_{UP})V \tag{6-1}$$

i.e. by employing the water vapor mass absorption coefficients $a_V(f_{UP})$. In (6-1), V is the integrated water vapor content along the slant path, which, as shown in Fig. 6-1, is derived from the water vapour attenuation at f_{DOWN} as $V = A_{wv}(f_{DOWN})/a_V(f_{DOWN})$.

Both water vapour mass absorption coefficients are calculated by means of ten years of RAOBS data collected at Milan/Linate airport (45.26° N; 9.17° E; 122-m a.m.s.l.), which are used as input to the Liebe MPM93 [Liebe et al., 1993] mass absorption model to calculate A_{wv}. The final step is to derive a_V as the slope of the line fitting the data on the V/A_{wv} plane. The overall procedure to calculate a_V is summarized in Fig. 6-2.

DISTRIBUTION A: Distribution approved for public release. Distribution unlimited

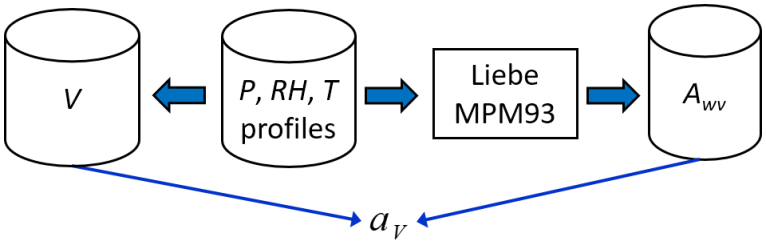

Fig. 6-2. Procedure to calculate a_V from RAOBS data.

The mass absorption coefficients for water vapor at Ka, Q and W bands are listed in Table 6-1.

Table 6-1. Water vapor mass absorption coefficient values at different frequencies.

Frequency	**Water vapor mass absorption coefficient a_V**
19.7 GHz	0.0119 dB/mm
39.4 GHz	0.0105 dB/mm
80 GHz	0.0366 dB/mm
90 GHz	0.0463 dB/mm

6.2.2. Cloud attenuation

The attenuation due to clouds is linearly proportional to the integrated liquid water content L, which, in TAFS, is obtained from A_{cloud} at the lower frequency f_{DOWN} (e.g. at Ka), divided by the liquid water mass absorption coefficient $a_L(f_{DOWN})$:

$$L = A_{cloud}(f_{DOWN})/a_L(f_{DOWN}) \quad (6\text{-}2)$$

The calculation of a_L is achieved exploiting again the RAOBS data, which, as a first step, are provided as input to the TKK model to identify clouds and quantify the liquid water content (hence L by vertical integration) [Salonen and Uppala, 1991]. The calculation procedure, which includes again a linear regression on the L/A_{cloud} plane, is described in detail in Fig. 6-3.

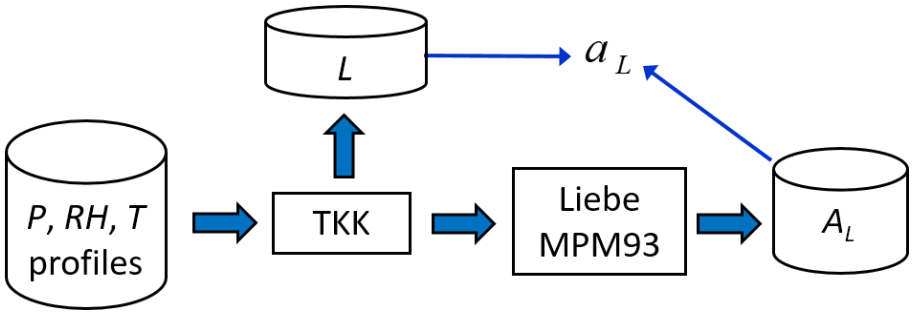

Fig. 6-3. Procedure to calculate a_L from RAOBS data.

The mass absorption coefficients a_L at Ka, Q and W band are listed in Table 6-2.

Table 6-2. Liquid mass absorption coefficient values at different frequencies.

Frequency	**Liquid water mass absorption coefficient a_L**
19.7 GHz	0.391 dB/mm
39.4 GHz	1.338 dB/mm
80 GHz	3.714 dB/mm
90 GHz	4.277 dB/mm

Using the coefficient at the desired frequency $a_L\ (f_{UP})$, the attenuation due to clouds is calculated as:

$$A_{cloud}(f_{UP}) = \ a_L(f_{UP})L \tag{6-3}$$

6.2.3. Rain attenuation

In TAFS, rain attenuation is scaled using the accurate microphysical information on the DSD, i.e. the instantaneous frequency scaling ratio R_{FS}^{DSD} defined in (5-16) of Section 5.4.2: indeed, based on the tests carried out in Chapter 5, this approach has proven to offer the best accuracy in scaling rain attenuation. As a result, rain attenuation at the higher frequency f_{UP} is calculated as:

$$A_{rain}(f_{UP}) = R_{FS}^{DSD} A_{rain}(f_{DOWN}) \tag{6-4}$$

6.2.4. Total attenuation

Finally, the total attenuation at frequency f_{UP} is calculated by simply summing up the time series of the different attenuation components:

$$A_t(f_{UP}) = A_{ox}(f_{UP}) + A_{wv}(f_{UP}) + A_{cloud}(f_{UP}) + \ A_{rain}(f_{UP}) \tag{6-5}$$

The application of TAFS to the stratiform event collected on the 4th of February 2017 is shown step by step below: the attenuation data are scaled from 19.7 GHz to 39.4 GHz. More specifically, the separation between the atmospheric components described in Chapter 5 is depicted in Fig. 6-4, the scaling for each component (i.e. water vapor, oxygen, cloud and rain) is reported in Fig. 6-5 to Fig. 6-8, while Fig. 6-9 presents the total attenuation.

DISTRIBUTION A: Distribution approved for public release. Distribution unlimited

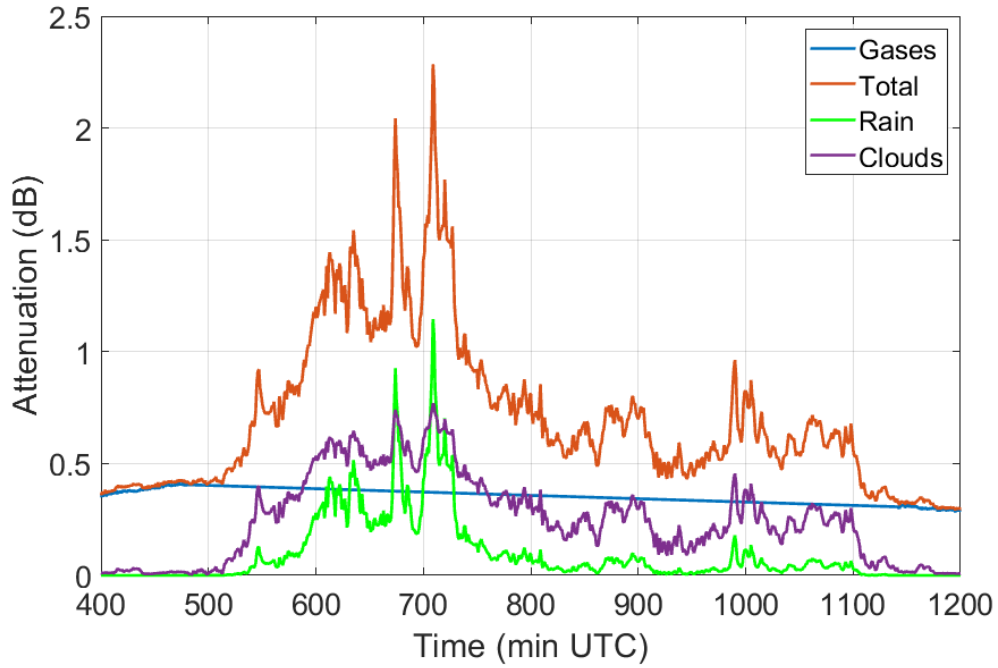

Fig. 6-4. Separation of the attenuation contributions due to gases, clouds and rain for the stratiform rain event collected on the 4th of February 2017 at Ka band.

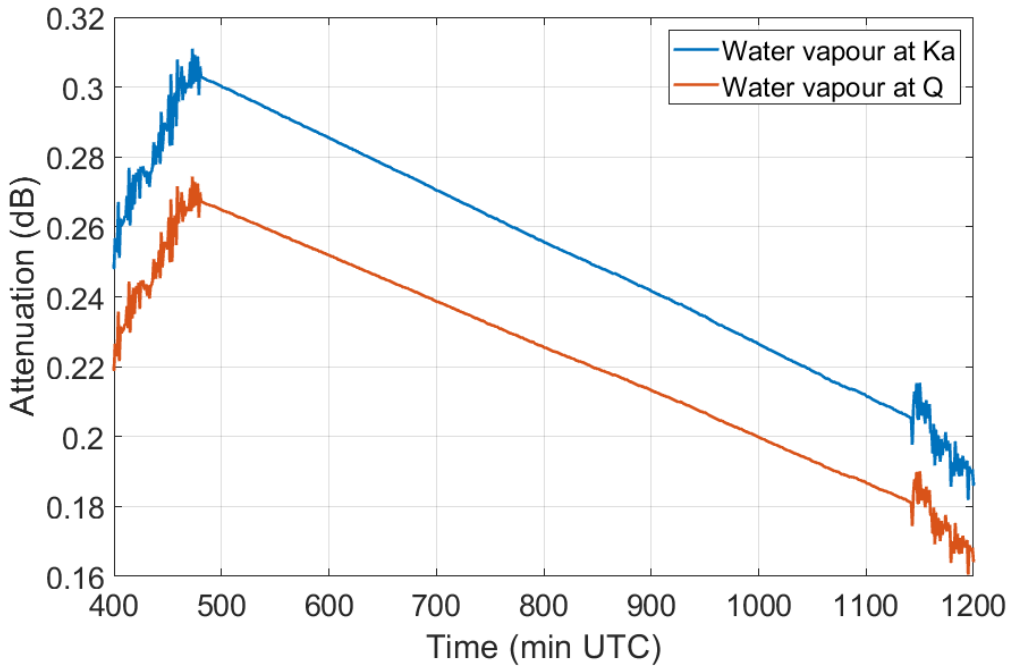

Fig. 6-5. Scaling of the water vapour attenuation for the stratiform rain event collected on the 4th of February 2017 from Ka to Q band.

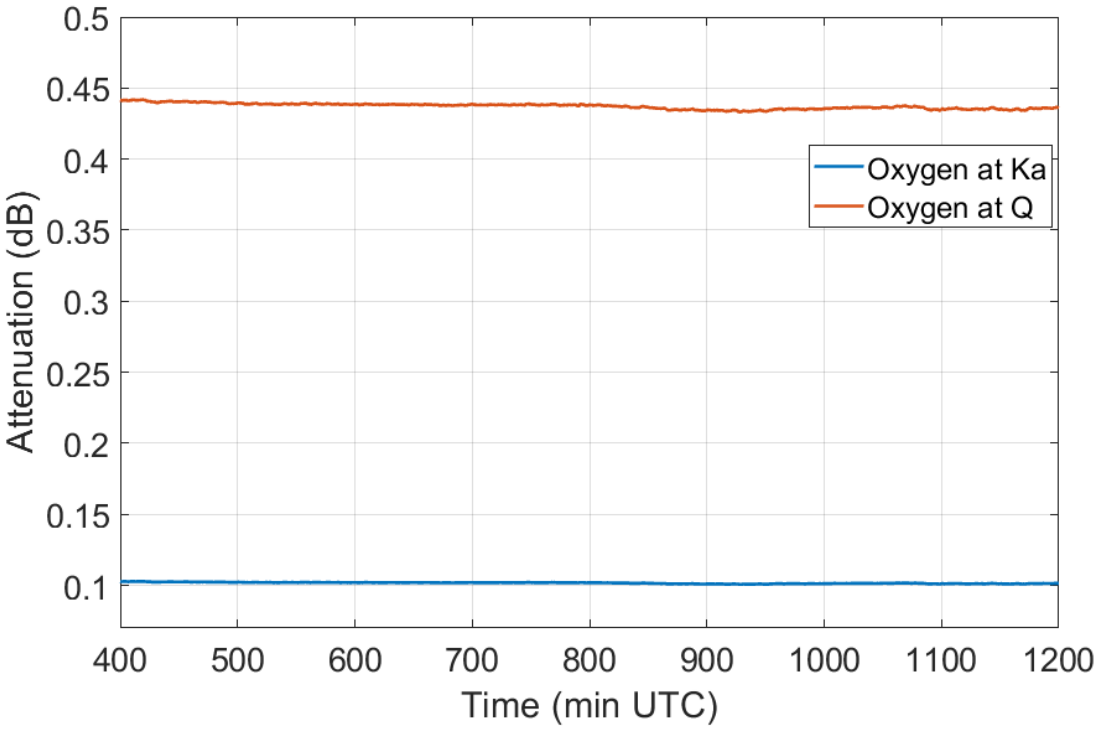

Fig. 6-6. Scaling of the oxygen attenuation for the stratiform rain event collected on the 4th of February 2017 from Ka to Q band.

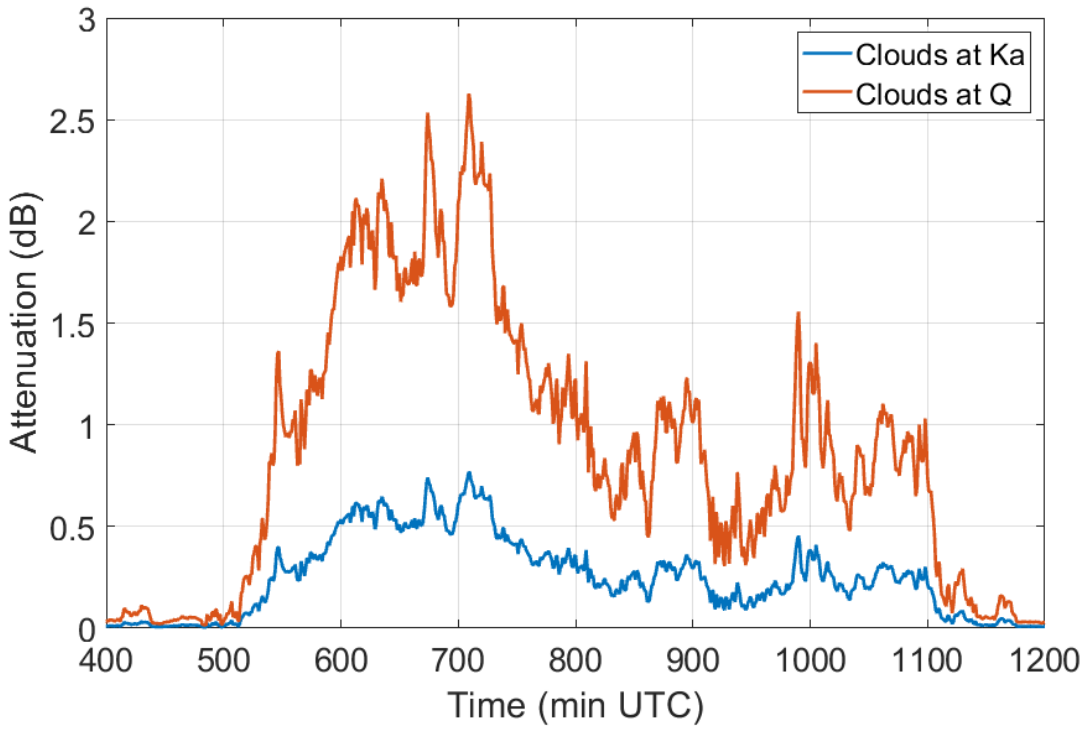

Fig. 6-7. Scaling of the cloud attenuation for the stratiform rain event collected on the 4th of February 2017 from Ka to Q band.

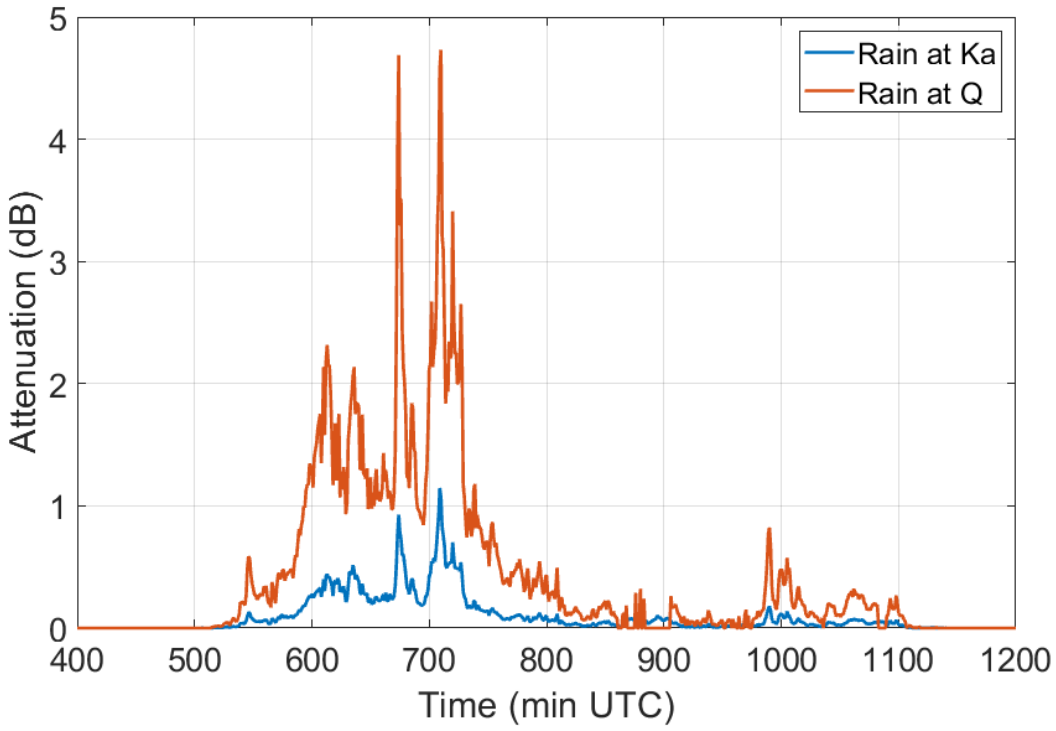

Fig. 6-8. Scaling of the rain attenuation for the stratiform rain event collected on the 4th of February 2017 from Ka to Q band.

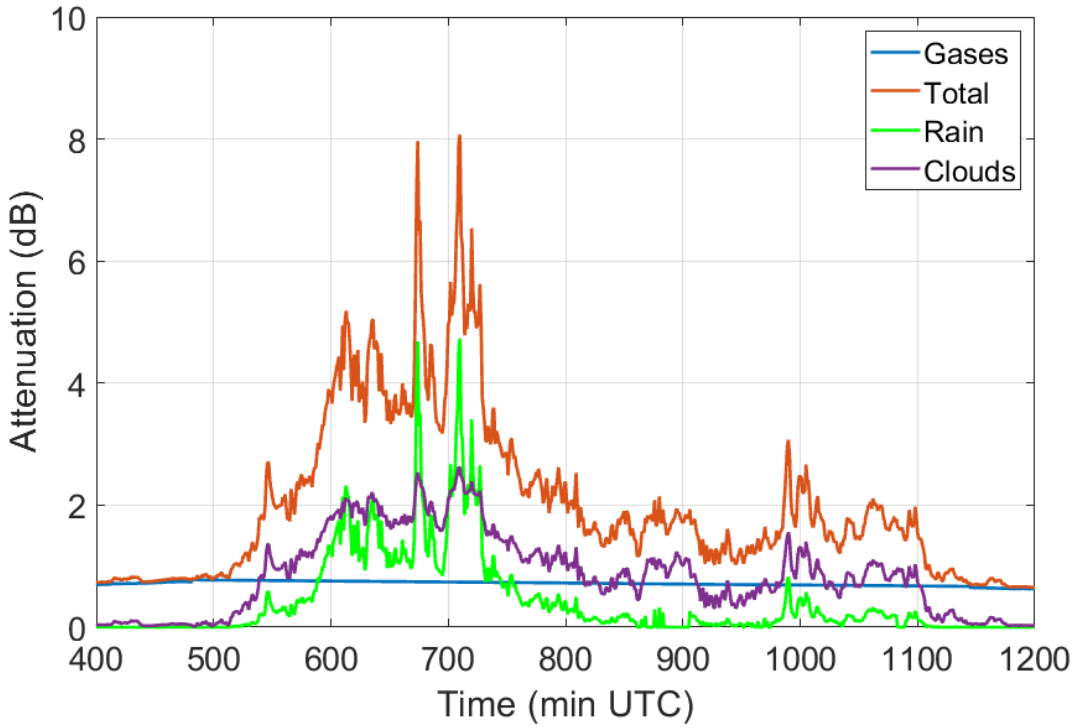

Fig. 6-9. Application of TAFS to the stratiform rain event collected on the 4th of February 2017; attenuation data scaled from 19.7 GHz to 39.4 GHz.

DISTRIBUTION A: Distribution approved for public release. Distribution unlimited

6.3. Frequency scaling of tropospheric attenuation: the simplified model

Despite its very good prediction accuracy (duly investigated in Section 6.4 below), the application of TAFS requires ancillary instruments such as disdrometers and radiometers, which are seldom available. As an alternative, this Section proposes the development of a simpler model, hereinafter referred to as Simplified Total Attenuation Frequency Scaling (S-TAFS) model, which does not require such detailed input information, but still offers a good prediction accuracy. In fact, the input dataset of S-TAFS is limited to the local mean annual probability to have rain, the surface meteorological measurements (e.g. pressure, temperature and relative humidity), and the attenuation time series at the lower frequency (e.g. Ka band), which can be collected quite easily from the numerous space-borne beacons available nowadays. Further information, i.e. the time series of the rain rate, the mean yearly rain height and the mean yearly wind speed, are needed only for an improved version of S-TAFS, also presented hereinafter below as well.

6.3.1. Separation of tropospheric attenuation components: the simplified approach

Similarly to TAFS, the simplified model is based on separately scaling the different components of tropospheric attenuation, which, in turn, requires to identify the contribution of each constituent to the total attenuation measured at frequency f_{DOWN}.

As in (6-5), the total attenuation can be expressed as:

$$A_t = A_{rc} + A_{ox} + A_{wv} \tag{6-6}$$

where A_{ox} is the oxygen attenuation, A_{wv} is the water vapor attenuation and A_{rc} is the attenuation due to rain and clouds, which can be further split into

$$A_{rc} = A_{rain} + A_{cloud} \tag{6-7}$$

The first step in the separation process consists in obtaining the time series of A_{rc} by subtracting A_{ox} and A_{wv} from A_t. However, differently from the procedure reported in Section 5.2.3, the gaseous attenuation $A_G = A_{ox} + A_{wv}$ is not derived from radiometric measurements (which are assumed to be unavailable), but it is estimated using directly recommendation ITU-R P.676-12, which defines, in Annex 2, two approximate models to calculate both A_{ox} (the same one used for TAFS) and A_{wv} using as input only surface meteorological measurements (namely pressure *P*, temperature *T* and relative humidity *RH*). These data, which are far more easily retrievable on a global basis, in Milan, are collected by the weather station deployed by NASA and by the additional sensors installed on the radiometer. In particular, A_{ox} and A_{wv} are calculated through the procedure detailed in the section 2.2 of the Annex 2 of the said recommendation, which presents the algorithms for estimating the gaseous attenuation along slant paths by defining an equivalent height by which the specific attenuation calculated in paragraph 1 of Annex 2 is multiplied to obtain the zenith attenuation and then scaled with the elevation angle for the slant path attenuation. Specifically, equations from 25 to 28 of recommendation ITU-R P.676-12 are adopted.

Fig. 6-10 depicts an example showing the time series of the meteorological parameters and the gaseous attenuation calculated according to recommendation ITU-R P.676-12 (Q band – 39.4 GHz, 4th of February 2017).

DISTRIBUTION A: Distribution approved for public release. Distribution unlimited

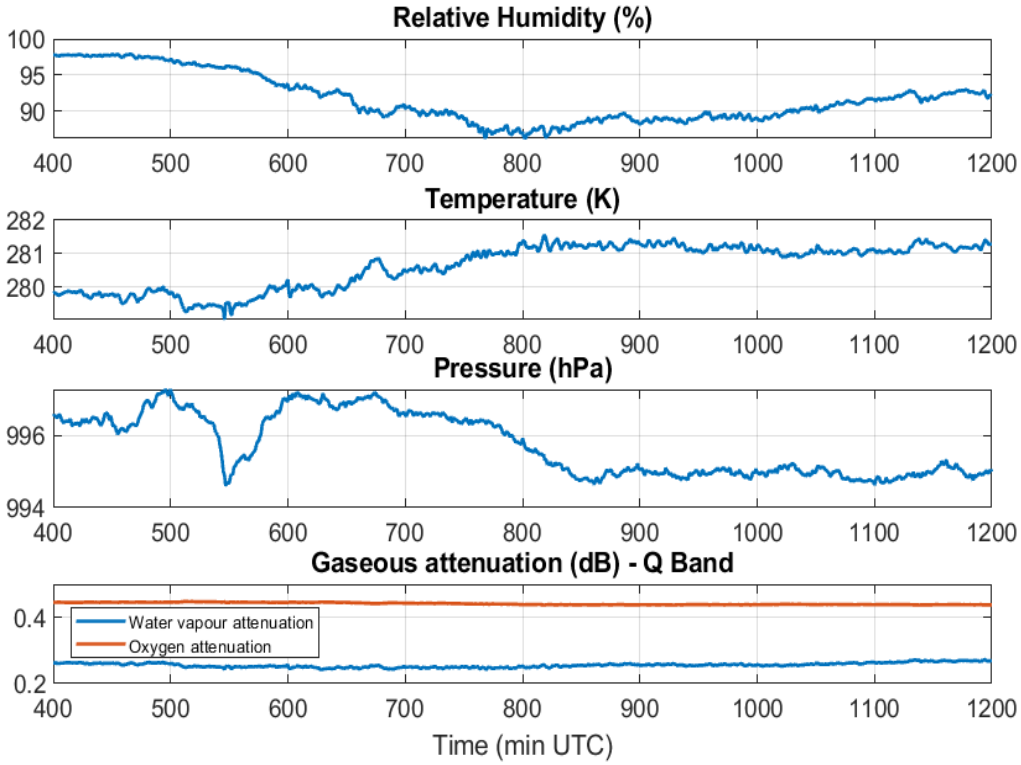

Fig. 6-10. The meteorological parameters and the gaseous attenuation prediction on the 4th of February 2017 at Q band (39.4 GHz).

After subtracting the predicted gaseous attenuation from A_t, the next step consists in the separation of the cloud and rain attenuations starting from A_{rc}, which is not an easy task. To this aim, it is necessary to introduce some simplifying hypotheses.

The rationale of the separation algorithm consists in identifying a fixed attenuation threshold A_f: the instantaneous attenuation A_{rc} is completely associated to the cloud component (A_{cloud}) if its value is equal or lower than A_f; conversely, if $A_{rc} > A_f$, part of the attenuation is ascribed to clouds ($A_{cloud} = A_f$) and part to rain ($A_{rain} = A_{rc} - A_f$). Fig. 6-11 summarizes the rain attenuation/cloud attenuation separation procedure.

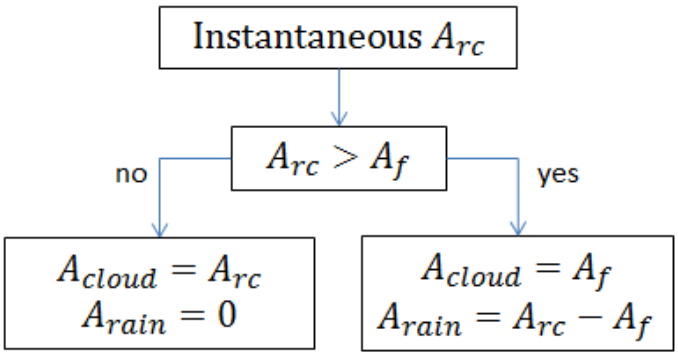

Fig. 6-11. Procedure to separate between cloud attenuation and rain attenuation.

In order to derive the value of A_f, we exploit $P_0 = P(R > 0)$, i.e. the probability to have rain in the period when the measurements are collected (i.e. 2017 in this study), which, in turn, can be calculated from the time series of the rain rate, if available (note that, to this purpose, a disdrometer is not needed: a tipping bucket is sufficient), or extracted, on a yearly basis, from global digital maps attached to recommendation ITU-R P.837-7 [ITU-R P.837-7]. The separation procedure actually makes use of P_{R0}, i.e. the probability to have rain attenuation along the link in the same period (2017), which is expected to be slightly higher than P_0 for links to geostationary satellites with ground stations at mid-latitude sites: in fact, a rain event might affect the link, but not the rain sensor. Though more complex prediction models could be used to estimate P_{R0} from P_0 and the link geometrical features, as a rule of thumb, based on the analysis of the experimental data, the reference P_{R0}^* can be simply calculated by increasing P_0 by 1%, i.e.; expressed in probability:

$$P_{R0}^* = P_0 + 0.01 \tag{6-8}$$

The value of A_f is obtained as shown in Fig. 6-12: the goal is to iteratively change the value of A_f until the P_{R0} calculated from the data as $P_{R0} = P(A_{rain} > 0)$ matches the reference value P_{R0}^*. Using the data collected during 2017 in Milan, P_0 = 5.2 % (as calculated from the rain rate time series), the value of A_f at 19.7 GHz is 0.26 dB.

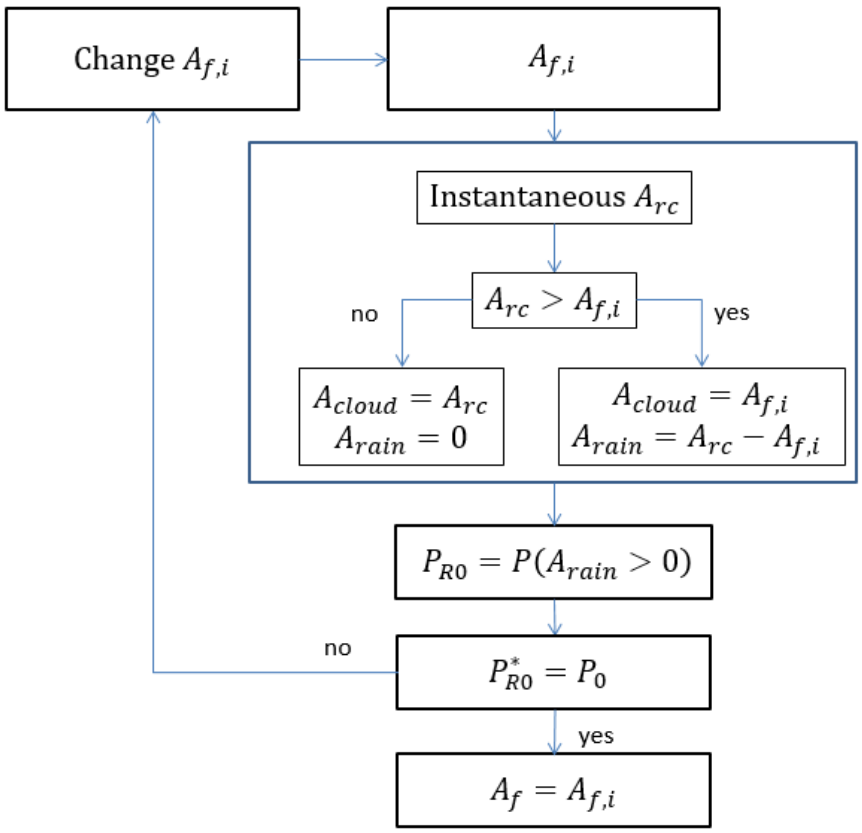

Fig. 6-12. Workflow to identify the threshold value of A_f, the key parameter to carry out the separation between cloud attenuation and rain attenuation.

DISTRIBUTION A: Distribution approved for public release. Distribution unlimited

Once the value of A_f is identified, the separation procedure detailed in Fig. 6-11 is applied to the whole database of A_{rc} data to obtain A_{rain} and A_{cloud}: together with A_{ox} and A_{wv}, they represent the datasets at the lower frequency f_{DOWN} necessary to start the frequency scaling process. As an example, Fig. 6-13 depicts the separation of total attenuation into its components using S-TAFS (Ka band data, 4th of February 2017). It is worth pointing out that:

- If compared to the separation procedure defined in Section 5.2.3., the results reported in S-TAFS are obviously less realistic: in the central part of the rain event, A_{cloud} is limited to A_f. However, the final goal of S-TAFS is to provide a reliable frequency scaling of the total attenuation, and not of all its separate components.
- Strictly speaking, the separation between rain attenuation and cloud attenuation should be applied only to the A_{rc} data associated to rain events. However, the identification of rain events requires the inspection of the rain rate time series, which might not be available at the site: this is the reason why S-TAFS was devised to be applicable even in the absence of rain rate time series. Indeed, using the disdrometer data available in Milan, we have verified that A_f turns out to be sufficient to perform a rough identification of rain events: when $A_{rc} < A_f$, only clouds are actually affecting the link, as also indicated, most of the times, by the time series of the rain rate.

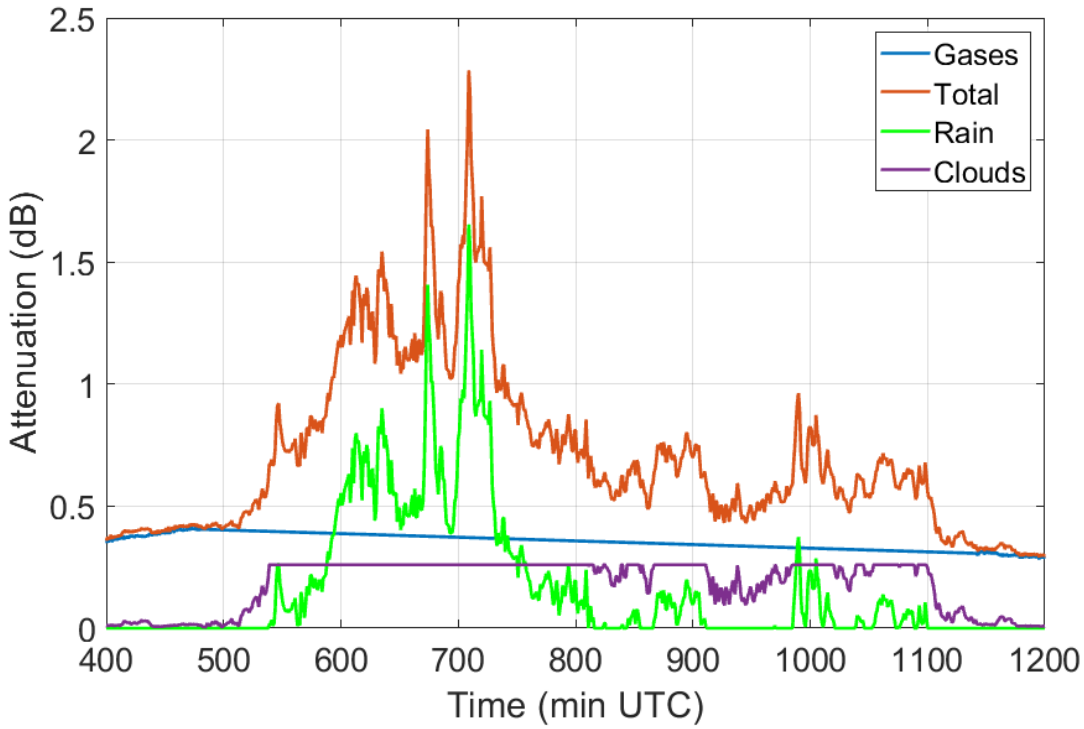

Fig. 6-13. Separation of the attenuation contributions due to gases, clouds and rain for a sample day (4th of February 2017) at Ka band, adopting S-TAFS.

6.3.2. Frequency scaling using the simplified approach

Fig. 6-14 summarizes the full step-by-step frequency scaling procedure, applied separately to each tropospheric component, using S-TAFS.

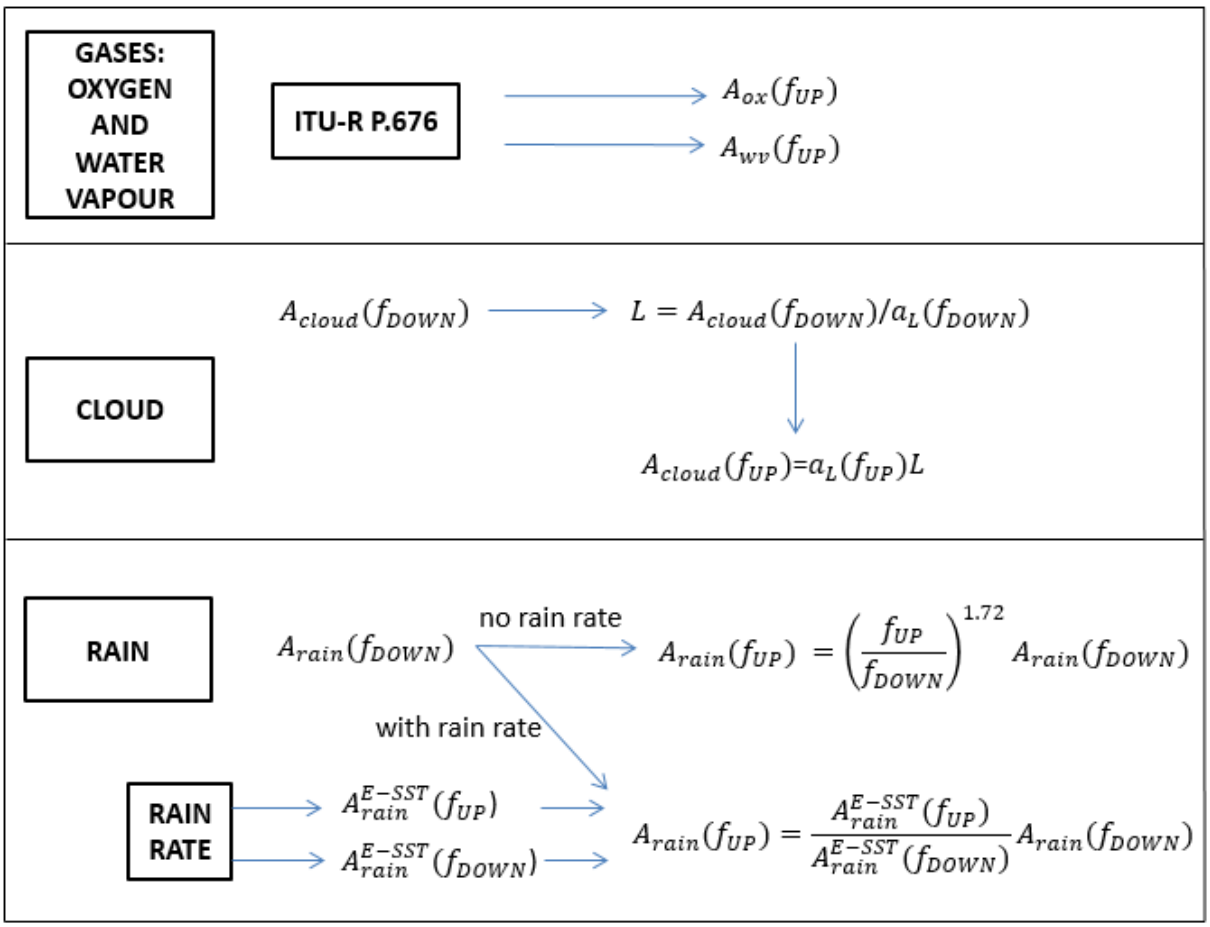

Fig. 6-14. Workflow for the Simplified Total Attenuation Frequency Scaling model.

As previously mentioned, the gaseous attenuation $A_{ox}(f_{UP})$and $A_{wv}(f_{UP})$ are directly predicted by applying the same simplified prediction models included in recommendation [ITU-R P.676-12] (Annex 2) already mentioned in Section 6.3.1.

Cloud attenuation is scaled as in the case of TAFS, i.e. by employing equations (6-2) and (6-3), but obviously using as input $A_{cloud}(f_{DOWN})$ obtained in Section 6.3.1.

Concerning rain attenuation, when no rain rate time series are available, simple statistical models exist requiring as input only the time series of $A_{rain}(f_{DOWN})$. Among the various rain attenuation frequency scaling methods proposed in the literature, the simple power law model presented by Drufuca in [Drufuca, 1974] is adopted in S-TAFS, according to which:

$$R_{FS}^{D} = \frac{A_{rain}\,(f_{UP})}{A_{rain}\,(f_{DOWN})} = \left(\frac{f_{UP}}{f_{DOWN}}\right)^{1.72} \tag{6-9}$$

As a result, the rain attenuation at higher frequency f_{UP} is estimated as:

$$A_{rain}\,(f_{UP}) = \left(\frac{f_{UP}}{f_{DOWN}}\right)^{1.72} A_{rain}(f_{DOWN}) \tag{6-10}$$

On the other hand, if rain rate time series are available, a different rain attenuation frequency scaling ratio can be used: in fact, while the ratio defined in (6-9) is constant, the use

of E-SST, duly presented in Chapter 5, allow the definition of an instantaneous frequency scaling ratio, which was shown to enhance the prediction performance. According to E-SST:

$$R_{FS}^{E-SST} = \frac{A_{rain}^{E-SST}(f_{UP})}{A_{rain}^{E-SST}(f_{DOWN})} \tag{6-11}$$

It is worth mentioning that, while the E-SST in chapter 5 is applied by using as input all the ERA5 hourly wind speed and temperature profiles, for the sake of simplicity, S-TAFS receives as input only the mean yearly value of the 0 °C isotherm height and of the 700 mbar isobar wind speed.

The final step for the application of S-TAFS is to sum up all the attenuation components using (6-5). As an example, Fig. 6-15 to Fig. 6-19 show the application of S-TAFS to the stratiform event collected on the 4th of February 2017 at 39.4 GHz.

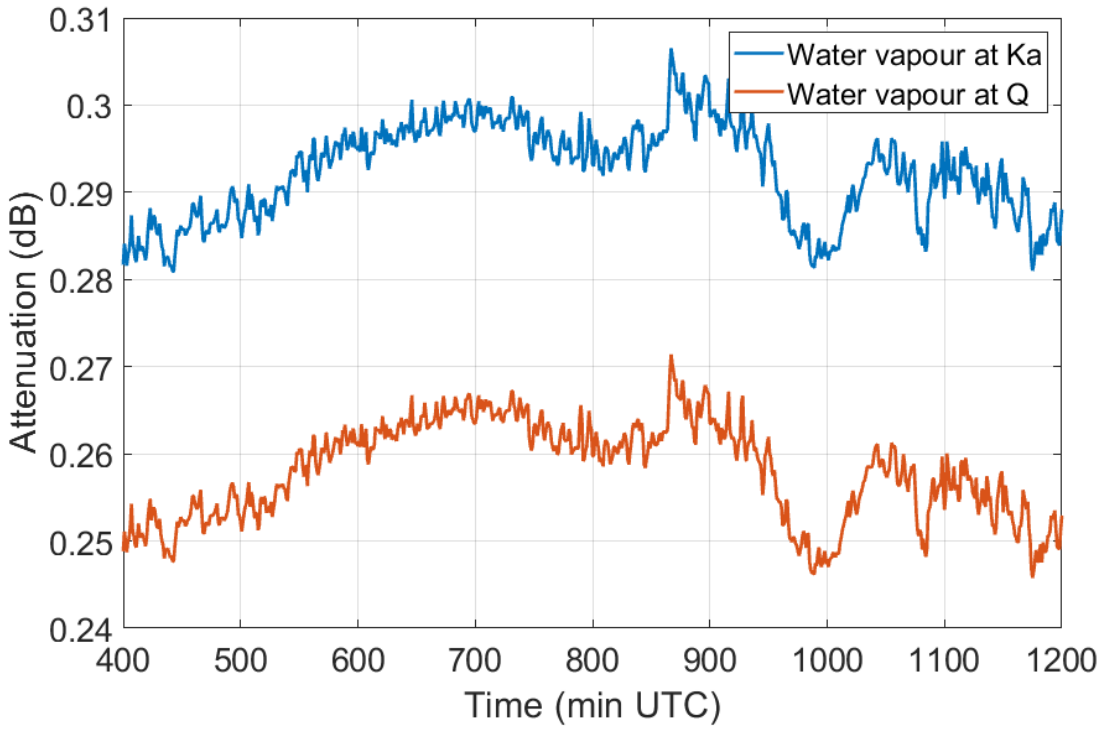

Fig. 6-15. Scaling of the water vapour attenuation for the stratiform rain event collected on the 4th of February 2017 from Ka to Q band.

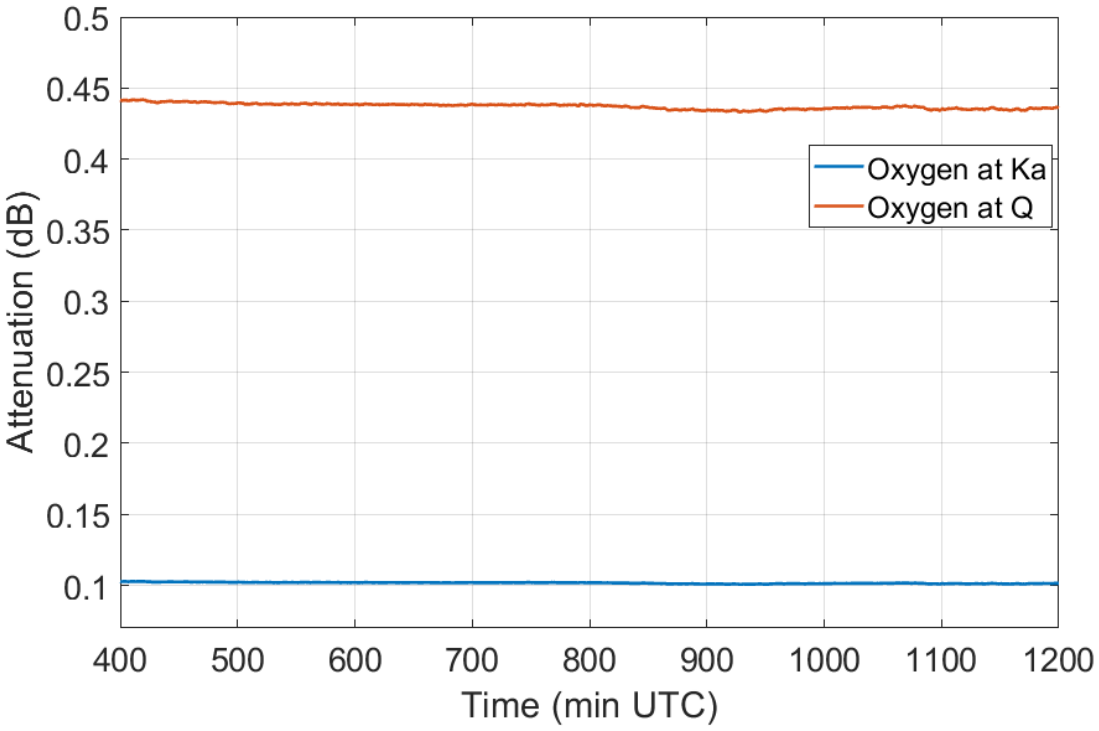

Fig. 6-16. Scaling of the oxygen attenuation for the stratiform rain event collected on the 4th of February 2017 from Ka to Q band.

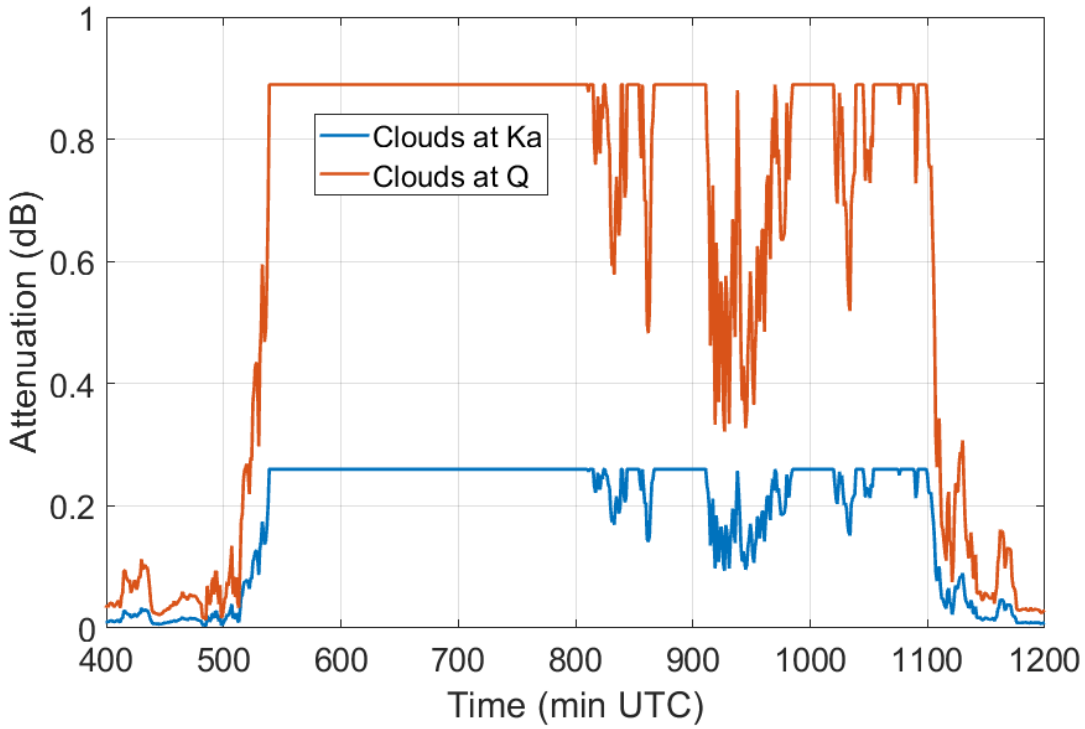

Fig. 6-17. Scaling of the cloud attenuation for the stratiform rain event collected on the 4th of February 2017 from Ka to Q band.

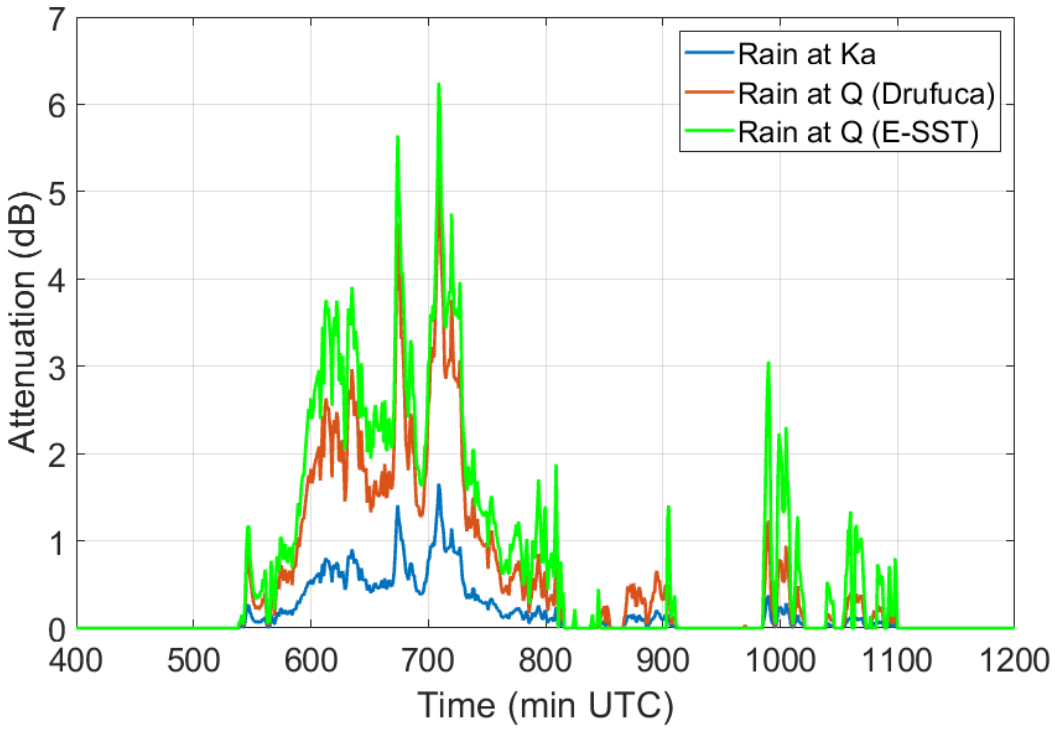

Fig. 6-18. Scaling of the rain attenuation for the stratiform rain event collected on the 4th of February 2017 from Ka to Q band.

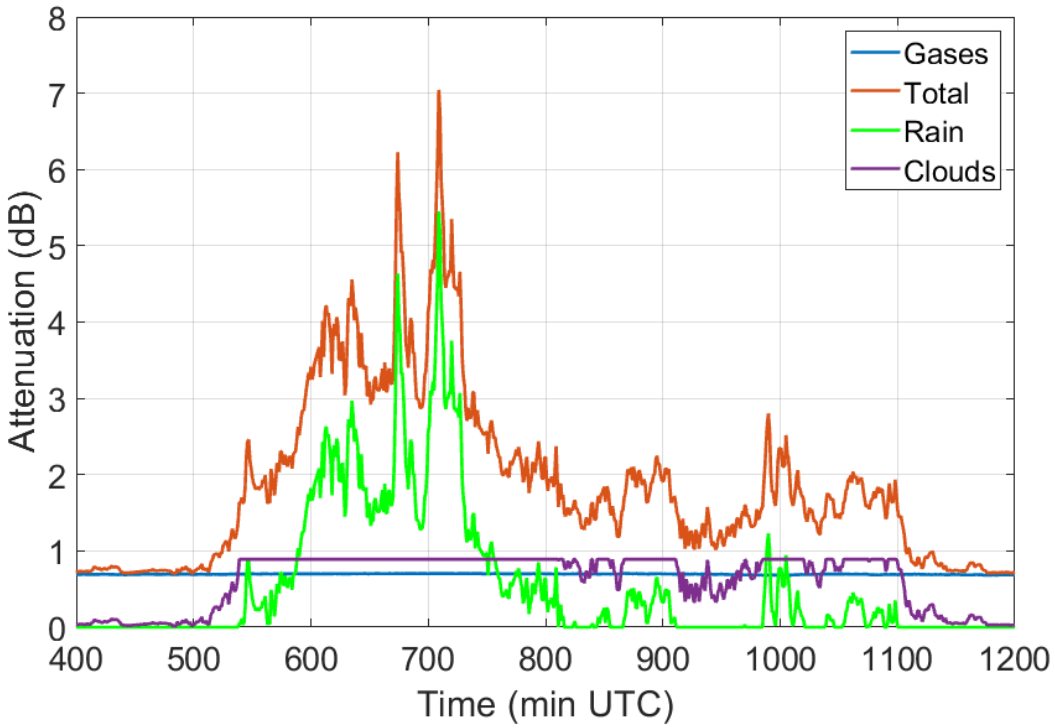

Fig. 6-19. Application of S-TAFS (Drufuca power law for rain attenuation) to the stratiform rain event collected on the 4th of February 2017, at Q band.

DISTRIBUTION A: Distribution approved for public release. Distribution unlimited

6.4. Results and discussion

This section focuses on assessing the accuracy of TAFS and S-TAFS in predicting total tropospheric attenuation. The tests are performed by exploiting a full year (2017) of propagation data collected in Milan using the NASA equipment: total attenuation data at 19.7 GHz are used as input to TAFS and S-TAFS to predict A_t at 39.4 GHz, which is compared to the reference total attenuation measured at 39.4 GHz.

Fig. 6-20 compares the CCDF of total tropospheric attenuation at 39.4 GHz in 2017. As expected, due its simplified approach, S-TAFS shows a lower prediction performance than TAFS. This conclusion is confirmed by the results reported in Table 6-3, which lists the mean (E) and root mean square (RMS) value of the error figure already defined in (5-13).

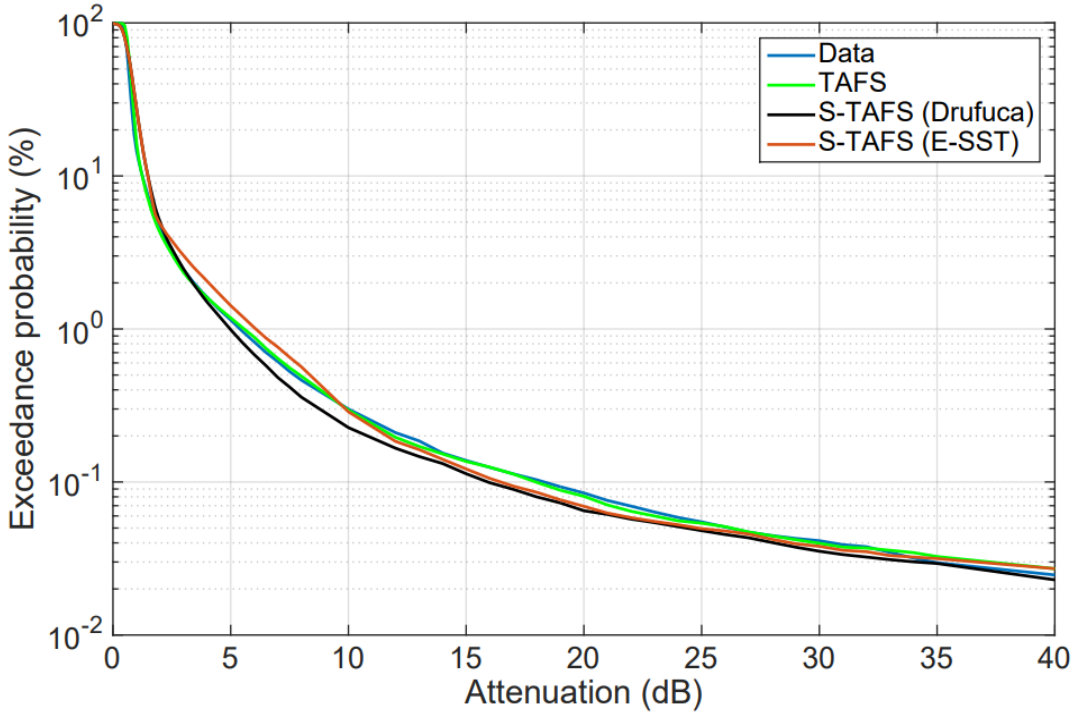

Fig. 6-20. Application of TAFS and S-TAFS for the prediction of the CCDF of total attenuation at 39.4 GHz band; whole year statistics.

Table 6-3. Overall prediction accuracy of TAFS and S-TAFS: total attenuation CCDFs (full 2017), Q band (CCDF).

	E (%)	RMS (%)
TAFS	-0.16	1.72
S-TAFS WITH E-SST (RAIN)	-0.32	4.22
S-TAFS WITH DRUFUCA (RAIN)	-1.05	4.7

The increased accuracy of TAFS is corroborated also by the tests performed on the time series of total attenuation, which are crucial for the design and the operation of the necessary fade mitigation techniques when the frequency increases to a point that fixed power margins

DISTRIBUTION A: Distribution approved for public release. Distribution unlimited

are no longer sufficient to provide the expected system performance. As an example, Fig. 6-21 compares the estimated and measured time series of total attenuation (4th of February 2017) at 39.4 GHz, while Table 6-4 lists E and RMS of the absolute error figure defined in (5-18) considering all the data collected in 2017.

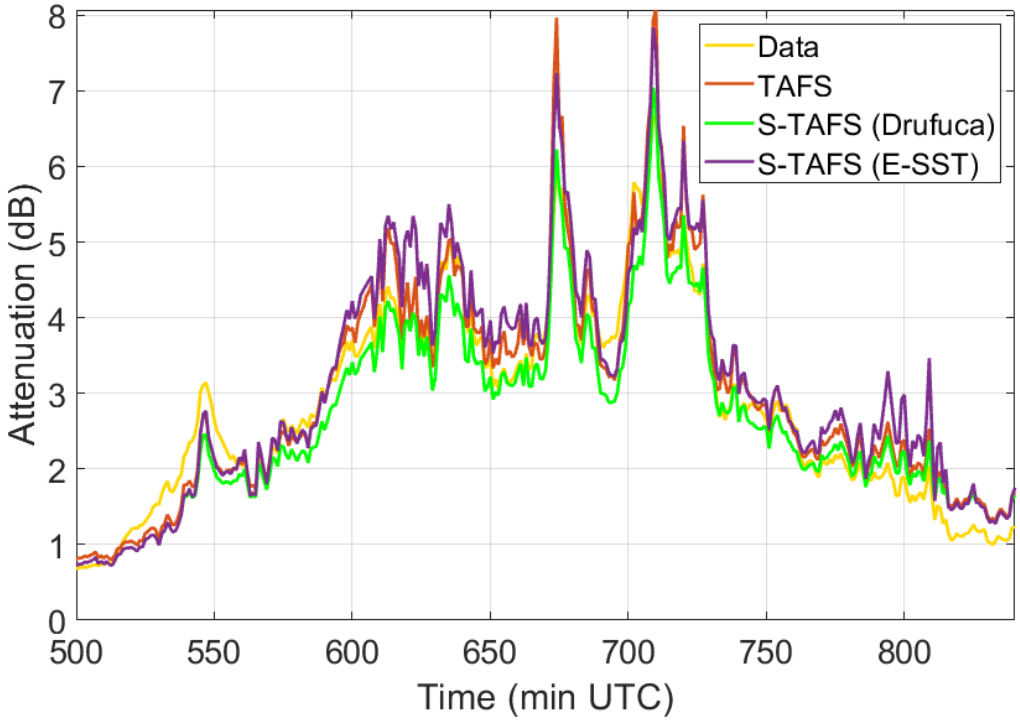

Fig. 6-21. Time series of total attenuation (4th of February 2017) at 39.4 GHz as measured by the experimental equipment and as estimated using TAFS and S-TAFS.

Table 6-4. Overall prediction accuracy of TAFS and S-TAFS: total attenuation time series (full 2017), Q band (time series).

	E (dB)	RMS (dB)
TAFS	0.05	0.38
S-TAFS WITH E-SST R-FS	0.01	0.43
S-TAFS WITH DRUFUCA R-FS	0.06	0.41

6.5. Prediction of total attenuation at W band

The interest in the W band (75 GHz-110 GHz) for Earth-space and terrestrial communication systems is quickly increasing mainly because of large bandwidth available around such high carrier frequencies. No experimental measurements are currently available for Earth-to-satellite links at frequencies above 50 GHz, against which attenuation prediction models can be tested. TAFS relies on solid physical bases (e.g. use of the DSD for rain attenuation frequency scaling) and thus it can be quite reliably used to provide predictions at higher frequency bands. On the other hand, S-TAFS includes some simplifying assumptions, which increase its applicability to sites where limited input data are available (e.g. DSD). Given

DISTRIBUTION A: Distribution approved for public release. Distribution unlimited

the enhanced reliability and accuracy of TAFS, the results reported in this section are obtained only by applying the latter model.

Fig. 6-22 shows the CCDFs of total attenuation obtained from TAFS (whole of 2017) at 80 GHz and 90 GHz.

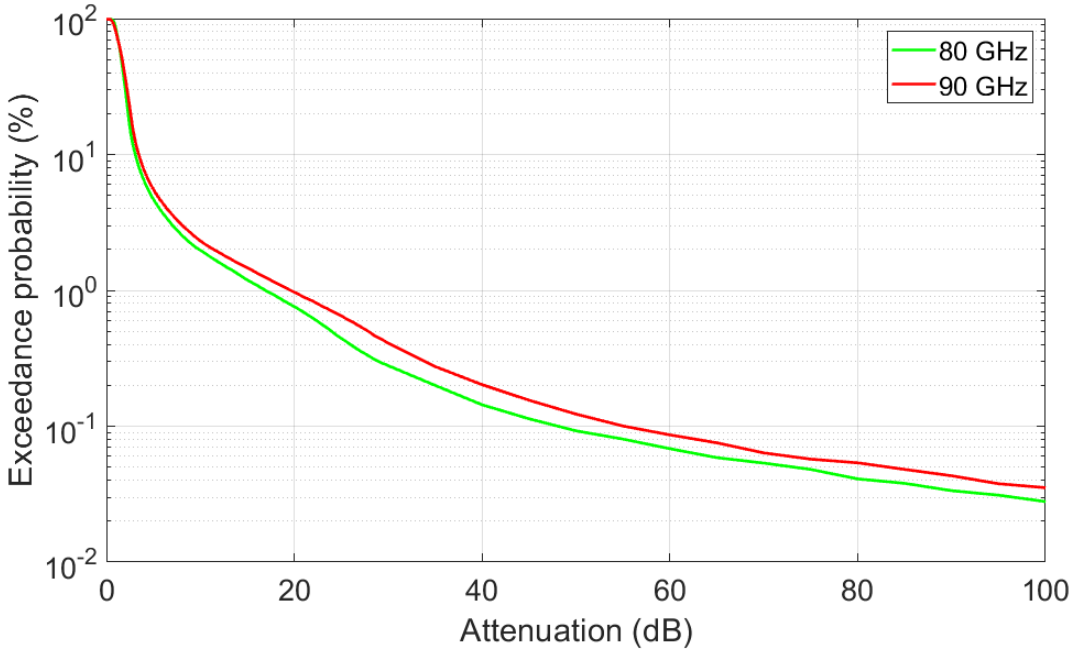

Fig. 6-22. Application of TAFS at 80 and 90 GHz, whole year statistics.

Fig. 6-23 shows, for the 4th of February 2017, the time series of total attenuation at 80 GHz and 90 GHz, obtained using TAFS.

DISTRIBUTION A: Distribution approved for public release. Distribution unlimited

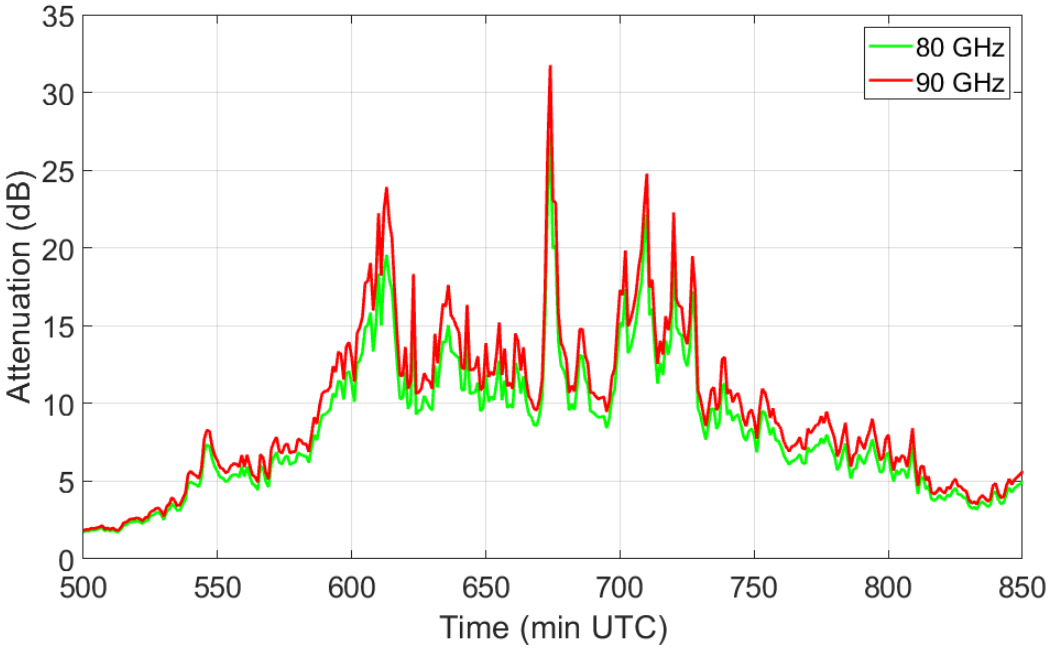

Fig. 6-23. Total attenuation scaled from 19.7 GHz to 80 and 90 GHz using TAFS, for the stratiform rain event on the 4th of February 2017.

6.5.1. Time diversity

Fig. 6-23 clearly shows that the amount of tropospheric attenuation in the W band is so high that the system availability is typically limited between 99.9% and 99%. Among Fade Mitigation Techniques (FMTs), time diversity represents a good option to increase the system performance: the same data stream is transmitted at time t and at time $t + \Delta t$, where the delay Δt is chosen so as to guarantee that the attenuation values impairing the link in the two instants are sufficiently statistically uncorrelated: thus, the receiver can select, ideally each second, the best data sample (of the 'original' time series and of the 'delayed' copy of it), i.e. the one subject to less attenuation. In fact, time diversity is effective to counteract the rain impairments because it takes advantage of the time decorrelation of the rainfall process. Its effectiveness depends on the choice of the delay Δt; a larger value of Δt provides a higher gain, which was presented in Chapter 3, defined as:

$$G(\Delta t, A_s) = A_s(P) - A_j(\Delta t, P) \quad (6\text{-}12)$$

where A_s and A_j are the attenuation values of the complementary cumulative distribution functions (CCDFs), at the same probability level P, respectively related to a simple receiver (without time diversity) and to a time diversity system.

Fig. 6-24 and Fig. 6-25 report the results of the application of time diversity at 80 and 90 GHz, calculated using the time series of attenuation scaled from 19.7 GHz to 80 and 90 GHz. Specifically Fig. 6-24 and Fig. 6-25 depict the CCDF of the total attenuation for several values of Δt (80 and 90 GHz, respectively), while Fig. 6-26 (80 GHz) and Fig. 6-27 (90 GHz) focus on the time diversity gain as a function of Δt and of the outage probability level P: as expected, a higher diversity gain is obtained with longer Δt.

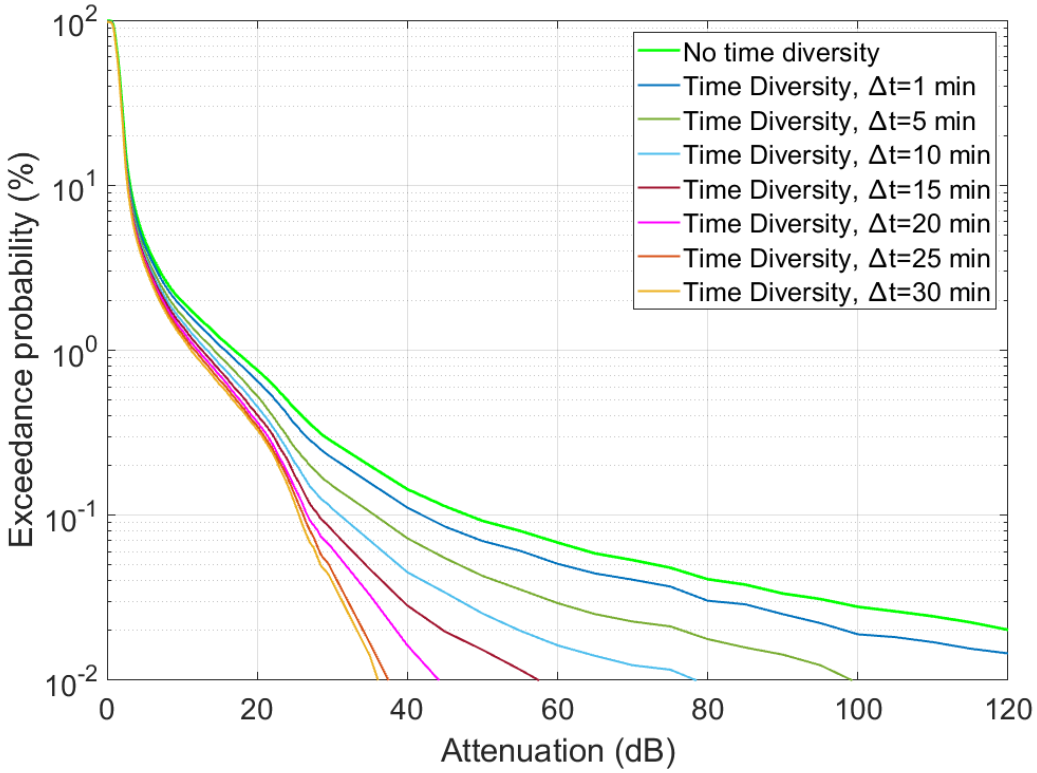

Fig. 6-24. Application of TAFS at 80 GHz, whole year statistics. Results without time diversity and implementing time diversity, for different retransmission delays.

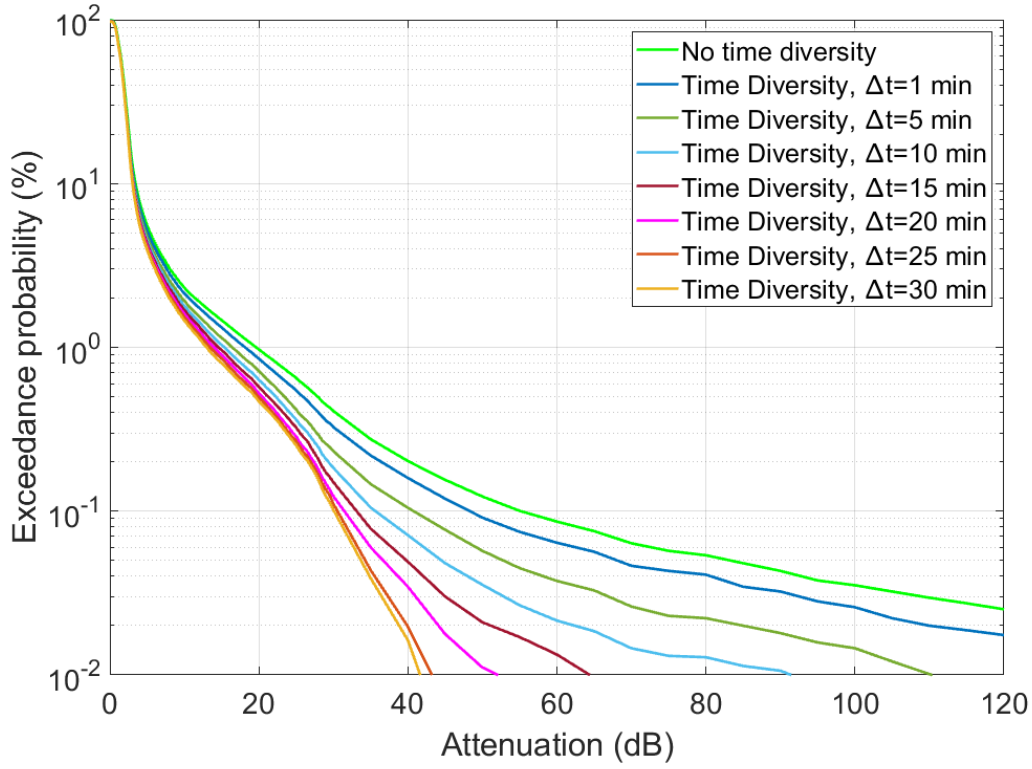

Fig. 6-25. Application of TAFS at 90 GHz, whole year statistics. Results without time diversity and implementing time diversity, for different retransmission delays.

DISTRIBUTION A: Distribution approved for public release. Distribution unlimited

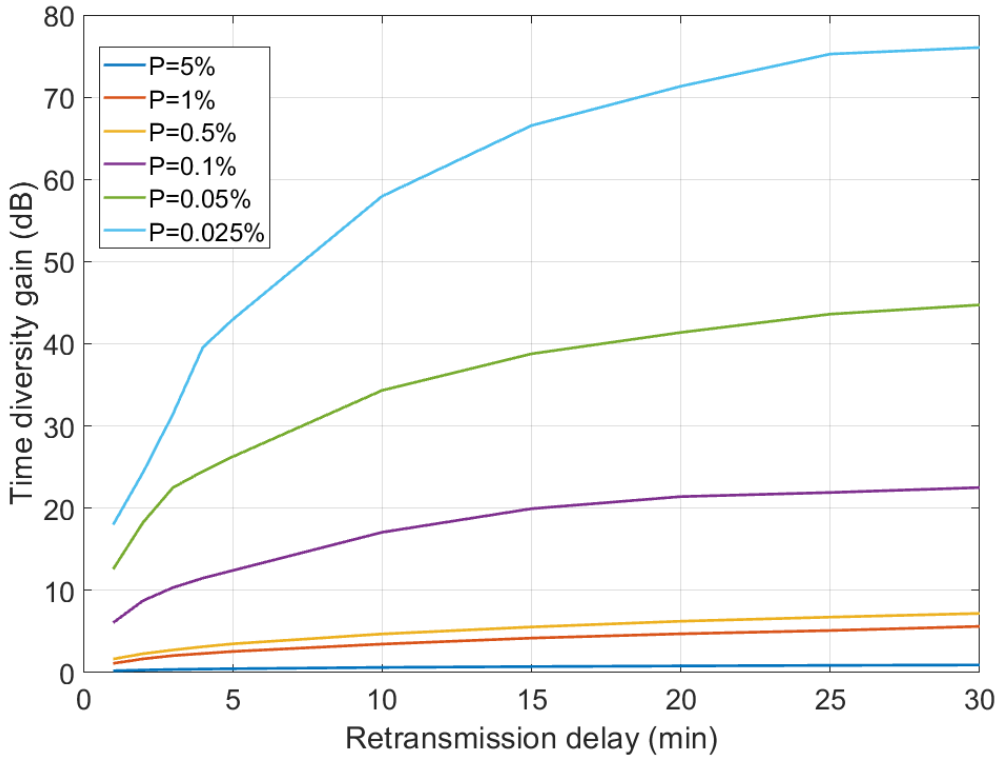

Fig. 6-26. Time diversity gain G as a function of the retransmission delay and of the outage probability P (f = 80 GHz, year 2017).

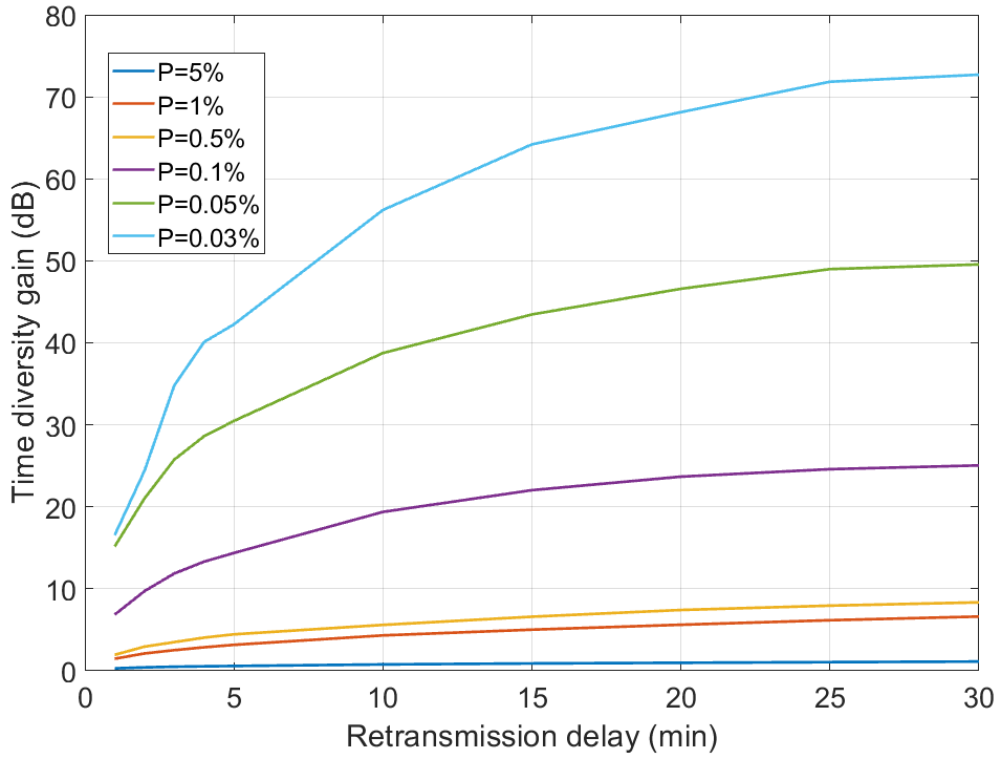

Fig. 6-27. Time diversity gain G as a function of the retransmission delay and of the outage probability P (f = 90 GHz, year 2017).

DISTRIBUTION A: Distribution approved for public release. Distribution unlimited

6.5.2. Fade duration

The second order statistics are useful for the design of the Fade Mitigation Techniques: fade duration leads to the evaluation of the long-term behavior of the fade countermeasures. Fig. 6-28 and Fig. 6-29 show the fade duration conditional CCDFs, obtained from the predictions of TAFS at 80 GHz and 90 GHz, respectively, for given threshold values (e.g. 5, 7, 10, 12, 15, 18, 20, 22, 25, 30, 35 dB). The 60-seconds fade are considered as the reference case: the statistical distributions are calculated with respect to it.

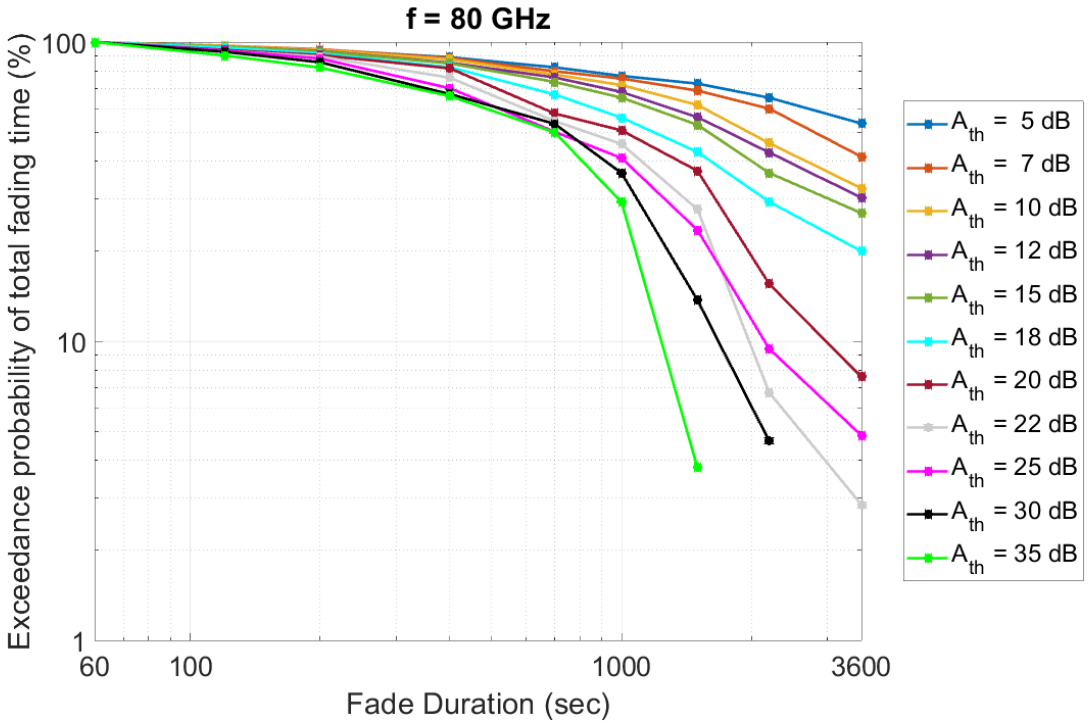

Fig. 6-28. CCDFs of the fade duration (f = 80 GHz), obtained from the TAFS predictions, considering different attenuation thresholds.

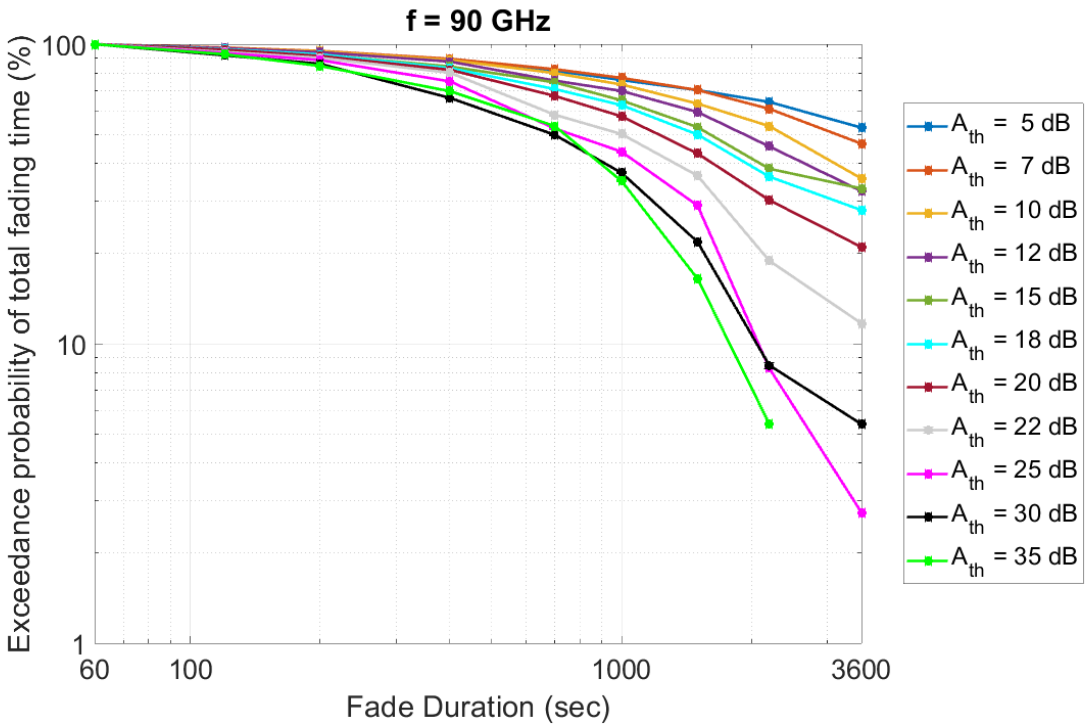

Fig. 6-29. CCDFs of the fade duration (f = 90 GHz), obtained from the TAFS predictions, considering different attenuation thresholds.

The fade duration analysis is completed by the number of the fade events: their CCDFs at both W-band frequencies are reported in Fig. 6-30 and Fig. 6-31.

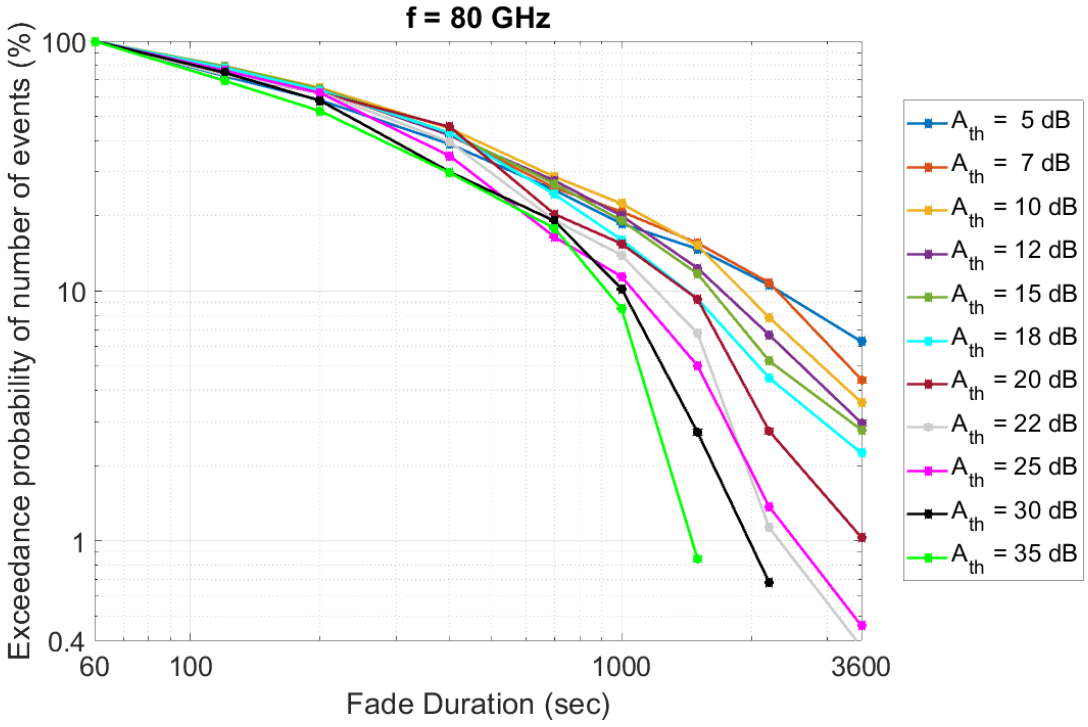

Fig. 6-30. CCDFs of the number of fades (f = 80 GHz), obtained from the TAFS predictions, considering different attenuation thresholds.

DISTRIBUTION A: Distribution approved for public release. Distribution unlimited

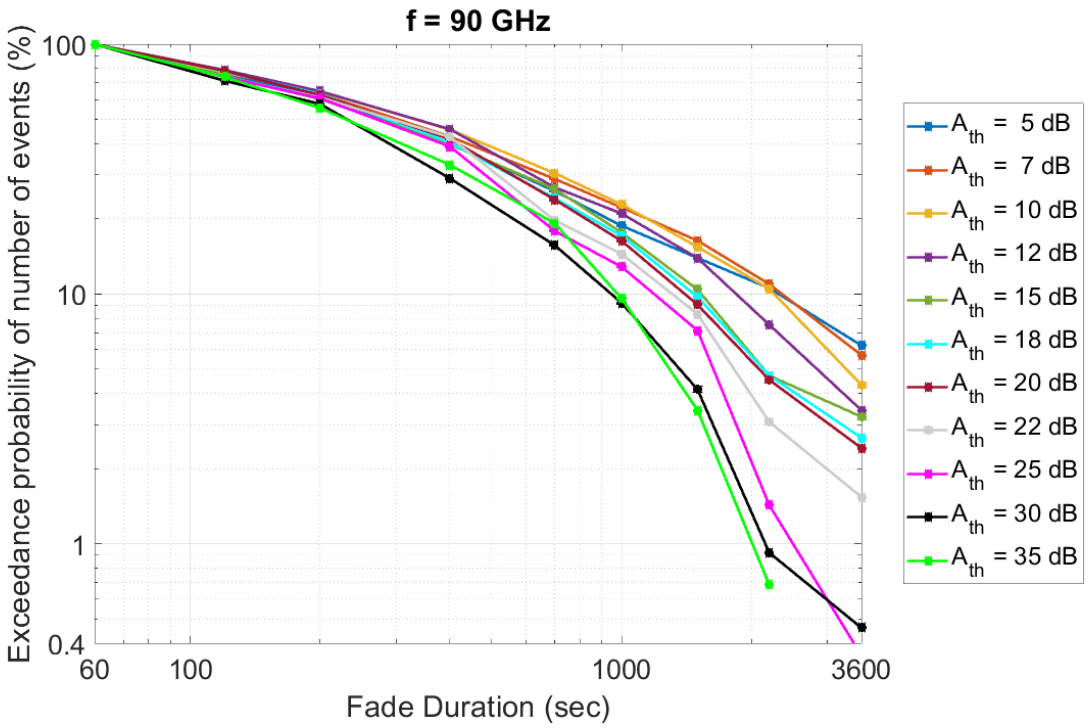

Fig. 6-31. CCDFs of the number of fades (f = 90 GHz), obtained from the TAFS predictions, considering different attenuation thresholds.

6.5.3. Fade slope

Fade slope statistics could be key for the short-term prediction of fade attenuation as they provide information on the instantaneous rate of attenuation change of the attenuation. The fade slope CCDFs for the W-band predictions obtained with TAFS are presented in Fig. 6-32 and Fig. 6-33, by considering the fixed attenuation values of 1, 3, 5, 10, 15, 20, 25, 30, 35 dB. Fig. 6-34 and Fig. 6-35 depict the distribution of the fade slope probability of occurrence. The time interval considered for the fade slope computation is 60 seconds.

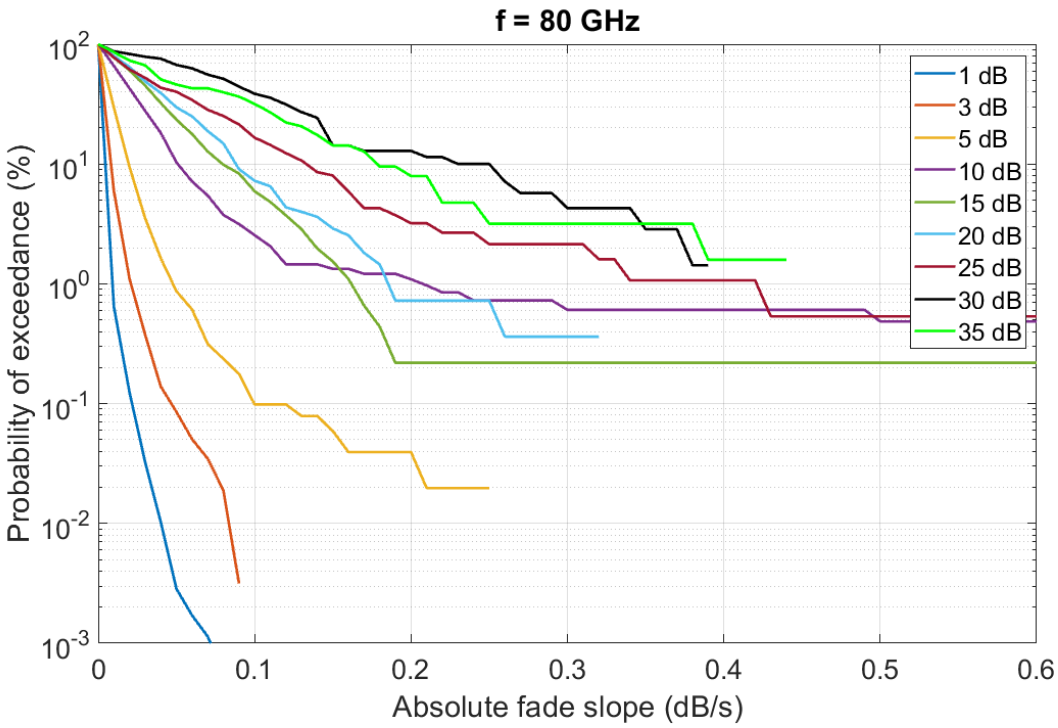

Fig. 6-32. CCDFs of the absolute fade slope (f = 80 GHz), obtained from TAFS predictions, considering different attenuation thresholds.

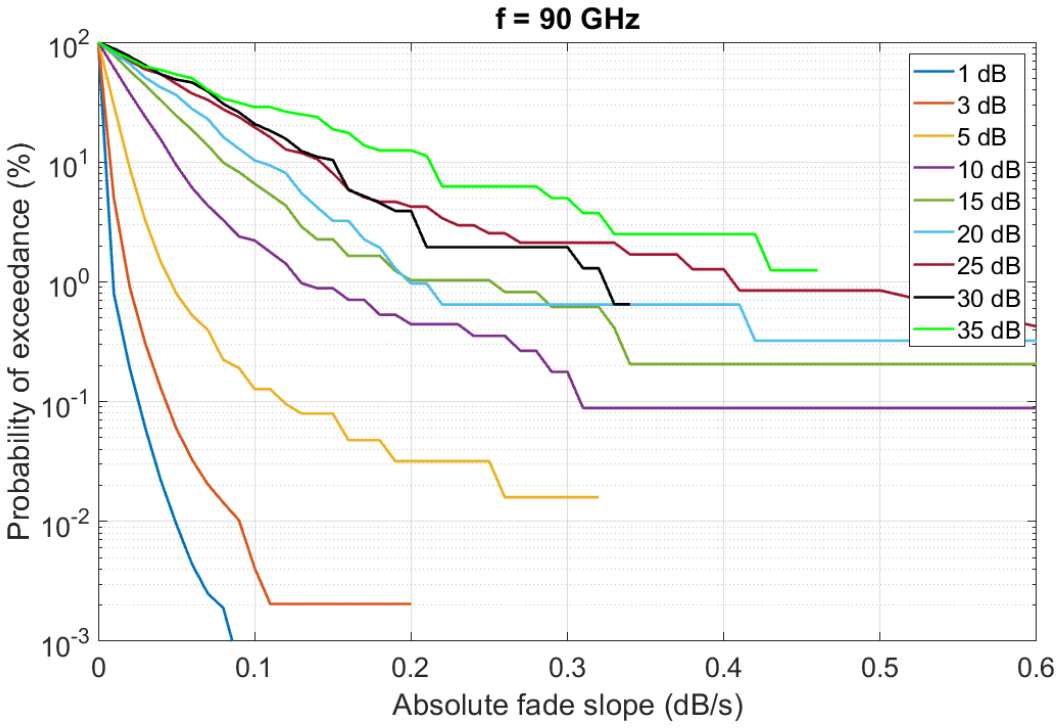

Fig. 6-33. CCDFs of the absolute fade slope (f = 90 GHz), obtained from the TAFS predictions, considering different attenuation thresholds.

DISTRIBUTION A: Distribution approved for public release. Distribution unlimited

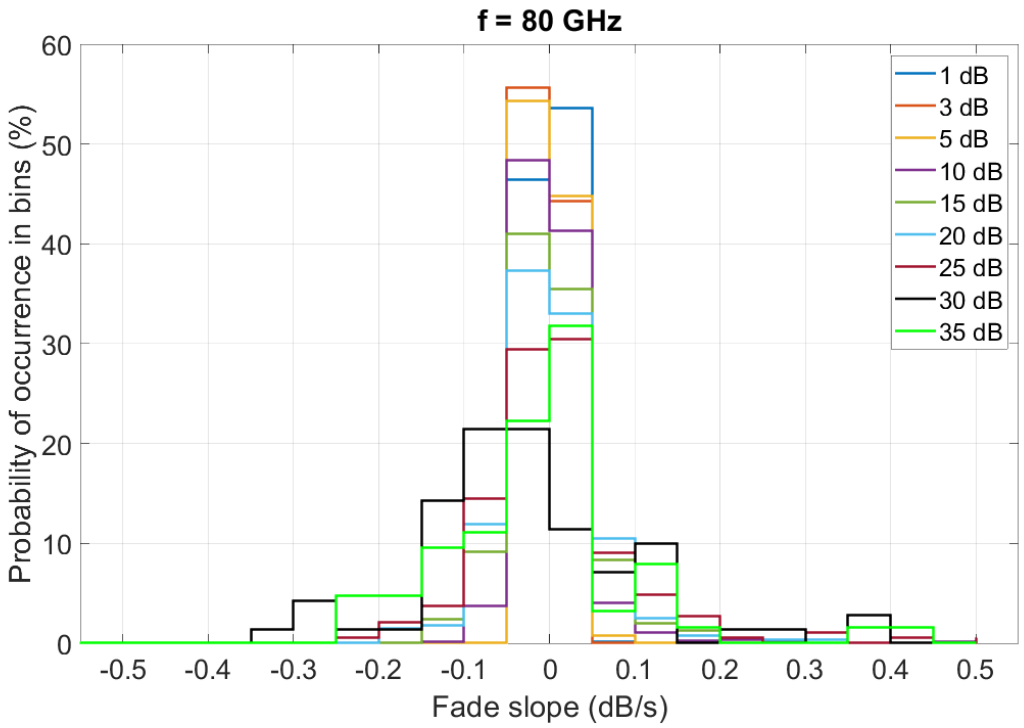

Fig. 6-34. Fade slope distribution (f = 80 GHz), obtained from TAFS predictions, considering different attenuation thresholds.

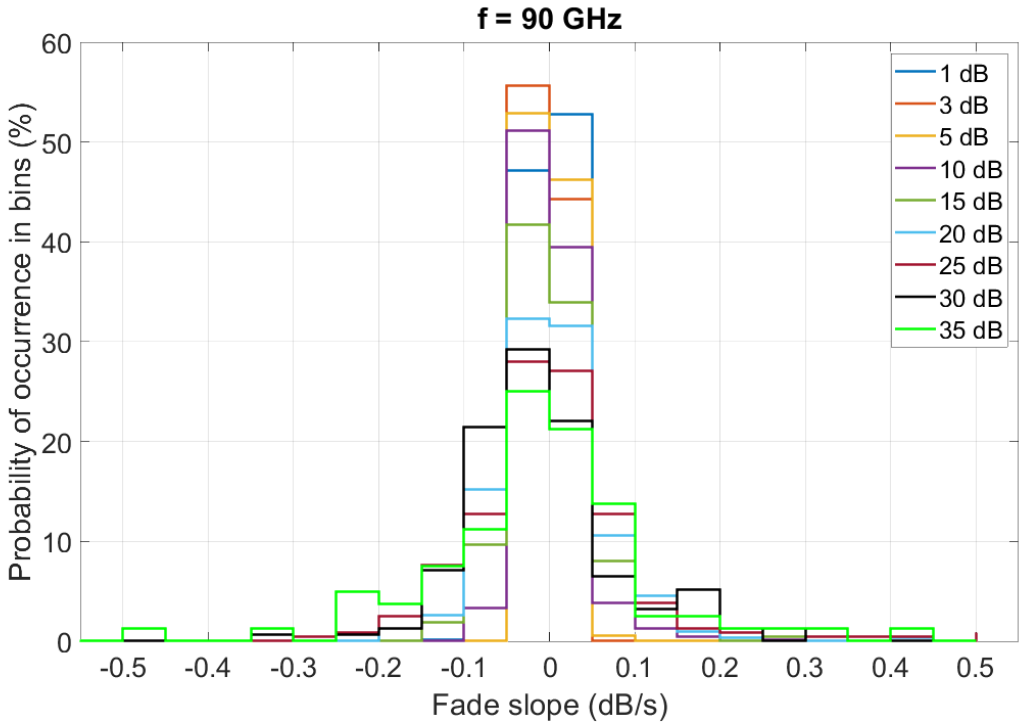

Fig. 6-35. Fade slope distribution (f = 90 GHz), obtained from TAFS predictions, considering different attenuation thresholds.

DISTRIBUTION A: Distribution approved for public release. Distribution unlimited

7. CONCLUSIONS

The main goal of this work was to develop physically-based models, which can be used to predict the propagation conditions for Earth-space communication systems operating at W band, for which no experimental data are currently available. To this aim, the first part of this work was devoted to a brief overview on the main impairments induced by tropospheric constituents on EM waves in the 10-100 GHz range, among which the signal attenuation is the prevalent one. More specifically, fades are mainly caused by rain (which is strongly dependent on the Drop Size Distribution), and to a lesser extent, by clouds. Also tropospheric gases need to be taken into account, namely water vapor and oxygen, as they induce high amount of attenuation on EM waves at specific frequency bands, due to resonant effects taking place at molecular level.

Given the importance of experimental data for modeling purposes, a significant part of the present work focused on the involvement of NASA in the framework of the Alphasat experiment. Specifically, the first part of the report presented all the activities devoted to the installation and operation of the NASA receiving equipment on the roof of the Dipartimento di Elettronica, Informazione e Bioningegneria (DEIB) of Politecnico di Milano. The Alphasat experiment (motivation, objectives, architecture) was described, together with the experimental equipment installed at the Italian ground stations of Spino d'Adda and Tito Scalo. Significant work was performed to develop algorithm and techniques to pre-process the raw data collected by all the instruments that are part of the NASA equipment, as well as to retrieve useful additional data, such as vertical profiles of the atmosphere (pressure, temperature and relative humidity) provided by the radiosonde observations collected at the Milano-Linate airport (5 km from the DEIB) and by the ECMWF NWP operational data. More specifically, beacon data were pre-processed to exclude erroneous samples using semi-automated procedures and visual inspection. The received beacon signal levels were turned into total tropospheric attenuation by taking advantage of the Ka-/W-band collocated radiometer: brightness temperature measured at 23.8, 31.4 and 82.5 GHz were exploited to estimate the tropospheric attenuation in nonrainy conditions at 19.7 and 39.4 GHz, and hence, derive attenuation time series from the received beacon power levels with higher accuracy.

Statistics of total and excess (rain-only) attenuation (both on a yearly and on a monthly basis) were derived using 5 full years of attenuation data (from June 2014 to May 2019): results point out quite a limited year-to-year variability and that approximately 10 dB and 35 dB are required at 19.7 and 39.4 GHz, respectively, to guarantee that the link is available for 99.95% of the time in a year. These results were produced with a mean yearly data availability of 89.3% and 90.9% for the Ka and the Q band, respectively. The data unavailability was not due to the limits in the dynamic range of the receivers, but mostly to the unavailability of beacon signals (e.g. during sun eclipse periods), to days with intense wind, blackouts, satellite mispointing issues, etc.

The second part of the work on the experimental activities was devoted to evaluating the effectiveness of two Fade Mitigation Techniques. First, time series of attenuation at Ka and Q band were processed to assess the gain originating from implementing time diversity. Results point out the usefulness of such a technique: as an example, for a target availability level of 99.99%, using a retransmission delay of 30 minutes, time diversity would allow to reduce the power margin to cope with atmospheric attenuation at 19.7 GHz from 21 dB to 11 dB. An

DISTRIBUTION A: Distribution approved for public release. Distribution unlimited

even more marked advantage was found from the application of site diversity; taking advantage of the data collected both at Spino d'Adda and Milan, joint attenuation statistics were derived: as an example of the results obtained, the power margin to achieve a system availability of 99.99% at Q band shifts from approximately 40 dB using a single link to roughly 22.5 dB using both stations. The experimental data were also processed to investigate the dynamics of the signal attenuation at Ka and Q band, specifically by calculating fade duration and fade slope statistics, both of which are tightly linked to the correct operation of FMTs: as an example, the results indicate that fade events higher than 15 dB exceed 1000 seconds for 20% and 30% of the yearly time at Ka band and Q band, respectively; on the other hand, fade slope statistics point out that the maximum increase rate of the attenuation is around 0.35 dB and 0.45 dB at Ka band and Q band, respectively.

Taking advantage of the experimental data, the research activities also focused on the development of physically-based propagation prediction models. A significant effort was devoted to devising ST (Space-Time) MultiEXCELL, a propagation oriented methodology for the synthesis of rain fields correlated in space and time. ST MultiEXCELL reproduces the local rainfall process by means of an ensemble of synthetic cells whose position in space and evolution in time statistically resemble the rain cell features observed in real rain fields. ST MultiEXCELL embeds all the features of MultiEXCELL (preservation of the input $P(R)$ and of the rain rate spatial correlation), but, in addition, aims at overcoming its main limitation, i.e. the lack of temporal correlation among the synthetic rain fields. This new features was introduced by modeling the temporal evolution of single rain cells: more intense rain cells are modeled so as to evolve faster than stratiform ones; moreover, as the cell becomes more intense, its size reduces, and vice versa. At the same time, in each rain event, the rain cell ensemble is constrained to evolve in such a way to match a target linear trend of the fractional rainy area, whose slope steepness depends on the event type (convective or stratiform, respectively). Besides structural evolution, each rain cells also moves across the map according to a velocity and a path that are linked to the wind intensity and direction corresponding to the 700-mbar isobar height. In turn, such values are extracted from the ERA40 database produced by the ECMWF. The only additional inputs to ST MultiEXCELL are the ERA40 time series of the rain accumulated in 6 hours, M_t, and the local $P(R)$. The former are used as a reference to retain the correct temporal correlation among rainy and dry periods, as well as the seasonal/monthly rain accumulation tendency, while the latter serves as an indication of the overall yearly rain accumulation and of the proportion between stratiform and convective rain events affecting the site. Tested against local data collected in Spino d'Adda, ST MultiEXCELL has shown to correctly reproduce the spatial and temporal correlation of the rain rate. In fact, as for the former, the decorrelation trend with distance derived from ST MultiEXCELL follows the one obtained from the rain maps synthesized by MultiEXCELL, which, in turn, was found to correctly reproduce the spatial correlation of the rain rate. As for the latter, the long-term data collected by the Spino d'Adda rain gauge were used as a reference to assess the temporal decorrelation of the rain rate derived from ST MultiEXCELL maps.

ST MultiEXCELL was used to simulate the performance of a realistic site diversity system using as the reference scenario two ground stations deployed in the area of Rome, NY, and operating at V-band and W-band, namely at 50, 70, 80, 90 GHz. The interaction between the system and rain fields was simulated to calculate single- and two-site rain attenuation

DISTRIBUTION A: Distribution approved for public release. Distribution unlimited

statistics. Taking full advantage of ST MultiEXCELL (time correlated rain maps), a realistic site diversity system was simulated: given that the switching between the stations is associated to a delay intrinsic to the system (i.e. traffic re-routing), too many switches, if too close one to the other, might limit the system performance. A possible way to avoid this is to associate a proper attenuation threshold A_{th} to one station (e.g. the slave one in a master-slave system) such that the switch will occur only if the differential attenuation between the two stations exceeds A_{th}. The results were elaborated to assess the impact of such a threshold on the number of switches and on the limitation thus induced on the site diversity gain. The results indicate that a good tradeoff for the choice of A_{th} is 10 dB, which allows reducing the number of switches to 2000-4000 – depending on the frequency and baseline distance – with a maximum gain loss of 1.3 dB at outage probability P = 0.01%, if compared to the ideal site diversity system, in which the switch is assumed to occur instantaneously. As an example, considering the 20 km-baseline and A_{th} = 10 dB, the attenuation using two sites is 30.4 dB at 50 GHz, reaching 40, 43.15 and 45.4 dB respectively at 70, 80 and 90 GHz, again for P = 0.01 %. The associated yearly number of switches are 2125, 3010, 3350 and 3660, respectively. With the same threshold and same level of probability, for D = 50 km, the diversity system margin ranges between 23.35 dB (50 GHz) and 35.6 dB (90 GHz), with the corresponding yearly number of switches between 2210 and 3310.

Besides ST MultiEXCELL, taking strong advantage of the experimental data collected by means of the NASA equipment, the modeling activity also focused on developing the Enhanced Synthetic Storm Technique (E-SST), a new model introducing improvements to the original Synthetic Storm Technique (SST). The specific novel key features of the E-SST are: 1) it receives as input detailed information on the rain height and on the storm velocity, which, in this work, are extracted from ECMWF NWP products every hour (ERA5 database); 2) it discriminates between stratiform and convective events; 3) it makes use of different rain heights depending on the type of event. The accuracy of E-SST was tested against a full year (2017) of the propagation data collected by the NASA equipment installed at Politecnico di Milano. To this aim, a novel approach to isolate rain attenuation from the received beacon power was conceived and presented. The accuracy in reproducing the CCDF of the total attenuation A (both at 19.7 and 39.4 GHz) was first evaluated by directly applying the E-SST; compared to the SST, the RMS of the (ITU-R defined) error figure reduces from 24.8% (SST) to 8.1% (E-SST) at Ka band and from 22.7% (SST) to 5.2% (E-SST) at Q band. A further improvement in the prediction performance was achieved by embedding the E-SST into a more accurate frequency scaling technique, i.e. by using as an additional input to the model also A measured at 19.7 GHz, with the RMS of the error on first-order statistics reaching 4.83% (Q band). The advantage of using such a frequency scaling approach is even more visible when the time series of A are considered: results show that the frequency scaling accuracy achieved by using the E-SST is approximately comparable to the one obtained by relying on DSD data, which, however, are seldom available: the RMS of the absolute error at Q band is 1.8 dB and 1.7 dB using E-SST and DSD data, respectively.

Starting from the results achieved with E-SST, two methodologies (TAFS and S-TAFS) aimed at up-scaling in frequency (including the W band) the total tropospheric attenuation time series measured at a lower frequency (e.g. Ka band) were developed. Both methods include a procedure to isolate the attenuation induced by the different atmospheric constituents, each of which is separately up-scaled to the target frequency with a solid

DISTRIBUTION A: Distribution approved for public release. Distribution unlimited

physically-based approach. Though more accurate, TAFS requires more detailed information as inputs (e.g. radiometric and disdrometer data); on the other hand S-TAFS makes use of limited inputs and it is based on simplified assumptions, which reflect in a slightly worse performance, but also in a wider applicability. In order for S-TAFS to be applicable to as many sites as possible, it does not strictly require the rain rate time series as input, though better results are achievable with such input data. Tests against the NASA propagation data collected in Milan in scaling total attenuation from the Ka band to the Q band indicate that, on first-order statistics, TAFS provides an RMS error of 1.72%, while that associated to S-TAFS ranges between 4.22% and 4.7%. Similar results are obtained for instantaneous predictions, which are key for the design and operation of Fade Mitigation Techniques (FMTs): the average RMS of the error on the time series was found to be 0.38 dB for TAFS, while it varies between 0.41 dB and 0.43 for S-TAFS.

Given the positive results achieved with these tests and the solid physical basis underpinning TAFS, this model was applied to predict time series of the total tropospheric attenuation *A* at W band (namely 80 and 90 GHz), for which no measurements are currently available, starting from the Ka band attenuation data measured in Milan. The CCDF of *A* indicate that approximately 26 dB and 30 dB are required at 80 and 90 GHz, respectively, to guarantee that the system is available for 99.5% of the yearly time. Lower margins are needed taking advantage of time diversity, whose gain was explored thanks to the availability of time series of *A* at W band: as an example, with a retransmission delay of 30 minutes, the system availability increases to 99.95% using a margin of roughly 30 dB and 35 dB at 80 and 90 GHz, respectively. Finally, also the fade dynamics were investigated: as an example, to be compared with what is obtained at Ka band and Q band, the results indicate that fade events higher than 15 dB exceed 1000 seconds for probabilities ranging between 60% and 70% of the yearly time at 80 and 90 GHz, respectively.

DISTRIBUTION A: Distribution approved for public release. Distribution unlimited

REFERENCES

[Ahrens, 1994] D. Ahrens, 1994, "Meteorology Today: an introduction to weather, climate and the environment", 9th edn. Brooks/Cole, Belmont.

[Allnutt, 2010] J. E. Allnutt, 2010, "Satellite to Ground Radiowave Propagation", 2nd Edition, The Institution Of Engineering And Technology, May.

[Arapoglou and Panagopoulos, 2011] P. Arapoglou, A. D. Panagopoulos, 2011, "A tool for synthesizing rain attenuation time series in LEO Earth observation satellite downlinks at Ka band", EuCAP 2011, pp. 1467 – 1470, Prague, Czech Republic.

[Atlas et al., 1973] D. Atlas, R. C. Srivastava, R. S. Sekhon, "Doppler radar characteristics of precipitation at vertical incidence", Rev Geophys Space Phys, 2, pp. 1 –35, 1973.

[Beard and Chuang, 1987] K. Beard, C. Chuang, 1987, "A New Model for the Equilibrium Shape of Raindrops", Journal of the Atmospheric Sciences, Vol. 44, No. 11, pp. 1509 – 1524.

[Biscarini et al., 2016] M. Biscarini, F. S. Marzano, M. Montopoli, K. De Sanctis, L. Iess, M. Montagna, M. Mercolino, M. Lanucara, 2016, "Optimizing Data Volume Return for Ka-Band Deep Space Links Exploiting Short-Term Radiometeorological Model Forecast," IEEE Transactions on Antennas and Propagation, vol. 64, issue 1, pp. 235-250, Jan. 2016.

[Boulanger et al, 2013] X. Boulanger, L. Feral, L. Castanet, N. Jeannin, G. Carrie, F. Lacoste, 2013, "A Rain Attenuation Time-Series Synthesizer Based on a Dirac and Lognormal Distribution", IEEE Transactions on Antennas and Propagation, vol. 61, issue 3, pp. 1396-1406, March 2013.

[Boulanger et al., 2015] X. Boulanger, B. Gabard, L. Casadebaig, L. Castanet, 2015, "Four Years of Total Attenuation Statistics of Earth-Space Propagation Experiments at Ka-Band in Toulouse," IEEE Transactions on Antennas and Propagation, vol. 63, no. 5, pp. 2203-2214, May 2015.

[Boulanger et al., 2019] X. Boulanger, B. Benammar, L. Castanet, 2019, "Propagation Experiment at Ka-Band in French Guiana: First Year of Measurements", IEEE Antennas and Wireless Propagation Letters, Vol. 18, No. 2, pp. 241-244, 2019.

[Bryant et al., 2001] G. H. Bryant, I. Adimula, C. Riva, G. Brussaard, 2001, "Rain attenuation statistics from rain cell diameters and heights", Int. J. Satellite Commun., vol. 19, no. 3, pp. 263–283, 2001.

[Capsoni and Luini, 2009] C. Capsoni, L. Luini, 2009, "Analysis of the spatial and temporal properties of rain cells for rainfall modeling purposes", Italian Journal of Remote Sensing, 41 (3): 51-62.

[Capsoni et al., 1987] C. Capsoni, F. Fedi, C. Magistroni, A. Paraboni, A. Pawlina, 1987, "Data and theory for a new model of the horizontal structure of rain cells for propagation applications", Radio Science, Volume 22, Number 3, Pages: 395-404, May-June.

[Capsoni et al., 2006] C. Capsoni, L. Luini, A. Paraboni, C. Riva, 2006, "Stratiform and convective rain discrimination deduced from local P(R)," IEEE Transactions on Antennas and Propagation, vol. 54, issue 11, pp. 3566-3569, Nov. 2006.

[Capsoni et al., 2009a] C. Capsoni, L. Luini, A. Paraboni, C. Riva, A. Martellucci, 2009, "A new prediction model of rain attenuation that separately accounts for stratiform and convective rain", IEEE Transactions on Antennas and Propagation, Vol 57, No. 1, January, Page(s): 196 - 204.

DISTRIBUTION A: Distribution approved for public release. Distribution unlimited

[Capsoni et al., 2010] C. Capsoni, L. Luini, M. D'Amico, 2010, "The MultiEXCELL model for the prediction of the radio interference due to hydrometeor scattering", EuCAP 2010, pp. 1-5, 12-16 April, Barcelona, Spain.

[Crane, 1996] R. K. Crane, 1996, "Electromagnetic Wave Propagation Through Rain", New York, Wiley.

[D'Amico et al., 1998] M. G. D'Amico, A. R. Holt, C. Capsoni, 1998, "An anisotropic model of the melting layer", Vol. 33, Issue 3, pp: 535–552, May-June.

[Deirmendjian, 1969] D. Deirmendjian, 1969, "Electromagnetic Scattering on Spherical Polydispersions", Elsevier, 290 pp.

[Dissanayake et al., 1997] A Dissanayake, J.E. Allnutt, F. Haidara, 1997, "A prediction model that combines rain attenuation and other propagation impairments along Earth-space paths," IEEE Transactions on Antennas and Propagation 45 (10): 1546 – 1558, November 1997.

[DoD] DoD/USAF Contract FA8650-04-C-0049, "MEMS-Enabled W-Band SATCOM Phased Arrays".

[Drufuca, 1974] G. Drufuca, 1974, "Rain attenuation statistics for frequencies above 10 GHz from rain gauge observations," J. Rech. Atmos., 1-2, 399-411, 1974.

[Dvorak and Capsoni, 2016] P. Dvorak, C. Capsoni, 2016, "Model for synthesis of short-term tropospheric amplitude scintillation", EuCAP 2016, pp. 1-4, 10-15 April, Davos, Switzerland

[DTV] Available online: http://space.skyrocket.de/doc_sdat/directv-10.htm.

[DVB-S2] ETSI EN 302 307 vl.2.l (2009-08), European Standard, 2009, "Digital Video Broadcasting (DVB); Second generation framing structure, channel coding and modulation systems for Broadcasting, Interactive Services, News Gathering and other broadband satellite applications (DVB-S2)".

[EOARD, 2013] EOARD Award FA8655-12-1-2062, 2013, "Performance evaluation of Satellite Communication systems operating in the Q/V/W band".

[EOARD, 2017] EOARD Award FA8655-13-1-3081, 2017, "Development of a comprehensive propagation model for SatCom systems at high frequency in the framework of the Alphasat experiment".

[ESA 17760] ESA/ESTEC/Contract 17760/03/NL/JA, "Characterisation and modelling of propagation effects in 20-50 GHz band".

[ESA 18278] ESA/ESTEC/Contract 18278/04/NL/US, "Assessment of radiowave propagation for satellite communication and navigation systems in tropical and sub-tropical areas".

[ESA 20887] ESA/ESTEC/Contract 20887/07/NL/LvH, "Verification of propagation impairment mitigation techniques".

[ESA 21083] ESTEC Contract No. 21083/07/NL/JA, "Study of Data Downlink Systems for Earth Observation Satellites operating in the 26 GHz Band".

[Féral et al., 2003] L. Féral, H. Sauvageot, L. Castanet, J. Lemorton, 2003, "HYCELL - A new hybrid model of the rain horizontal distribution for propagation studies: Part 1, Modeling of the rain cell", Radio Science, 38(3).

[Ghirardin et al., 2016] S. Ghirardin, C. Capsoni, L. Luini, 2016, "Time Evolution of Synthetic Rain Cells for the Synthesis of Attenuation Time Series", EuCAP 2016, 10-15 April, pp. 1-5, Davos, Switzerland.

[Gunn and Kinzer, 1949] R. Gunn and G. D. Kinzer, "The terminal velocity of fall for water droplets in stagnant air", J. Atmos. Sci., vol. 6, no. 4, pp. 243–248, 1949.

DISTRIBUTION A: Distribution approved for public release. Distribution unlimited

[ITU-R P.311-14] Acquisition, presentation and analysis of data in studies of radiowave propagation. Geneva, 2013, ITU-R recommendation P.311-14.

[ITU-R P.618-13] Propagation data and prediction methods required for the design of Earth-space telecommunication systems. Geneva, 2017, ITU-R recommendation P.618-13.

[ITU-R P.676-12] Attenuation by atmospheric gases. Geneva, 2019, ITU-R recommendation P.676-12.

[ITU-R P.837-7] Characteristics of Precipitation for Propagation Modelling. Geneva, 2017, ITU-R recommendation P. 837-7.

[ITU-R P.838-3] Specific attenuation model for rain for use in prediction methods. Geneva, 2005, ITU-R recommendation P.838-3.

[ITU-R P.839-4] Rain height model for prediction methods. Geneva, 2013, ITU-R recommendation P.839-4.

[ITU-R P.840-8] Attenuation due to clouds and fog. Geneva, 2019, ITU-R recommendation P.840-8.

[Karasawa et al., 1988] Y. Karasawa, M. Yamada, J. E. Allnutt, 1988, "A New Prediction Method for Tropospheric Scintillation on Earth-Space Paths", IEEE Transactions on Antennas and Propagation, Vol. AP-36, n. 11, November, pp. 1608-1614.

[KASAT] Available online: http://www.eutelsat.com/en/satellites/the-fleet/EUTELSAT-KA-SAT.html.

[Jeannin et al., 2012] N. Jeannin, L. Féral, H. Sauvageot, L. Castanet, F. Lacoste, 2012, "A large-scale space-time stochastic simulation tool of rain attenuation for the design and optimization of adaptive satellite communication systems operating between 10 and 50 GHz", International Journal of Antennas and Propagation, Article ID 749829, 16 pages.

[Jeannin et al., 2014] N. Jeannin, L. Castanet, J. Radzik, M. Bousquet, B. Evans, P. Thompson, 2014, "Smart gateways for terabit/s satellite", International Journal of Satellite Communications and Networking, vol. 32 (n° 2). pp. 93-106.

[Lam et al., 2012] H.Y. Lam, L. Luini, J. Din, C. Capsoni, A. D. Panagopoulos, 2012, "Investigation of Rain Attenuation in Equatorial Kuala Lumpur", IEEE Antennas and Wireless Propagation Letters, vol. 11, Page(s): 1002-1005.

[Liebe et al., 1993] H. J. Liebe, G. A. Hufford, M. G. Cotton, 1993, "Propagation modeling of moist air and suspended water/ice particles at frequencies below 1000 GHz", in Proc. AGARD 52nd Spec. Meeting EM Wave Propag.

[Loreti and Luglio, 2002] P. Loreti, M. Luglio, 2012, "Interference evaluations and simulations for multisatellite multibeam systems", Wiley international journal of satellite communications, vol. 20, no. 4, pp. 261-281.

[Luini, 2016] L. Luini, 2016, "Modeling and Synthesis of 3-D Water Vapor Fields for EM Wave Propagation Applications", IEEE Transactions on Antennas and Propagation, vol. 64, no. 9, Page(s): 3972 - 3980, September.

[Luini, 2017] L. Luini, 2017, "A Comprehensive Methodology to Assess Tropospheric Fade Affecting Earth-Space Communication Systems", IEEE Transactions on Antennas and Propagation, vol. 65, no. 9, Page(s): 3654 - 3663, July.

[Luini and Capsoni, 2010] L. Luini, C. Capsoni, 2010, "A physically based methodology for the evaluation of the rain attenuation on terrestrial radio links", EuCAP 2010, pp. 1-5, 12th-16th April, Barcelona, Spain.

[Luini and Capsoni, 2011] L. Luini, C. Capsoni, 2011, "MultiEXCELL: a new rain field model for propagation applications", IEEE Transactions on Antennas and Propagation, vol. 59, no. 11, Page(s): 4286 – 4300, November.

DISTRIBUTION A: Distribution approved for public release. Distribution unlimited

[Luini and Capsoni, 2012] L. Luini, C. Capsoni, 2012, "Estimating the Spatial Cumulative Distribution of Rain from Precipitation Amounts", Radio Sci., 47, RS1005, 2012.

[Luini and Capsoni, 2013] L. Luini, C. Capsoni, 2013, "A Unified Model for the Prediction of Spatial and Temporal Rainfall Rate Statistics", IEEE Transactions on Antennas and Propagation, vol. 61, no. 10, Page(s): 5249 - 5254, October 2013.

[Luini and Capsoni, 2013b] L. Luini, C. Capsoni, 2013, "A Rain Cell Model for the Simulation and Performance Evaluation of Site Diversity Schemes", IEEE Antennas and Wireless Propagation Letters, Vol. 12, No. 1, Page(s): 1327-1330, doi: 10.1109/LAWP.2013.2285400.

[Luini and Capsoni, 2013c] L. Luini, C. Capsoni, 2013, "On the Relationship Between the Spatial Correlation of Point Rain Rate and of Rain Attenuation on Earth-Space Radio Links," IEEE Transactions on Antennas and Propagation, vol. 61, no. 10, Page(s): 5255 - 5263, October.

[Luini and Capsoni, 2014] L. Luini, C. Capsoni, 2014, "Modeling High Resolution 3-D Cloud Fields for Earth-space Communication Systems", IEEE Transactions on Antennas and Propagation, vol. 62, no. 10, Page(s): 5190 - 5199, October.

[Luini and Capsoni, 2015] L. Luini, C. Capsoni, 2015, "Joint Effects of Clouds and Rain on Ka-Band Earth Observation Data Downlink Systems", pp. 1-5, EuCAP 2015, 12-17 April 2015, Lisbon, Portugal.

[Luini and Riva, 2016] L. Luini, C. Riva, 2016, "Improving the Accuracy in Predicting Water Vapor Attenuation at Millimeter-wave for Earth-space Applications", IEEE Transactions on Antennas and Propagation, vol. 64, no. 6, Page(s): 2487 - 2493, June.

[Luini and Riva, 2017] L. Luini, C. Riva, 2017, "A Simplified Model to Predict Oxygen Attenuation on Earth-space Links", IEEE Transactions on Antennas and Propagation, vol. 65, no. 12, Page(s): 7217 - 7223, December.

[Luini et al., 2007] L. Luini, C. Riva, C. Capsoni, A. Martellucci, 2007, "Attenuation in non rainy conditions at millimeter wavelengths: assessment of a procedure", IEEE Transactions on Geoscience and Remote Sensing, pp. 2150-2157, Vol. 45, Issue 7, July.

[Luini et al., 2011a] L. Luini, L. Emiliani, C. Capsoni, 2011, "Planning of Advanced SatCom Systems Using ACM Techniques: The Impact of Rain Fade", EuCAP 2011, pp. 3965-3969, April, Rome, Italy.

[Luini et al., 2011b] L. Luini, N. Jeannin, C. Capsoni, A. Paraboni, C. Riva, L. Castanet, J. Lemorton, 2011, "Weather radar data for site diversity predictions and evaluation of the impact of rain field advection", Int. J. Satell. Commun. Network.; 29:79–96.

[Luini et al., 2018a] L. Luini, C. Riva, R. Nebuloni, M. Mauri, J. Nessel, A. Fanti, "Calibration and Use of Microwave Radiometers in Multiple-site EM Wave Propagation Experiments", EuCAP 2018, 9-13 April 2018, London, UK.

[Luini et al., 2018b] L. Luini, G. Roveda, M. Zaffaroni, M. Costa, C. Riva, 2018, "EM Wave Propagation Experiment at E Band and D Band for 5G Wireless Systems: Preliminary Results," EuCAP 2018, 9-13 April 2018, pp. 1-5, London, UK.

[Manabe et al., 1987] T. Manabe, H. J. Liebe, G. A. Hufford, 1987, "Complex permittivity of water between 0 and 30 THz", 12th International Conference on Infrared and Millimeter Waves, pp. 229-230, 1987.

[Martellucci et al., 2002] A. Martellucci, J. P. V. Poiares Baptista, G. Blarzino, 2002, "New climatological databases for ice depolarisation on satellite radio links," COST 280 "Propagation Impairment Mitigation for MillimetreWave Radio Systems", PM3037, 1st Int. Workshop, Malvern, U.K, July.

DISTRIBUTION A: Distribution approved for public release. Distribution unlimited

[Matricciani, 1996] E. Matricciani, 1996, "Physical-mathematical model of the dynamics of rain attenuation based on rain rate time series and two layer vertical structure of precipitation," Radio Science, Vol. 31, No. 2, March-April 1996, pages 281-295.

[McCartney, 1976] E. J. McCartney, "Optics of the Atmosphere: Scattering by Molecules and Particles", New York: Wiley, 1976.

[Mishchenko et al., 2002] M. Mishchenko, L. Travis, A. Lacis, 2002, "Scattering, Absorption, and Emission of Light by Small Particles", Cambridge University.

[Mukherjee et al., 2010a] S. Mukherjee, M. De Sanctis, T. Rossi, E. Cianca, M. Ruggieri, R. Prasad, 2010, "On the Optimization of DVB-S2 Links in EHF Bands", IEEE Aerospace Conference 2010, Big Sky (Montana), ISBN: 978-1-4244-3887-7, pp. 1-11, March 6-10.

[Mukherjee et al., 2010b] S. Mukherjee, M. De Sanctis, T. Rossi, E. Cianca, M. Ruggieri, R. Prasad, 2010, "Mode Switching Algorithms for DVB-S2 Links in W Band", IEEE Globecom 2010, ISBN: 978-1-4244-5637-6, Miami (Florida), 6-10 December.

[Nebuloni et al., 2017] R. Nebuloni, C. Riva, L. Luini, 2017, "Ka-to-W band EM wave propagation: tropospheric effects and countermeasures". Chapter, Wave Propagation Concepts for Near-Future Telecommunication Systems, May 3rd, 2017.

[Nessel et al., 2015] J. Nessel, M. Zemba, L. Luini, C. Riva, 2015, "Comparison of Instantaneous Frequency Scaling from Rain Attenuation and Optical Disdrometer Measurements at K/Q bands," 21st Ka and Broadband Communications, Navigation and Earth Observation Conference, Bologna (Italy), pp. 1-10, 12-14 October, 2015.

[O3b] http://www.o3bnetworks.com/.

[Oguchi, 1983] T. Oguchi, 1983, "Electromagnetic wave propagation and scattering in rain and other hydrometeors", Proc. IEEE, vol. 71, pp. 1029-1077.

[Pruppacher and Klett, 2010] H.R. Pruppacher, J.D. Klett, "Microphysics of Clouds and Precipitation", Springer, 2010.

[Quinn and Fernandes, 1991] B. G. Quinn, J. M. Fernandes, "A Fast Technique for the Estimation of Frequency", Biometrika, vol. 78, pp. 489–497, Sept. 1991.

[Raynaud et al., 2000] L. Raynaud, I. Chenerie, J. Lemorton, 2000, "Modeling of Radiowave Scattering in the Melting Layer of Precipitation", IEEE Transactions on Geoscience and Remote Sensing, 38(4), 1574–1584.

[Riva et al., 2014] C. Riva, C. Capsoni, L. Luini, M. Luccini, R. Nebuloni, A. Martellucci, 2014, "The Challenge of Using the W Band in Satellite Communication", Int. J. Satell. Commun. Network.; 32:187–200.

[Rosenkranz, 1998] P. Rosenkranz, 1998 , "Water vapor microwave continuum absorption: A comparison of measurements and models", Radio Sci., vol. 33, no. 4, pp. 919–928, Jul./Aug.

[Rossi et al., 2009] T. Rossi, E. Cianca, M. Lucente, M. De Sanctis, C. Stallo, M. Ruggieri, A. Paraboni, A. Vernucci, L. Zuliani, L. Bruca, G. Codispoti, 2009, "Experimental Italian Q/V Band Satellite Network", IEEE Aerospace Conference 2009, Big Sky (MT, USA), paper no. 1463, pp. 1-9, ISBN: 978-1-4244-2622-5, March 7-14, 2009.

[Rossi et al., 2011] T. Rossi, M. De Sanctis, D. Di Mattia, M. Ruggieri, 2011, "Performance Analysis and Optimization of Site Diversity Techniques for EHF Satellite Links", Proc. Of IEEE Aerospace Conference 2011, Big Sky (MT), Mar.

[Rossi et al., 2014] T. Rossi, F. Maggio, M. De Sanctis, M. Ruggieri, S. Falzini, M. Tosti, 2014, "System analysis of smart gateways techniques applied to Q/V-band high

DISTRIBUTION A: Distribution approved for public release. Distribution unlimited

throughput satellites," IEEE Aerospace Conference, pp. 1-10, 1-8 March 2014, Big Sky, Montana, USA.

[Rossi et al., 2016] T. Rossi, M. De Sanctis, M. Ruggieri, C. Riva, L. Luini, G. Codispoti, E. Russo, G. Parca, 2016, "Satellite Communication and Propagation Experiments Through the Alphasat Q/V Band Aldo Paraboni Technology Demonstration Payload", IEEE Aerospace and Electronic Systems Magazine, Vol. 31, No. 3, Page(s): 18 – 27, March 2016.

[Salonen and Uppala, 1991] E. Salonen, S. Uppala, 1991, "New prediction method of cloud attenuation", Electron. Lett., vol. 27, no. 12, pp. 1106–1108, Jun.

[Shettle, 1989] E. P. Shettle, 1989, "Models of aerosols, clouds and precipitation for atmospheric propagation studies", in AGARD conference 454(15), pp:. 1-13.

[Stallo et al., 2009] C. Stallo, M. Lucente, T. Rossi, E. Cianca, M. Ruggieri, A. Paraboni, C. Cornacchini, A. Vernucci, M. T. Nocerino, A. Ceccarelli, L. Bruca, G. Codispoti, M. De Sanctis, 2009, "TRANSPONDERS: Research and Analysis for the Development of Telecommunication Payloads in Q/V Bands", IEEE Aerospace Conference 2009, Big Sky (MT, USA), paper no. 1412, pp. 1-9, ISBN: 978-1-4244-2622-5, March 7-14.

[STD ATM] U.S. Standard Atmosphere, 1976, Report Number: NASA-TM-X-74335; NOAA-S/T-76-1562, 241 pages, U.S. Government Printing Office, Washington, D.C.

[Taylor, 1938] G. I. Taylor, 1938, "The spectrum of turbulence," Proc. R. Soc. London A, 164, 476-490, 1938.

[Thurai et al., 2014] M. Thurai, V. N. Bringi, A. B. Manić, N. J. Šekeljić, B. M. Notaroš, 2014, "Investigating raindrop shapes, oscillation modes, and implications for radio wave propagation", Radio Sci., 49, 921-932.

[Thompson, 2007] A. Thompson, 2007, "Simulating the Adiabatic Ascent of Atmospheric Air Parcels using the Cloud Chamber", Department of Meteorology, Penn State.

[Ulbrich, 1983] C. W. Ulbrich, "Natural variations in the analytical form of the raindrop size distribution", J. Climate Appl. Meteor., 22, 1764–1775, 1983.

[Van de Hulst, 1957] H. C. Van de Hulst, 1957, "Light Scattering by Small Particles", Wiley (NY, 1957; Dover, NY, 1981).

DISTRIBUTION A: Distribution approved for public release. Distribution unlimited

LIST OF SYMBOLS, ABBREVIATIONS, AND ACRONYMS

ACM	Adaptive Coding and Modulation
ACTS	Advanced Communications Technology Satellite
AFRL	Air Force Research Laboratory
AES	Ancillary Equipment Subsystem
APSK	Asymmetric Phase-Shift Keying
ARTES	Advanced Research in Telecommunications Systems
ASI	Italian Space Agency
ATM PROP	ATMospheric simulator for PROPagation applications
ATS	Applications Technology Satellite
BBS	BaseBand Subsystem
BCH	Bose-Chaudhuri-Hocquenghem
BER	Bit Error Rate
CDF	Cumulative Distribution Function
CCDF	Complementary Cumulative Distribution Function
CNES	Centre national d'études spatiales
CNR	Carrier-to-Noise Ratio
CW	Continuous Wave
DAQ	Data Acquisition
DEIB	Dipartimento di Elettronica, Informazione e Bioingegneria
DRX	Data Receiver
DSD	Drop Size Distribution
DVB	Digital Video Broadcasting
E-SST	Enhanced-Synthetic Storm Technique
EBCM	Extended Boundary Condition Method
ECC	Experimental Control Center
ECMWF	European Centre for Medium-range Weather Forecast
EHE	Electrical Harness Element
EHF	Extremely High Frequency
EIRP	Effective Isotropic Radiated Power
EM	ElectroMagnetic
EO	Earth Observation
EOARD	European Office of Aerospace Research and Development
EOC	End Of Coverage
ERA	ECMWF Re-Analysis
ERA5	ECMWF Re-Analysis 5
ERA40	ECMWF Re-Analysis 40
ESA	European Space Agency
ETS	Engineering Test Satellite
ETSI	European Telecommunications Standards Institute
EVM	Error Vector Magnitude
EXCELL	EXponential CELL

DISTRIBUTION A: Distribution approved for public release. Distribution unlimited

FEC	Forward Error Correction
FER	Frame Error Rate
FIM	Fredholm-Integral-Method
FFT	Fast Fourier Transform
FGE	Frequency Generator Element
FMT	Fade mitigation Technique
GEO	Geosynchronous Earth Orbit
GSBS	Ground Station Back-End Subsystem
GSFS	Ground Station Front-End Subsystem
HPAE	High Power Amplifier Element
IE	Infrastructure Element
IF	Intermediate Frequency
IFEE	Intermediate Frequency Equipment Element
IOV	In-Orbit Validation
ITU-R	International Telecommunication Union – Radiocommunication sector
LDPC	Low-Density Parity Check
LEO	Low Earth Orbit
LNA	Low Noise Amplifier
MEO	Medium Earth Orbit
MODCOD	MODulation and CODding
MultiEXCELL	Multi EXponential CELL
MWR	MicroWave Radiometer
NASA	National Aeronautics and Space Administration
NNIAD	Nearest Neighbour InterAggregate Distance
NNICD	Nearest Neighbour InterCellular Distance
NWP	Numerical Weather Prediction
NY	New York
ONERA	Office National d'Etudes et de Recherches Aérospatiales
PC	Personal Computer
PDF	Probability Density Function
PI	Principal Investigator
PL	Physical Layer
PLL	Phased-Locked Loops
PLFRAME	Physical Layer Frame
POLIMI	Politecnico di Milano
PSD	Particle Size Distribution
PSK	Phase Shift Keying
QoS	Quality of Service
QPSK	Quadrature Phase Shift Keying
RAL	Rutherford Appleton Laboratory
RAOBS	RAdiosonde OBServation
RF	Radio Frequency
RMS	Root Mean square

DISTRIBUTION A: Distribution approved for public release. Distribution unlimited

RH	Relative Humidity
RPG	Radiometer Physics GmbH
RSS	Received Signal Strength
S-TAFS	Simplified-Total Attenuation Frequency Scaling
SatCom	Satellite Communication
SE	Space Exploration
SHE	Signal Harness Element
SMOC	Stochastic MOdel of Clouds
SMOV	Stochastic MOdel of water Vapor
SNR	Signal-to-Noise Ratio
SSI	Sky Status Indicator
SST	Synthetic Storm Technique
ST MultiEXCELL	Space-Time Multi EXponential CELL
TAFS	Total Attenuation Frequency Scaling
TDP	Techonology Development Payload
TKK	Teknillinen KorkeaKoulu
TLC	Telecommunication
TLE	Two-Line Element
ULPC	Up-link Power Control
UPS	Uninterruptible Power Supply
US	United States
USA	United States of America
UTC	Coordinated Universal Time

DISTRIBUTION A: Distribution approved for public release. Distribution unlimited